Lightweight, affordable, low power solar groundwater piston pump for rural remote regions.

AZEEM UDDIN, A.I.

2020

LIGHTWEIGHT, AFFORDABLE, LOW POWER SOLAR GROUNDWATER PISTON PUMP FOR RURAL REMOTE REGIONS

AZEEM UDDIN AZEEM ISLAM

PhD **2020**

LIGHTWEIGHT, AFFORDABLE, LOW POWER SOLAR GROUNDWATER PISTON PUMP FOR RURAL REMOTE REGIONS

PhD THESIS

AZEEM UDDIN AZEEM ISLAM

This research programme was carried out in collaboration with Daima Energy Ltd. (UK)

Supervisors: Dr. Firdaus Muhammad Sukki
Prof. James Njuguna

July 2020

This thesis is submitted in partial fulfilment of the requirements for the degree of Doctor of Philosophy

DEDICATION

I dedicate this thesis to my family, especially to my parents for being the heart of my success, showing me the way to education and encouraging in hardships that I faced during my studies.

ACKNOWLEDGEMENTS

Thanks to GOD, the merciful and the passionate, for providing me the opportunity to step in the excellent world of science. To be able to step strong and smooth in this way, I have also been supported and supervised by many people to whom I would like to express my deepest gratitude.

Dr. Firdaus Muhammad Sukki and Prof. Dr. James Njuguna have been the ideal thesis supervisors. Their sage advice, insightful criticisms, and patient encouragement aided the writing of this thesis in innumerable ways.

Their steadfast support for this project was greatly needed and deeply appreciated. In addition, I would like to forward my deep gratitude to Daima Energy Ltd., Scottish Institute of Remanufacture and Robert Gordon University for sponsoring my PhD study and living financial support. The Daima Energy Ltd. also provided technical inputs to this project which were the basis of this design study.

Azeem Uddin Azeem Islam

ABSTRACT

Solar photovoltaic powered groundwater pumping systems (SPWPS) are popular way of fetching water from boreholes in semi-arid areas in rural remote regions of most developing countries where commercial water and electricity supply is out of reach. As the climate change, borehole depth is ever increasing into hundreds of metres below the ground surface due to water table drop in such marginal regions.

In a SPWPS, the required energy to fulfil water demand at a certain head is termed as the required hydraulic energy which is maintained by the pump unit of SPWPS. However, this acts ultimately as a load on the PV generator. The pump unit typically requires more power in order to maintain this hydraulic energy. For high head systems, groundwater piston pumps perform better than centrifugal pumps. A detailed literature review established that the current piston pumps have designs limitations that acts as load on the pump driver which use extra external and internal mechanical components. These include long piston drive rods, connecting rod, meshing gears, crossheads and crossways.

This study put forth a new concept design of a groundwater piston pump optimised for power consumption using scotch-yoke mechanism that excludes unnecessary components in the pump in order to conserve power usage. A mathematical model was built to support the claim of low power consumption by the new pump design. Widely used computer aided design and finite element analysis (CAD/FEA) technique was used to ensure the structural viability of the concept design for high head application which is based on material selection process. The study also compares the concept pump power consumption among existing photovoltaic (PV) operated pumps including piston rod and non-piston rod pumps. The developed mathematical model for power consumption finds

significant power savings when compared with benchmarked low power consuming long piston rod pumps such as for a 200 m head and 10.2 lpm flow demand, concept pump saves power up to 22.4% and 7% against steel and glass fibre reinforced composite (GFRC) (e.g. polyester) rod, respectively. Hydraulic efficiency calculations show an increase up to 76.7% compared to 59.5% and 71.4% using steel and GFRC piston rods, respectively. Additionally, significant energy savings of 1505.7 Wh/day and 383.7 Wh/day are also found for daily pump operation compared to commercial steel and GFRC piston rods pumps, respectively, which consequently reduce associated costs of PV panels.

The structural FE analysis of the concept pump for high head loads such as 200 m is conducted to evaluate the design safety factors. Material selection process based on performance indices is also carried out using Cambridge Engineering Selector (CES Selector) program. The design of concept pump components was also optimised for mass based on fatigue life constraint of selected materials using FE parametric approach coupled with material variation. The optimisation model developed in this study optimally reduces the mass with optimum fatigue safety factors contrary to yield strength criteria only, additionally incorporated with performance factors i.e. material cost and energy consumption. Stainless steel 'BioDur 108' was found to be overall best contender with optimised dimensions saving up to 29.39% of mass and material cost, along with 29.25% reduction in power consumption.

Conclusively, the developed concept groundwater piston pump in this study is optimised for low power consumption along with structural suitability for SPWPS with high head requirements in rural remote areas. The pump design structural adequacy is checked by FE analysis, material selection and design optimisation. The pump is also suitable for other locations depending on its structural ability to withstand loads with suitable materials.

Keywords: Conceptual design, FEA, Material selection, CES, Mass Optimisation.

TABLE OF CONTENTS

LIST OF FIGURES

LIST OF TABLES

NOMENCLATURE

A_{pipe}	Cross-sectional area of the pipe
b	Contact half width
d	Diameter of contact body
e	Energy error of the entire model
E_{error}	Percentage error in energy norm
D_{pipe}	Pipe diameter
F	Force
F_{atm}	Force due to atmospheric pressure
E	Young's modulus
$F.o.S$	Factor of safety
F_{crit}	Critical buckling load
$F_{manifold}$	Resistive force in pump flow manifold
F_{max}	Maximum force on piston
F_{valve}	Resistive force in valves
$F_{resistive}$	Resistive force in pipe
$F_{water\ weight}$	Weight of water in pipe
g	Gravitational acceleration
H	Head
H_L	Head loss
I	Area moment of inertia
I_{shaft}	Mass moment of inertia of shaft
J	Polar moment of inertia
L	Length of the piston mid-section

$l_{contact}$	Contact length
$L_{dayhours}$	Day operation hours
M	Bending moment
M_e	Combined equivalent moment
M_{piston}	Mass of piston
$M_{piston\,rod}$	Mass of piston rod
M_w	Mass of water in pipe
N_{pump}	Pump speed
P_{atm}	Atmospheric pressure
P_{max}	Maximum pressure in pipe
P_{piston}	Power consumption by piston
$P_{piston\,rod}$	Power consumption by piston rod
P_{shaft}	Power consumption by shaft
P_{pump}	Power consumption by pump
P_{water}	Power consumption for the lifted pipe water
Q	Flowrate
R_e	Reynold's number
r	Radius
S_e	Endurance limit of material
S_l	Stroke length
t_{rev}	Time for one revolution
T	Torque moment or twisting torque
U	Strain energy of the entire model
v	Flow velocity
V_{piston}	Piston velocity

$Y_{contact}$	Contact yield stress
y	Distance from the neutral axis
AL	Aluminium
CF	Centrifugal pump
HD	High density
PA	Polyamide
PD	Positive displacement
PE	Polyethylene
PP	Polypropylene
PREN	Pitting corrosion resistance number
PV	Photovoltaic
PVC	Poly vinyl chloride
S/N	Stress and number of cycles
S.S	Stainless steel
SPWPS	Solar photovoltaic water pumping system
GFRC	Glass fibre reinforced composite
AISI	American iron and steel institute

Greek Symbols

ρ_w	Density of water
ε	Pipe absolute roughness
δ	Deformation
f	Darcy-Weisbach friction factor
η_{hyd}	Pump hydraulic efficiency

η_m	Motor efficiency
η_p	Pump efficiency
η_{seal}	Piston seal friction coefficient
σ_a	Cyclic stress amplitude
σ_b	Bending stress
σ_e	Equivalent stress
σ_m	Mean cyclic stress
σ_y	Yeild strength of material
τ	Shear stress
$\tau_{contact}$	Contact shear stress
ϑ	Poisson's ratio
ϑ_w	Kinematic viscosity of water
ω	Angular velocity of the shaft

CHAPTER 1

INTRODUCTION

1.1 Research Statement

Water scarcity affects more than 40% of global population, which is an alarming figure that is projected to rise as temperatures increase due to climate change, rise in water pollution and dwindling drinking water supplies in the world. More and more countries are experiencing water stress, and increasing drought and desertification is already worsening these trends. For example, 844 million people lacked basic drinking water in 2020 [1]. On the other hand, 2.6 billion people in developing countries do not have access to constant electricity and most of them live in rural areas in developing countries [2,3].

Fetching water from beneath the ground surface through boreholes is still a fact in semi-arid or rural remote regions in most developing countries where domestic water and electricity supply is scarce or limited. Water from boreholes is either used widely for domestic or irrigation purposes. Standalone pumping systems are installed in such areas which are normally powered by wind, biomass, diesel generators or solar photovoltaic source. Among these, solar photovoltaic water pumping system (SPWPS) has become popular for such regions due to its cost effective and lower maintenance characteristics.

In a SPWPS, the photovoltaic (PV) source generates electricity directly which powers groundwater pump located few feet to hundreds of metres below the ground surface inside a borehole. The depth of water in a borehole is also ever increasing especially in semi-arid areas (such as 200 m, a new increased

required head in Nairobi and Machakos surrounding areas in Kenya, as referred by Daima Energy Ltd. [4]). The size of a SPWPS is designated with its capacity to deliver amount of water for a day (demand) and for a certain required head. The power needed to maintain water flowrate at certain head remains constant and is mostly used to size the solar PV generator. Such a load on PV source is termed as hydraulic power. Apart from this load on PV source, the pump device in a SPWPS requires more power in order to maintain this hydraulic energy i.e. to maintain the flowrate at certain head. High head systems require high power pumps. This high-power consumption by the pumps needs to be optimised for rural remote regions with high head requirements. Optimising the pump power for such areas would not only contribute to the whole SPWPS there as it may reduce load on the PV source but also benefit people living in such regions in terms of cost savings.

1.2 Motivation and Research Gap

Rural groundwater pumping systems are backed by solar PV or diesel pumping of which solar is currently the most cost-effective solution. Among the conventional groundwater pumps, positive displacement (PD) pumps are independent of head and can perform in variable conditions compared to centrifugal (CF) pumps. This is the reason why most of the scientific attempts in the literature have been made relating their designs modifications. To the author’s best knowledge, the induced flow and linear actuators positive displacement groundwater pumps are the only found conceptual design

attempts. Unfortunately, the induced flow concept is not suitable for higher heads.

On the contrary, linear actuator pumps have been developed with submerged and unsubmerged models both utilising sophisticated electronics and are very less power efficient than traditional PD and centrifugal pumps. The submerged models with linear actuator built-in electronics are prone to water leakages. The unsubmerged model uses traditional long piston-drive rod which is costly, difficult to install or disassemble during maintenance and acts as significant load on pump power and ultimately on PV source. Therefore, a gap in groundwater piston pump design is eligible to be thought to exist that a simpler pump design is needed which does not include any of these limitations and to optimise the power consumption for higher head SPWPS.

The design of a solar PV operated groundwater pump can be optimised for low power consumption for high head applications. Currently, groundwater piston pumps perform better than centrifugal pumps for high heads in terms of pump efficiency. However, piston pumps use such mechanical components which act as load on PV source such as long piston drive rod and other internal moving parts such as connecting rods, meshing gears and crossheads. The pump power could be improved by eliminating these components. To address this, a new power optimised groundwater piston pump concept design has been developed. The research gap is outlined in Figure 1.1.

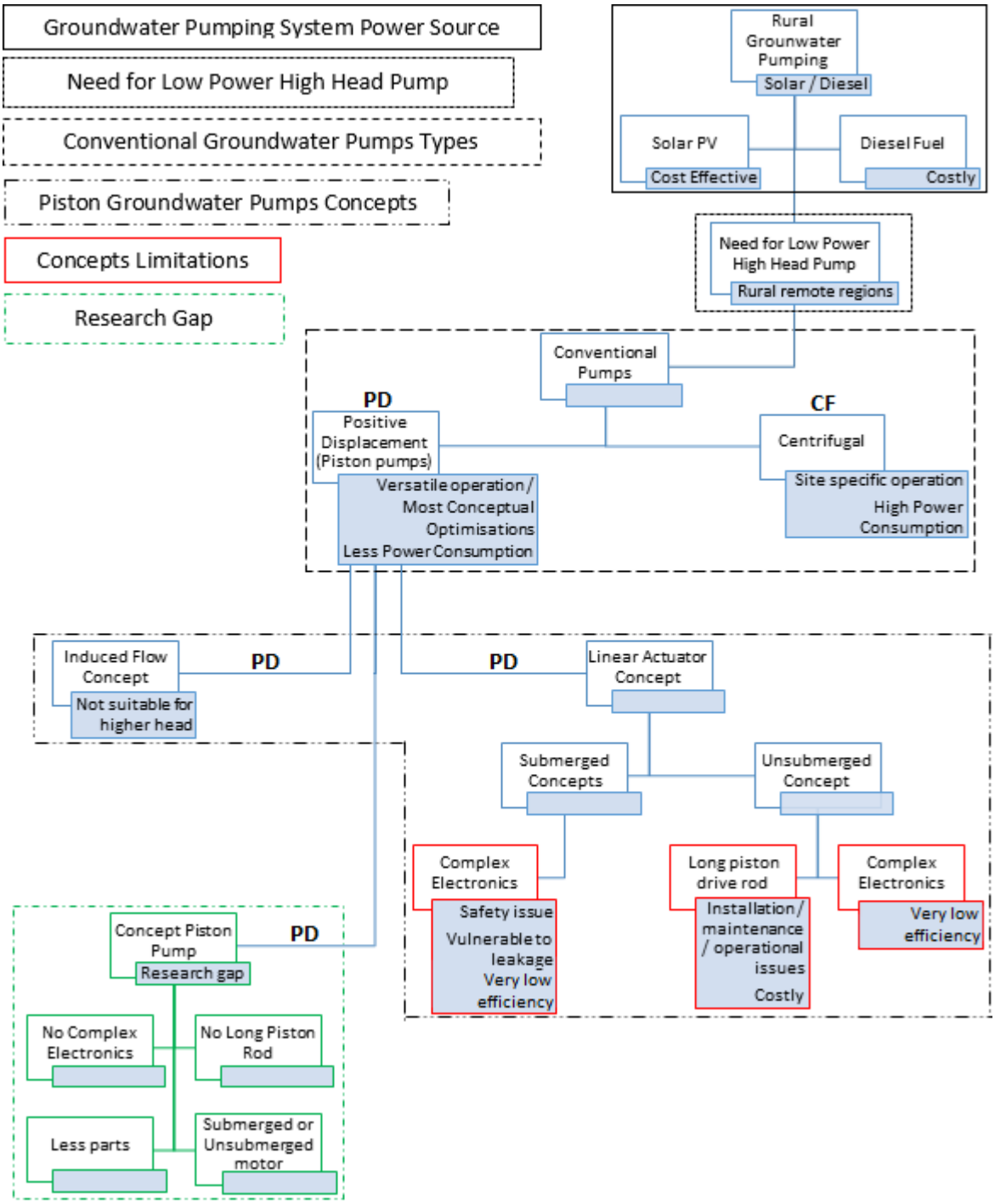

Figure 1.1: Research gap chart. This study's research gap highlighted with green boxes, while blue and red boxes describe groundwater pumping hierarchy and the limitations to current conventional groundwater pumps, respectively.

This research is an attempt to devise a power optimised groundwater pump for semi-arid rural remote areas based on a case study in Kenya and technical inputs provided by Daima Energy Ltd. which represent most semi-arid areas [4]. The inputs for such regions (Nairobi & Machakos, Kenya) include required flow demand of 25k L/day, at 200 m head and limited maximum borehole size of 10 inches.

1.3 Aim and Objectives

The main aim of this research work is to optimise the power consumption of groundwater pump with high head application for rural remote regions. This was achieved through following objectives;

- To develop a conceptual design of a groundwater pump optimised for low power consumption based on findings from literature review on existing pumps. The concept pump model to be developed using computer aided designing.
- To develop a mathematical model for validating and comparing the concept pump power consumption with existing groundwater pumps.
- To conduct structural analysis of the developed concept pump design for high head loading condition using finite element numerical method in order to evaluate loading safety factors.
- To perform material selection for concept pump components with low mass but high strength required for high heads.

- To carry out optimisation of the developed concept design for mass which in turn optimises power consumption. Mass optimisation for prolong life of pump components.

1.4 Methodology Overview

The development of a concept design of a groundwater piston pump is based on a computer aided product development methodology. The selection of pump type to be developed as a concept with low power consumption for high heads is based on literature review findings. Computer aided design (CAD) technique is used to develop a concept pump initial model based on the literature review findings and technical inputs from Daima Energy Ltd. for rural remote areas. A mathematical model is used to theoretically calculate the low power consumption by the concept pump and compare with current pumps. The finite element (FE) numerical technique is then used to analyse the structural ability of the developed concept pump model to withstand high head loads. A material selection is carried out to find suitable materials with low mass but high strength using reliable material database. Finally, with selected suitable materials, the initial concept pump model is optimised for mass which optimises the power consumption and associated material costs. The maximum fatigue life constraint is incorporated with the optimisation so as to have long life of the concept pump with selected materials.

1.5 Thesis Layout

This thesis consists of seven chapters arranged in a logical order to give details on the facts, observations, arguments and procedures in order to meet its objectives and provide a smooth transition between the chapters. Below is a summary of the overall content of the chapters.

Chapter 1 provides main introduction to the research work. It highlights the main area of the research which is the groundwater pump power optimisation for high head applications in rural remote regions powered with solar PV source.

Chapter 2 provides a detailed literature review on SPWPS pumps including high head SPWPS feasibility studies, attempts to conceptual design optimisations, and methodology to develop the concept pump model, material selection and mass optimisation.

Chapter 3 details the development of an initial concept design of a groundwater pump based on design considerations related to low power consumption. The chapter also establishes a mathematical model in order to support the claim about low power consumption by concept pump and also compares with existing groundwater pumps.

Next, Chapter 4 structurally analyse the developed concept pump in Chapter 3 using numerical method of Finite Element (FE) analysis. The chapter details necessary boundary conditions depicting the actual proposed working of the concept pump under highest calculated load condition. The chapter also discusses theoretical model for validating analytically the stresses found in numerical results.

In Chapter 5, material selection process for finding suitable materials with low mass, cost but high strength and stiffness for concept pump components is pursued. The chapter also validates the selection process using alternative selection method. FE analysis is also carried out on the pump components based on the selected materials to further validate the selection process.

In the follow-up, Chapter 6 discusses the mass optimisation process for the initial design of concept pump developed in Chapter 3 with selected materials from Chapter 5. Piston-shaft important power consuming components were analysed in this chapter. Dimensional and materials variation was incorporated with FE analysis to support the optimisation process which helps to identify the best suitable geometrical parameters and associated material. The enhancements related to mass, material cost and power consumptions were also evaluated in the chapter.

Finally, Chapter 7 concludes the research findings and outlines the scope for further works.

CHAPTER 2

LITERATURE REVIEW

2.1 Introduction

A water pump is a device which is used to push or pull water from one location to another location by using mechanical energy of its moving components by generating pressure. The water outflow location could be a parallel farther distance from the pump or it could be at a certain elevation vertically. A pump that works against the gravity to lift water to the surface located several metres below the ground in a borehole is called a 'groundwater pump'. One of the promising applications of groundwater pumps is the solar photovoltaic water pumping system (SPWPS) used in remote regions where water supply and grid electricity are a scarcity.

There are mainly two kinds of groundwater pumps; (1) rotary such as a centrifugal pump [5], and (2) positive displacement (PD) such as a piston pump [6]. The generated water lift is continuous in rotary pumps due to the continuous force exerted by rotating impeller compared to that of a piston pump where fixed amount of water is displaced in repeated cycles. The ideal and actual performances of a positive displacement and centrifugal pump in terms of head and flow is shown in Figure 2.1. It is evident that for higher heads, the flow from PD pump is ideally independent of the head compared to centrifugal pump. The actual performance curves show diversion from ideal case due to losses in operation. Centrifugal pumps operate optimally at specific requirements of flow and head. Nevertheless, extra pipework is needed when the head changes [7]

or relocating the borehole. Piston pumps are versatile operating pumps i.e. more suitable for higher heads as the performance is independent of head besides maintaining the flowrate, ideally (without any losses). The efficiency of piston pumps is also high compared to the centrifugal pumps besides having less efficiency losses [8]. Piston pumps require few components and their manufacture and assembly are simple compared to centrifugal pumps for instance, high precision tooling is needed to manufacture an impeller [9]. The average overall efficiencies of centrifugal pumps are in 25 – 35% range compared to 70% for PD pumps [10]. The PD pumps present a better efficiency compared to centrifugal pumps under low power conditions [11,12]. A general comparison is drawn between the centrifugal and positive displacement groundwater pumps in Table 2.1.

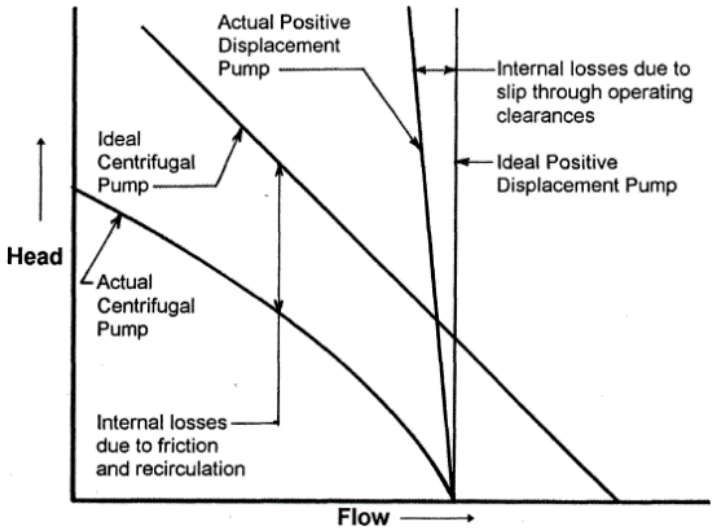

Figure 2.1: Ideal/actual performance comparison of positive displacement and centrifugal pumps [8].

Table 2.1: Generalized comparison between centrifugal and positive displacement pumps [11,13–16].

Parameter	SPWPS Centrifugal Pump	SPWPS Positive Displacement Pump
1. Maintenance	Normally low maintenance.	Comparatively require recurrent maintenance.
2. Volume Flowrate	Liquid pumping volumes are high.	Generally, low flowrates. It depends on the pump speed and size.
3. Head (height of discharge) dependency	Flowrate varies with the total dynamic heads. As flowrate increases, head reach decreases.	Flowrates are independent of the heads.
4. Efficiency	Delivers maximum efficiency for certain head and flowrate at a certain speed. While, efficiency varies with speed. Ranges between 25-35% [10]	Since flowrate is independent of the head, efficiency remains quite constant over a wide range of speed. Above 70% [10]
5. Solar Radiation Dependency	Can start on low PV input. But takes relatively more time to pump due to suction limitations & pressure generation.	Comparatively require high torque (i.e. the PV input) but takes no time for pumping to start.
6. Energy Losses	High energy losses.	Less energy losses particularly for high heads.

Every modern pump uses electric motor to operate. In groundwater centrifugal pumps, the motor is caged within the casing itself and is coupled to the impellers shaft as shown in Figure 2.2. Generally, in any piston pump, motor rotational motion is converted into linear reciprocating piston motion through meshing gears, crankshaft, crank pins, connecting rod and crosshead. The component 'crosshead' in a piston pump is connected before the piston and is used to hold the piston in position as it translates. The pathway in which crosshead moves is called a 'crossway'. A typical piston pump with drive

components is shown in Figure 2.3, whereas crosshead and crossway are shown in Figure 2.4.

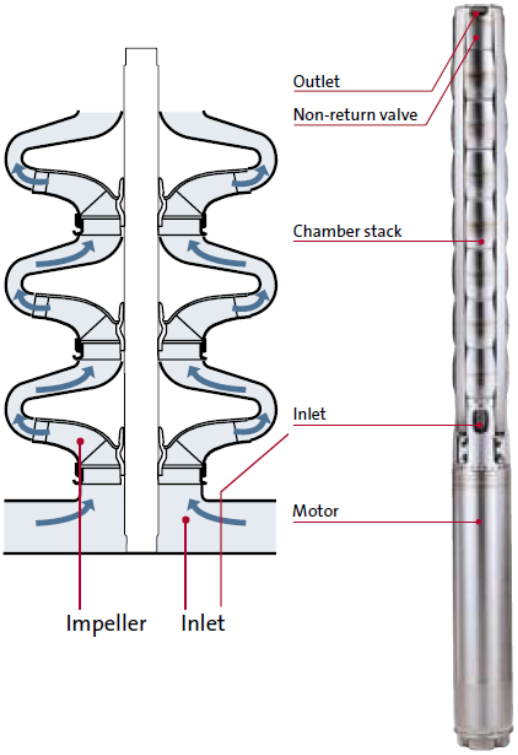

Figure 2.2: Schematic diagram of a submersible centrifugal pump [17].

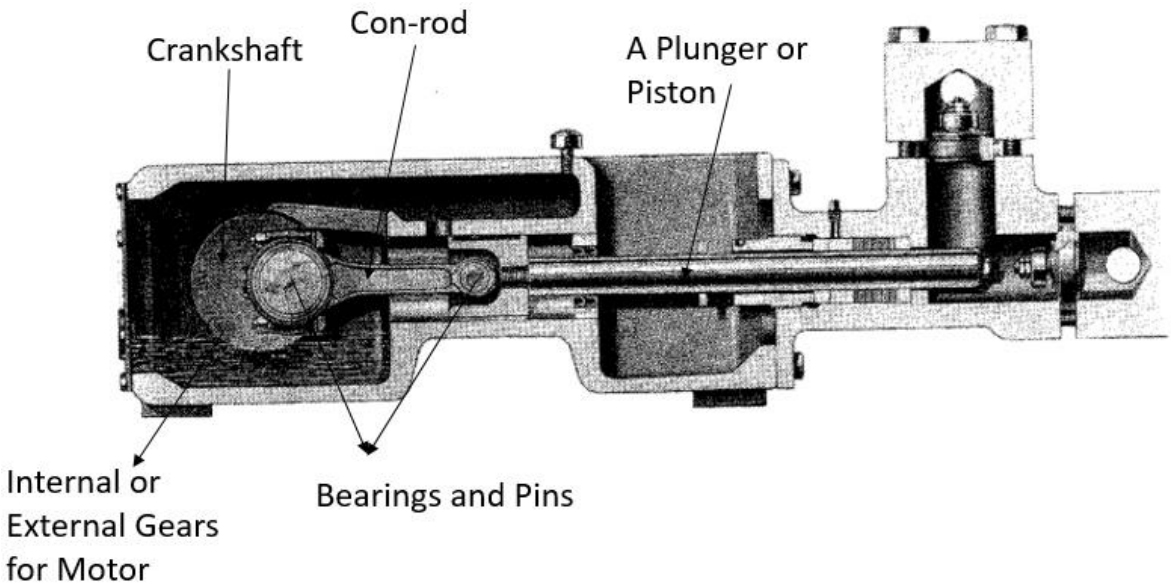

Figure 2.3: A typical piston/plunger pump with components [18].

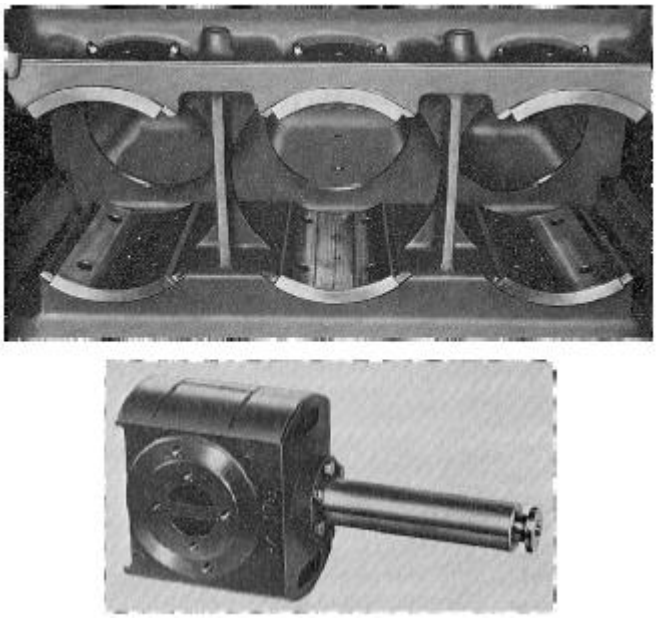

Figure 2.4: Crossways (top) and crosshead (bottom) in a piston pump [18].

There is another type of traditional groundwater piston pump that has the driving motor located at the ground surface while the piston is placed deep down into the borehole. A long piston drive rod connects the piston at depth to the motor on top as shown in Figure 2.5. For higher heads, this rod goes hundreds of metres down to reciprocate the piston. Generally, the piston rod is made of heavy steel material or lighter but expensive fibre glass reinforced composites (GFRC) [19]. Load is exerted on the motor to move this long rod along with the piston during each stoke. The weight of these rods ultimately is borne by the powering source. This may also create transmission losses in the pump [20]. The electrical energy from the motor is converted into the mechanical energy of moving pump components and finally into hydraulic energy of lifted water.

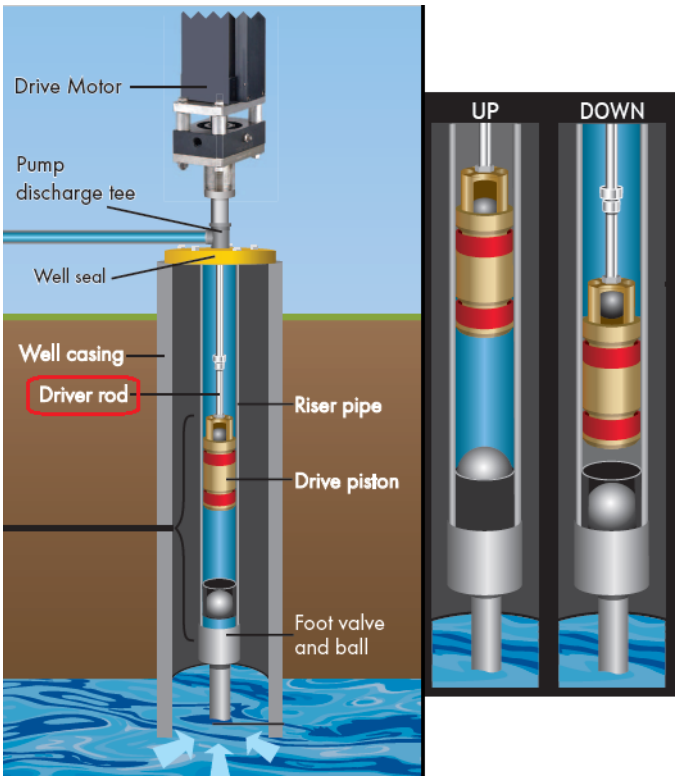

Figure 2.5: Groundwater piston pump with the long driver rod [19].

2.2 Solar Photovoltaic Water Pumping System (SPWPS)

In a SPWPS, electrical energy is generated by the PV-generator (consists of PV panels), optimised by the electronic components (i.e. controller maintaining optimum supply of voltage and current) and is converted by the motor into mechanical energy for the pump. The pump normally submerged in water deep down into the borehole finally converts this energy into the hydraulic energy of the water for a certain elevation. This is a four-way energy conversion process which is illustrated in Figure 2.6 and a typical off-grid SPWPS along with its components is shown in Figure 2.7. The SPWPS during low radiation period such as early morning hours or during night is capable of operating by using auxiliary power from either storage batteries or connected diesel generator to

assist initial start-up or extended operation run. This auxiliary power is disengaged when the input from PV generator becomes significant and takes over.

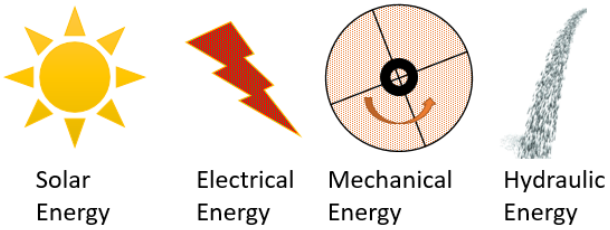

Figure 2.6: General energy conversion process in a SPWPS.

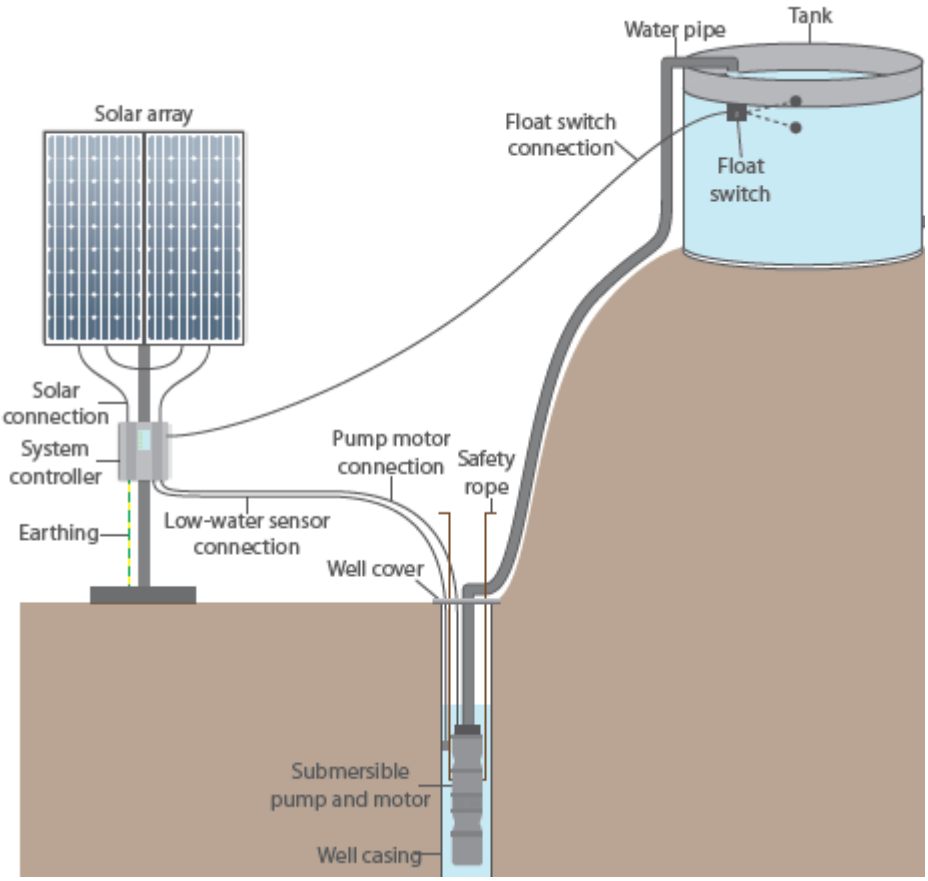

Figure 2.7: Diagram of a solar photovoltaic water pumping system (SPWPS). Adapted from [21].

Commonly, groundwater water pumping systems are operated using the diesel fuels [14,22] in remote regions which exerts high daily operational and

maintenance costs. In rural remote areas of the developing countries, borehole photovoltaic water pumping is becoming a popular way of fetching water beneath the ground. Number of research studies have shown that a SPWPS is much cost effective compared to diesel-based pumping. Bucher et al. [22] conducted experimental observations for both SPWPS and diesel fuelled pumping systems, and after cost per water output comparisons it was found that the SPWPS costs 0.31 £/m^3 less than 0.77 £/m^3 charged by diesel systems. Another unique study was conducted by Parajuli et al. [23] comparing SPWPS with petrol based diesel and bio-diesel fuels in Nepal. The cost effectiveness of SPWPS per litre of water surpassed other fuels due to low operational and maintenance costs. The total unit litre cost was recorded to be 0.0003 £/L for SPWPS compared to 0.00041 £/L diesel based and 0.00039 £/L for bio-diesel based system. A study by Al-Smairan et al. [5] based on Jordon case study concluded that SPWPS is the cheapest compared to diesel based system. Despite the high initial investment costs, the operation costs of the SPWPS were quite low within hundreds compared to thousands of a diesel system. The unit cost of water was also calculated to be very low (see Table 2.2). Similarly, another comparison study by Gopal et al. [13] compared the costs of various water pumping systems in India running on solar, wind, biomass, hybrid solar-wind, diesel and grid connected systems of same size (3.73 kW and 20 m head). The operational cost of solar PV backed system was found to be quite low compared to the diesel and electrical systems. The cost comparison data is presented in Table 2.3. Another study by Bannister [24] found that 1 kW of SPWPS in South Africa overtakes the cost of diesel system just after the period of 3 years. Similarly, other studies [20,25,26] confirms that SPWPS can prove

to be more economical and efficient in contrast to the diesel based or on-grid systems.

Table 2.2: Comparison among photovoltaic and diesel engine based water pumping systems [5].

Costs	Photovoltaic System	Diesel System
Investment Cost (£)	16039.59	3471.77
Operational Cost (£)	320.95	5664.78
Present Value Cost (£)	18952.79	54891.04
Annual Cost (£)	2088	6038.03
Unit water output cost (£/m^3)	0.15	44.75

Table 2.3: Cost analysis of various water pumping systems backed by different energy sources [13].

Water Pumping System	Initial Cost (£)	Operational & Maintenance Costs (£/year)	Life Span (years)
Solar Photovoltaic	4009.35	21.67	20
Wind Energy	5688.94	-	20
Biomass Energy	758.53	-	20
Solar-Wind Energy (Hybrid)	10294.27	-	20
Diesel Engine	433.44	1753.28	20
Electrical Grid	238.39	585.36	25

Being well adopted as a low cost option, there is a growing demand of low power pumps for high heads SPWPS in rural remote regions* [4]. The cost of PV panels remain high in developing Nations [7]. The load on PV generator with respect to required water and head demand remains constant because of associated constant hydraulic energy. Such a load is normally termed as hydraulic power and is related to the sizing of PV generator. The load on PV generator apart from energy related to flow and head demand is linked to the pump unit itself which maintains this hydraulic energy. The power required by the pump is always higher than the hydraulic power due to the mechanically associated loads such as pump components. Optimising the power of pump unit would contribute to the whole SPWPS and besides meet the demands of such rural remote regions. Reduction in a groundwater pump power requires considering factors associated with power consumption such as pump components, water weight for a respective head and resistive forces due to flow. In order to select the type of pump to optimise, the performance comparison of commonly used groundwater pumps was reviewed as discussed in the next section.

2.3 Groundwater Pumps in SPWPS studies

A number of SPWPS feasibility studies were reviewed in the literature in order to gather data relating pumps specifications and their performances. The scope of literature review here was on studies focusing on experimental works with high heads and flowrates [4]. The other reason behind collecting this data was to get a rough estimation of the required PV power input for the pump type.

* Rural remote regions in Kenya. Maximum borehole 10 inch. Demand of 25k L/day (34.72 lpm) and 200 m head (varying). Personal conversation with Daima Energy Ltd. UK.

The data of from SPWPS studies is presented in Table 2.4. It is reviewed that majority of SPWPS research studies conducted does not exceed 200 m depth [27]. However, from Table 2.4 data, experimental 'Study 3' by Setiawan et al. in Indonesia [28] came out to be the only study with maximum head (218.34 m) and flowrate per day (11,520 L/day to 25,920 L/day). The power input for this system was 3.2 kW. The average efficiency of the motor-pump set was calculated to be 60% and the overall efficiency of the whole SPWPS came to be 5.9%. The pump used in this study was Lorentz helical rotor PD pump installed with a DC motor. Similarly, it is observed among studies that when the head is low, the required power input is also low, as evident in the Studies 1 and 2 [29,30]. Despite greater head, the PD pump efficiency in 'Study 3' is also evident to be higher in comparison to other centrifugal pumps from (Studies 4-6, [5,31,32]), and so is the effect on overall SPWPS efficiencies.

Table 2.4: Shortlisted data of various experimental studies in SPWPS.

STUDIES / PARAMETERS	Study 1	Study 2	Study 3	Study 4	Study 5	Study 6
System Efficiency	4.41	4.12	5.868	4.1076	3 to 5	4.267014
Motor Pump Set Efficiency	from > 45.06	45.06	60%	42%		43.63
Average Flowrate (L/day)	Maximum 21k	Need 22k Delivery 21.8k	Need 6.4k Delivery 11.52k to 25.92k	45k	5k-110k	Need 50k Delivery 70k
Head (m)	80	80	218.34	105	5 - 125	150
Pump Model	Grundfos SQFlex SQF2.5-2 Submerged	Grundfos SQFlex Helical Rotor SQF2.5-2	Lorentz PS1800HR-05HL	Grundfos SP8A-37	Submerged KSB-UPA	Lorrentz PS9kC-CJ8-44
Pump Type	PD	PD	PD	Centrifugal	Centrifugal	Centrifugal
PV Power (Wp)	1800	1800	3200	5900	1000 to 2000 (45%) to 4000	14800
No. of PV & Configuration	24 (8Sx3P)	24 (8Sx3P)	32 (8Sx4P)	108	90 SWPS installed	80
Location	Madinah, Saudi Arabia	Madinah, Saudi Arabia	Purwodad, Indonesia	Tall Hassan, Jordan	7 different countries	Garissa, Kenya
Motor		PMDC-1ph	DC	AC-3ph	AC	3ph

Furthermore, a study by Protogeropoulos et al. [33], used 'Fluxinos SolaFlux 200' PD pump which uses coaxial horizontal pistons and compared with 'Grundfos SP8A-5' centrifugal pump under the same setup. The test results showed that PD pump hydraulic efficiency kept increasing with head rise i.e. 6 – 31.2% from 2 – 24 m. While, centrifugal pump achieved 18.5 – 13.5% from 3 – 24 m, and with 27% peak efficiency reaching at 12 m (see Figure 2.8). The authors also tested the PD pump at 60 m where efficiency exceeded 45%. Besides, PD pump used less power (150 W) than centrifugal pump (440 W).

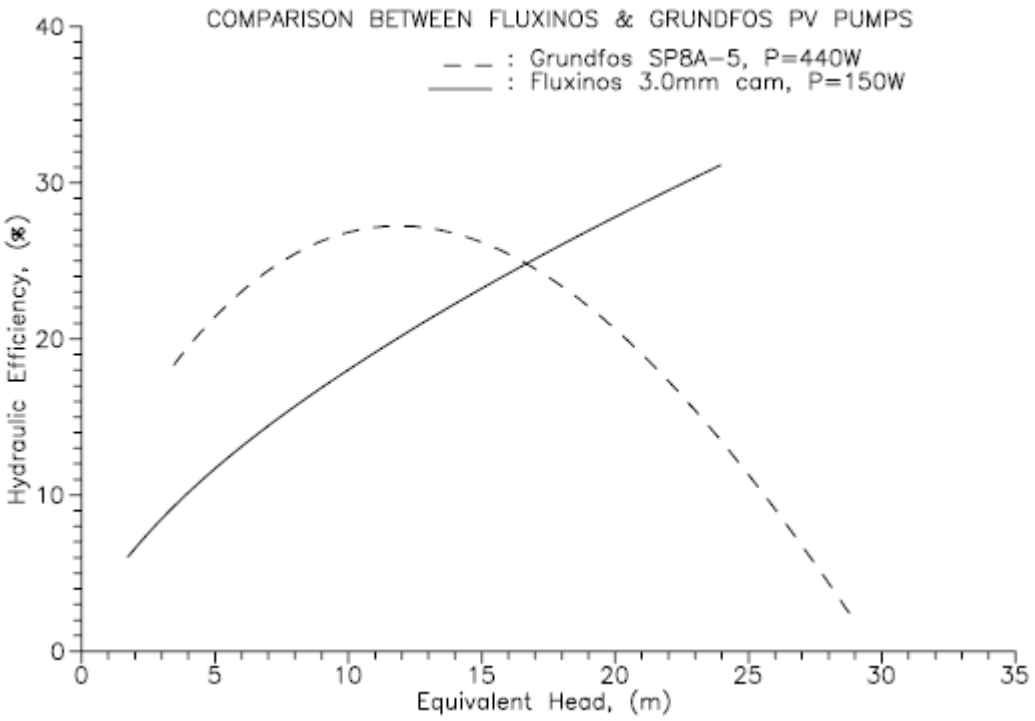

Figure 2.8: Hydraulic efficiency curves of 'Fluxinos' PD and 'Grundfos' centrifugal solar pump [33].

Table 2.5: Comparison of different pump types used in SPWPS [34].

SPWPS Pump	**Centrifugal Pump [Single Phase-230V, 3-Phase 230V]**	**PD Helical Pump [Grundfos 6SQF-2, Lorentz HR07-2]**	**PD Diaphragm Pump [Sun, Shurflo, Sun Quad]**
Outcome	Suitable for low head and high flow rates.	Suitable for high heads and low flow requirements.	For low heads and low flow requirements.
	If the motor cost is same, 3-phase motor should be used due to better performance.	Grundfos pumps performance was recorded better without any loss compared to the Lorentz pump (50% losses) for a span of 3 years.	Sun pumps performed better than the Shurflo pumps for high heads. However, for lower heads Shurflo pumps performance was good.

Vick et al. [34] compared the performances of centrifugal, helical rotor and diaphragm pumps. The outcome of the types of pumps used are presented in Table 2.5. It was also suggested by Burton et al. [35] that positive displacement pumps are more appropriate in PV groundwater pumping compared to centrifugal pumps in terms of versatility in operation. Furthermore, it was also investigated from the performance data of different pumps (used in SPWPS experimental studies, see Table 2.4) based on same flow and head that the power usage of positive displacement pumps is relatively lower than that of centrifugal pumps as presented in Table 2.6. This further firms the decision to select positive displacement pump type for concept generation and power optimisation. It is also evident that a commercial 'Blackhawk Apollo' piston rod PD groundwater pump uses the minimum power compared to others i.e. 280 W delivering 10.2 lpm at 122 m head. This pump was benchmarked to estimate the data for other pumps. The reason for choosing this head and flow benchmark was because 'Blackhawk' pump used least power among all pumps and no higher heads data was available for all. The higher power usage for other pumps for same head and flow rate is due to the larger pipe diameter compared to the benchmarked pump.

Table 2.6: Comparison of different commercial pumps performance specifications [19,36–39].

Pump Specifications	Blackhawk Piston rod pump	Grundfos SQFlex SQF2.5-2	Lorentz PS1800HR-05HL	Grundfos SP8A-37	Lorentz PS9kC-CJ8-44
Pump type	PD	PD	PD	Centrifugal	Centrifugal
Pump Power (W)	280 300 (PV)	650*	390*	8200*	1700*
Flow rate (Lpm)	10.2	~10.2*	~10.2*	71.67* (does not operate for 10.2 lpm)	10.2*
Head (m)	122	120*	125*	122*	122*
Pipe diameter (in)	1	1.25	1.25	2	2
* Data extracted from performance curves at around 122 m and 10.2 lpm (if available)					

From above comparisons concerning different pumps, the performance of PD pumps is found to be better than centrifugal pumps for high head applications and in terms of efficiency in a SPWP system. Therefore, in this study, focus was formed towards the selection of PD pump type for conceptual design development for optimising pump power based on the requirements of rural remote region (see Section 1.4). This was further firmed after reviewing a few found piston pump related conceptual design studies, presented in next section.

2.4 Conceptual Optimisations Studies of PV groundwater Pumps

Traditionally, a groundwater PD hand pump uses a connecting rod and a lever coupled to the piston in borehole through long piston rod [6]. To avoid using long rods, piston pumps designs were changed that used cam shaft

arrangements to convert motor rotational motion into linear. It may not be an issue for a surface pump but deep down into the borehole with size restrictions (circular diameter [40]), (generally 100 to 150 mm), it is a challenge to design such pump components. The use of cam shafts or connecting rods have however, proved to be a limitation in piston pump designs such as seen in 'Fluxinos SOLAFLUX' and 'Divwatt SOLASTAR' where much energy loss is due to the friction between these components [7]. Additionally, any deviation in force or cam shaft rotational speed results in violation of pure rolling condition (equal surface velocities of cam and roller at contact) and that is when slippage occurs [41].

To the best ability of author's knowledge, only a very few studies were found which based on new conceptual ideas with design changes in groundwater lifting i.e. targeting the pump unit of SPWPS particularly the piston type pumps. However, none of the found studies discussed about the power optimisation of pumps. The studies were related to modifying the lifting mechanism to improve design simplicity for remote regions or to enhance water output.

Studies discussed in the following have used linear actuator pumps attempted to avoid using rotational motor and its related components such as cam shafts. The linear actuator is a device that replaces rotational motor to drive the piston. Andrada et al. [42] modified the traditional design of SPWPS by testing a linear actuator for lifting groundwater. The actuator was connected to a pulley weight mechanism as shown in Figure 2.9. The actuator gets electromagnetically charged by the PV array and reciprocates itself along with the piston connected through long piston drive rod. A counterweight linked to the actuator shaft assists in the repetition of the cycle. The authors concluded

that the proposed design was cost effective and required less maintenance. The system consisted of 2 parallel and 2 series PV array configuration (2Px2S) of 540 W, with the requirement to deliver 12 m^3/day of water output for a head of 18 m. The pump power consumption was measured to be 210.72 W. Linear actuator pump seems to be a simple device, however, the usage of long piston rod (20.4 kg) going deep into the borehole is another limitation which acts as extra load on the prime mover (consequently on PV source) and may result in transmission losses plus difficulty in installation and maintenance for higher head systems [6,19,42]. These rods are costly as well made of steel or composite materials such as 'Blackhawk Apollo' piston rod made of lighter Glass Fibre Reinforced Polymer (GFRC) with 400 pieces costs $1600 (£1227) for 122 m [19]. The counter-weight (46 kg) component may not be feasible to match higher speeds (strokes or rpm) of the pump for higher flowrates. Furthermore, when comparing with the 'Blackhawk Apollo' piston rod pump specifications (see Table 2.6) which uses no counter-weight consumes only PV power of 300 W (1.8 times less) and delivers nearly half output of 4.9 m^3/day (10.2 lpm) at much higher head of 122 m (6.8 times higher) using a traditional DC motor [19]. This means that the most PV power in the Andrada et al. [42] study is possibly being consumed by the linear actuator itself and to lift the heavy piston rod which causes low efficiency. The less efficiency reason for linear actuator is further strengthen by other studies discussed below. Thus, this kind of system may require high power for higher heads such as 200 m a requirement in rural remote regions [4].

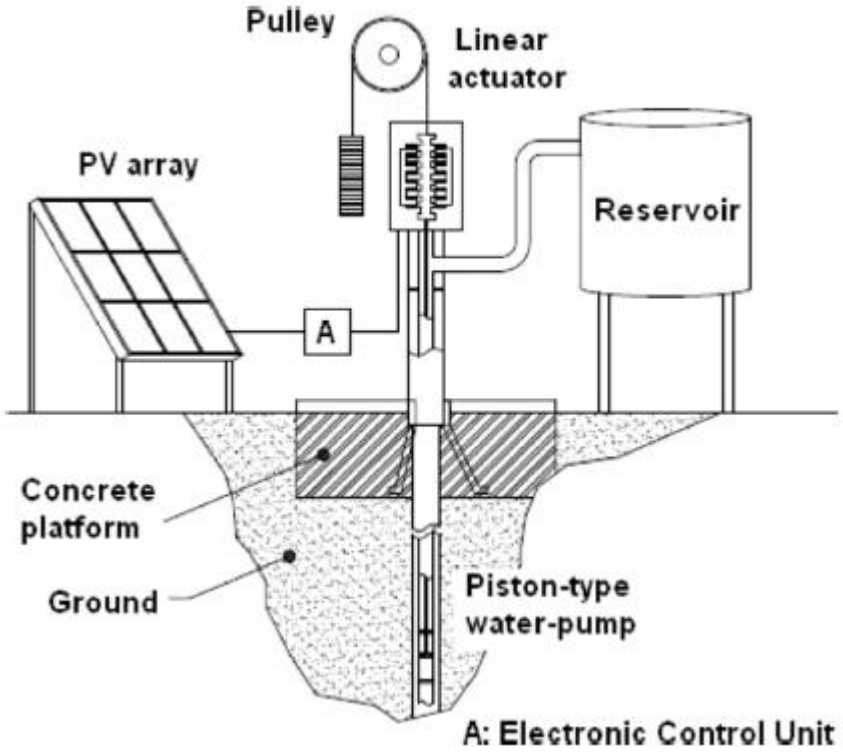

Figure 2.9: Solar powered linear actuator driven well piston pump [42].

Wade et al. [6,43] also worked on the same technology, but instead suggested to use this linear actuation within the submerged piston pump body eliminating the long piston rod as shown in Figure 2.10. The prime mover was itself the linear actuator. The pump was tested experimentally and it was recorded delivering 50 L/h at a head of 2.5 m with just 80 W from PV power. The pump mechanical efficiency was reported 8% which is very low. The peak electrical to hydraulic work efficiency was recorded just 0.4% which is very insignificant compared to 25 – 35% of centrifugal and 70% of positive displacement pumps [10].

This low hydraulic efficiency could possibly be due to the linear actuation which demands high input power from the PV source. This is not feasible for large scale systems or systems with varying high heads conditions. Apart from

no use of long piston rod, limitation for this concept is that it is a fully submerged pump with piston and seals only separating the dry region (consists of actuator with electronic components) and wet region (water flow passages) shown in Figure 2.10. If any chances of slight leakage occur due to the linear 'to and fro' reciprocation motion of piston between wet and dry regions, the electronics safety could be compromised [44]. It is therefore plausible to minimise the use or even eliminate electronic parts which inhibits the chances of repair, maintenance or re-manufacturing in rural remote regions [40]. This is often beyond the means, understanding and skills of local communities living in rural areas of developing Nations [7].

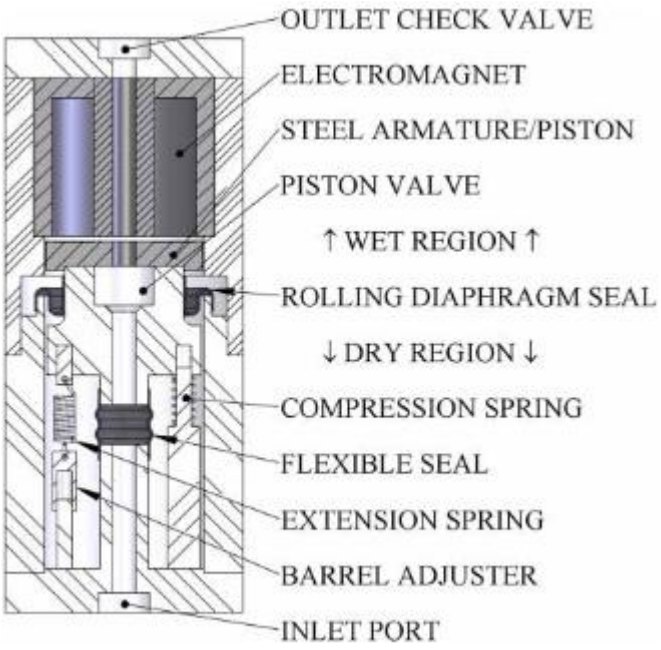

Figure 2.10: Enclosed linear actuator rod driven pump [6].

Another study by Wade et al. [40] investigated the same pump to have an optimum hydraulic output and increased efficiency by proposing geometrical and electrical configurations changes in the design as shown in Figure 2.11. The efficiency was increased slightly, i.e. 2.5% at the 5 m head which still the author

claimed is insignificant. To improve it, the study suggested further investigation by involving double actuator mechanism and an electronic buffer, which is another compromise between complexity and design simplicity for rural areas. The same limitations are applicable here for this concept regarding electronics safety as the linear actuator piston slides between wet fluid flow and dry regions similar to author's previous studies.

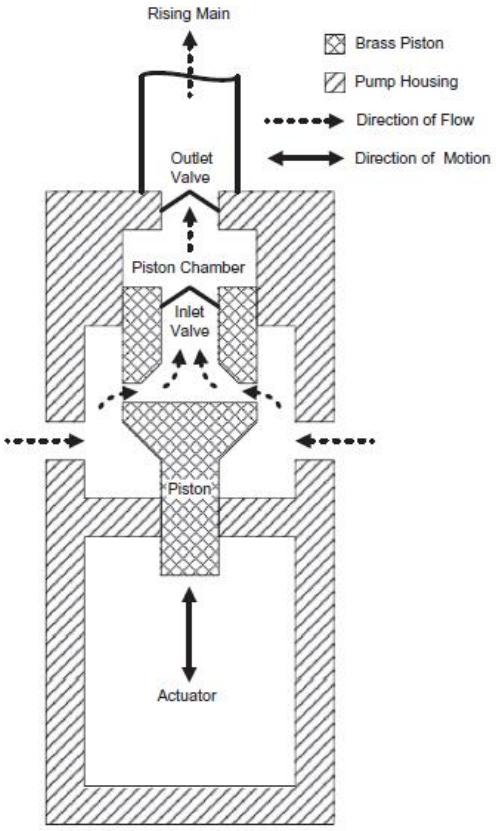

Figure 2.11: Enclosed linear actuator rod driven pump [40].

A study by Short and Burton [45] tried integrating the characteristics of centrifugal and PD pumps in a diaphragm pump by using induced flow technique to enhance output. The study used a hydraulic resonator at the discharge of the diaphragm pump. The resonator creates an induction effect at every stroke of the pump. Near the inlet of the pump, induction effect is created by a chamber

containing ‘voids’ (polyurethane made capsules enclosed within nitrile skin) as shown on Figure 2.12. ‘H’ is the static head, ‘L’ is the pipe length, and ‘K’ is the stiffness of the ‘voids’.

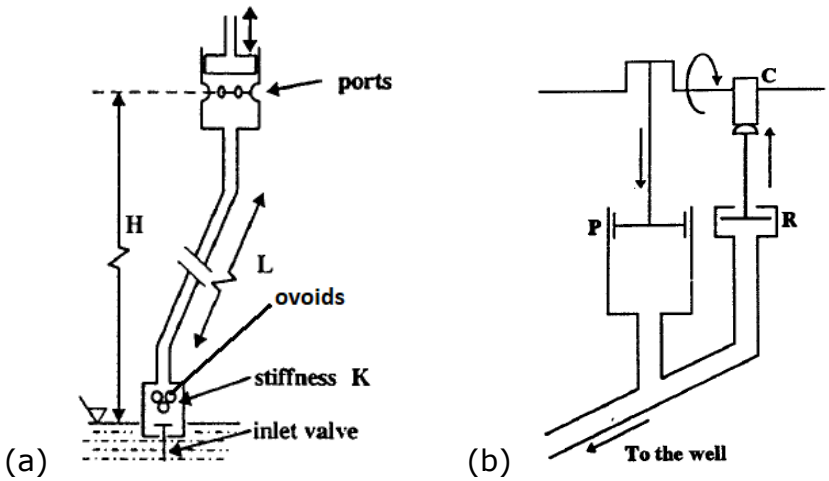

Figure 2.12: (a) Rebound-induced flow pump layout (b) Components shown, Release valve (R), Piston (P) and Cam (C) [35].

When the piston (P) is having the stroke, the outlet release valve R does not open due to the push of water, rather it is allowed to remain closed by mechanical means of cam ‘C’ for some time. During this time, at inlet, the ‘voids’ inside the enclosed volume and during the ongoing discharge stroke, are continuously being compressed. As, the valve opens mechanically, the ‘voids’ release their compressive pressure (just like a spring release) and the water is forced to move out from the outlet. This is the induction effect which gives some additional output of the water with every stroke of the piston. The tested system delivered maximum 15 lpm at a head of 20 m. This concept has limitations in terms of higher heads. For lower heads, the performance is significant but as the head rises just after a few metres, it degrades to act like a non-induced pump as illustrated in Figure 2.13.

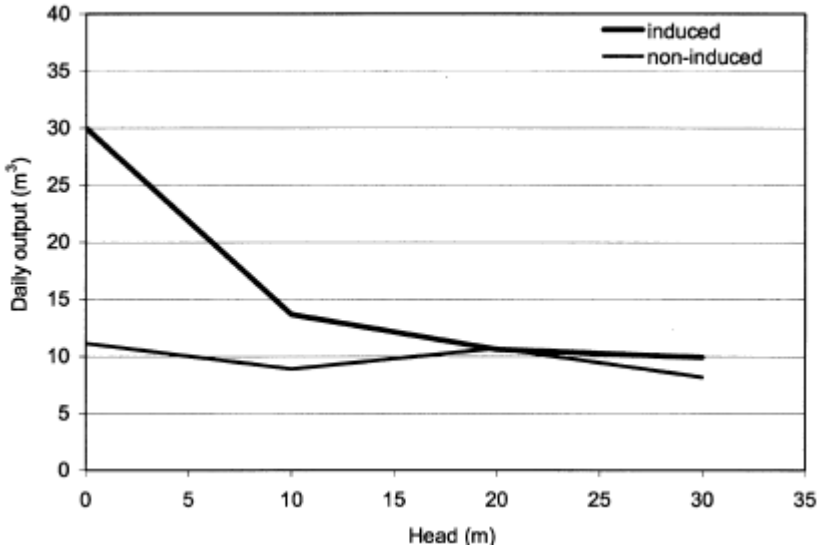

Figure 2.13: Flow discharge from induced and non-induced flow pumps [45].

Fiaschi et al. [46] proposed to divide the impeller shaft with some stages permanently coupled to motor while some could be engaged or disengaged for the centrifugal pump aimed to improve its output performance. When the solar radiation increases to a limit, the pump is allowed to operate at high speed by disengaging impeller stages using automatic mechanical clutch, while during the early hours of the day, the pump operates utilising all stages because of low speed of the pump. The experimental results showed that pump output was increased 9 – 10% annually compared to the single shaft pump. The schematic of the devised idea is shown in Figure 2.14. This study was aimed at increasing the output from the pump rather than the simplicity in design for rural communities. This conceptual optimisation holds the manufacturing complexity such as high precision tooling is needed to manufacture an impeller [9]. The authors also estimated that the modified pump is 1.5 times more expensive than the unmodified conventional centrifugal pump. The complexity and pump cost may limit this study for the rural regions in developing countries.

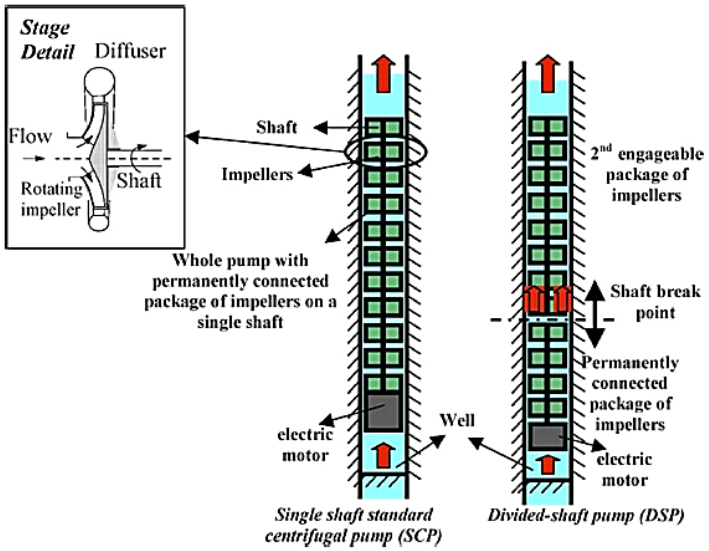

Figure 2.14: Divided shaft centrifugal pump for low and high solar radiation levels and increase water output [46].

2.5 Conceptual Design Development

Since the advanced development and firm footing of the computer-aided engineering (CAE) in product development field, it is nowadays, a well-established factual practice to develop any conceptual product model using the computer aided drafting tools before it is being analysed computationally and finally fabricated for experimental testing in order to save both time and money. For any computer-based engineering analysis, 'Computer Aided Designing' (CAD) is the first and important step where geometrical model is developed, followed by the most widely applied 'Finite Element Analysis (FEA)' numerical technique for engineering analysis [47]. FEA provides a way of virtually testing a product design. It helps users understand their designs and implement appropriate design changes early in the product development process [47]. In FEA, a FE model is assigned with boundary conditions, assumptions and

simplifications which possibly depicts real conditions. The model is then simulated using computational algorithms to predict the results of product behaviour. The product manufacturing using computerised process is termed as computer aided manufacturing (CAM). A sketch of a computer aided product development process is shown in Figure 2.15 where the process is also influenced by market.

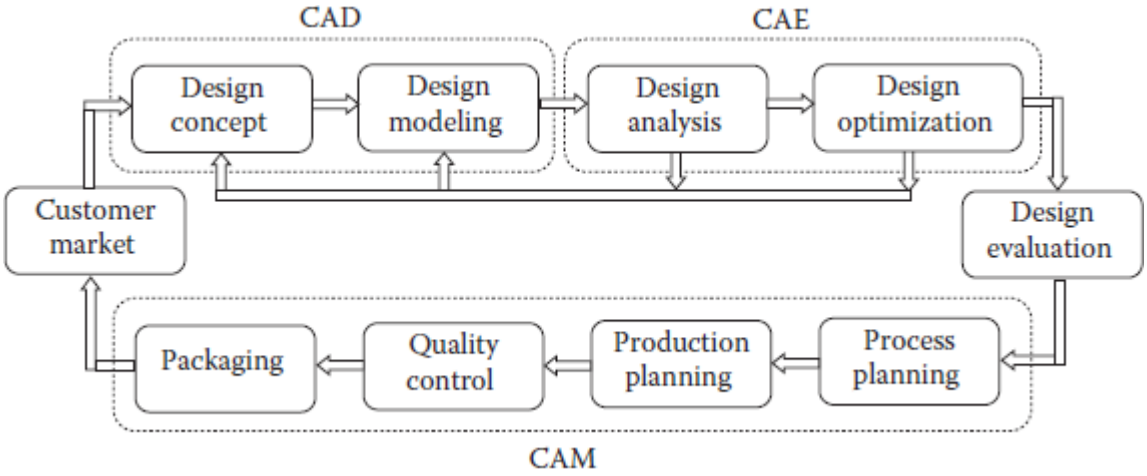

Figure 2.15: A sketch of computer aided product development process [47].

There are many studies [48 – 58] related to design evaluation in pumps using CAE which incorporate CAD technique to develop the model first, and later go through engineering structural analysis using FEA and finally fabrication and testing. For instance, Guangjie et al. [48] optimised the cast steel casing of a large scale ship dredge pump. The heavy loading conditions were causing cracks in the pump casing at the ribs due to the stress concentrations. For optimisation, the whole casing was drafted as 3D CAD model and then FEA was conducted using inputs from real-world loading conditions. In order to reduce these stresses, some CAD changes in the casing ribs were proposed (removal of radial ribs and increased the material thickness of annular ribs). Following the analysis,

the results predicted significant reduction in the maximum equivalent stresses much lower than the material yield stress compared to the original design i.e. from 205 MPa to 171 MPa. Comparing the maximum equivalent stress against the material yield strength was set as the failure criteria. The experimental testing of the new design showed no cracks and a maximum distortion of 3 mm was also verified with the simulated results.

A similar kind of structural analysis using same method was done by Golbabaei et al. [49] which studied the crack during the hydrostatic pressure in a real centrifugal pump casing and optimised the mechanical capacity to absorb much higher pressures (0.9 MPa) than original model (0.6 MPa) by proposing CAD geometrical modifications in the inner volute wall thickness. The thickness was increased just 2 mm, and the computation showed that equivalent stresses were reduced from 324 MPa to 305 MPa. The stresses were compared against the yield strength of the material (450 MPa). The modified casing was fabricated and tested experimentally where the computed results were verified. The experimental analysis also noted subsequent increase in the casing life of 10,000 operational hours compared to 2,000 hours of the initial design at no extra cost by the slight increase in thickness.

Another industry based study by Lienau and Welschinger [50] concluded that FE method is significant in the pump design optimisation by determining the stress concentration points and adjusting appropriately by introducing the modifications either in the thicknesses or relocating or removing other geometrical features in the design, such as in the study flanges thicknesses were increased, the studs bores were relocated away from the pressure area (high stress region). Repeated modifications were done in the CAD model until

desired results got verified by the experimental hydro tests. The study highlights that both money and time were saved by doing FE analysis of the pump rather carrying the testing of fabricated part from the initial step.

Mohammadian et al. [51] numerically analysed a centrifugal casing design (CAD model) on ANSYS FE program to determine the design safety by comparing the FE stresses (384.4 MPa) with the allowable yield stress (480 MPa) of the EN 1.0619 steel material. The authors reported the maximum deformations of 0.124 mm and 0.233 mm for the upper and lower sections were small and could be ignored. Similarly, research by Rezvani et al. [52] conducted structural FE analysis using ANSYS by developing a CAD model first of a mixer pump at Hanford site, reported stresses around 103.87 MPa compared to 159.3 MPa yield strength of carbon steel. A short study by Bachche et al. [53] used static structural FEA to evaluated stresses and deflection of a centrifugal pump carbon steel shaft design under rotational thrust load. A 3D mesh based on solid hexahedral elements was used. The authors found the shaft design maximum equivalent stress of 238 MPa below the yield limit of 290 MPa with maximum deformation of 0.783 mm. The validation was done analytically using (bending moment and stress relationship) with an error of 5.64%.

There are examples of FE analysis on piston pumps such as a study by Cho [54] who used FEA to optimise the design of an existing swashplate in an axial piston pump for targeted pressure of 40 MPa based on various design factors including plate dimensions and materials (steel and yellow brass). The static structural FEA was conducted on each combination of design factors and the design with minimum stresses was selected as optimum. The study found out that the optimum swashplate design under yellow brass material only uses

23.9% of yield strength compared to that of the 36.4% of steel in existing design (under 35 MPa pressure). The author emphasised that the new design was suitable to be used for high pressures application.

Similarly, Du and Carlson [55] applied static structural FE method to maximise the fatigue life of swashplate roller bearings of axial piston pumps which were failing in 3,000 operating hours despite targeted life of 12,000 hours. The FEA based on linear elastic material properties and high-quality 3D hex mesh, was conducted on the initial design of the bearing rollers and contact stresses were evaluated. It was found that failure was due to high roller contact stresses at the edge of the roller adjacent to the swashplate surface. An inclined chamfered profile of the edge was proposed where the stresses were high. The study found lower stresses than the original design and predicted 12,186 hours fatigue life which was also experimentally confirmed when no failure in pumps was reported at 10,000 hours.

Another axial piston pump study by Zloto and Stryjewski [56] evaluated the contact stresses between the piston and cylinder wall due to the variation in swashplate inclination angle and gap height with steel piston and steel/bronze cylinder materials combination. The 2D FE contact analysis (using ADINA program) found steel piston and bronze cylinder contact had maximum stress of 36.12 MPa compared to 39.69 MPa for steel only. The authors declared steel-bronze combination advantageous to pump. Other studies using CAD/FE technique include, study by Rosu and Vasiliu [57] which analysed a positive displacement reciprocating pump, NASA based study by Shannon [58] had done static FE structural analysis using ANSYS where a CAD model of a space shuttle pump located in the engine section was developed.

2.6 Material Selection

Material selection is summarised as a process of identification of suitable materials to serve the purpose of a product's functionality generally in a very cost-effective manner. In engineering design field, it is a function that is performed by the design and material engineers to select befitting material for their products [59]. Speaking as a mechanical design perspective, a material selection should incorporate various aspects of a product such as material, product design and functionality [59,60]. There are various material selection methods and tools available which include material handbooks, computerised databases, artificial intelligence systems and other computer aided tools. A materials handbook include detailed information and properties data while a computer material database is just a digitalised handbook in a form of software program [59]. Nowadays, material databases are computerised for easy access, retrieval of such information and are kept up-to-date.

There are many computerised databases available, some of well-known are; CAMPUS, FUNDUS for composites [59], CES Selector, Matweb (online database for materials) etc. Some databases are only specific to one family of materials (CAMPUS, Prospector Plastics etc.) and some include more than one such as Matweb, CES Selector etc. CES Selector for material selection has been used by many mechanical design based research studies [61–70] and has been found to be a versatile database with more features, user friendly interface and well-structured data representation [60,71,72].

There are numerous methods or techniques that are applied on these databases to filter out or select the suitable material encompassing the desired

needs of the user. Some methods are based on selection charts to identify promising materials such as Ashby's method (CES Selector) [73], while others involve computational algorithms to screen out an optimum single materials or a ranking list of candidates [60]. These include WPM (Weighted Property Method) and MCDM (Multi-Criteria Decision Making) which include TOPSIS (Technique for Order of Preference by Similarity to Ideal Solution), VIKOR (Vise Kriterijumska Optimisacija Kompromisno Resenje) and ELECTRE (ELimination Et Choix Traduisant la REalité ~ ELimination and Choice Expressing Reality) etc. Ashby's chart based approach has been found to be intuitive and relatively simple with limited amount of calculations than other methods in detailed comparative studies and is mostly recommended for initial screening of materials during the initial design phase [60,74]. TOPSIS method on the other hand, is based on MCDM technique which involves generating alternatives (e.g. choosing materials) from one or more established criteria, evaluating sets of weights for materials and finally ranking out a list of best possible candidates [60]. TOPSIS is found to be the most advantageous and popular method for material selection among other MCDM methods [74,75]. Many studies have used Ashby's method alongside with MCDM methods such as TOPSIS. Ashby's method is applied for initial screening of materials and MCDM methods are applied to further aid the selection process or to validate the Ashby's method outcomes [69,70,76].

There are various research studies which have used Ashby's method for material selection. Studies from [61–63] used Ashby's chart selection with performance indices to select most suitable materials for early stage mechanical design of micro electromechanical systems (MEMS) such as actuators and

sensors. Similarly, Parate and Gupta [64] also used this approach for choosing material for an electrostatic actuator based on performance indices involving variables such as actuation voltage versus displacement versus speed and fracture strength.

Rashedi et al. [65] used CES Selector for determining best suitable materials for large scale onshore and offshore wind turbines components i.e. blade and tower. The study termed Ashby's approach suitable for exploring the vast material database, translating design necessities as objectives and which finally screens out best possible materials candidates. Performance indices were developed for weight, cost, carbon footprint and energy objectives. The best materials for the components were carbon composites and cast iron, both dominant in their respected criteria such as composites in weight and cast iron in strength, cost, carbon footprints and energy. The authors concluded that final outcome stood as a compromise with each best candidate advantageous over the other. However, the results were not validated with other methods, only CES was used for selection.

Weaver et al. [66] used CES Selector tool in a case study where material selection was carried out for a refrigerator considering environmental impact minimisation. Relevant performance indices were formulated and suitable materials were shortlisted via a scatter chart. Another industrial case study by Sophie et al. [67] at Tecumseh used CES Selector tool for reducing the costs while enhancing overall quality and reliability of refrigeration components. Reduction in weight of an electrical box cover was the objective which is associated with the appropriate material. The authors applied the CES Selector chart-performance index method, and after conducting CAE analysis among

shortlisted candidates, polymeric material PET (35% Glass Fiber) was successfully reported as suitable material. The study also reported cost savings of €2 million and a production time savings up to three-fold.

Another case study by Fredriksson and Galos [68] used CES Selector program to reduce the weight of a truck trailer. The authors incorporated CES program with a customised material data of an end-grain Balsa sandwiched between Glass Fiber Reinforced Polyester face-sheets. It was claimed that new material compares well with traditional plywood and hardwood options for its mechanical properties. The study was verified experimentally with bending tests and reported that about 300 kg of weight could be saved with the new customised material for the trailer. This study showed the ability of CES Selector to create and input new materials and compare against already existing ones. Some studies have used CES or Ashby's approach just for initial screening only and then incorporating additional MCDM methods to further support the material selection process. Such as, a study by Thakker et al. [69] selected material for impulse turbine blade where CES was used for initial broad screening material families just based on density and strength. Later, Value Engineering and then TOPSIS methods were used for additional properties such as corrosion resistance, specific weight, and cost, stiffness, fatigue strength, respectively. The whole material selection was carried out in stages i.e. first with CES, Value Engineering and TOPSIS. The best material selection was named in TOPSIS outcome as 'Glass Fibre Reinforced Composite' (GFRC). FE analysis was conducted for the selected material and found GFRC would perform adequately in the real situation. Another study by Ermolaeva et al. [70] used CES for browsing possible material families based on stiffness, strength, buckling and

cost for a supporting beam placed beneath the chassis of DutchEVO car to distribute the loading. Relevant performance indices for stiffness, buckling and cost were developed in CES, however no strength-based index was evaluated. The indices were coupled with pair-wise weighting factors to give ranking list. The FE analysis was conducted based on the selected materials using MSC.NARC program for two loading scenarios i.e. heavy and light. Different materials were shortlisted for the loading types i.e. for stiff, light, cheap material under heavy loading, medium carbon steel was best candidate, and under light loading, Polypropylene fibre composite was selected.

A comparative study by Yazdani et al. [76] used Ashby's chart-index method, VIKOR and TOPSIS methods for three MEMS actuators cases i.e. (1) high speed, high force, (2) low voltage, large displacement and (3) high speed low voltage and low electrical resistivity. The authors found good agreement among the results of three methods with weighting factors assigned directly to performance indices in VIKOR and TOPSIS methods. For case (1), same ranking was seen among the methods, for case (2), 98% results were same with Ashby's method and for case (3) 91% closeness was seen. The authors concluded that for case (3), number of indices were increased to three contrary to two in both case (1) and (2), which created difficulty in Ashby's method ranking.

2.7 Mass Optimisation

Mass optimisation is necessary from restraining a concept being developed from overdesigning and to achieve a lightweight design. The benefits of mass optimisation may include reduced production, operational and

maintenance costs and time. It is linked to the weight, performance, material cost savings and overall quality of a mechanical component. However, such optimisation should not compromise the mechanical operational life of the concept or its components [77], as any initial design may sustain the loading in first instances of operation but may fail much sooner than expected under cyclic loadings. Fatigue, as understood by materials technologists, is a process in which damage accumulates due to the repetitive application of loads that may be well below the yield point [78]. This means, the stresses may be below the yield strength limit of a material but failure may initiate well below the expected operational period or runs of the component under repetitive loading if fatigue life was not incorporated during the design analysis phase. Material removal for mass optimisation increases the risks of compliance and potential for failure [79]. Consequently, this is where fatigue life becomes an important design criterion in optimisation.

There are various design studies that have used mass optimisation to improve quality of respective products. A study by Lee et al. [79] tried reducing the weight of a commercial hydraulic piezoelectric pump steel housing by reducing the wall thickness. ANSYS program was used for static structural FE modelling and a safety factor constraint involving equivalent stresses within 50% of the material yield limit was setup to avoid structural failure. The FE model was simulated for the maximum pressure of 15 MPa. The authors reported up to 64% weight reduction compared to the initial housing design. The optimised model was fabricated and tested experimentally with no structural failure reported. A study by Saoudi et al. [80] optimised the mass of a commercial lower suspension arm (aluminium alloy) of an automobile using

Abaqus FE program. The study used three arbitrary geometrical designs of the arm with removed unnecessary material with minimum stresses. Each alternate design was simulated for fatigue life prediction. Compared to the referenced initial design of the arm with 3.5 kg mass and fatigue life of 5.2e7 cycles, first alternate design was reported 3.34 kg with 1e8 cycles, second with 3.32 kg with 2e7 cycles and third with 3.1 kg and 5.2e7 cycles. Although the third design reported minimum weight yet the authors chose first design due to its maximum life. The authors reported that 5 to 11% of mass optimisation was achieved by just removing 10% of unnecessary material i.e. elements with minimum stresses. Similarly, a study by Ruiqiang [81] optimised the weight of a stiffened cylinder under axial loading with different shaped stiffeners. The author used analytical iterative technique for the dimensions i.e. shell radius, length, stiffeners dimensions etc. and setup critical buckling stress constraint with material yield limit as a failure criterion. The cylinder mass was reduced up to 8.48% compared to the initial value.

Thejasree et al. [82] used ANSYS FE program to optimise the weight of commercial engine connecting rod by removing material under low stress regions and devising three alternate concepts. Up to 12.8% maximum weight reduction was evaluated with slight increase in stresses yet within the yield limit. Likewise, Gopinath et al. [83] used FEA to optimise the weight of connecting rod using three concept alternatives with reduced web and rib thicknesses in lower stress regions. A maximum of 10.38% mass reduction was calculated. Another automotive study by Neelakandan et al. [84] optimised weight of a commercial engine starter motor bracket with fatigue life as constraint. ANSYS FE static structural analysis was used for identifying low stress regions. The referenced

bracket geometry was optimised by reducing the various thicknesses and necessary material removal and addition. The authors reported that optimised geometry resulted in an increase in fatigue life from 8.69e6 to 9.1e6 cycles with weight reduction of 21%.

Elsewhere, Kirthanna et al. [85] optimised the weight of a Chevrolet Beat car engine mounted bracket with three modified designs for three different materials under the same load while restricting the stress concentrations below the ultimate tensile strength. A reduction of highest 91 g (from 2444 g to 2353 g) was seen for grey cast iron compared to Aluminium silicon carbide and Aluminium alloy 5052. A large scale study by Elhewy et al. [86] optimise the offshore supply commercial vessel (OSV) for weight reductions. The original structure was modelled with FE method and the dimensions (scantlings thicknesses) were gradually reduced to the point of failure. The set of dimensional values below the failure point was designated as the optimum point of weight reduction analysis. The researchers found out that about 121.9 tons of weight is reduced from the vessel original structure i.e. up to 42.4%. The reduction in material ultimately saves 42.4% steel cost and fuel consumptions along with improvement in other service accessibilities such as ship sailing (improved speed) and harbouring.

Mass optimisation is generally carried out as parametric iterative approach using FE method. The parametric approach inputs a range of reduced geometric dimensions or design alternatives with material removed and if required a certain range of materials into the FE model, the outcome of which delivers the best optimum decision in terms of dimension values along with best material. As a design safety criteria in mass optimisation, most studies found in

literature retain stress values below material yield or tensile limits such as [79,81–85]. However, setting yield or tensile limits as criteria does not optimally reduce mass with respect to a material fatigue strength limit i.e. if the fatigue limit is lower than the yield strength and occurring stresses are above the fatigue limit under cyclic loading then the material life would be less than the maximum cycles for that fatigue limit. On contrary, if the stresses are below the fatigue strength then material life would be greater than the fatigue life cycles and components could operate for infinite lifetime [87]. Hence, incorporating fatigue-based mass optimisation is vital for prolong life estimation of the component being optimised.

2.8 Conclusion

Solar PV groundwater pumping is the most reliable and cost-effective option to fetch water compared to diesel backed systems in rural remote areas of developing countries which accounts for daily operational and maintenance costs. Being well adopted as a low cost option, there is a growing demand of low power pumps for high heads SPWPS in rural remote regions [4].

Two conventional groundwater pumps are widely used commercially i.e. centrifugal and positive displacement pumps. The performance of PD pumps is found to be better than centrifugal pumps for high head applications and in terms of efficiency in a SPWP system. Centrifugal groundwater pumps are site specific or work optimally under specific design conditions only. Positive displacement piston pumps can perform under variety of conditions as they are independent of head. There have been a few attempts to modify PD piston pump

designs for design simplicity or to improve pump output for rural areas. To the author's best knowledge, induced flow and linear actuators positive displacement groundwater pumps are the only found PD design attempts made in literature as per author's knowledge.

However, induced flow concept is not found to be suitable for higher heads. On the contrary, linear actuator pumps have been developed with submerged and unsubmerged models both utilising sophisticated electronics and are very less power efficient than traditional PD and centrifugal pumps. The submerged models with linear actuator built-in electronics are prone to water leakages. The unsubmerged model uses traditional long-piston drive rod which is costly, difficult to install or disassemble during maintenance and acts as significant load on pump power and ultimately on PV source. Therefore, a gap in groundwater piston pump design exists for a simplified pump design which curtails these limitations and further reduce the power consumption for higher head SPWPS i.e. no complex electronics and less power consuming parts such as long piston drive rod or internal components (crossheads, crossways, connecting rod, meshing gears etc.).

The development of the concept design of the pump can be initiated with modern computerised techniques in order to save both time and cost. The widely adopted CAD/FEA method is effective to generate the initial concept pump model and analyse numerically the design's ability to withstand high head loads such as 200 m. In addition, modern digital databases with accurate materials information could be used to select proper materials for the concept pump. Finally, the mass optimisation of the initial design contributes towards the

improvement in power consumption by the pump due to associated lightweight advantages.

CHAPTER 3

CONCEPT PUMP MODEL DESIGN AND VALIDATION FOR POWER CONSUMPTION

The main objective of this study is to optimise the power consumption of the groundwater piston pump backed by a PV source. By light weighting the pump by mechanical design modifications, load or power requirements for the PV source could be lessen during its operation. Groundwater piston pumps have the potential to be modified for simplicity without using any complex precision engineered electronic components or external long piston rods.

3.1 Design Considerations

The new conceptual design piston pump was generated with following proposed design specifications (PDS) and characteristics.

- The pump size should be less than 10-inch (0.254 m) [4] borehole size so the shape, with 1 inch assumed clearance. Typically, borehole pumps can range from 4 to 26 inches in diameter [30].
- The long piston drive rod used in sucker-rod pumps should be removed and replaced with a submersible motor directly assembled to pump body reducing power consumption besides eliminating installation, operational and maintenance issues. For instance, expensive ($1600 - £1227) polyester GFRC composite rod with 400 pieces make for only 122 m head [19], thus excluding the rod saves costs as well. The motor placement

within 10-inch borehole size is only possible as vertical as the length of motors exceed the diameter of the borehole. Some of commercial submersible motors lengths are highlighted in Table 3.1.

Table 3.1: Submersible pump motors sizes.

Pump	**Motor Size (L x W mm^2) – (length in inches)**
Lorentz PSk2-9 C-SJ8-44, [39]	**645** x 144 – **(25.4 in)**
Grundfos SP8A-37, [38]	**547** x 139.5 – **(21.5 in)**
Grundfos SQF 2.5-2, [36]	**1247** x 74 – **(49 in)**

- The pump should use reduced number of components compared to conventional design of piston pumps such as connecting rod, pins, meshing gears (consume 2 – 6% power [88,89]), crossways and cross heads. Less components mean lower losses and less load on the motor and consequently on photovoltaic source.
- The pump flowrate is taken to be 34.72 lpm based on 12 hours of daily operation per day [4]. The pump speed should be slow to have minimal friction and so the wear [90,91]. To account this, it is assumed that pump speed is same as the flowrate. This means that the piston should displace 1 litre of water volume per discharge stroke or per cycle.
- The pump should pump the water up to 200 m [4] i.e. its components should bear water weight for this height.

The required power to run pump only must be as minimal as possible (depends on the components and materials). For instance, the groundwater piston pump concept aims to eliminate the use of long piston rod to improve the power consumption and if comparing with a commercial 'Blackhawk Apollo'

piston rod pump model, the concept pump power consumption should be less than 280 W (see Table 3.2) for same head and flow without the use of long piston rod. The specifications of a commercial PV piston rod 'Blackhawk Apollo' pump are presented in Table 3.2. It is evident that the current pump model does not operate for heads up to 200 m.

Table 3.2: Specifications of Blackhawk Apollo piston rod pump [19].

Pump Specifications	**Blackhawk Piston rod pump**
Pump type	**Positive displacement**
Motor Power (W)	280
Flow rate (lpm)	10.2
Head (m)	122
Piston Rod material	Steel / Polyester fibre glass reinforced composite (GFRC)

In order to address above mentioned design considerations a new simplistic and optimised conceptual model of groundwater piston pump for PV water pumping system is developed using computer-aided design (CAD) eliminating any unnecessary features used in current groundwater piston pumps' designs. A detail design considerations flowchart for low power groundwater piston pump is presented in Figure 3.1. A mathematical model is also presented to support the optimised concept model for its power consumption, discussed later.

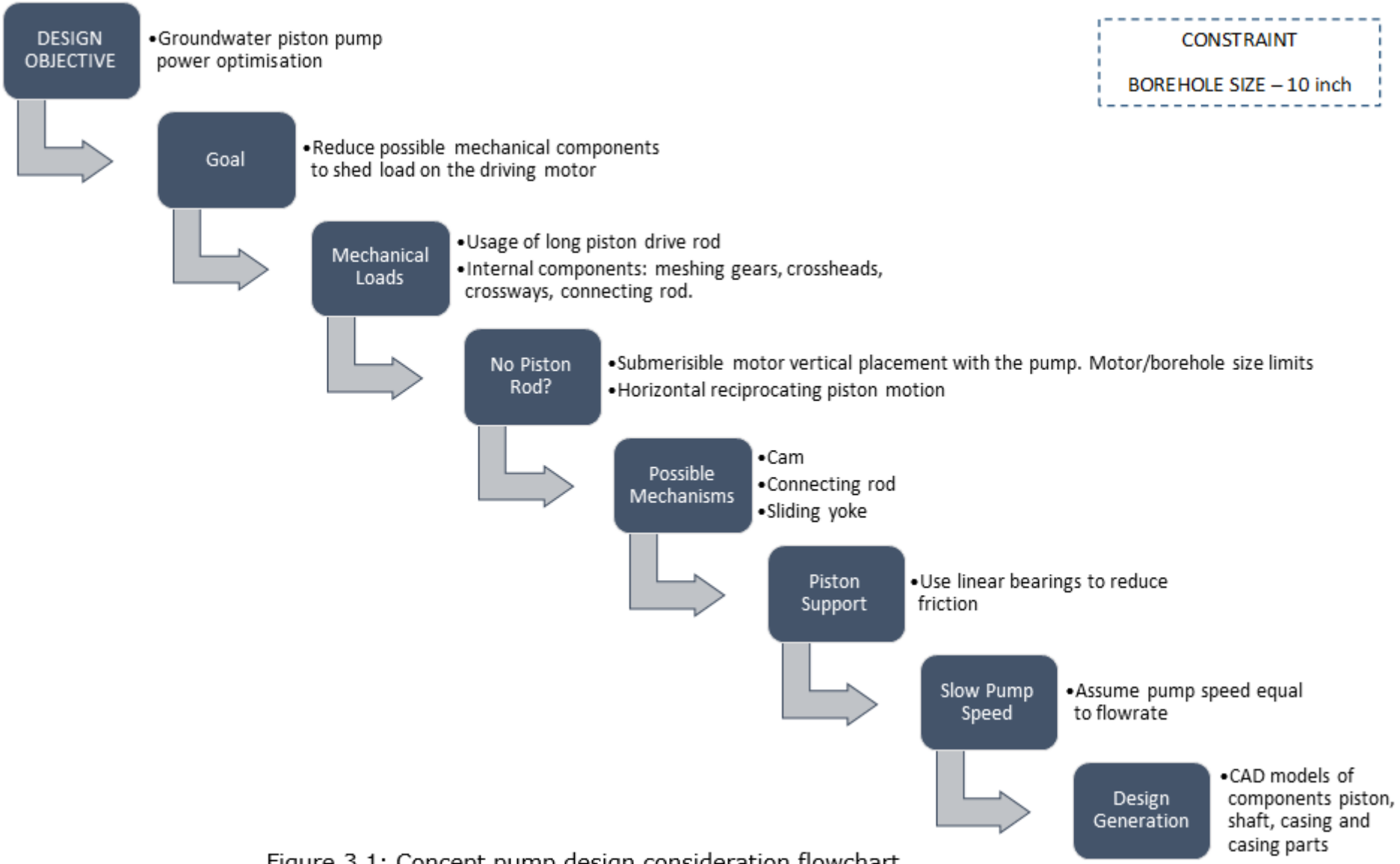

Figure 3.1: Concept pump design consideration flowchart.

3.2 Conceptual Pump Design Generation

The concept piston pump design generation is based upon the considerations presented in Figure 3.1. The components such as long piston rod, gears, connecting rod, crossheads and crossways are not supposed to be in the design in order to save power as much as possible required by the motor. The whole design should obey the borehole size constraint of 10 inches (actually 9 inches – 1 inch clearance) [4]. It is worth mentioning here that without the borehole size limitation, some conceptual ideas were generated at the very initial stage of this study which were expected to require larger borehole sizes (presented in Appendix A).

The 'non-use of transmission gears' constraint restricts the piston motion to be horizontal as the motor placement is vertical only (see Table 3.1 for motor lengths). Based on this, the horizontal piston could be displaced with a vertical rotating shaft (directly coupled to the motor). The piston-shaft mechanism could be possible with either cam shaft or connecting rod (although restricted in proposed design specifications) or scotch-yoke mechanisms.

The advantage of horizontal piston placement is that its size could be extended along the borehole length within the pump such as an oval piston (also used in automobile engines [92,93]) resulting in an increase in piston displacement volume with smaller stroke and slow pump speed (such as 1 litre discharge per stroke). The piston could be held in place with supports using linear shaft guided bearings [94] which are feasible for slow motion with less friction unlike crossheads sliding on crossways normally found in a piston pump (see Figure 2.4), or energy loss between cam shafts and cams as notified by

Short and Thompson [7] for ‘Fluxinos SOLAFLUX’ and ‘Divwatt SOLASTAR’ groundwater piston pumps. For instance, using bearings, the friction is reduced due to lower coefficient of friction compared to sliding i.e. 0.0015 – 0.002 (ball bearings) [95] and 0.08 – 0.20 (steel on steel) [96,97], respectively. A linear shaft guided bearing is shown in Figure 3.2. The allowable linear speed for these bearings is also high ranging 2 – 5 m/s (compact series) which means higher revolutions from 752 – 1880 rpm could be achieved (e.g. for a 2-inch stroke). These bearings are also lubricated, sealed and made with corrosion resistant materials [94].

Figure 3.2: A linear shaft guided bearing.

Based on the above piston-shaft possible arrangement, the cam, connecting rod and scotch-yoke mechanisms are conceptually developed as CAD models (initial drafts) using SolidWorks version 2017. The cam mechanism (Figure 3.3) requires compression springs attached with the piston body. The cam shaft pushes forward the piston through the in-contact bearing during the discharge stroke, while the springs pull back the piston afterwards. The reciprocating piston motion is supported by the ‘piston-supports’ which reciprocate within the ‘supports channels’ containing linear bearings inside. The possible drawbacks of this mechanism were also judged. The main drawback is

the mismatch of the timing between the shaft rotation during discharge stroke and pulling back of the springs during intake. The deviation in cam shaft rotational speed causes rolling slippage [41]. For instance, if the pump speed increases, the timing to pull back the piston could mismatch resulting in the incompletion of the strokes particularly the intake stroke which solely rely on springs' retraction. If any of the four springs lose retraction force (i.e. show slow retraction or unmatched retraction than other springs set) then again jeopardising the completion of intake stroke plus one side of piston may tilt against the cylinder wall enhancing seal wear. In other words, piston motion is not strongly linked with the shaft motion and relies partially on the springs. Additionally, every forward stroke has to overcome additional initial springs' excitation force to initiate the discharge, thus consuming additional power which is against the design considerations.

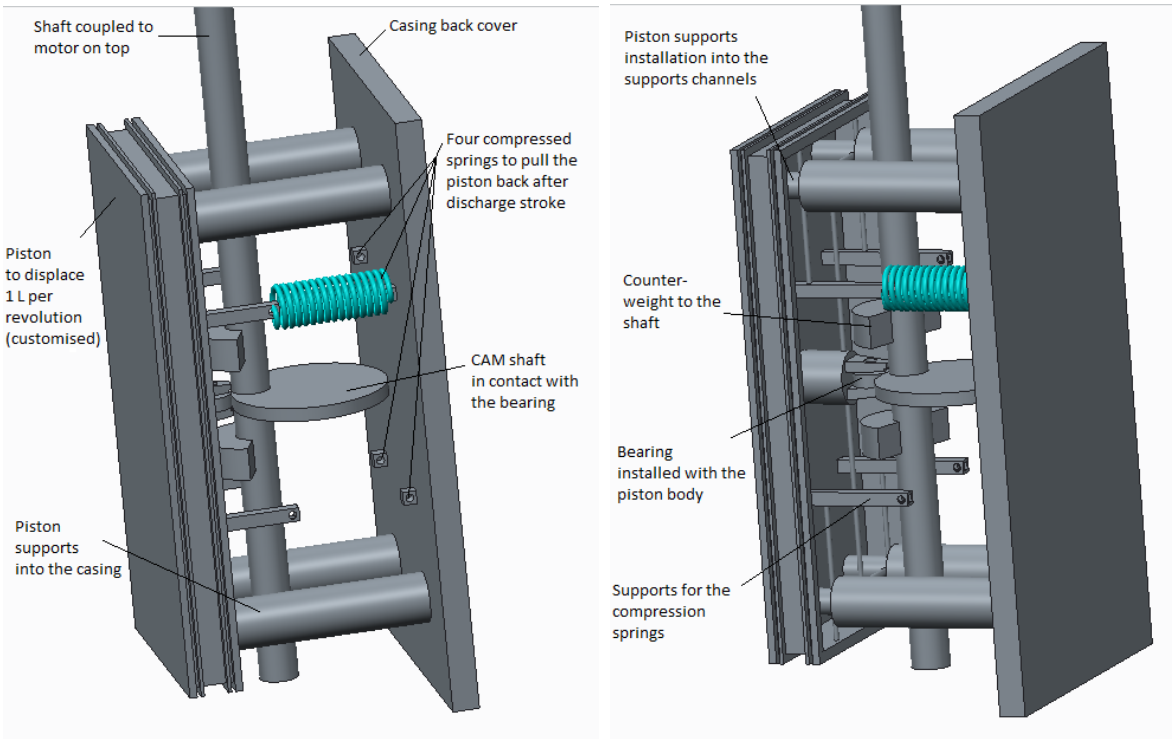

Figure 3.3: Cam mechanism with piston, shaft and casing back cover.

The connecting rod mechanism which has firm piston-shaft linkage (Figure 3.4) was also brought into consideration to check whether the mechanism fits within the borehole size limit. The total size of the pump including the casing and casing parts was found to be 13.9 inches exceeding the 10-inch limit. This is due to the connecting rod length which adds to the stroke length (assumed as small as 2 inches). This required extra spacing for casing and its parts. Furthermore, a connecting rod mechanism creates lateral forces (also called piston side force) between the piston and cylinder walls due to joint force transmitted via connecting rod through the inclination angle link with the rotating shaft, a cause of piston wear, vibration and heat generation [9,98]. The joint force acts in a direction oblique to the cylinder axis. The need of a compact design with a smaller connecting rod creates much higher lateral forces [99] because the lateral force is related to the ratio of connecting rod length and crank length which makes a design difficult to miniaturise [9]. Thus, this mechanism kind violates the compactness of the pump design for borehole size constraint.

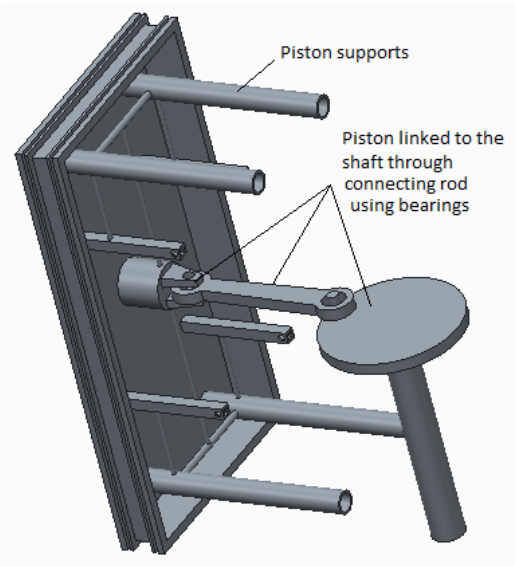

Figure 3.4: Connecting rod mechanism with piston and shaft.

On the contrary, a scotch-yoke mechanism exhibit very little lateral forces on the piston [9,100]. Therefore, the main advantages include reduce friction, vibration, piston wear and as well as encourages smaller dimensions or design compactness along with weight reduction [98–101]. A scotch-yoke mechanism is a reciprocating motion mechanism, converting the linear motion of a reciprocator (e.g. piston) into rotational motion of a crank or vice versa. A schematic of scotch-yoke mechanism is shown in Figure 3.5. Some common applications include high pressure oil control valve actuators, internal combustion engines such as SyTech engine, Bourke engine and other hot air and steam engines [98,101,102]. Due to minimum lateral forces, this mechanism requires less torque as well. A detailed study by Yoshizawa et al. [9] compared input torques from connecting rod and scotch-yoke mechanisms with same stroke, cylinder and crank rotational speed both theoretically and experimentally. It was found that up to 10% reduction in torque was observed using scotch-yoke mechanism. The concept piston-shaft model with scotch-yoke mechanism is shown in Figure 3.6. The mechanism allows the shaft to directly engage with the piston for its reciprocating motion without any use of a connecting rod. The piston was modified with middle-web extending from the piston head to slotted link where shaft pin (slider) is placed.

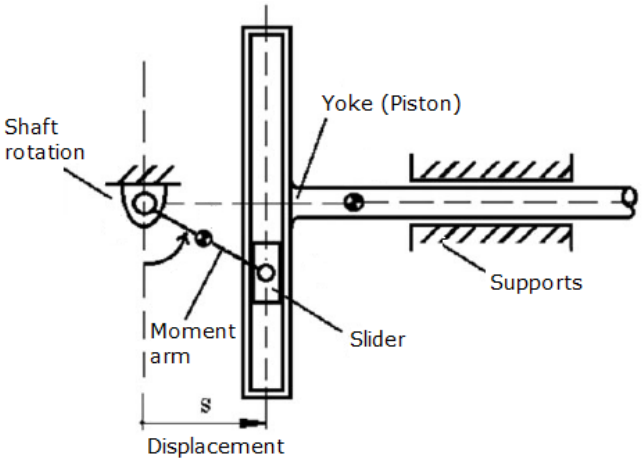

Figure 3.5: Schematic of scotch-yoke mechanism [98].

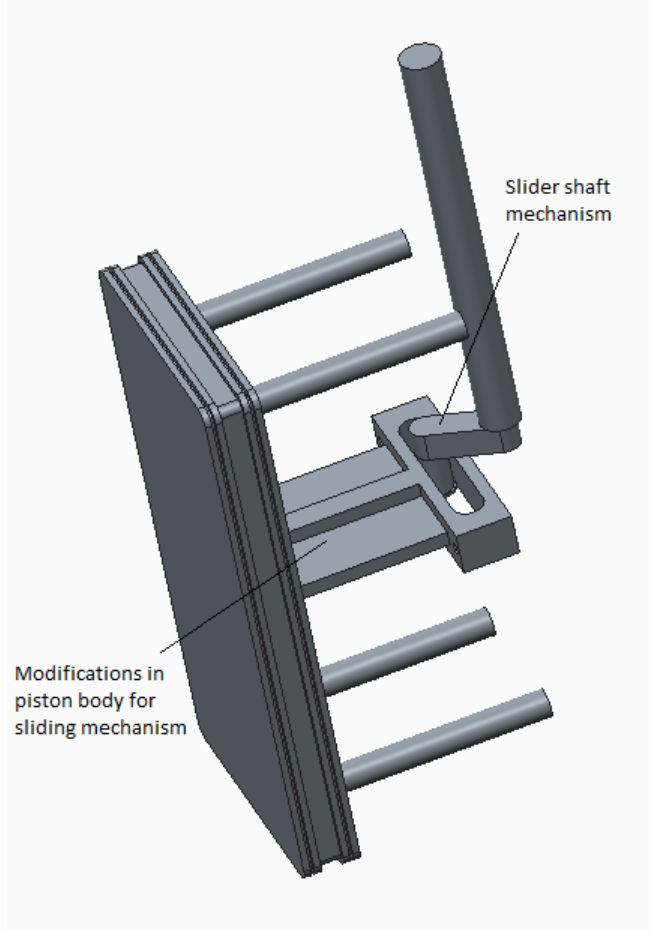

Figure 3.6: Scotch-yoke mechanism with piston and shaft.

The scotch-yoke mechanism supports all the design considerations i.e. eliminates use of long piston rod, meshing gears, connecting rod, crossheads,

crossways, firmly engages piston and shaft with no chance of slippage (unlike in cam mechanism), supports compact design, reduced frictional reciprocation for supports using linear bearings (unlike crossheads and crossways) and slow pump speed for reduce wear. Final drafts of the piston and shaft components were developed. The piston changes (see Figure 3.7) include oval shape instead of rectangular to account seal durability with less wear, ball bearings placement on the shaft slider which would slide in the slotted rectangular channel of the piston, a clearance of 1 mm was assumed for the bearings' diametrical contact in the channel for smooth motion, and fillets were introduced on the piston middle web to support bending of the piston head on the application of load. The shaft changes (see Figure 3.8) include modelling the shaft as full with additional lower section instead of top half only to have minimum deformation as possible and avoid bending in just top half when load from the piston exerts, and shaft webs were filleted adjacent to the middle bearings locations to support smooth flow of stresses when load is applied. The four ball bearings hold the shaft in position with two extreme top and bottom bearings to be fitted inside the main casing body while the two middle bearings fitted inside the bearing supports attached to the back cover.

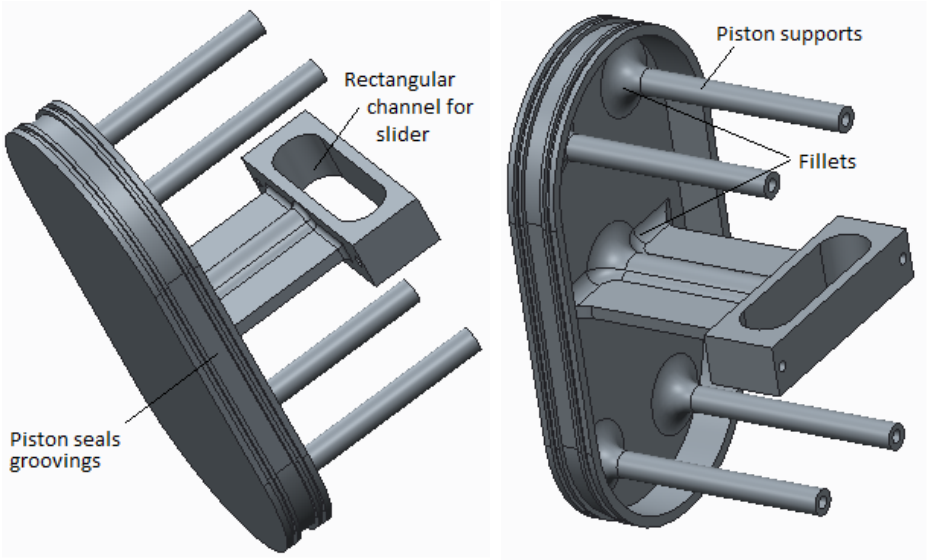

Figure 3.7: Oval piston design with rectangular channel for slider (left), piston back view showing fillets at piston supports and middle web (right).

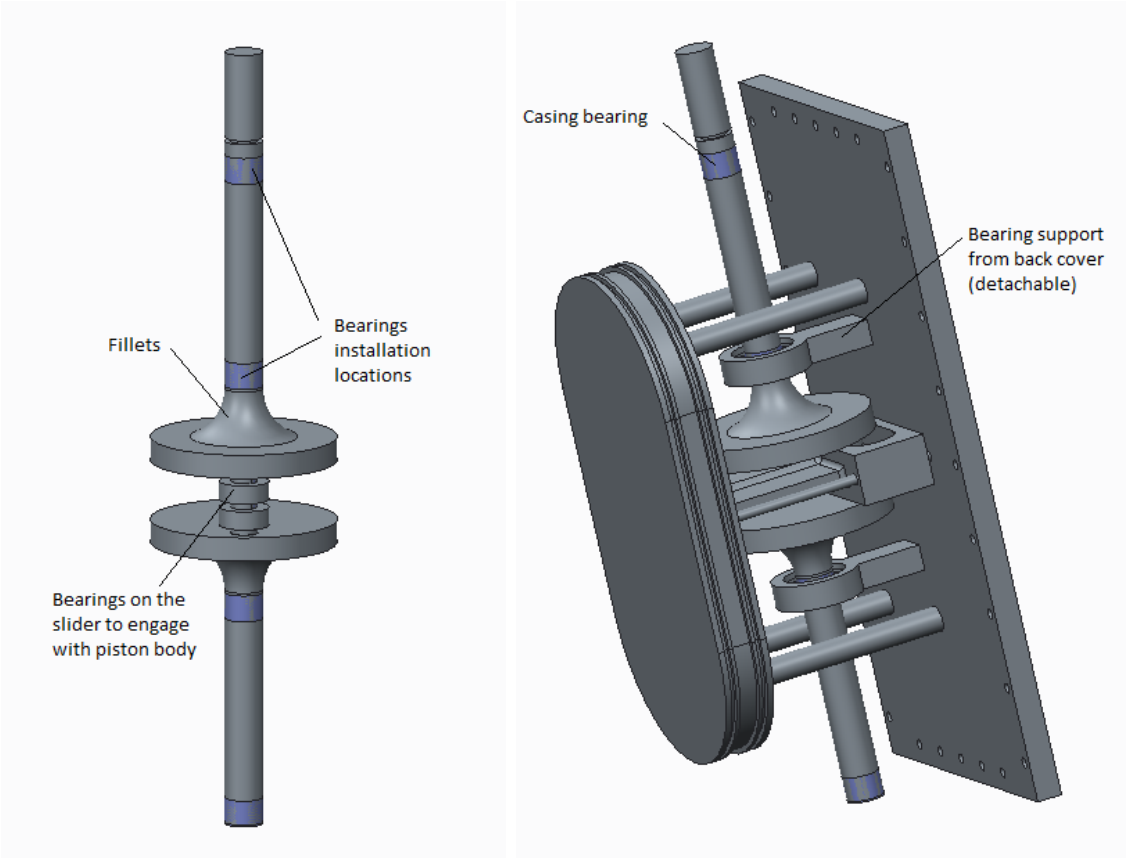

Figure 3.8: Full shaft design with fillets (left), and piston engagement with shaft positioned by bearings fitted in supports attached to the casing back cover (right).

Piston-shaft components being the main driver of the concept design, the main casing body was developed based on them, shown in Figure 3.9. The channels to fit linear bearings for piston supports are also shown. The whole complete assembly of the concept pump with front cover (with flow manifold with inlet and outlet), main casing body (transparently shown with internal components) and the back cover is presented in Figure 3.10. The highlighted blue circumferential lines around the pump assembly shows the diameter of 8.98 inches which means that the design is within the 1-inch tolerance for a 10-inch borehole size constraint. An arbitrary clearance of 1.5 mm was assumed between the piston rectangular slotted channel and the casing back cover to accommodate any backward deformation within the piston and the shaft.

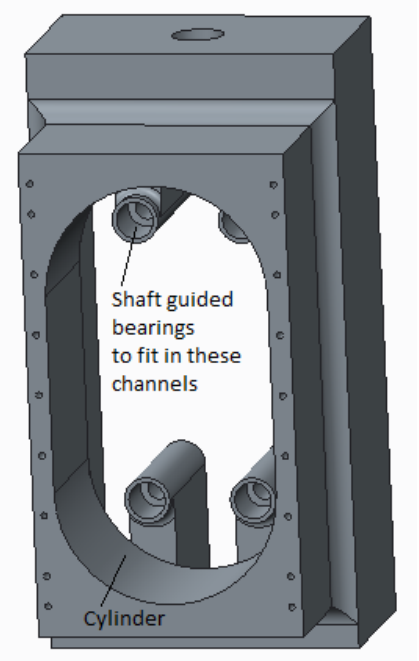

Figure 3.9: CAD model of concept pump main casing body.

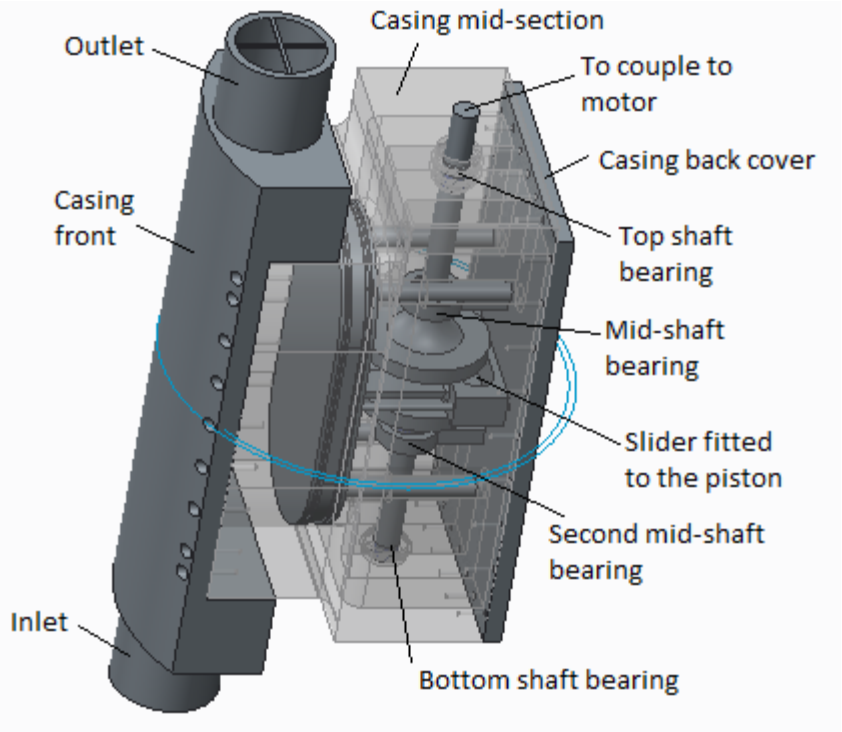

Figure 3.10: CAD model of concept pump full assembly.

Furthermore, the mechanism and submerged pumping operation of the developed concept pump was tested via full scaled 3D printing of the concept pump. The experimental testing supported the working of the pump as per the proposed mechanism along with pumping operation. The 3D printing process and experimental testing is discussed in Appendix B.

3.3 Evaluation of the Final Pump Design Concept

The conceptual pump working mechanism is a simple scotch-yoke principle also called as slotted link mechanism, where a rotating slider directly engages the yoke during revolution to make it reciprocate. The piston acts here as the yoke plate and the shaft pin act as the slider. The pump front cover (manifold) is equipped with check valves both at the inlet and outlet. Check valves are non-return valves which does not allow the fluid to flow back. During

the intake stroke, inlet check valve is forced to open drawing water in due to the suction effect of the backward moving piston and as the outlet check valve is closed. Water gets filled inside the piston cylinder during half of a revolution. In the other half of revolution, as the piston moves forward the intake valve remains closed and the outlet valve opens to let discharge of the water into the pipe attached. Hence, the cycle repeats in the next revolution of the shaft which is coupled to the motor. During the rotating motion, the linear bearings helps the piston remain intact in position with less friction during the reciprocating motion. The advantage of scotch yoke mechanism is that it is a simplistic mechanism using no auxiliary components to convert rotating motion to reciprocating motion and is suitable for low speeds.

3.3.1 Calculations of Power Consumption of the Conceptual Pump during Operation

In this section, a mathematical calculation model is presented which evaluates the power consumption by the developed conceptual pump and its components. The mathematical model also compares the results with the commercial solar operated groundwater pumps. The conceptual pump with no piston rod is surely expected to have some power savings. The analysis of validating this claim is presented in this section using the results from the mathematical model and are compared and discussed side by side.

In order to put a fair comparison with the developed conceptual pump, the mathematical model should be compared under the same specifications of commercial pump such as 'Blackhawk Apollo' (see Table 3.2) [19]. Furthermore, in order to compare the conceptual model and commercial pump,

a global environment settings of groundwater pumping operation are necessary as to depict the actual working conditions such as location data and flow demands.

The location is important because the daily operating hours of a PV operated pump designated as '$L_{dayhours}$' and atmospheric pressure 'P_{atm}'. These attributes along with water properties, pipe material and pump efficiency factors have been presented in Table 3.3. The pipe diameter 'D_{pipe}', head 'H' and flow requirement 'Q' are variables which depend as per requirement. The flow rate is linked to the running speed of the pump or rpm (revolutions per minute) of the motor 'N_{pump}', which is also a variable.

Table 3.3: Global settings for the mathematical model for the groundwater pump.

GLOBAL ATTRIBUTES	VALUE / DESCRIPTION
Location	Nairobi, Kenya [103]
Day hours, $L_{dayhours}$	12 hr [4]
Pipe material	PVC
Pipe absolute roughness, ε	0.0000015 m [104]
Water temperature	20 °C
Water Kinematic viscosity, ϑ_w	1.004e-6 m^2/s
Water density, ρ_w	1000 kg/m^3
Motor efficiency factor, η_m	0.89 [105]
Pump efficiency factor, η_p	0.85 [105]

The required power in a borehole groundwater pump is mostly affected by the total weight of water in pipe for a certain head, flowrate which generates resistive forces or pressure head loss, flow speed and the pump components load.

The mathematical model initiates with the calculation of mass of water 'M_w' in the pipe with respect to the head elevation (Equation 3.1) which is then converted as the weight '$F_{water\ weight}$', Equation 3.2.

$$M_w = \rho_w \times A_{pipe} \times H \tag{3.1}$$

$$F_{water\ weight} = M_w \times g \tag{3.2}$$

where, 'g' is the gravitational acceleration. 'A_{pipe}' is the cross-sectional area of the pipe.

The resistive forces inside the pipe due to flowrate which contribute along with the water weight as acting load on the pump components are calculated by evaluating the Reynold's number 'R_e' which determines the nature of flow (laminar or turbulent), given by Equation 3.3. The resistive forces responsible for pressure or head loss 'H_L' in pump operation are calculated by Equation 3.4,

$$R_e = \frac{v \times D_{pipe}}{\vartheta_w} \tag{3.3}$$

$$H_L = f \times \frac{H}{D_{pipe}} \times \frac{v^2}{2g} \tag{3.4}$$

where, 'v' is the flow velocity and 'f' is the Darcy-Weisbach friction factor given by '$\frac{1}{\sqrt{f}} = -2log\left(\frac{\varepsilon}{3.7D_{pipe}} + \frac{2.51}{R_e\sqrt{f}}\right)$'.

The head loss is converted into the resistive force '$F_{resistive}$' inside the pipe which ultimately acts on the piston using Equation 3.5. The resistive force also includes minor losses due to pump discharge manifold '$F_{manifold}$' and valves 'F_{valve}'.

$$F_{resistive} = \rho_w g H_L \times A_{pipe} + F_{manifold} + F_{valve} \quad (3.5)$$

The atmospheric pressure on the pipe '$F_{atm} = P_{atm} \cdot A_{pipe}$' also contributes to the total force on the piston. Hence, the total force 'F_{max}' acting on the piston face is summed up as,

$$F_{max} = F_{water\ weight} + F_{atm} + F_{resistive} \quad (3.6)$$

The mathematical model now evaluates the power consumption by the pump per stroke during the operation. This includes pump components and the maximum force on the piston. The piston linearly reciprocates while the shaft rotates on its axis. The power consumptions by each of the component are given by Equations 3.7 and 3.8, respectively and the power consumption by water inside the pipe to be lifted is calculated by Equation 3.9.

$$P_{piston} = \eta_{seal} \cdot g \cdot M_{piston} \cdot V_{piston} \quad (3.7)$$

$$P_{shaft} = I_{shaft} \cdot \frac{\omega^2}{t_{rev}} \quad (3.8)$$

$$P_{water} = F_{max} \cdot v \quad (3.9)$$

where, '$V_{piston} = \frac{2\pi S_l N_{pump}}{120}$' is the piston velocity per revolution, 'S_l' is the stroke, 'N_{pump}' is the pump speed, 'ω' is the angular velocity of the shaft in radians per second, and 't_{rev}' is the time for one revolution which is also called as the piston stroke time. Hence, the total power consumed by the conceptual pump per stroke 'P_{pump}' is,

$$P_{pump} = \frac{P_{piston} + P_{shaft} + P_{water}}{\eta_m \cdot \eta_p} \quad (3.10)$$

The quotient of water output from the pump to the pump motor power is normally termed as the hydraulic efficiency of a pump. This is prescribed by how much energy is converted by the electrical motor power of the pump to the water flowing from the pipe at head, calculated as,

$$\eta_{hyd} = \frac{Q g \rho_w H}{P_{pump}} \times 100 \tag{3.11}$$

where, 'Q' is the flow rate.

It is important to note that the power extracted from the model results estimates the motor power sizing incorporating the pressure drop losses and constant flowrate at every instantaneous rise of head. In other words, it predicts motor power sizing for the any specific head requirement.

3.3.2 Power Consumption Theoretical Model of the Piston Rod Pump

The mathematical model for a piston rod pump is almost same as discussed in previous section apart from the effects of long piston rod which are just added in the components power evaluation as the rod also reciprocates along with the piston. The long piston rod power consumption per stroke '$P_{piston\,rod}$' is given by Equation 3.12. Hence, the total power consumption with piston is calculated using Equation 3.13.

$$P_{piston\,rod} = g \cdot M_{piston\,rod} \cdot V_{piston} \tag{3.12}$$

$$P_{pump} = \frac{P_{piston\,rod} + P_{piston} + P_{shaft} + P_{water}}{\eta_m \cdot \eta_p} \tag{3.13}$$

where, '$M_{piston\,rod}$' is the mass of the long piston rod.

3.4 Power Consumption Estimations - Validation of the Mathematical Model of the Selected Final Conceptual Design

Next, it is necessary to validate the mathematical model before it could be applied on the conceptual pump to calculate its power consumption and compare with a piston rod pump. For this purpose, a commercial groundwater piston rod solar pump 'Blackhawk Apollo' was selected as a reference (because of low power consumption, see Chapter 2 – Table 2.6, and much availability of data related to pump power and design). The model was validated with Blackhawk Apollo pump's published power specifications. Additionally, the model was further compared to another piston rod pump with linear actuator, tested in an experimental study conducted by Andrada et al. [42]. The specifications of commercial 'Blackhawk Apollo', experimental study's piston rod pumps and concept pump are side-by-side presented in Table 3.4.

Table 3.4: Specifications of solar tested piston rod pumps and concept pump.

	VALUE / DESCRIPTION		
ATTRIBUTES	**Blackhawk Apollo Piston Rod Pump** [19]	**Experimental Piston Rod Pump** [42]	**Concept Pump**
Pump speed, N_{pump}	42 rpm	11.46 rpm	Up to 34.72 rpm
Piston stroke, S_l	6 in (0.1524 m)	4.92 in (0.125 m)	2 in (0.0508 m)
Pipe diameter, D_{pipe}	1 in (0.0254 m)	2.5 in (0.0635 m)	1 in (0.0254 m)
Pipe material	PVC	PVC (assumed)	PVC
Piston seal material	Ultra-high molecular weight polyethylene (UHMWPE)	UHMWPE (assumed)	UHMWPE [106]
Piston seal coefficient of friction, η_{seal}	0.2 [107]	0.2 [107]	0.2 [107]
Maximum head, H	122 m	18 m	Up to 200 m
Maximum flow, Q	10.2 lpm	26 lpm	Up to 34.72 lpm
Maximum motor power	280 W (GFRC rod)	210.72 W	1.67 kW
Suggested PV power	300 W		

Pump Components Attributes		
Blackhawk Apollo Piston Rod Pump	**Experimental Piston Rod Pump**	**Concept Pump**
Piston Brass Mass, M_{piston} 0.5 kg (assumed) **Piston rod (material 1)** GFRC (400 pcs ~ $1600) Mass, $M_{piston\,rod}$ 3.7 kg/100m Diameter 0.375 in (9.525e-3 m) **Piston rod (material 2)** Steel Density 7750 kg/m^3 Diameter 5e-3 m [108]	**Piston / rod mass** 20.39 kg **Counterweight mass** 46 kg	**Components Material** Steel Density 7750 kg/m^3 **Piston mass** 1.33 kg (calculated from CAD) **Shaft mass** 0.96 kg (calculated from CAD) **Mass inertia of shaft** 3.72e-4 kg.m^2

3.4.1 Conceptual Pump vs Commercial Blackhawk Apollo' Piston Pump

The 'Blackhawk Apollo' pump commercial data from Table 3.4 with polyester GFRC piston rod was used as input into the mathematical model for validation, and the model outcome as pump power consumption was in found out to be in good agreement with the published data. An illustration of the power consumption by the pump per head rise is shown in Figure 3.11. The callout value shows that at 122 m head, the estimated power by the model is 293.53 W compared to actual value of 280 W (see Table 3.4). The power linearly increases due to the linear rise in the pipe water and piston rod weights along with the head rise. The percentage difference of total motor power between the model results and commercial data, around 4.83%. The small error is due to the assumed inputs into the model such as pump and motor efficiencies, piston mass etc. An error margin below 10% between experimental and numerical results was designated as 'good' in the literature e.g. by Zhang et al. [109] research. This allowed to further use the model to compare the commercial pump with conceptual pump based on their individual design characteristics as discussed next.

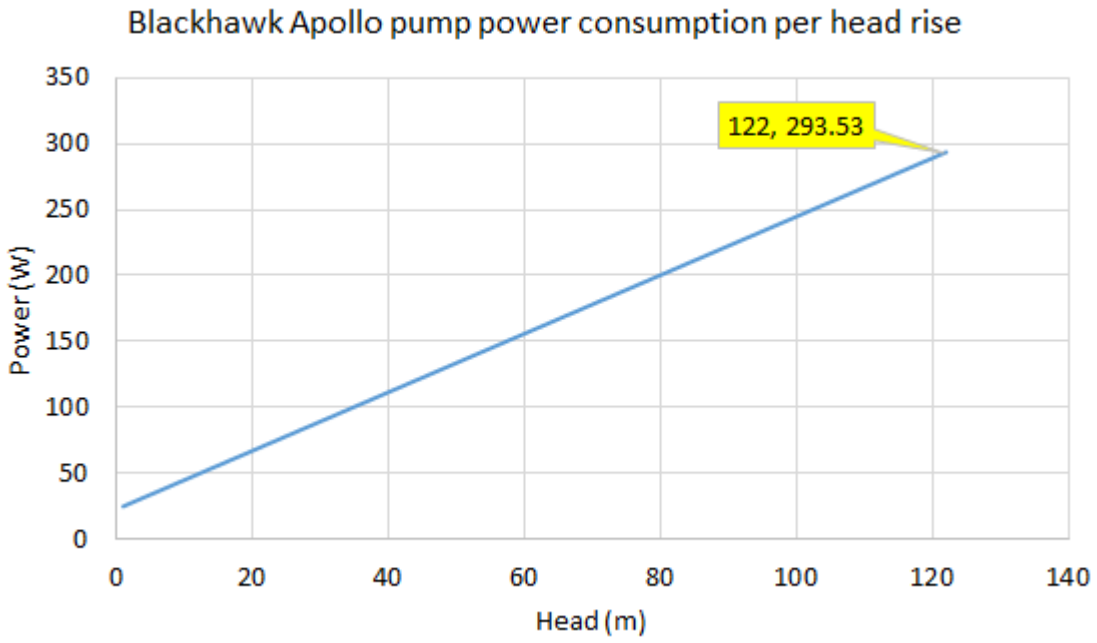

Figure 3.11: Power consumption estimation of 'Blackhawk Apollo' pump using mathematical model.

Next, the comparison was made between the concept pump and commercial 'Blackhawk Apollo' piston rod pump at similar flowrate requirement of 10.2 lpm set for both pumps. This method allowed to evaluate the power consumption per stroke for each pump more effectively i.e. on equal flow demands. The other attributes remain same as per their individual designs data (see Table 3.4).

The commercial piston rod pump was also compared with steel rod besides GFRC rod as the pump uses both as per required application. The mathematical model was extended beyond operating limit of the commercial rod pump i.e. 122 m to observe the results when compared head to head with conceptual pump operation which is targeted at operational head of 200 m.

In principle, the power in both pumps is mostly affected by the components masses because the water weight is same due to the similar pipe parameters (material, diameter and length). A comparison of components' masses for both pumps with respect to head rise is shown in Figure 3.12. The piston and shaft mass in concept pump remain the same throughout head whereas drive rod mass in piston rod pump exhibit constant rise, see Figure 3.12(a). The percentage difference was also drawn between the masses as explained on Figure 3.12(b) where negative values show the concept pump components' mass is higher with head rise than the piston rod pump mass until they supersede the concept pump. The difference is significant for lower head values due to piston rod pump mass constantly rise whereas the concept pump mass remains same throughout the head rise. For a head of 200 m, the difference with steel rod is up to 92.6% and 71% with fibreglass rod.

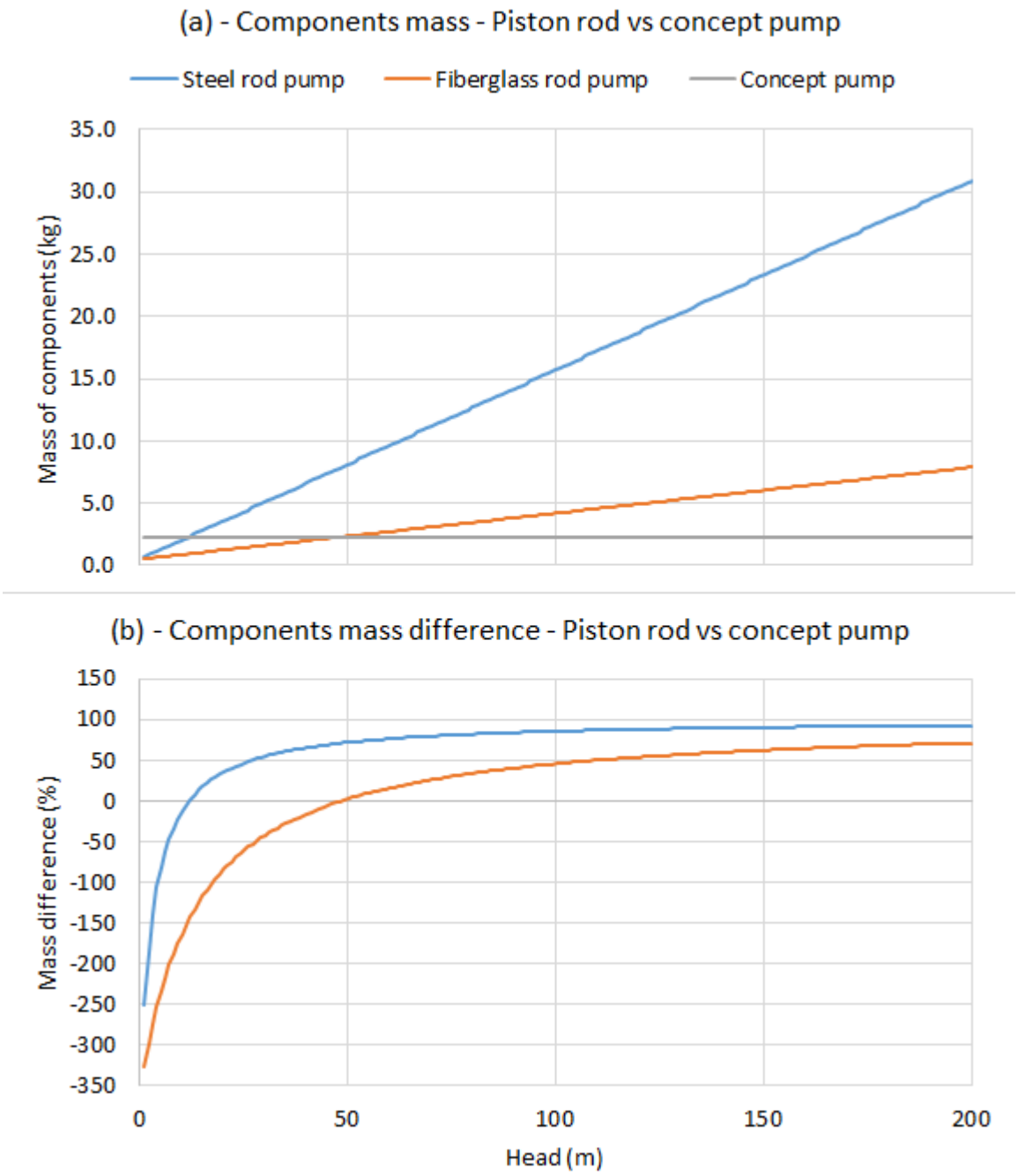

Figure 3.12: Components mass with head rise comparison between piston rod and concept pump (a) Mass of components; (concept pump – piston and shaft. Piston rod pump – piston and fibreglass/steel rods) (b) Mass difference of fibreglass/steel rod pumps against concept pump.

The model results show significant improvement for conceptual pump in terms of power consumption while comparing steel and GFRC piston rod pumps as evident in Figure 3.13. The steel rod consumes higher power than the lighter GFRC composite rod. Hence, elimination of long piston drive rods not only reduces power consumption, it also saves installation time and cost of expensive drive rods, for example, 400 pieces of a GFRC rod costs $1600 (£1227) for 122 m head [19] (based on Blackhawk Apollo piston rod pump quotation, see Appendix E). This means that for a high head of 200 m, up to £2011 could be saved by not using 656 pieces which makes long piston drive rod, consequently contributing to less installation and maintenance time during assembling and disassembling.

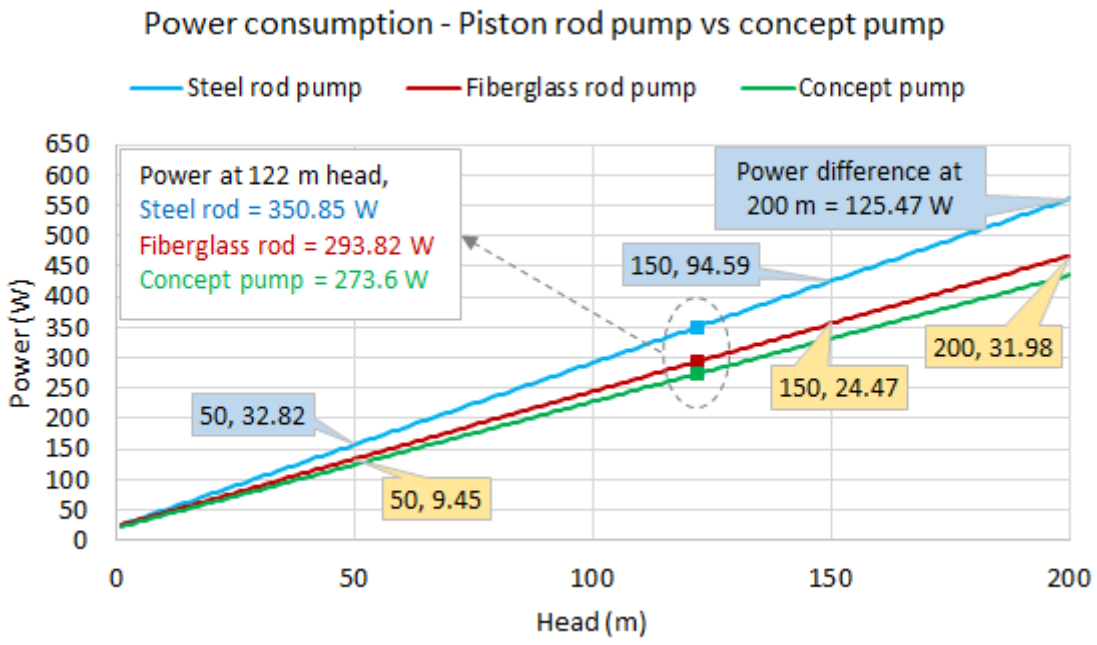

Figure 3.13: Power consumption comparison of 'Blackhawk Apollo' piston rod pump (until 122 m and extended) and the concept pump.

The power consumption difference shows significant improvements for concept pump i.e. around 22% less consumption at 122 m against 'Blackhawk' with steel rod and peaked 22.4% at 200 m. Against the GFRC rod, the concept pump moderately improved power consumption of around 7% throughout the head as illustrated by Figure 3.14. The downward trend of the GFRC rod power consumption against concept pump is due to the insignificant rise is rod weight with respect to head against the water weight in the pipe. On the contrary, the steel rod weight adds significant effects against the water weight. However, by just comparing the difference of components' powers only, positive trends are seen for concept pump against both types of piston rods as shown in Figure 3.15. This means it does not include the power required for lifting the water weight which is constant for both pumps. The hydraulic power to pump power was also compared between the piston rod and concept pump. The ratio highlighted further the efficiency of concept pump dominating over the steel and GFRC composite rod pumps as shown in Figure 3.16.

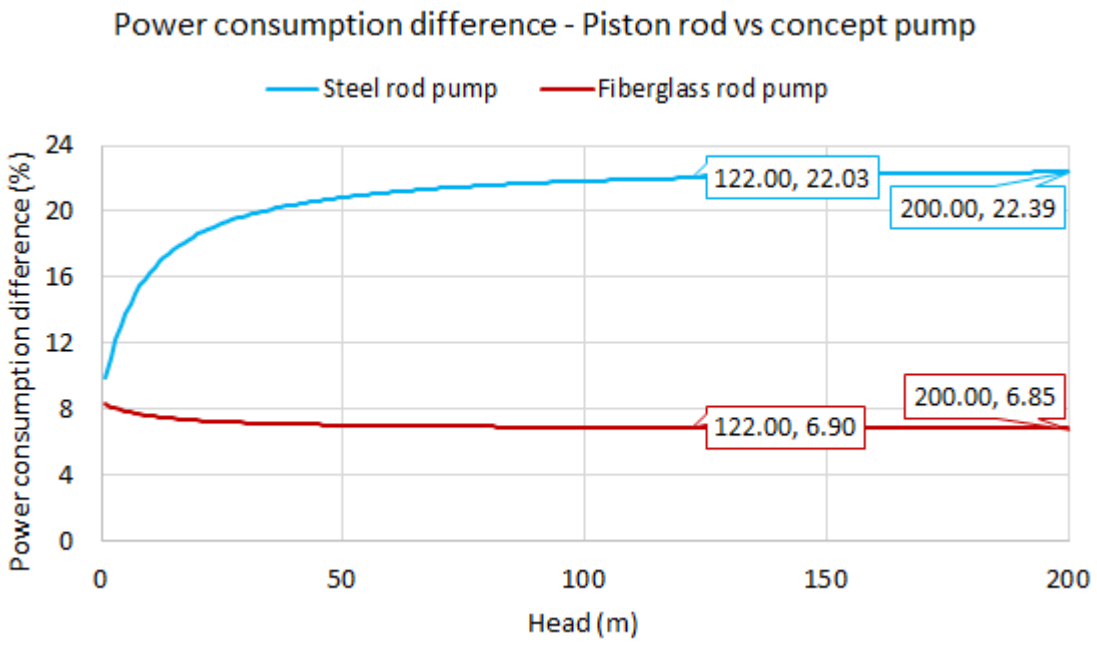

Figure 3.14: Power consumption difference comparison of 'Blackhawk Apollo' piston rod pump (until 122 m and extended) and the concept pump.

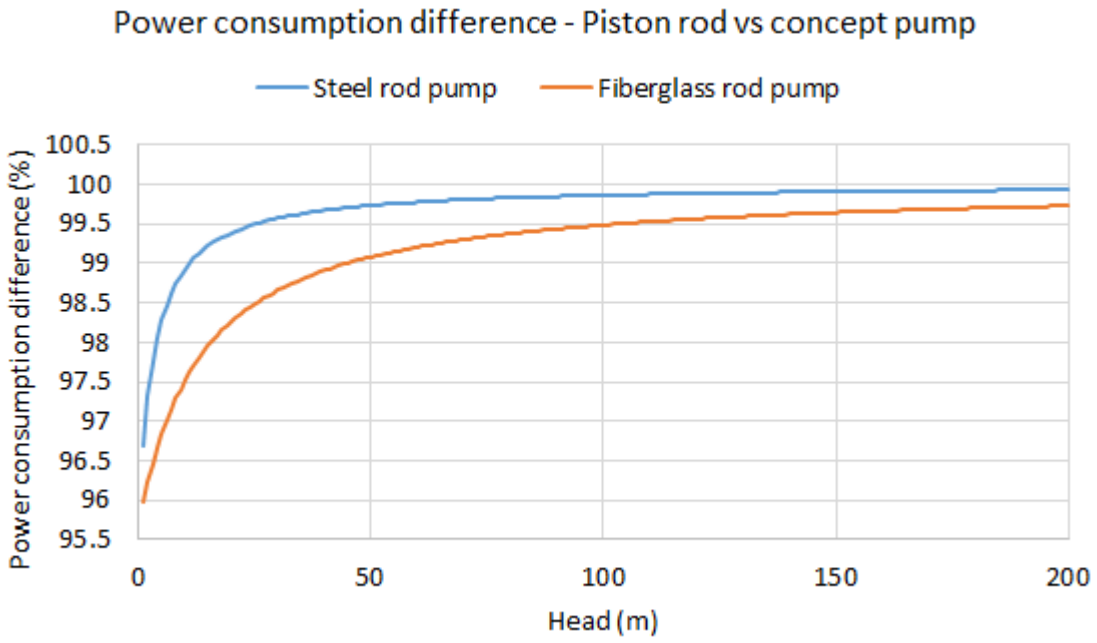

Figure 3.15: Pump components power consumption difference comparison of 'Blackhawk Apollo' piston rod (until 122 m and extended) and concept pumps.

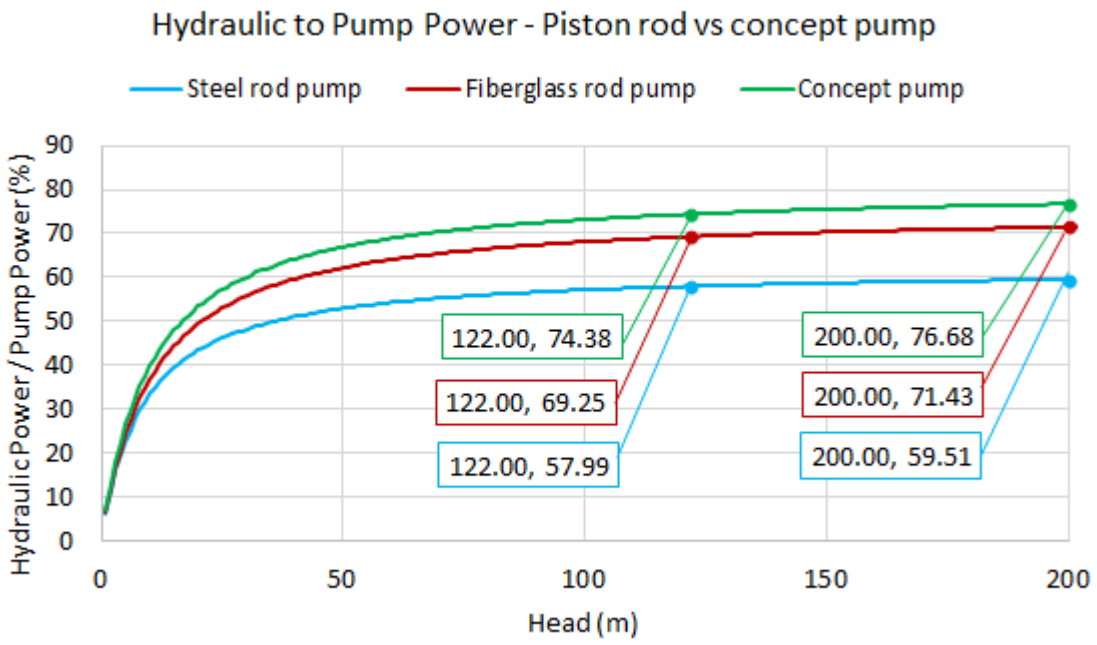

Figure 3.16: Hydraulic to pump power comparison of 'Blackhawk Apollo' piston rod pump (until 122 m and extended) and the concept pump.

The energy savings were also computed for concept pump against the commercial piston rod pump for 12 day-hours of daily operation with flowrate 10.2 lpm required at 122 m and predicted for 200 m heads as well, shown in Figure 3.17. Significant values are observed for daily and yearly basis for two rod materials. When compared per day operation, even with GFRC composite rod the power saving is around 243 W for 122 m, approximately equivalent to the power rating of a mid-range solar PV panel thus saving its cost daily (such as a 250 W solar panel range from £227 - £300 depending on PV cell material [110,111]). This means with steel rod, up to 4 PV panels costing up to £1100 can be saved. Similarly, higher head yields higher energy savings because of constant rise of the piston rod masses and so price of PV panels i.e. for 200 m head, using GFRC rod, up to 2 PV panels costing £462, and with using steel rod, up to 6 PV panels costing up to £1800 could be saved, respectively.

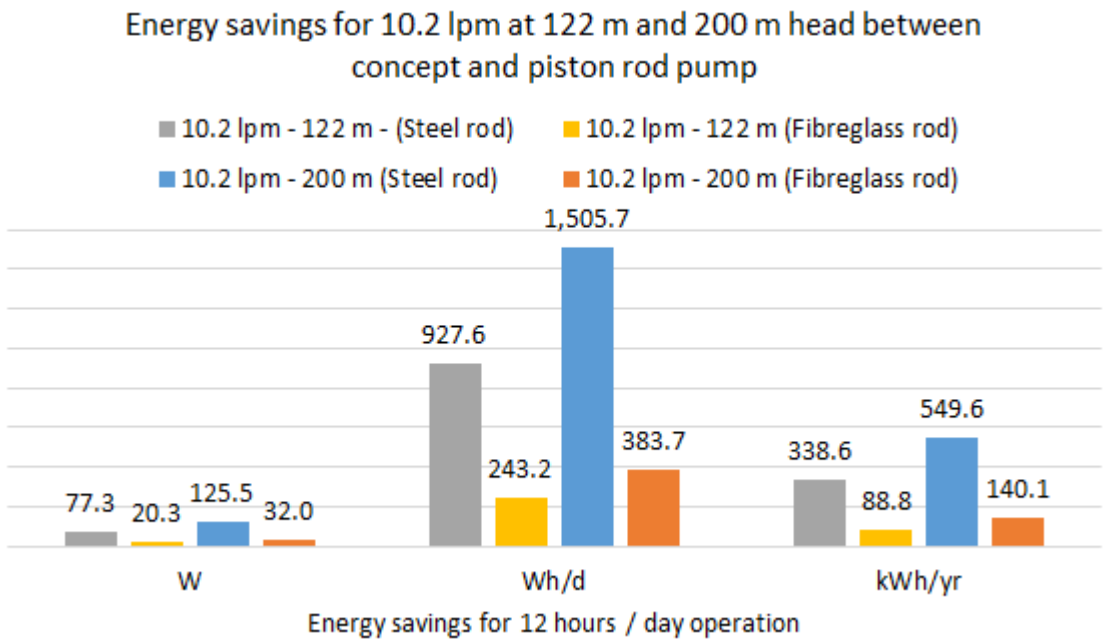

Figure 3.17: Energy savings (per stroke, day and year) of concept pump compared to 'Blackhawk' commercial piston rod pump (fibreglass/steel rod) for 122 m and 200 m heads.

The concept pump estimated power as per engineering design specifications i.e. 200 m head with flowrate of 34.72 lpm [4] (presented in Table 3.4), is evaluated using the model. The required pump power and hydraulic efficiency of the concept pump for such flow and head requirement is shown in Figure 3.18. At 200 m head, the pump motor power is estimated to be 1.67 kW with 68.2% hydraulic efficiency. The linear rise in power is directly proportional to the linear rise in water weight in the pipe. At lower heads, the lower hydraulic efficiency is due to the lower hydraulic energy compared to the power consumed by the pump and its components which include resistive forces (such as seal frictional force, constant atmospheric pressure etc.). As the head gets higher the effect of resistive forces diminishes (except the frictional head losses) due to the dominancy of the water weight and head losses which much contribute

to the required power against the required hydraulic energy (both linearly rise with head). Furthermore, it is worthy to mention here that the factors affecting the flowrate are the demand input (as a design parameter) and the Darcy-Weisbach friction factor 'f' which in turn results in head loss (see Equation 3.4). When the friction factor increases the flowrate decreases due to increase in head loss. However, the mathematical model already incorporates the head losses to predict the pump power with every rise in head (simultaneously increase in head losses) or flowrate.

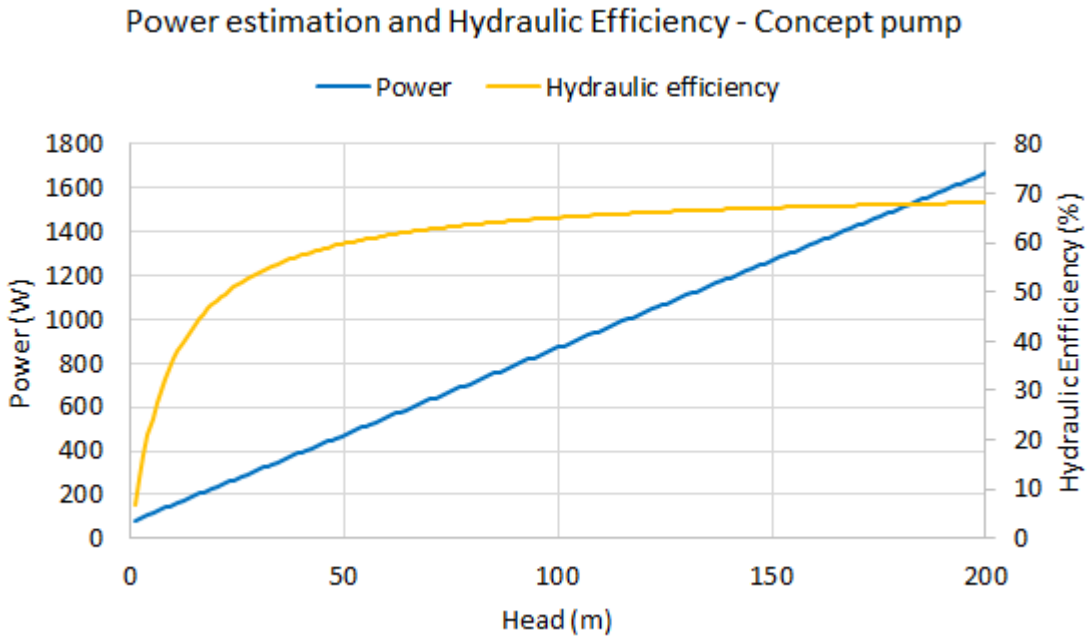

Figure 3.18: Estimated power and hydraulic efficiency of concept pump as per design specifications.

The developed concept pump is also simplified with reduced number of components i.e. piston and shaft as the only moving parts unlike a typical piston pump which has meshing gears (efficiency varies from 94% – 98% [88,89]), connecting rod etc. For instance, at 34.72 lpm and 200 m head, not using these components saves power up to 72 – 146 W i.e. 2.2% from connecting rod (based

on Figure 3.4), 2 – 6% from gears). Similarly, excluding the crossheads in the design saves up to 16.67% power (based on increase in total force due to 0.2 coefficient of friction between two lubricated stainless steel surfaces [97]).

Furthermore, it is reasonable to note that further improvement opportunities are surely expected after the appropriate optimisation of the components' mass in the concept pump which is done after validating the structural adequacy of the design.

3.4.2 Experimentally Tested Piston Rod Pump vs Conceptual Pump

Similarly, the mathematical model (Conceptual pump) performance results were compared to another piston rod pump with linear actuator, an experimental study by Andrada et al. [42], specifications of which are presented in Table 3.4. The flow demand for the concept pump was set same as that of the study's requirement.

The motor power estimation by the mathematical model was found to be closer to the experimentally measured results from the study with a difference of 7.48% calculated, as shown in Figure 3.19. The initial negative power values for the rod pump in the figure describe the power only consumed to lift the counterweight until the hydraulic flow power dominates over it i.e. around 4 m head. On the contrary, the concept pump is predicted by the model to deliver the required flow with an estimated motor power of 163 W for 18 m head, making a positive difference of 28.15% in power reduction. This comparison further validates the usage of mathematical model for concept pump power. The hydraulic to pump power ratio show similar trend for both pumps shown in

Figure 3.20. During the initial head rise, the ratio shows positive trend as the counterweight balances the water weight till it reaches maximum at 4 m head. At this point, the counterweight is totally in balance with the hydraulic weight. Further with the head rise, the weight of water starts dominating and thus the ratio shows a downward trend.

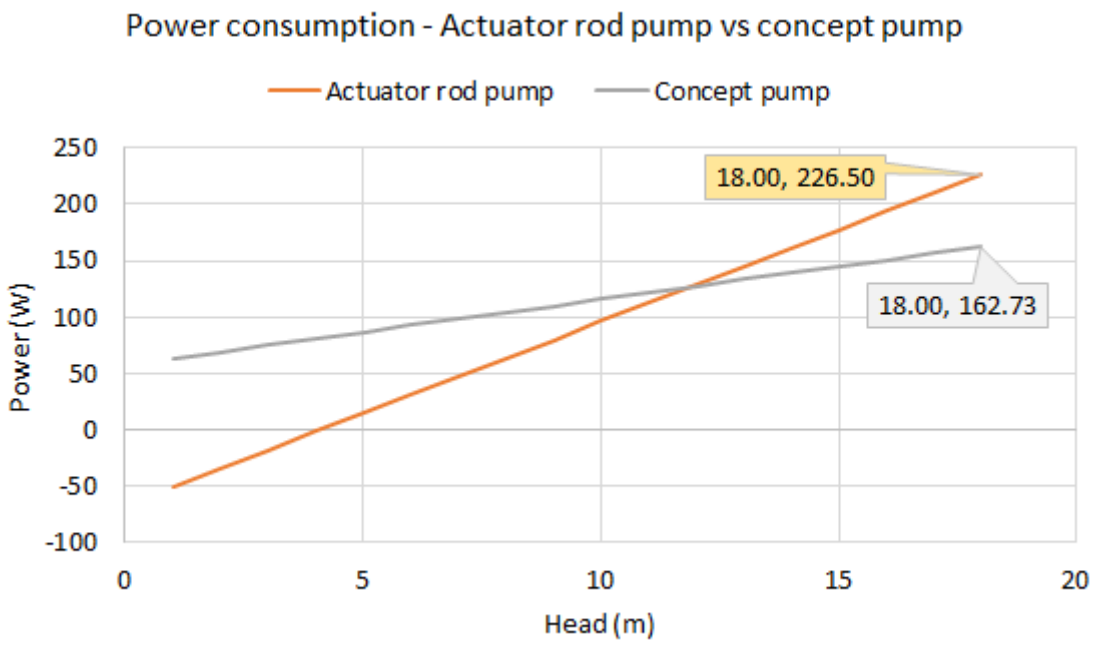

Figure 3.19: Power consumption comparison of actuator rod pump [42] and concept pump.

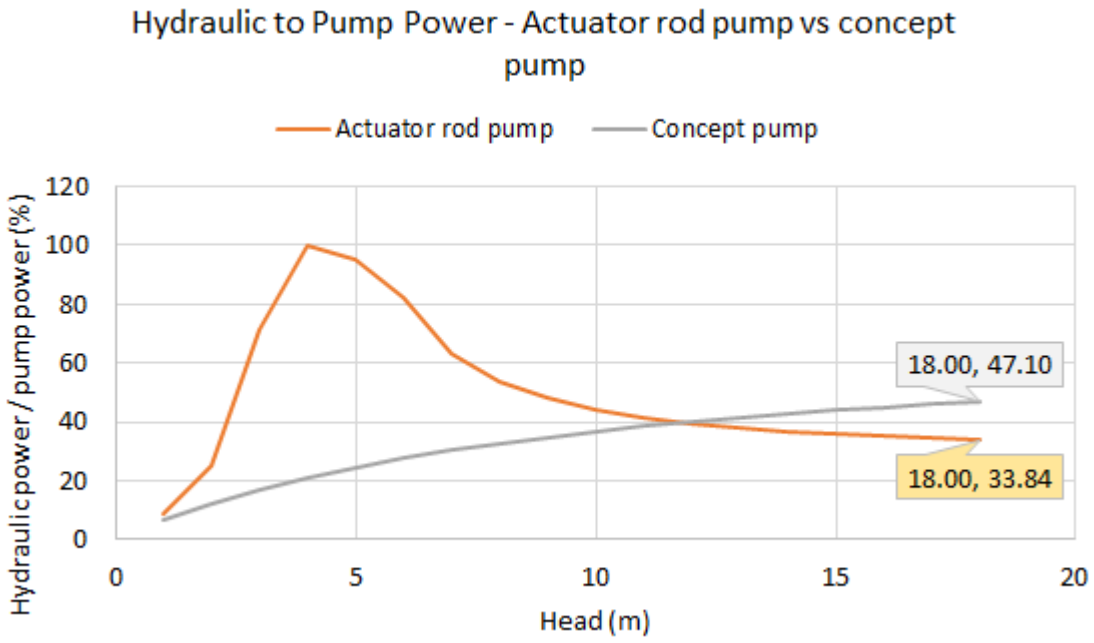

Figure 3.20: Hydraulic to pump power comparison of actuator rod pump [42] and concept pump.

3.4.3 Non-Piston rod Commercial pumps vs Conceptual Pump

The comparison was not only limited to the piston rod pumps for power consumption in conceptual pump but also it was compared with the commercially available non-piston rod pumps including helical rotor positive displacement (PD) and centrifugal (CF) pumps. The shortlisting of the commercial pumps were based on the literature [5,28–32] where they have been experimentally tested for solar PV groundwater pumping.

The power data for these pumps was extracted from their respective pump charts for a flow rate of 10.2 lpm at a head of 122 m same as that of 'Blackhawk' piston rod pump. The reason for choosing this head and flow benchmark was because 'Blackhawk' pump used least power among all pumps

and no higher heads data was available for all. As shown in Table 3.5, overall improvement for concept pump was observed in terms of motor power and hydraulic to pump power differences among the pumps. It is worth mentioning that centrifugal pumps consume more power than positive displacement pumps for same heads.

Table 3.5: Power comparison of concept pump with non-piston rod pumps.

Pump Specifications	**Blackhawk piston rod pump** [19]	**Grundfos SQF 2.5-2** [36]	**Lorentz PS1800HR-05HL** [37]	**Lorentz PS9kc-CJ8-44** [39]	**Grundfos SP8A-37** [38]
Pump type	PD	PD	PD	CF	CF
Head (m)	122	120*	125*	122*	300[(c)]
Flowrate (lpm)	10.2	~10.2	~10.2	~10.2	~30.933
Pipe diameter (in)	1	1.25	1.25	2	2
Power (W)	280[(a)] / 350.85[(b)]	639	390	1490	4374
Hydraulic to pump power (%)	72.66 / 58	31.32	53.45	13.66	34.69
Power Comparison with Conceptual Pump					
Power (W)	273.55	359.43	364.96	583.11	4155.69
Power difference (%)	2.31 / 22.03	44.73	6.42	60.86	4.99
Hydraulic to pump power (%)	74.4	55.67	55.85	34.89	36.5

* Data extracted from performance curves at around 122 m and 10.2 lpm (if available).

(a) – Motor power using fibre glass composite rod.

(b) – Motor power using steel rod.

(c) – 122 m head data was not available, instead highest head (300 m) flowrate selected.

3.5 Conclusions

This study shows that the generated concept model of a groundwater piston pump without the long piston rods save the driving motor power from loads with every rise in head. The conceptual pump is also optimised to use minimum components for its reciprocating motion made possible with a scotch-yoke mechanism within a limited borehole size of 10 inches.

A mathematical model is also presented in this chapter which allows to calculate the power sizing of solar groundwater piston pump (specifically the motor) with respect to head and flow demands. The mathematical model can be applied to any piston groundwater pumps whether piston rod and non-piston rod pumps. The model includes losses with hydraulic head, pump and motor losses using efficiency factors which enhances the adequacy of power estimation.

The purpose of the mathematical model was to estimate the power rating of the concept pump and put to comparison with the long piston rod pumps. The model was twice validated against two referenced solar operated piston rod pumps to estimate their power sizing with same head and flow demand i.e. (1) a commercial pump and (2) a pump from an experimental research study, with an error of 4.83% and 7.48% respectively. It is found out that the ever-increasing weight of the piston rod with respect to the head rise has significant effect on the pump power. Omission of the rod saves energy depending on the rod material. For instance, against the lighter GFRC composite rod in 'Blackhawk' pump saves around 7% of power and with the steel rod around 22.4% for 200 m head. Similar situation was observed for piston rod pump in

experimental research study by Andrada et al. [42] which saved 28.15% of power. The elimination of the piston rod also saves costs e.g. savings of $1600 (£1227) GFRC rod with 400 pieces for 122 m head [19] which leading into further time and cost savings on installation and maintenance.

The model validation became the basis of using it to predict the power rating for the conceptual pump which does not use piston rods. The results predicted lower power consumption and higher hydraulic efficiency by the concept pump compared to commercially available solar operated groundwater pumps including piston rod, positive displacement (helical rotor) and centrifugal pumps with same head and flow as summarised in Table 3.5.

The model calculated the concept pump power of 1.67 kW as per the actual design specifications i.e. head of 200 m and 34.72 lpm (see Table 3.4). No use of internal components could save power up to 2.2% from omitting connecting rod, 2 – 6% from meshing gears and 16.67% by excluding crossheads.

On the account of lower pump power consumption, the concept pump is then eligible to be subjected to the finite element analysis to see the structural validity of the design for these loading conditions which is discussed in the next chapter.

CHAPTER 4

FINITE ELEMENT ANALYSIS OF THE CONCEPT PUMP

The finite element analysis (FEA) is widely adopted in literature to study the structural ability to withstand loads of any component. There are many studies which have applied FE technique on pumps or their components' designs. In this chapter, finite element analysis was employed to structurally analyse for stresses and deformations in the generated conceptual model of a groundwater piston pump (developed in Chapter 3) under the maximum loading of 200 m head.

4.1 Theoretical Model

The detailed mathematical model and attributes of the conceptual pump are presented in Section 3.3.1. The FE structural analysis model requires maximum load acting on the pump components due to the water flow. In this study, the pump is designed for semi-arid areas and Nairobi is selected for the case study. Hence, the design consideration preferential to Nairobi [5] are given such that the head is taken averagely around 200 m [4]. Borehole pumps can range from 4 to 26 inches in diameter [30]. A 10-inch borehole size was assumed with 1-inch for pump casing clearance [4] and the pipe internal diameter of 1 inch [4]. Water density was taken as 1000 kg/m^3 and its flowrate as 34.72 lpm which is equivalent to around 25k litres per day [4]. The pipe material is poly vinyl chloride (PVC), for frictional head loss calculations [112]. The pump components were taken as stainless steel (S.S) (widely used in

commercial pumps [6,18,116–119,36–38,40,42,113–115]) and the properties as presented in Table 4.1. The stainless steel was taken as homogenous and linear isotropic [55].

Table 4.1: Properties of stainless steel for pump components [120].

Property	Stainless Steel (S.S) (ANSYS Database)
Density (kg/m³)	7750
Young Modulus (GPa)	193
Yield Strength (MPa)	207
Tensile Strength (MPa)	586
Poisson Ratio	0.31
Shear Modulus (GPa)	73.7
Shear Strength (MPa)	120

It is noteworthy that the piston and shaft are the two critical components to bear the load of the water contained in the pipe at first instance during the discharge stroke, and the force also transmits to the casing and its covers. On every discharge stroke, the piston has to lift weight '$F_{water\ weight}$' (see Equation 3.2) to a height equivalent to the stroke. In other words, the piston lifts a weight vertically as shown in Figure 4.1, though the motion of the concept piston is horizontal. For the required total head of 200 m and 1-inch pipe diameter, the mass of the water in the pipe is calculated to be 101.34 kg or weight of 994.16 N.

Figure 4.1: Illustration for piston lifting water contained in pipe as weight.

The constant force 'F_{atm}' due to atmospheric pressure 'P_{atm}' acting on the pipe outlet adds up to the weight and calculated to be 50.67 N. The resistive force '$F_{resistive}$' due to water flow in the pipe was calculated from the frictional head loss i.e. for flowrate of 34.72 lpm and total head of 200 m with pipe inner diameter of 1 inch and as per the material of the pipe (PVC, roughness 0.0015 mm [104]), the head loss was calculated to be around 12 m (see equation 3.4 and 3.5). The head loss in pressure head is equivalent to 117650 Pa. The resistive force of 59.61 N. All these forces add up to give the maximum force 'F_{max}' of 1104 N which acts on the piston face during the discharge stroke.

Next, the stresses in the components produced as a result of force can be calculated analytically at different locations in the pump components. Depending on the nature of loadings, the stresses can be evaluated, such as, when a location in the shaft is under torsional stress or pure twisting moment, then the shear stress in the shaft is calculated as,

$$\frac{T}{J} = \frac{\tau}{r} \tag{4.1}$$

where, 'T' is the twisting torque, 'J' is the polar-moment of inertia about the axis of rotation, 'τ' is the shear stress and 'r' is the radius.

Similarly, when a location in the shaft or piston, piston-supports or any other component is under pure bending moment, then the bending stress is calculated as [53,121],

$$\frac{M}{I} = \frac{\sigma_b}{y} \tag{4.2}$$

where, 'M' is the bending moment, 'I' is the cross-sectional area moment of inertia about the axis of rotation, 'σ_b' is the bending stress and 'y' is the distance from the neutral axis.

When a location in the shaft is under combined bending and twisting stresses, then the equivalent moment becomes dominant which is calculated as [29],

$$M_e = \sqrt{M^2 + T^2} \tag{4.3}$$

where, 'M_e' is the equivalent moment.

For the failure criteria, to determine the factor of safety at yield, the widely adopted maximum distortion energy or von-Mises theory [48–52,54,58], was used for this analysis. This theory is applicable to metals or ductile materials such as steel or aluminium alloys or other materials with elasto-plastic properties [122]. The equivalent or von-Mises stress 'σ_e' based on the bending and shear stresses in three dimension (x,y,z) is calculated as,

$$\sigma_e = \frac{1}{\sqrt{2}}\left((\sigma_x - \sigma_y)^2 + (\sigma_y - \sigma_z)^2 + (\sigma_z - \sigma_y)^2 + 6\left({\tau_{xy}}^2 + {\tau_{yz}}^2 + {\tau_{zx}}^2\right)\right)^{0.5} \tag{4.4}$$

According to the failure criterion, the yielding occurs at a location where equivalent stress becomes equal to or greater than the yield limit of the material [122,123]. Hence, the factor of safety '$F.o.S$' is calculated by,

$$F.o.S = \frac{\sigma_y}{\sigma_e} \tag{4.5}$$

where, 'σ_y' is the yield strength of the material.

Buckling may occur in the piston mid-section due to axial force on its face. Hence, it is evaluated using the critical buckling load 'F_{crit}' criteria for a fixed and free column which is calculated as,

$$F_{crit} = n\left[\frac{\pi^2 EI}{L^2}\right] \tag{4.6}$$

where, 'n' is the constant (0.25 for fixed and free condition), 'E' is the material young's modulus, 'I' is the area moment of inertia and 'L' is the length of the mid-section.

The line contact between the slider (as cylinder) and piston body (as plane) acts as a 'Hertz' contact region which can be evaluated for maximum contact and shear stresses to determine the plasticity or yielding. The contact half width 'b' is calculated as [124],

$$b = \sqrt{\frac{2F_{max}}{\pi l_{contact}} \frac{{(1-\vartheta_1^2)}/{E_1} + {(1-\vartheta_2^2)}/{E_2}}{{1}/{d_1} + {1}/{d_2}}} \tag{4.7}$$

The maximum contact shear stress in for a Hertz frictionless contact '$\tau_{contact}$' is calculated as [125],

$$\tau_{contact} = 0.3 \times \frac{2F_{max}}{\pi b l_{contact}} \tag{4.8}$$

The allowable cylindrical contact yield stress based '$Y_{contact}$' on maximum distortion energy theory for materials with Poisson's ratio of 0.3 can be predicted as [126],

$$Y_{contact} = 1.792 \times \sigma_y \tag{4.9}$$

Any FE method breaks any model into smaller elements which consists of nodes. The force acting on the elements causes deformation or displacement which can be equated as elemental stiffness given by [127],

$$F = K_{eq} \times \Delta l = \frac{(A_{i+1} + A_i)E}{2l}(u_{i+1} - u_i) \tag{4.10}$$

where, 'K_{eq}' is the equivalent stiffness of element, 'Δl' is the displacement change, 'A' is element area, 'u' is the elemental deformation, and the suffixes 'i' and '$i+1$' are the nodes. In force, stiffness and displacement matrix form, the Equation 4.10 is written as [127],

$$[F] = [K][u] \tag{4.11}$$

The FE model evaluates the stresses and deformation based on the strain in the elements given as [127],

$$\sigma = \frac{F}{A_{avg}} = \frac{\frac{(A_{i+1} + A_i)E}{2l}(u_{i+1} - u_i)}{A_{avg}} = \frac{E}{l}(u_{i+1} - u_i) = Ee \tag{4.12}$$

where, 'A_{avg}' is average element area and 'e' is the strain. In stress, strain and material matrix form, Equation 4.12 is written as [128],

$$[\sigma] = [D][e] \tag{4.13}$$

where, '$[D]$' is the elastic matrix containing information about the material properties. In three dimensional form (x,y,z), above matrices with normal and shear stresses and strains is given by [128],

$$[\sigma] = \left[\sigma_{xx}\sigma_{yy}\sigma_{zz}\tau_{xy}\tau_{yz}\tau_{zx}\right]^T$$

$$[D] = \frac{E}{(1+\upsilon)(1-2\upsilon)}\begin{bmatrix} 1-\upsilon & 0 & 0 & 0 & 0 & 0 \\ 0 & 1-\upsilon & 0 & 0 & 0 & 0 \\ 0 & 0 & 1-\upsilon & 0 & 0 & 0 \\ 0 & 0 & 0 & 0.5-\upsilon & 0 & 0 \\ 0 & 0 & 0 & 0 & 0.5-\upsilon & 0 \\ 0 & 0 & 0 & 0 & 0 & 0.5-\upsilon \end{bmatrix} \quad (4.14)$$

$$[e] = \left[\frac{\partial u}{\partial x}\frac{\partial v}{\partial y}\frac{\partial w}{\partial z} \quad \frac{\partial u}{\partial y}+\frac{\partial v}{\partial x} \quad \frac{\partial v}{\partial z}+\frac{\partial w}{\partial y} \quad \frac{\partial w}{\partial x}+\frac{\partial u}{\partial z}\right]^T$$

where, 'u, v, w' are the displacements is x, y and z directions. Superscript 'T' is the transpose of a matrix which indicate the rows in the matrix to be turned into columns or vice versa.

4.2 Finite Element Modelling (FEM)

CAD software 'SolidWorks (ver. 2017)' was used to develop the CAD model of the concept pump. The proposed concept model of the whole assembled pump along with components, piston, shaft, casing and casing covers is presented in Chapter 3 (see Figure 3.10). The FE modelling of the pump components was carried out using ANSYS Mechanical Structural program (ver. 17.0). The assumptions, simplifications, necessary boundary conditions and mesh generation for piston-shaft assembly, main casing body and covers are presented in the follow up. It should be noted that all components of the concept pump are under the weight load of the water inside the borehole pipe which acts as a loading force on all the pump components. This force is maximum at every discharge stroke of the pump and should be borne by all components when water in pipe is lifted at each stroke.

4.2.1 Piston-Shaft Assembly

Piston-shaft assembly being the important component in the pump, was evaluated first for steady state stress analysis. When the piston reaches half of discharge stroke, the shaft is in critical state as the force produces maximum moment of deformation on it. In such a state, the CAD model's geometry of the piston and shaft were modelled as shown in Figure 4.2. Steady state analysis was selected because the components face maximum constant force at critical position during every revolution as shown by the peak torque (at point 'b') in the revolutions cyclic plot of a piston pump, see Figure 4.3. The dynamic effects on the components due to varying force are always lower than the peak point in a revolution which occurs at one-fourth of the revolution during discharge stroke.

Before setting up the boundary conditions for FE simulations, certain assumptions were made to simplify the analysis. The CAD model of piston-shaft assembly was simplified by removing certain geometrical features such as piston grooves and slider bearings to make the analysis simpler in order to save computational resources. The piston and shaft were coupled together for analysis because the piston movement is restricted by the shaft slider which itself may move due to the rotational motion of the shaft. Further, it was taken that the maximum force is continuously acting on piston during the discharge stroke, and the force on bearings on the slider (see Figure 3.8) is neglected in FE model as they are fitted on the slider. The force transmitted to the bearings is the force faced by the slider, and the piston supports are assumed to be frictionless with the shaft guided bearings (see Figure 3.8 and 3.9).

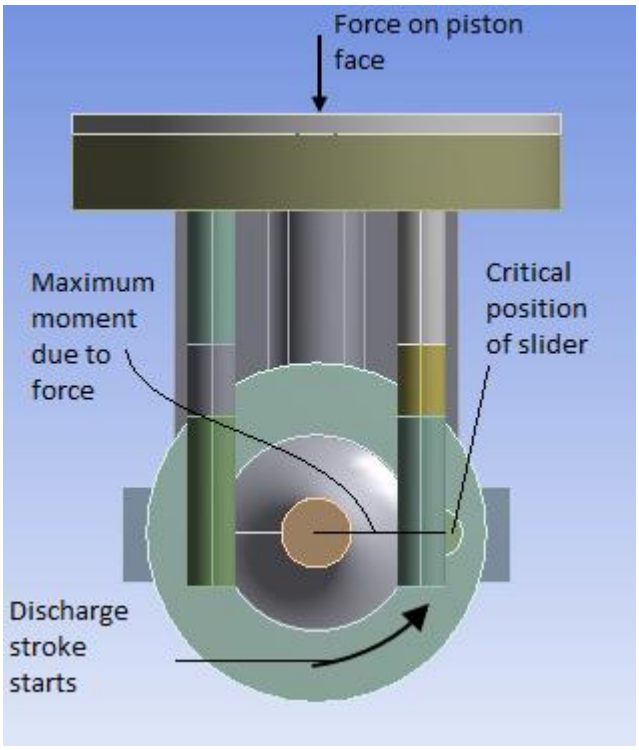

Figure 4.2: Top view of modelled position of piston-shaft assembly.

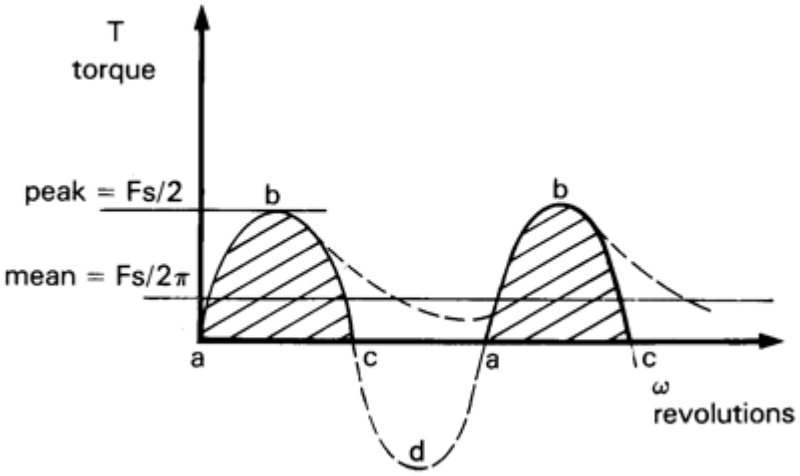

Figure 4.3: Torque versus piston pump speed – 'a-c' is discharge stroke, 'b' peak torque and 'c-a' is suction cycle [129].

Further, piston and shaft components being the main bases of the whole pump design shadowing designs of casing and its parts were analysed in detail with some geometrical variants. These were modelled to study feasibility on

various design models versus the original version. The piston middle web section was modelled with two separate variants, i.e. a rectangular and a circular type as shown in Figure 4.4. The piston variant discussed in the previous section (see Figure 4.2) is dubbed as 'hybrid' as it includes both a circular and rectangular web merged using filleted design. The two shaft variants included designs with smaller fillets at the middle bearing supports, and without a lower half, separately. The two piston variants were coupled with the two variants of shafts individually resulting in four different assemblies, see Figure 4.5. All the variants were subjected to the similar boundary conditions and their final results were compared with the hybrid piston-shaft assembly (see Figure 4.2).

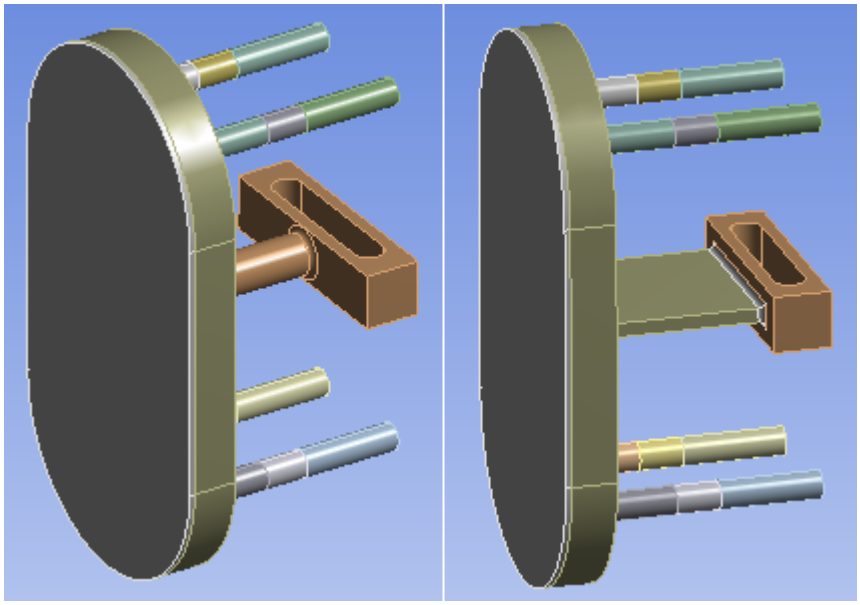

Figure 4.4: Piston variants for the concept pump with circular (left) and rectangular (right) web sections.

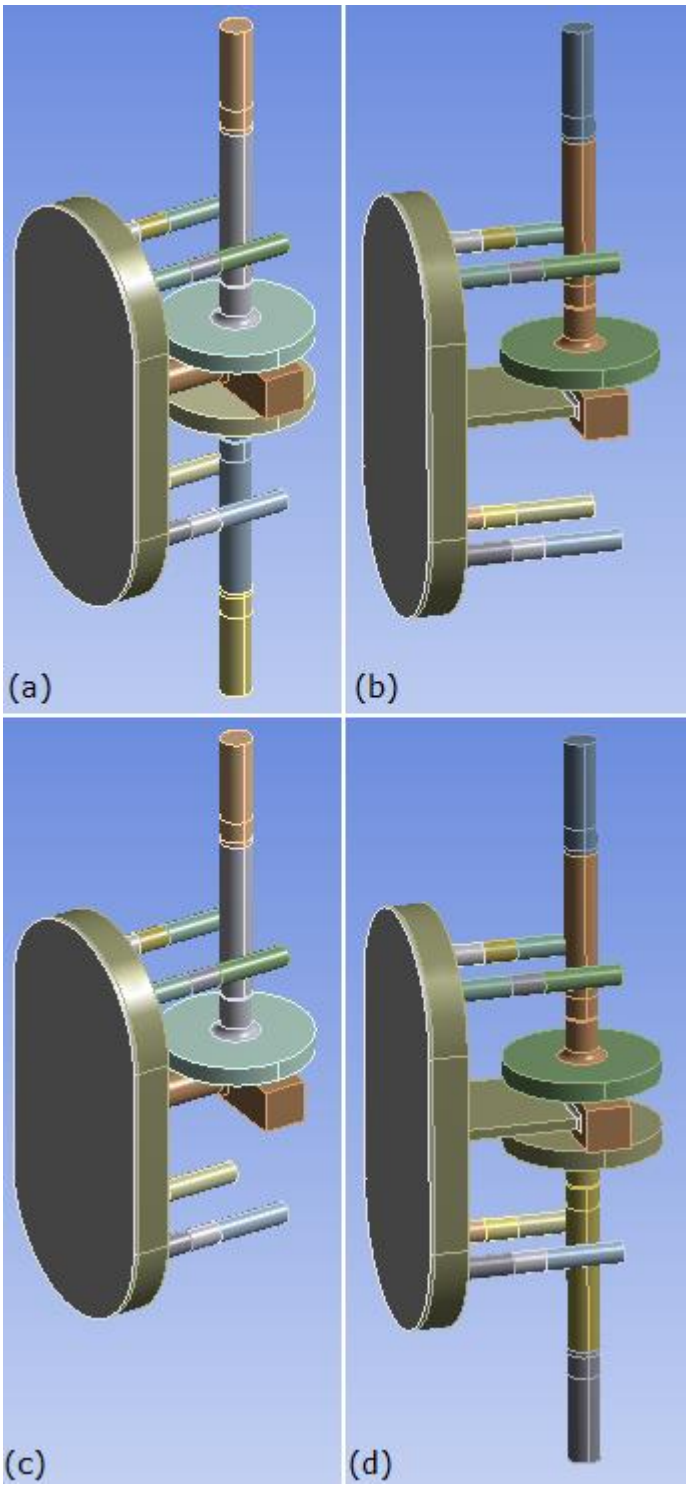

Figure 4.5: Piston shaft variants assemblies (a) circular web with full shaft, (b) rectangular web with semi-shaft, (c) circular web with semi-shaft and (d) rectangular web with full shaft.

The following boundary conditions depicting the critical state of the components during the pump operation (Figure 4.2 and 4.6) were setup for the steady state analysis. The slider of the shaft acts as the sliding contact region with the piston body, Figure 4.7. Since slider makes line contact with piston, the contact surfaces were modelled on both parts so as to have much refined mesh around the region.

- The force acts on piston face in opposite direction of its motion shown by red arrow in Figure 4.6(a).
- The top cross section surface of the shaft acts as the fixed support as the motor shaft is assumed to be coupled to it which restricts the circular motion of the shaft, Figure 4.6(b).
- The bottom surface of the shaft is free to revolve in the casing; therefore it is a free displacement in cylindrical motion, Figure 4.6(c).
- The shaft guided bearings are in the half way position on the piston supports and are free to move in only the direction of the piston (Z-axis), Figure 4.6(d).
- The piston mid rectangular section is also restricted to only move in the direction of the piston, Figure 4.6(e). Mark ‘A’ and ‘B’ shows restriction in Y and X directions, respectively.
- Four free to revolve boundary conditions are placed on the shaft to depict the placement of bearings which holds the shaft in position, Figure 4.6(f).

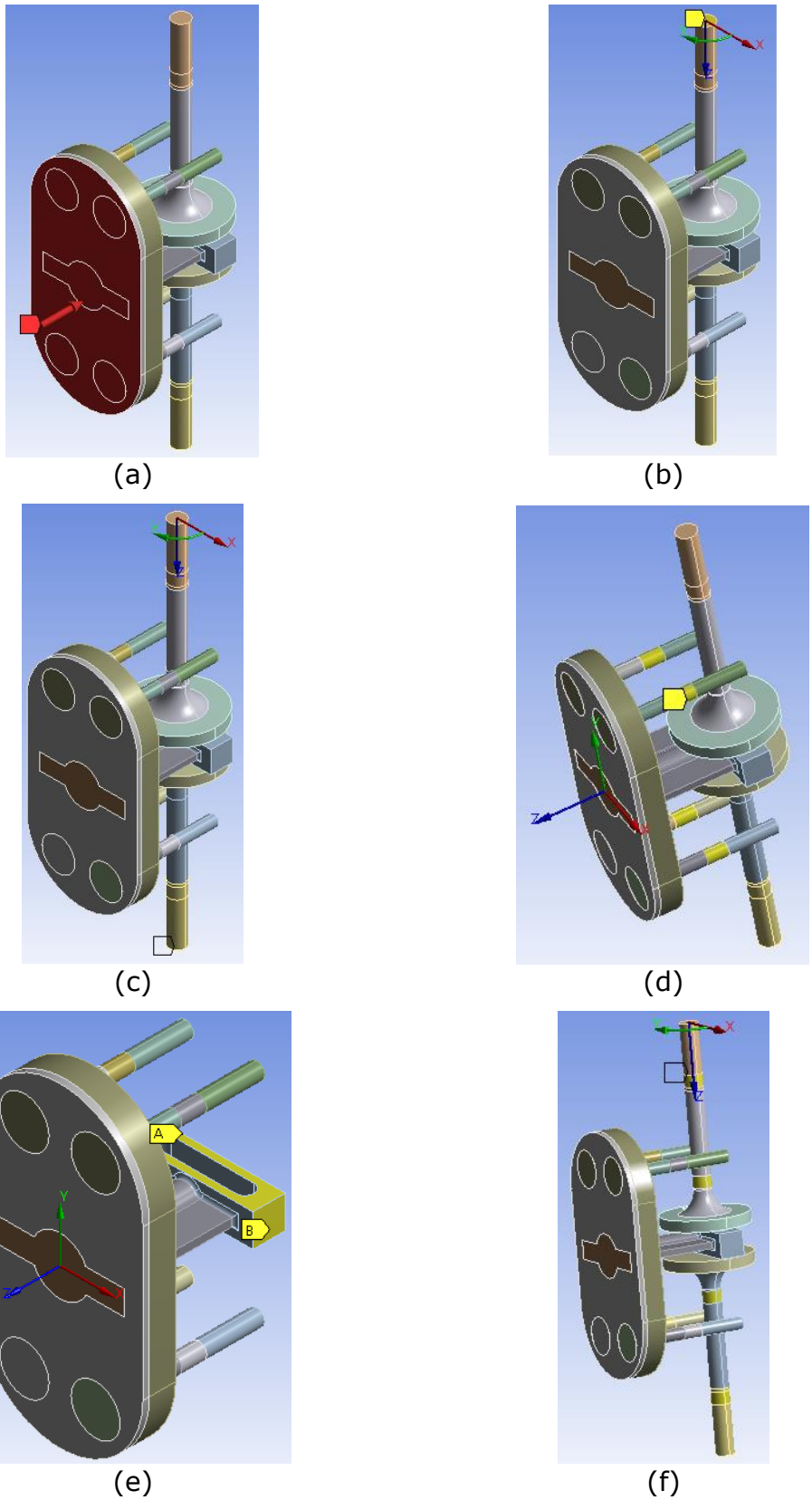

Figure 4.6: Piston-shaft assembly boundary conditions, (a) force, (b) fixed support, (d) and (e) z-axis motion only, (c) and (f) free to rotate.

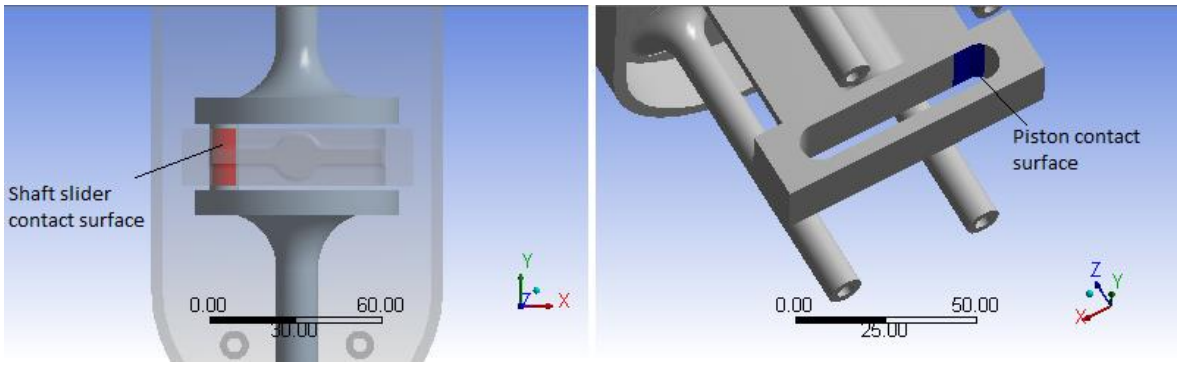

Figure 4.7: Shaft slider (left) and piston contact (right) regions.

Geometrical volume segmentation was carried out at various locations in the CAD model in order to get desired mesh type in that section and to make post-processing convenient for that location as shown in Figure 4.8. The piston shaft assembly was modelled with high quality 3D solid 20-nodes hexahedral (SOLID186) and 10-nodes tetrahedral (SOLID187) quadratic elements with active mid-side nodes so as to capture curved features such as fillets, shaft, and piston curvature and supports [10], [34]. 3D solid elements were used because of the complex nature of the geometry itself where the cross-sectional area varies in all dimensions and the applied force loading which will result in deformations in all three dimensions.

Hexahedral elements were employed in most of the sweepable geometry due to their robustness (mapping capability) and their accuracy in stress analysis results compared to tetrahedral elements [8]. The mesh generation on the assembly normally consisted of hexahedral mesh apart from the contact region between the shaft slider and piston body, where tetrahedral mesh refinement was needed for higher accuracy in mesh generation and results. The piston and shaft bodies were sectioned from various places to get the desired mesh shown in Figure 4.8.

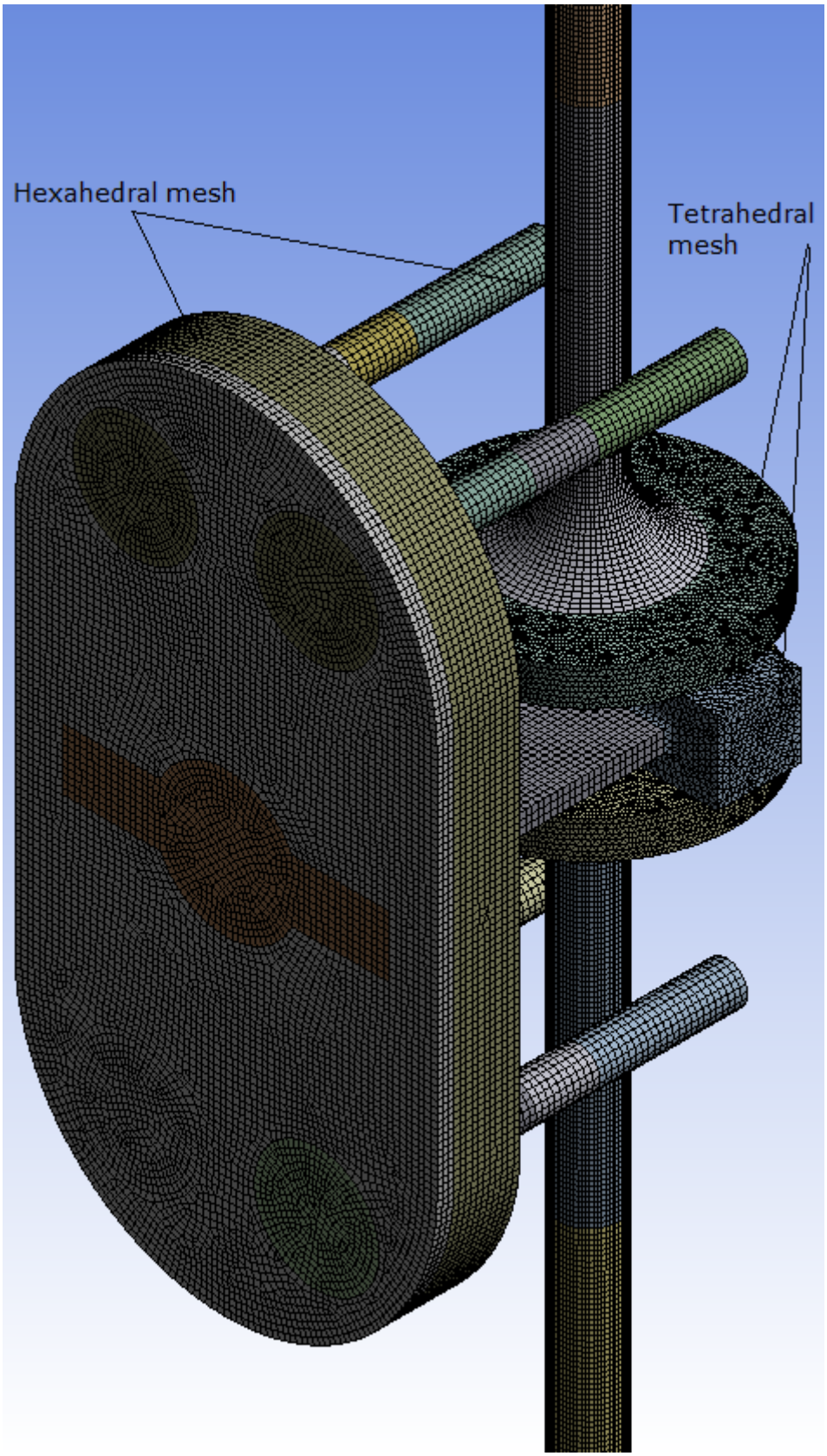

Figure 4.8: The generated hexahedral and tetrahedral mesh for the piston shaft assembly with 120494 elements.

Multiple simulations were carried out for mesh sensitivity or independency check with the mesh convergence was achieved at 120494 elements (see Appendix C). Additionally, the piston-shaft contact region was simulated separately as 2D due to limited computational resources as the analysis region requires a very high density of mesh to evaluate the results correctly and was not possible to model in the whole 3D analysis. The contact region acts like a Hertz contact (defined as; when contact between two bodies with point or line contact turns into an area contact under the application of compressive force, [124,125]) depicting a cylinder over a plane scenario. The shaft slider acts as the cylinder and the piston contact surface as the plane where both surfaces make a line contact as shown in a cut section of the piston-shaft assembly in Figure 4.9.

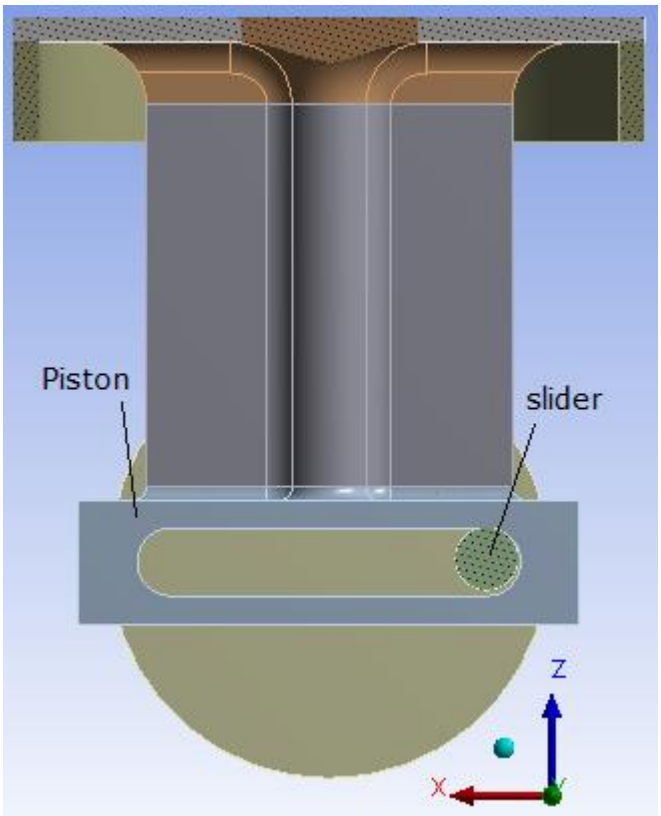

Figure 4.9: Top cut section view of shaft slider contact with the piston.

A 2D static structural analysis was carried out splitting the slider-piston contact as symmetry as shown in Figure 4.10(a). This made possible for achieving a very high density of structured mesh consisting of 2D quadrilateral elements (8-node PLANE183 SOLID) in the contact region [55,56] with an edge sizing of magnitude 10^{-3} mm, shown in Figure 4.10(b). Triangular elements were generated in the areas with less significance [120]. The contact was designated as frictionless based on Hertz contact assumptions [130]. The piston body was restricted from the base and the force of 1100 N (water body weight in pipe of 200 m head) was applied on the slider to act normal to the piston surface. It is worth mentioning here that a 3D version of the contact region with one-fourth of the geometry required 120137 elements which is nearly same as adopted by the whole piston-shaft 3D assembly (see Figure 4.8), hence generating such a mesh with whole assembly was not possible (computer memory limitations).

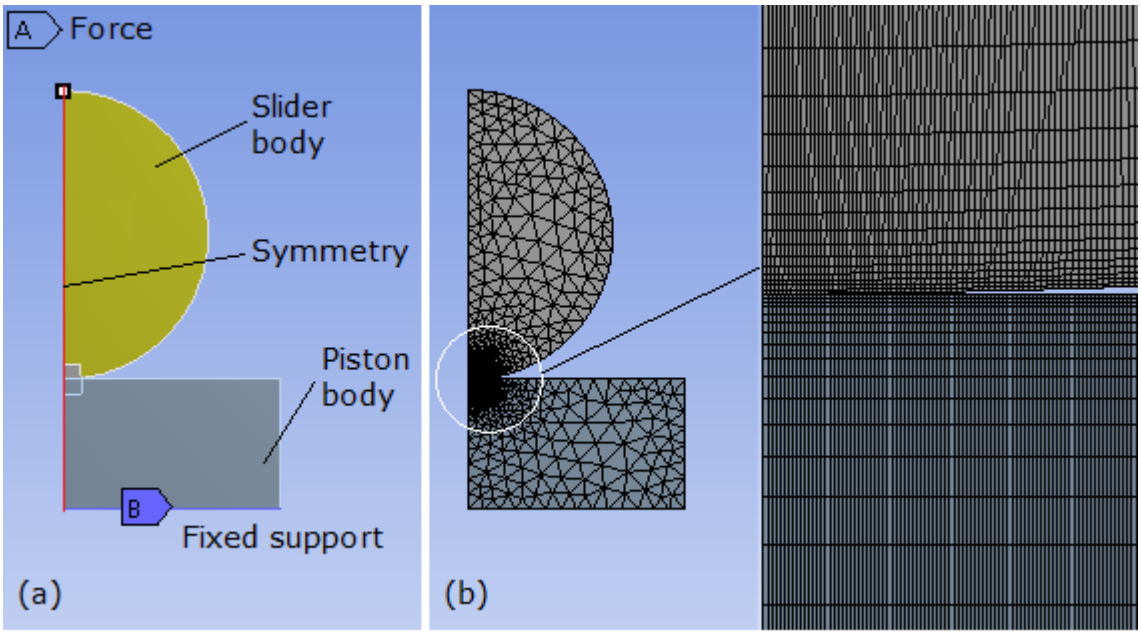

Figure 4.10: Slider-piston contact FE (a) boundary conditions and associated (b) 2D quadrilateral and triangular mesh model with 12365 elements.

4.2.2 Main Casing Body

Steady state FE analysis of the main casing body was done on the cylinder section where the piston displaces the water during the discharge stroke. The maximum pressure of water acts on the inner cylinder walls. The casing cylinder is subjected to the pipe water pressure 'P_{max}' due to maximum force which is also faced by the front casing manifold. The maximum pressure as per pipe area 'A_{pipe}' was calculated using Equation 4.15 to be 1.962 MPa.

$$P_{max} = {F_{max}}/{A_{pipe}} \tag{4.15}$$

The boundary conditions on the main casing body are shown in Figure 4.11. The maximum pressure was applied to the casing cylindrical walls, Figure 4.11(a). It was assumed that the maximum pressure is exerted on the walls once the discharge stroke commences. The bolts location surfaces at front and back of the casing are used as the fixed supports, Figure 4.11(b). The mesh for the main casing body analysis was done using very fine high-quality quadratic 10-nodes tetrahedral elements with much higher density at the cylinder walls in order to capture fine values of stresses as shown in Figure 4.12. The mesh independency check resulted in convergence with 784510 elements (see Appendix C).

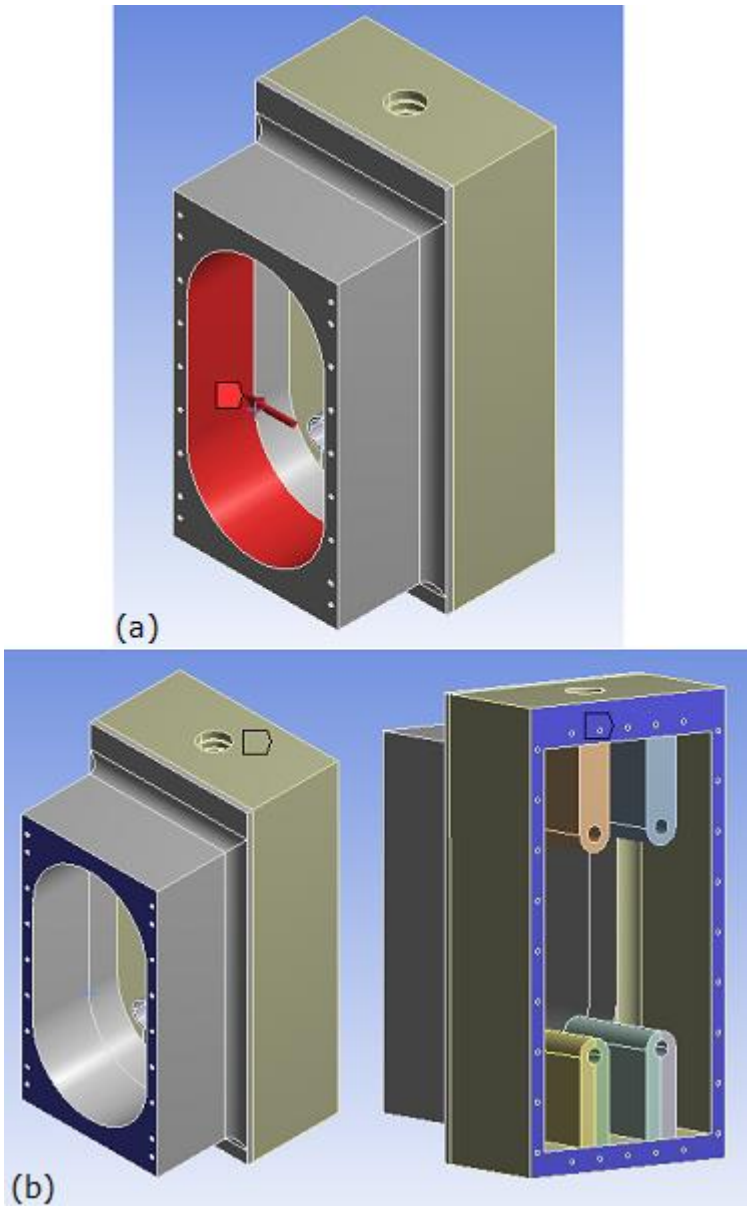

Figure 4.11: Main casing body boundary conditions; (a) applied pressure in the casing cylinder up to the displacement (b) fixed supports at front and back sides.

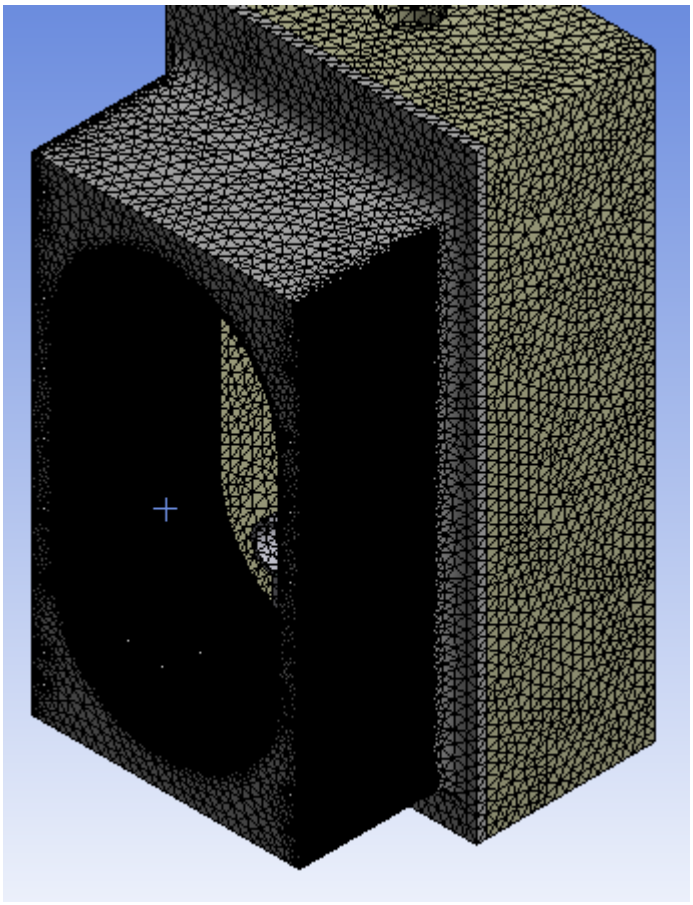

Figure 4.12: Tetrahedral mesh generation in the main casing body with much refinement at cylinder area (784510 elements).

4.2.3 Casing Covers

Steady state FE analysis was further extended to the casing covers. The manifold inside the front cover was the important section for stresses developed during the discharge stroke, whereas, for the back cover, the cover wall was the significant stress region where the force is transmitted from the piston face to the attached shaft bearing supports.

The boundary conditions for the casing front and back covers are shown in Figure 4.13. The casing front cover has to face maximum pressure acting at

the cylinder wall of the main casing. The casing pressure was set up on the inside manifold walls as shown by wireframe model in Figure 4.13(a). The dry surfaces of the cover attached to the main casing body were selected as the fixed supports. For the back cover, the bolts location surfaces were selected for fixed boundary condition as shown in Figure 4.13(b) and the same piston force was applied to the bearing supports inner surfaces as shown in Figure 4.13(c). The mesh was generated using quadratic 10-nodes tetrahedral elements of fine quality. Much higher density was allotted to the inside manifold of the front cover, and at the inner surfaces of the bearing supports on the back cover, as shown in Figure 4.14 and Figure 4.15, respectively. The mesh independency check resulted in convergence with 170562 and 84232 elements for front and back cover respectively (see Appendix C).

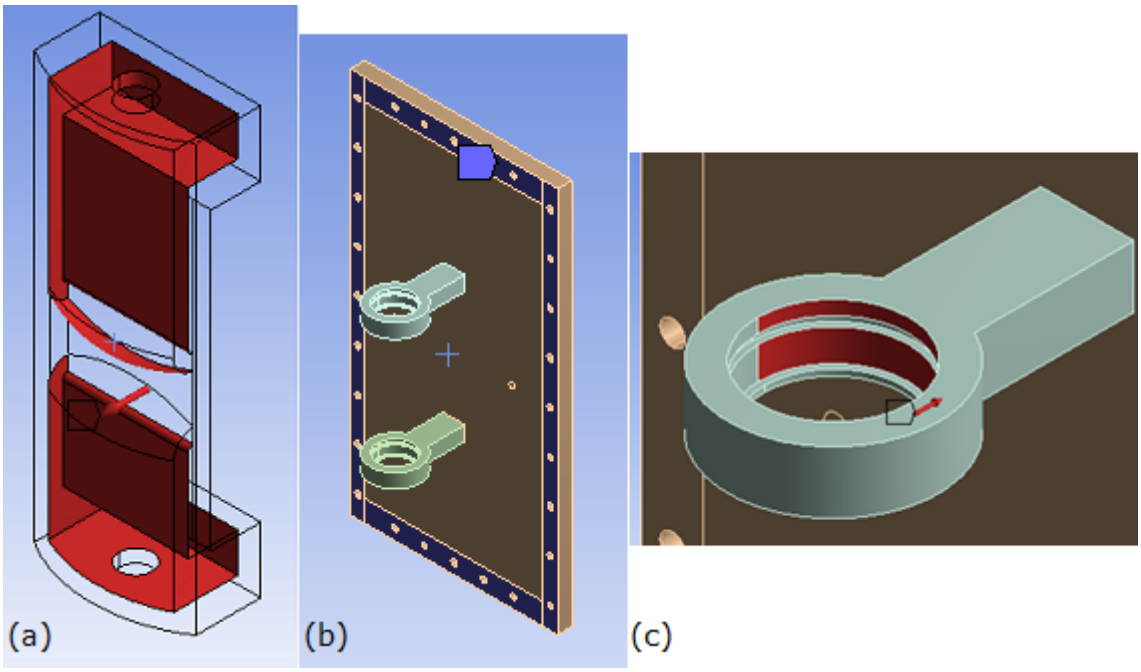

Figure 4.13: Casing covers boundary conditions; (a) pressure inside the flow manifold of casing front cover (wireframe view), (b) fixed support on back cover, and (c) force at inner bearing supports surfaces on back cover.

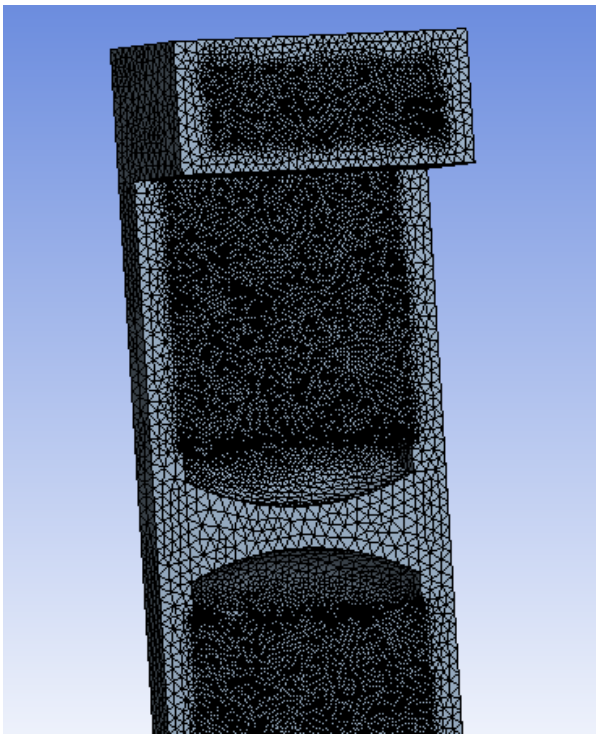

Figure 4.14: Tetrahedral mesh generation for the casing front cover (170562 elements).

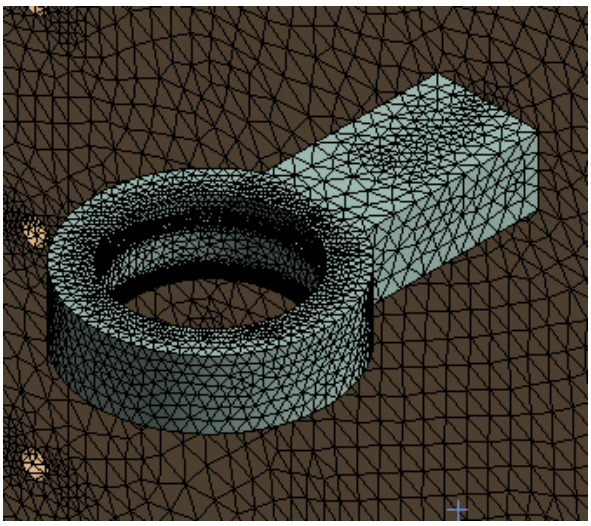

Figure 4.15: Tetrahedral mesh generation for the casing back cover (84232 elements).

4.3 FE Simulations' Results and Discussions

4.3.1 Piston Shaft Assembly

The stresses evaluated in the piston-shaft component should be below the current material elastic yield limit (207 MPa) and contact yield limit (370 MPa) for the contact region. The FE results predict that overall piston and shaft components can withstand the stresses produced by the maximum force (1100 N, from 200 m head) under the applied boundary conditions. However, the contact region between the two components bear highest stresses (discussed later). Excluding the contact region, maximum equivalent stress in the shaft occurs near the top bearing junction which is 147.4 MPa compared to the allowable 207 MPa stainless steel yield strength as shown in Figure 4.16. The rest of the shaft was in less stress values, with mostly the top region bearing the stresses averagely around 78 MPa, see Figure 4.17.

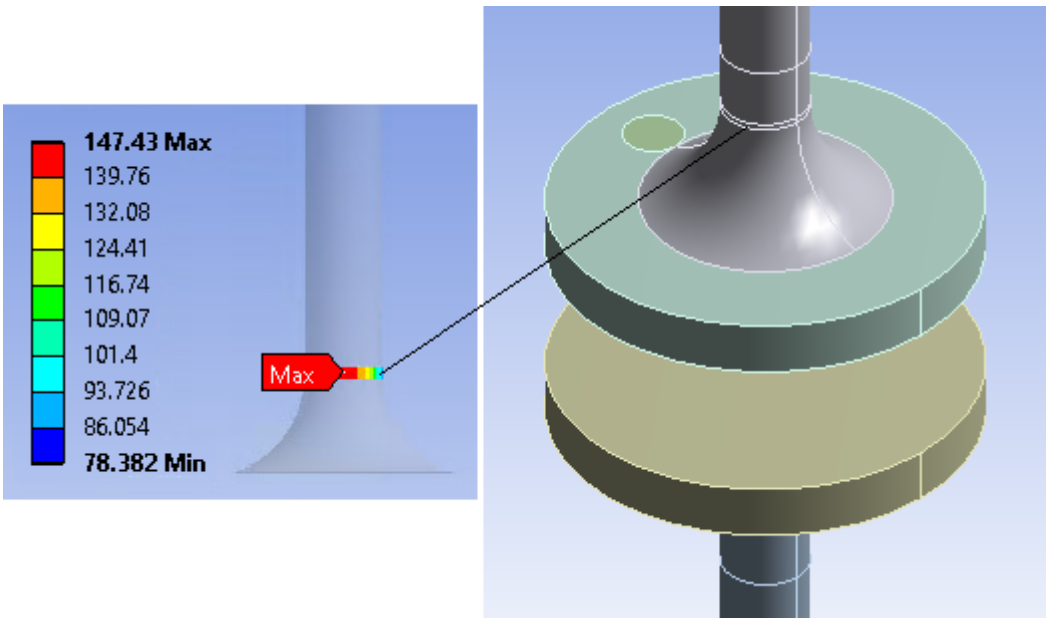

Figure 4.16: Maximum equivalent stress (MPa) on shaft top section.

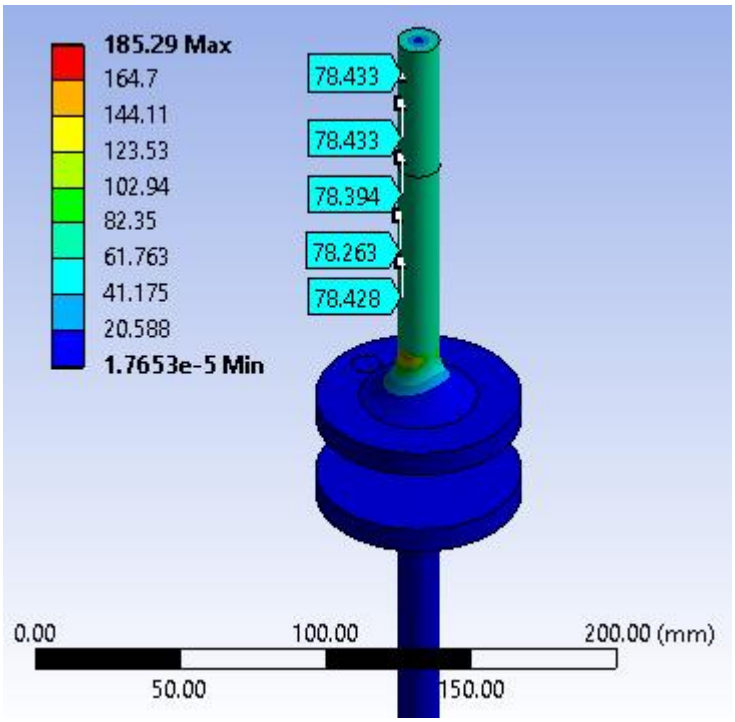

Figure 4.17: Equivalent stress (MPa) for the full shaft.

The lower section of the shaft has negligible stress concentration because of the fixed boundary condition on the top shaft surface and the lower surface is free-to-rotate, with maximum stress value found to be only 5.3 MPa as illustrated in Figure 4.18. On the other hand, the maximum equivalent stress in the piston is found to be around 41 MPa at the fillet area under compression near the piston head as illustrated in Figure 4.19.

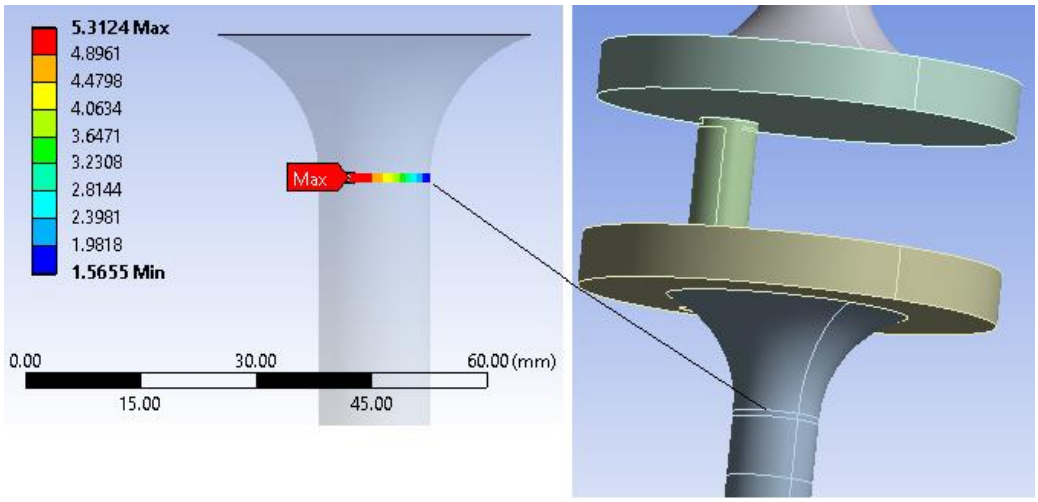

Figure 4.18: Maximum equivalent stress (MPa) on shaft lower section.

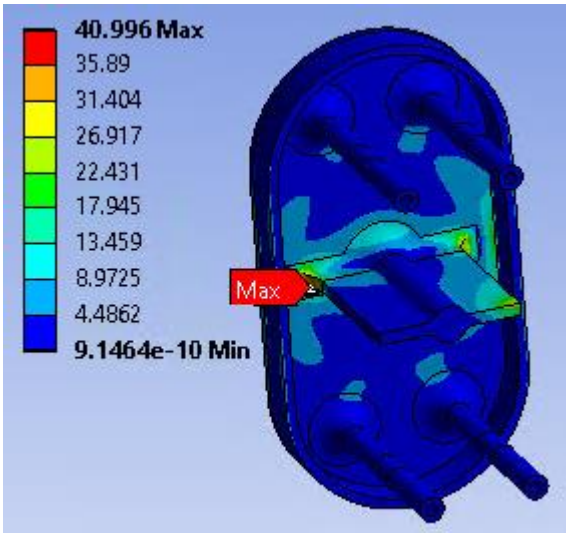

Figure 4.19: Maximum equivalent stress (MPa) in the piston.

The maximum deformation of 0.46 mm (absolute) occurs in the shaft where the slider slightly translates backward due to piston force and results in shaft rotation on its own axis. The piston maximum deformation of 0.34 mm was observed in the same backward direction and occurs at the piston supports (top and bottom sections). At the contact region piston-shaft maximum deformation is around 0.32 mm which shows that the piston and shaft are intact.

The piston and shaft deformations in backward direction are shown in Figure 4.20 where negative sign shows backward motion.

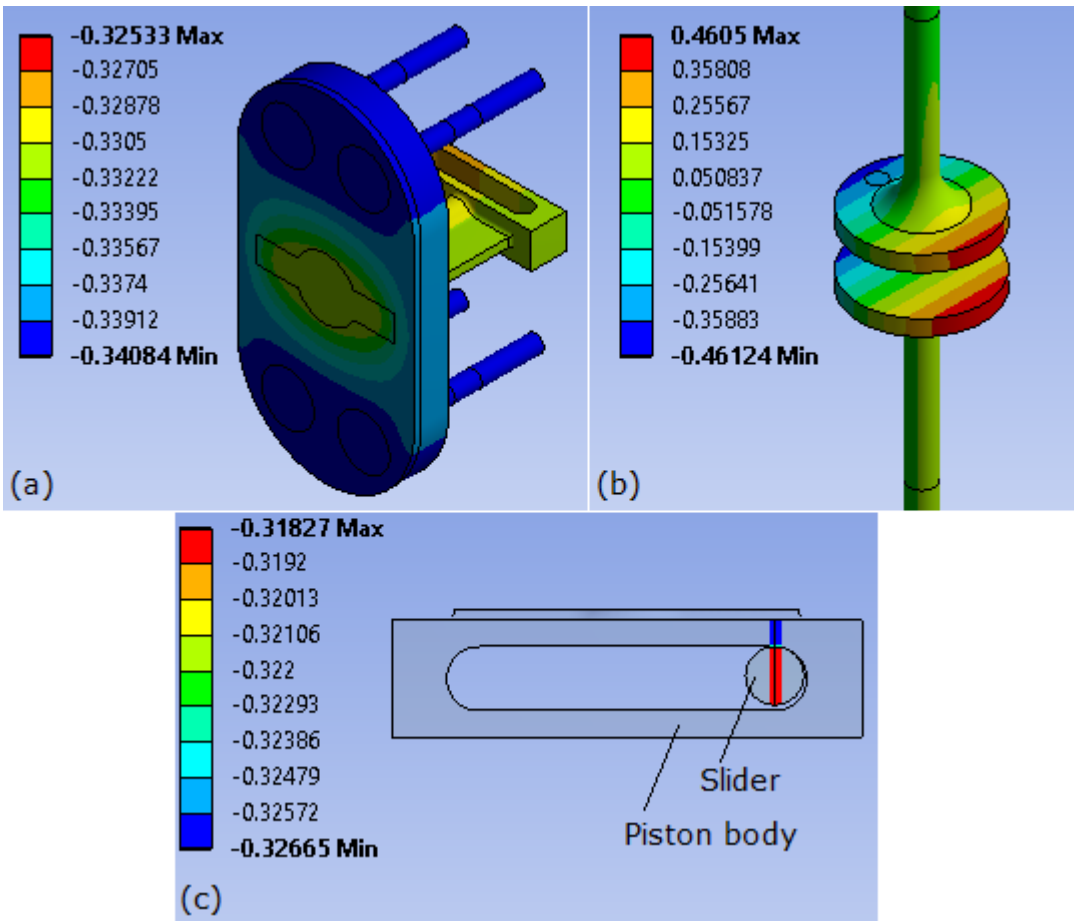

Figure 4.20: Deformation opposite to piston force (mm) in (a) piston, (b) shaft and (c) contact region.

Finally, the design factor of safety (F.o.S) (see Equation 4.5) excluding contact region and based on maximum equivalent stress was observed in the top shaft section and was calculated to be 1.4. It is consequently conclusive that a load of around 200 m head is withstood by the piston and shaft components excluding the contact region between the two components and the behaviour is within the material elastic limit.

The piston-shaft contact analysis FE results revealed higher contact stresses in the region compared to any other location in the piston-shaft assembly as shown in Figure 4.21. The compressive natured contact stress is found to be 604.45 MPa which is much higher than the yield strength of the material i.e. 207 MPa and the contact yield strength of 370 MPa (estimated using Equation 4.9) at which actual yielding initiates [126]. It is maximum at the contact line. The maximum shear stress occurs at 0.46 mm offset from contact line and is found to be 184.7 MPa which also exceeds the material shear strength of around 120 MPa. The analysis suggests that either a much stronger material must be assigned to the existing contact region with higher contact yield strength which could withstand the current loading condition of 200 m head or the geometry could be altered with much higher diameter of the slider or both.

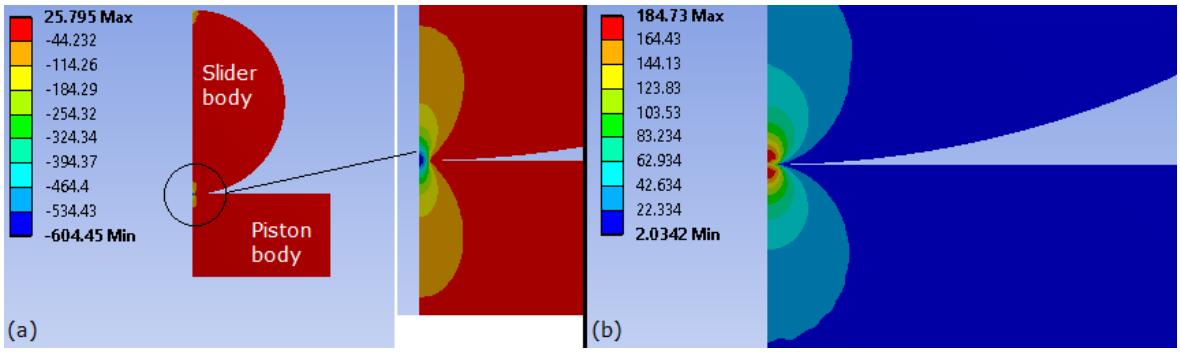

Figure 4.21: FE results of piston-shaft contact (a) contact stress (b) shear stress.

The contact width of 0.118 mm was evaluated against the contact stress on the piston surface, as shown by chart in Figure 4.22. The highlighted callout value is the contact half width shown on the chart which is the measure of the distance from the actual contact line where the maximum stress occurs to the point where its effects becomes nearly zero.

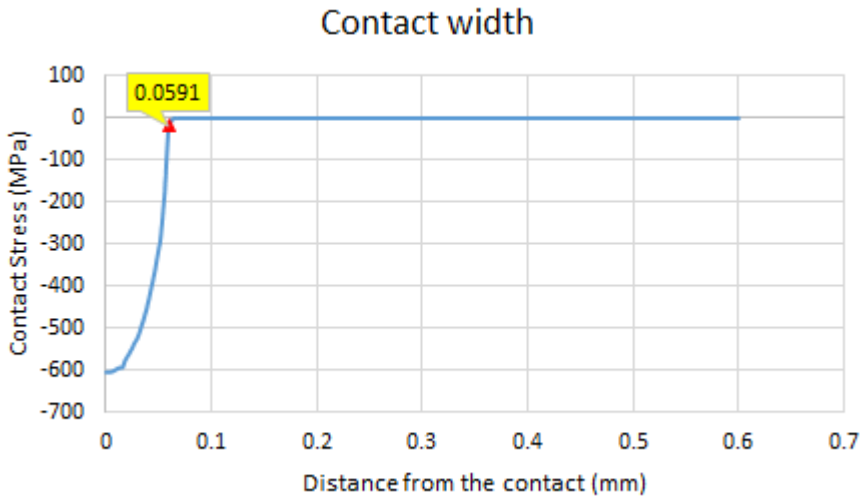

Figure 4.22: Piston-shaft contact width against the contact stress from FE results.

4.3.2 Piston-Shaft Variants

In this section, the FE analysis results of the four piston-shaft variants assemblies (see Section 4.2.1) were compared as illustrated in Figure 4.23 highlighting the Z-deformations (opposite to piston force). The parts in Figure 4.23, (a), (b) and (c), (d) consist of piston circular mid-web section, and rectangular mid-web section with semi-shaft variant respectively. The part (e) illustrates the 'hybrid' variant of the piston and shaft components. It is clearly observable from the scaled FE results that the variants in Figures 4.23, (a), (b), (c) and (d) are more deforming than the variant (e) in terms of the maximum deformation (backward piston motion due to applied load). The deformations in piston variants connected to full shafts are lesser than those coupled with the semi-shafts. The slight difference in piston variants deformations with full and semi-shafts is due to the top section of shaft bearing the maximum load. This

can be understood by looking at the stresses between the top and lower half sections of the shaft, see Figures 4.16 – 4.18.

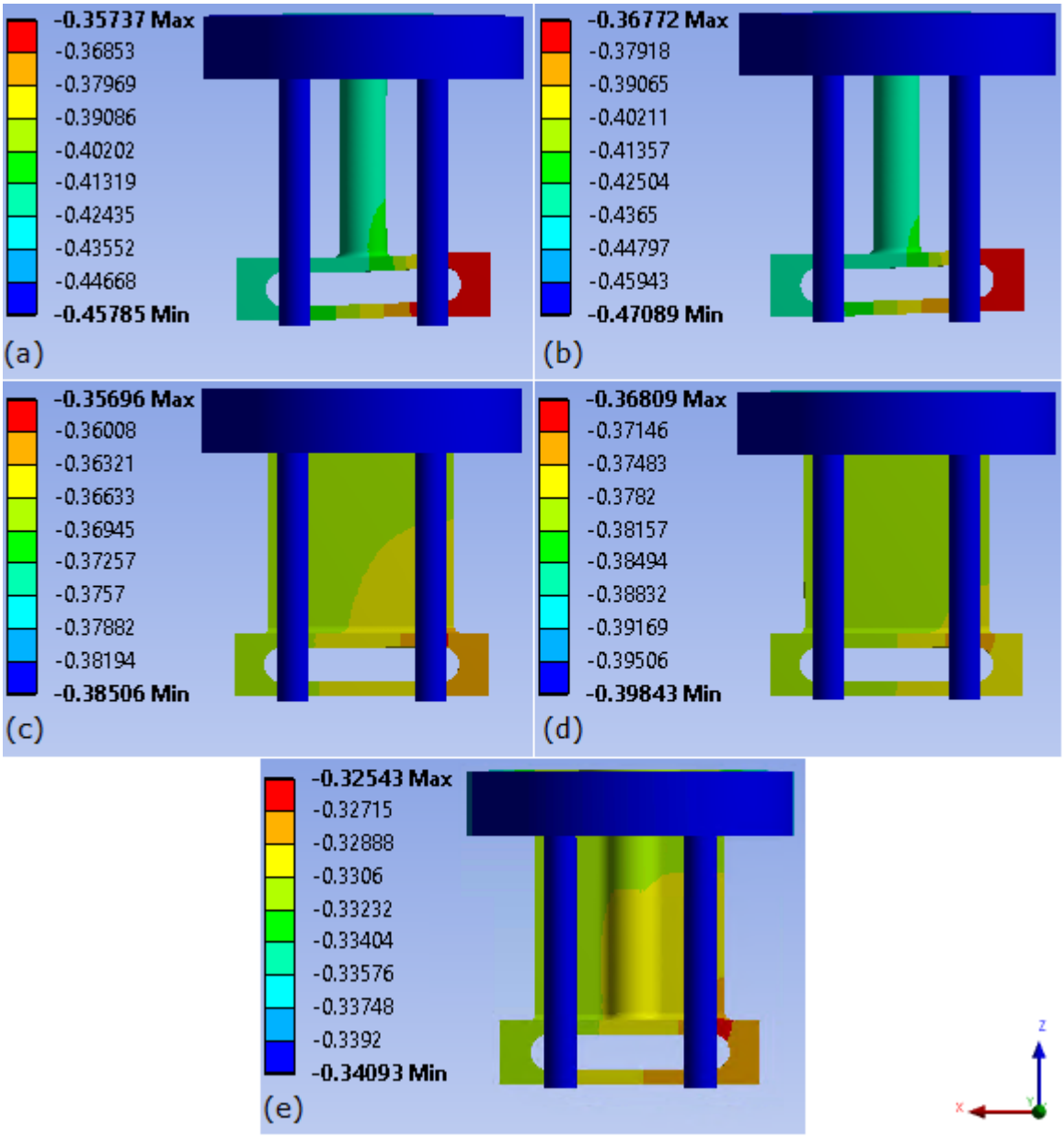

Figure 4.23: FE results – Z-deformation (mm) in piston variants (‘a, c and e’ with full shaft and ‘b and d’ with semi-shaft).

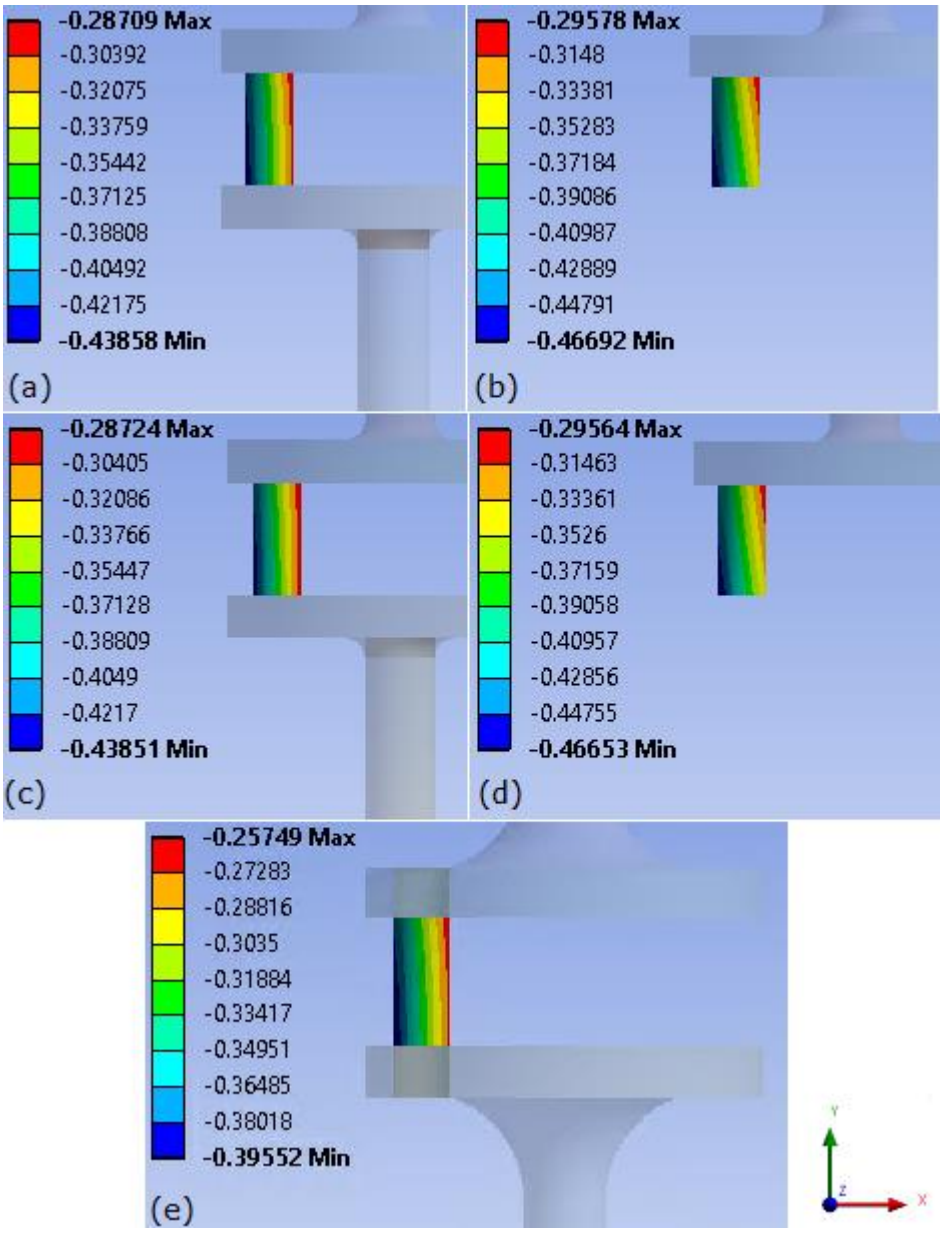

Figure 4.24: FE results – slider deformations (mm) in shaft variants (‘a, c and e’ with full shaft and ‘b and d’ as semi-shaft), (‘a and b’ and ‘c and d’ with circular and rectangular web pistons, respectively. Part ‘e’ with hybrid piston).

Similarly, the Z-deformations in the shaft variants follow the same pattern as the pistons particularly with the slider which is mainly in contact with the piston body as shown in Figure 4.24. The parts in the Figures 4.24, (a), (b) and (c), (d) consist of piston circular and rectangular mid-web sections,

respectively. The full shaft with larger fillets shown in part (e) is assembled with the 'hybrid' piston variant. As the piston leans backward, so is the slider. The slider in semi-shaft variants slightly deforms more than full shaft variants. The shaft in part (e) deforms less than other variants because of the larger fillets and less deformation by the hybrid piston variant (see Figure 4.23(e)). It is also evident that the maximum backward deformation (parallel to the applied load) in hybrid piston variant shaft slider 'part e' is around 0.32 mm which is found at the contact line in the centre. This is similar to the piston leaning back motion near the contact region (see Figure 4.20).

The overall deformation in the shaft variants is the rotation about its own axis due the twisting effect created by the piston on the slider causing backward motion. However, these rotations are found to be higher in full shaft variants than the semi-shaft variants as shown in Figure 4.25. The reason is because these deformations are linked with the deformations in the piston variants. The piston variants which are less deforming (due to nature of their geometries) transfer more deformations in their connected shafts variants in the form of rotation and vice versa. It is observable that the deformations in both piston and shafts are interlinked together. The FE analysis also shows that the shaft variant in Figure 4.25(e) coupled to the 'hybrid' piston variant experiences less deformation than other variants due to the lesser deformation in the connected piston (see Figure 4.23(e)).

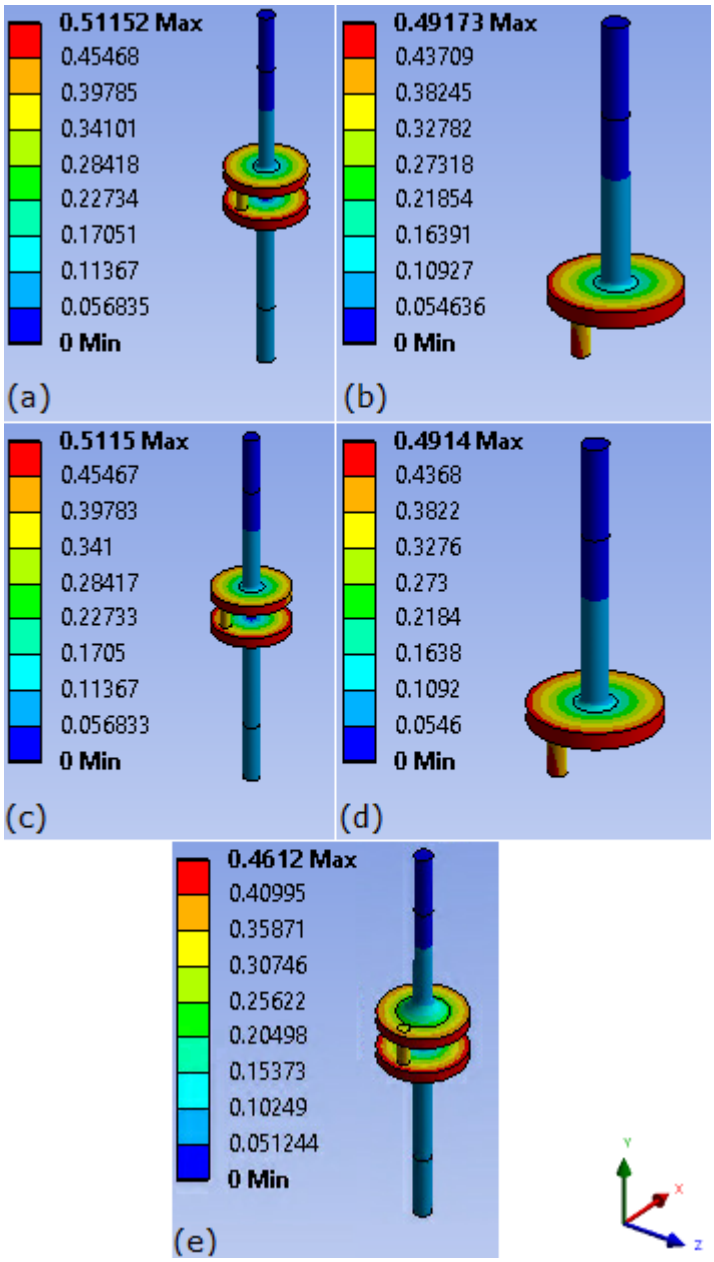

Figure 4.25: FE results – total deformations (mm) in shaft variants (‘a, c and e’ with full shaft and ‘b and d’ with semi-shaft), (‘a and b’ and ‘c and d’ with circular and rectangular web pistons, respectively. Part ‘e’ with hybrid piston).

The stresses produced in the piston variants were also compared excluding the contact region between the piston and shaft which experienced higher stresses (contact analysis was done separately), assuming same for all variants as the region of the piston and shaft remains geometrically unchanged.

The FE analysis of the piston variants found higher stresses compared to the hybrid variant of just 41 MPa as shown in Figure 4.26. It is observed that stresses are almost same among the similar variants due to identical geometries. The circular section middle web piston variants experience maximum equivalent stress at the fillet of the web, while rectangular section web variants have maximum stresses near the piston head and the web. The stresses in the hybrid variant is much lesser than others due to the hybrid nature of web geometry and inclusion of the larger fillets areas near the piston head merging the web section.

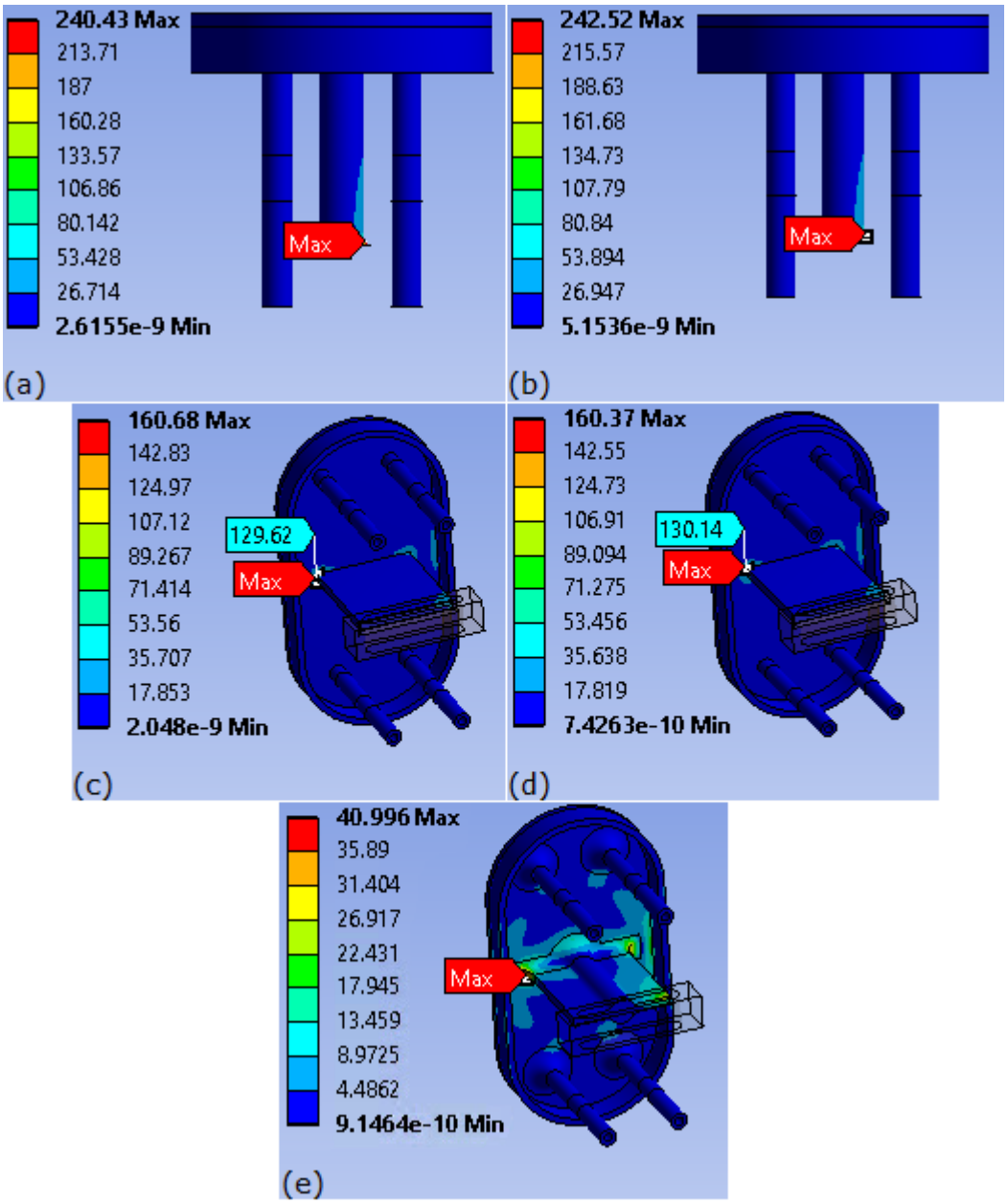

Figure 4.26: FE results – equivalent stresses in piston variants (‘a, c and e’ coupled with full shaft and ‘b and d’ with semi-shaft).

Similarly, the stresses among the shaft’s variants were compared excluding the contact region. The maximum stresses occur in the top section of the shaft just below the support bearing as shown in Figure 4.27. The stresses in the semi-shaft variants was found to be higher than the full shaft variants. The stresses in the full shaft variants ‘a’ and ‘c’ are less than larger fillet variant

'e' because the piston variants for shafts 'a and c' are much more deforming than the hybrid piston variant (for part 'e') (see Figure 4.23).

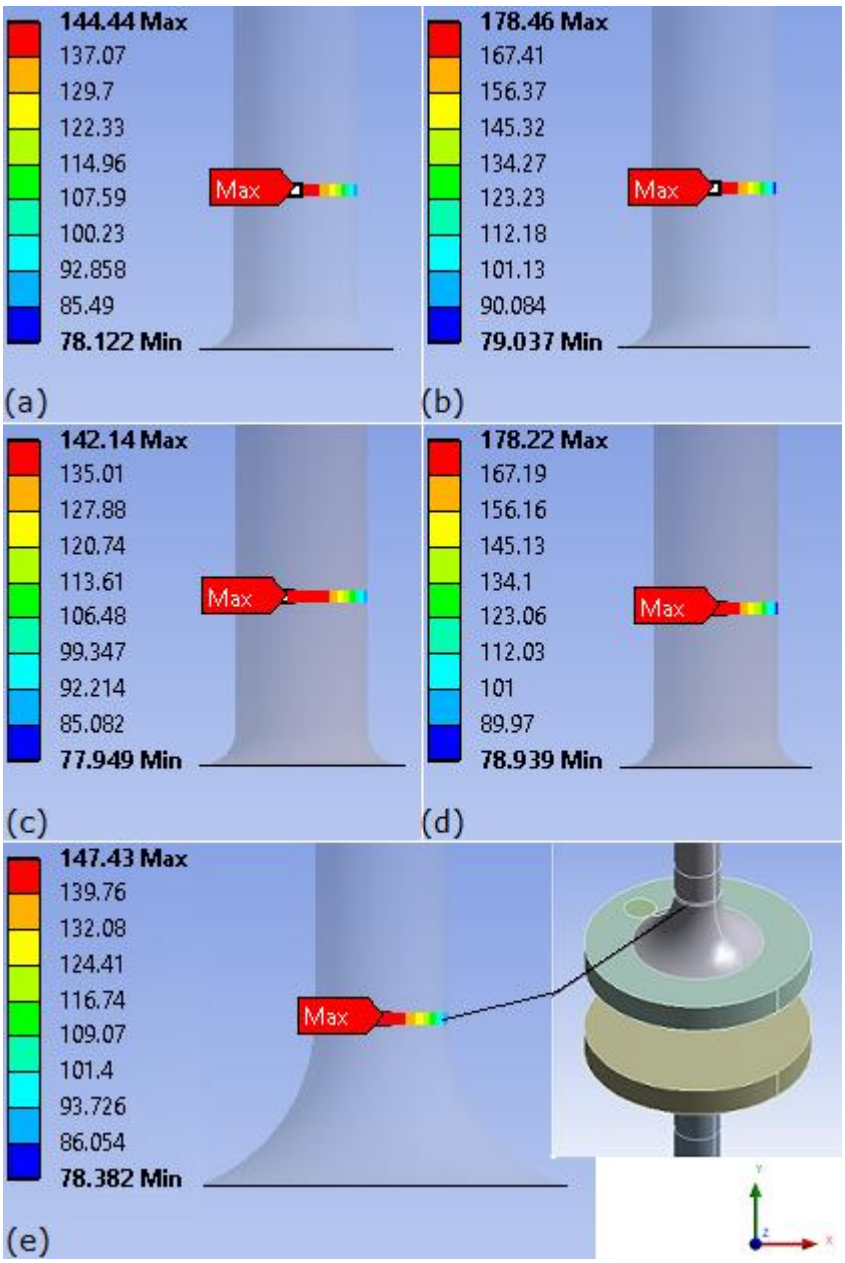

Figure 4.27: FE results – equivalent stresses in shaft variants ('a, c and e' with full shaft and 'b and d' with semi-shaft), ('a and b' and 'c and d' with circular and rectangular web pistons, respectively. Part 'e' with hybrid piston).

Overall, from the FE analysis involving piston-shaft assembly variants, it was subsequently judged that 'hybrid' piston variant i.e. with both circular and rectangular middle web section, and its associated full shaft variant was found to be less deforming than other variants. Thus, this hybrid piston-shaft assembly was selected for further analyses in this study based on its less deformations and stresses. The maximum backward motion deformations observed which were parallel to the force on piston is considered to be safe as they do not exceed the allowable tolerances against the casing housing (i.e. 1.5 mm set arbitrary during the CAD modelling). It was also found that larger fillets in the piston-shaft variants play significant role in reducing the deformations and stresses such as observed in rectangular mid-web section piston variant where higher stress concentrations were found near the piston head and web. Furthermore, the stresses in both piston and shaft components excluding the contact region stays within the yield strength of the material or say exhibit elastic behaviour with values around 41 MPa and 147.4 MPa for piston and shaft respectively.

4.3.3 Main Casing Body

The stress analysis of the main casing body showed that the pressure applied to the cylinder walls produced maximum equivalent stress of 60.9 MPa (averaged using the probe tool) well below yield strength as shown in Figure 4.28. However, the maximum stress is a singularity value which was observed at the edge of the cylinder. The total deformation in the main casing was seen within the cylinder with negligible maximum value of 1.54e-2 mm as illustrated

on Figure 4.29. The small values of stress and deformation show that the set thickness of the cylinder (10 mm) is safe for the design to bear the 200 m head load i.e. with a safety factor of 3.4.

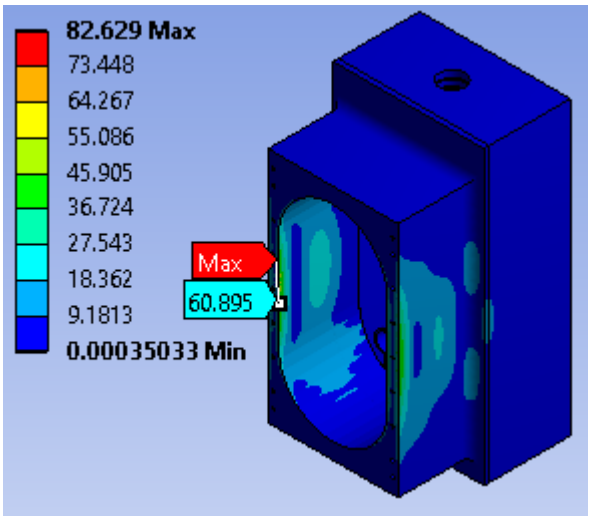

Figure 4.28: Equivalent stress (MPa) in the main casing body.

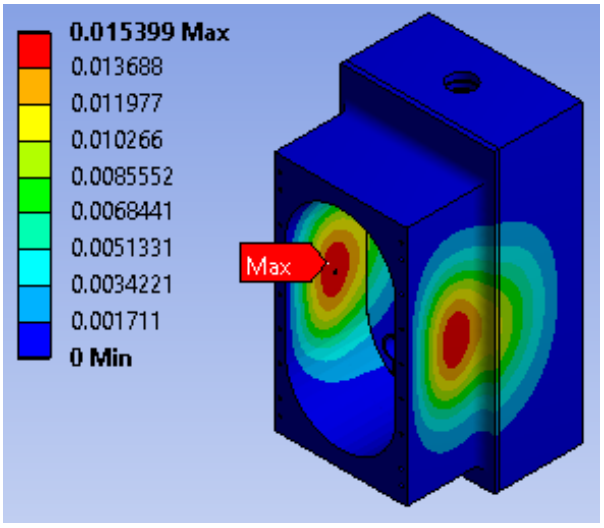

Figure 4.29: Total deformation (mm) in the main casing body.

4.3.4 Casing Front (manifold) and Back Covers

The results for casing front cover were simulated for the maximum equivalent stress and total deformation. The maximum stress without the

singularity point was found to be around 130 MPa (below yield limit, F.o.S is 1.6) which occurred at the inner surface of the cover as shown in Figure 4.30. The total deformation contours of the casing front cover show very negligible maximum deformation of 6.9e-2 mm shown in Figure 4.31.

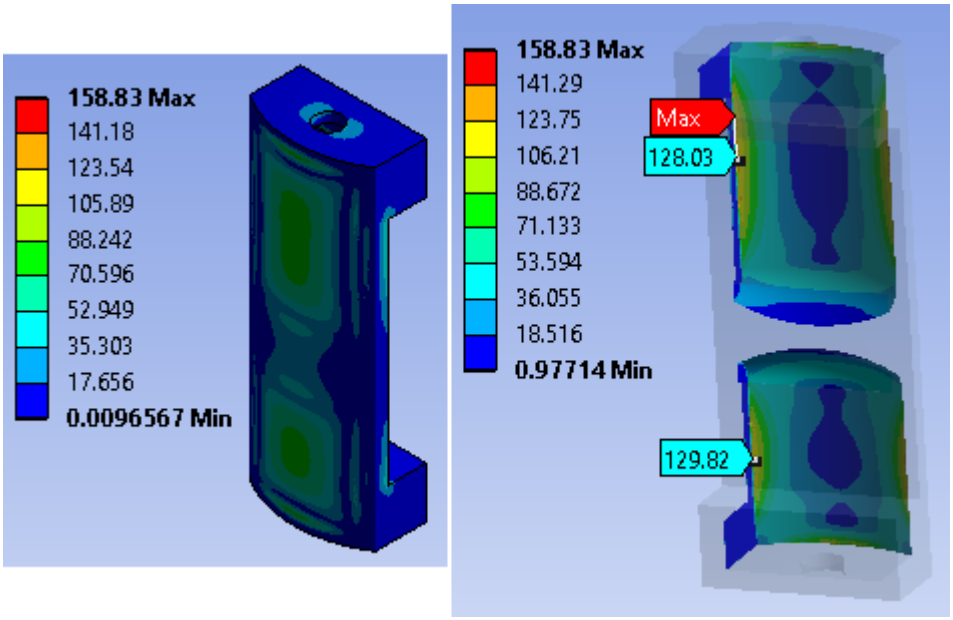

Figure 4.30: Equivalent stress (MPa) contour in casing front cover (left), cut section showing maximum stress location (right).

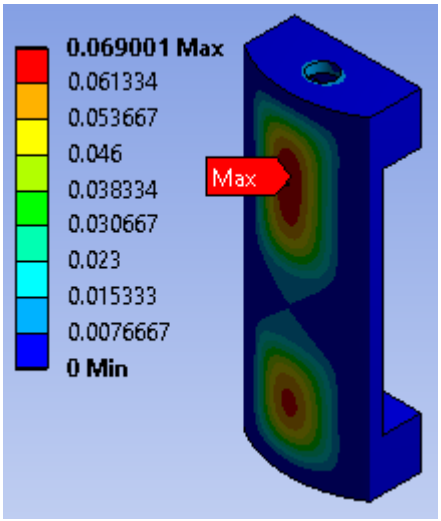

Figure 4.31: Total deformation (mm) in the casing front cover.

Similarly, the back cover was also simulated for stress and deformation checks. The equivalent stress analysis result was evaluated using the probe tool in ANSYS as the maximum stress location was a singularity point. Using the probe tool, the average stress in the cover was found to be around 13 MPa as shown in Figure 4.32. Very negligible total deformation of 6.9e-3 mm was observed as shown on Figure 4.33. The factor of safety was evaluated to be 15 which is high due to the thickness of the back cover and bearing supports.

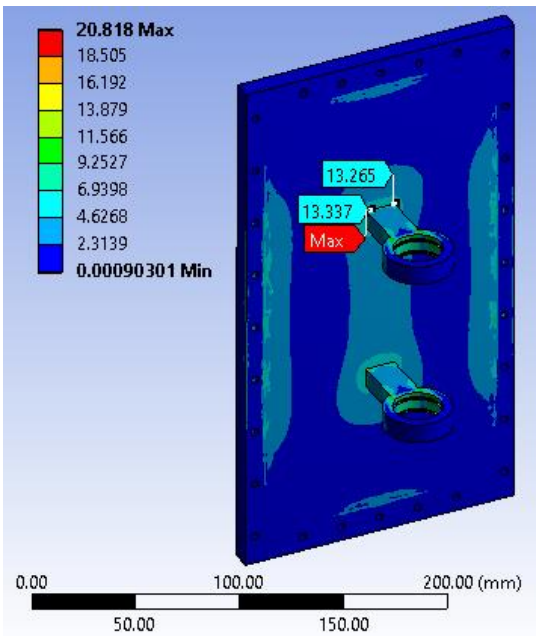

Figure 4.32: Equivalent stress (MPa) in the casing back cover.

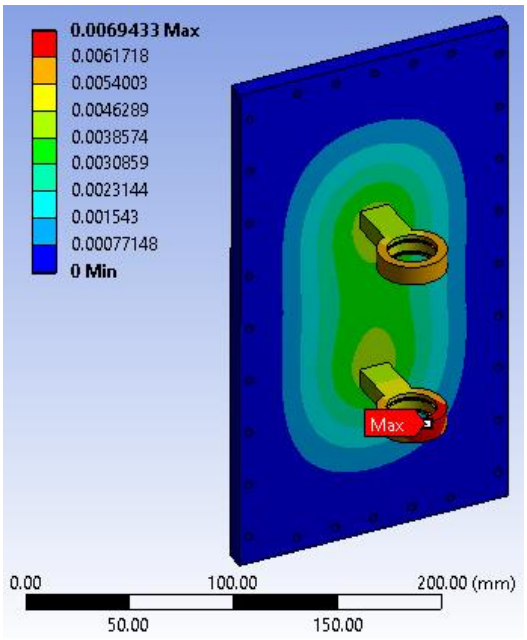

Figure 4.33: Total deformation (mm) in the casing back cover.

Overall, all components of the concept pump seem to withstand the stresses below the yield limit of the material except the contact region between piston and shaft which can be further improved. The current analysis of components is based on a fixed maximum head of 200 m with 1 inch pipe diameter and limited borehole size of 10 inches under the maximum required flow of 25k litres/day [4]. However, the design stresses are flexible to any change in the above parameters. Such as, increase in borehole size would reduce stresses in the components by altering the designs' dimensions. Similarly, increase in water weight (due to head or pipe size or resistive force due to high flowrates) would limit or fail the design (due to lower safety factors or dimensions limitation) provided borehole size remains as constraint, however, a much stronger material would then suffice that load.

4.4 FE Results Validation and limitations

The FE results validation was done for the piston shaft assembly as these components were under high stresses compared to the casing parts. The stresses in the piston and shaft components were calculated analytically at different locations in the components such as in the shaft top section, a section just below the centre top bearing (see Figure 4.16), the piston supports, buckling load check at piston mid-section and the contact region of piston-shaft assembly. A good agreement of results was seen in the comparison of FE and calculated analytical results (calculations performed in Appendix D). Averagely, the results are within 2.76% difference which is acceptable, for instance, when compared to the validation error of 5.64% reported by Bachche et al. [53]. Zhang et al. [109] designated an error margin below 10% as 'good' between experimental and numerical results. The results have been summarised in Table 4.2. The validation also supports the generated mesh quality as the FE results are much closer to the analytical solution.

Table 4.2: Numerical FE results validation with analytical results.

Location in the component	Loading condition	FE Result	Analytical Result	Error %
Shaft top section above centre top bearing	• Torsion (twisting moment)	• Max. shear stress 47.2 MPa	• Max. Shear stress 46.68 MPa	1.1
		• Equivalent stress 78.34 MPa	• Equivalent stress 80.86 MPa	3.1
Shaft section just below centre top bearing	• Bending and torsional	• Max. shear stress 75.95 MPa	• Max. shear stress 70.16 MPa	8.2
		• Equivalent stress 147.43 MPa	• Equivalent stress 142.32 MPa	3.6
Piston supports at linear bearing edge	• Bending	• Max. bending stress 27.17 MPa	• Max. bending stress 26.3 MPa	3.3
Piston mid-section buckling check	• Buckling load	• Critical buckling load 60657 N	• Critical buckling load 60843.4 N	0.3
Piston-shaft slider contact region	• Compressive contact (Hertz contact)	• Max. contact stress 604.45 MPa	• Max. contact stress 611.4 MPa	1.1
		• Max. shear stress 184.73 MPa	• Max. shear stress 183.42 MPa	0.7
		• Contact half width 0.0591 mm	• Contact half width 0.0573 mm	3.1

The casing parts (including main body, front manifold and back cover) experienced lesser stress concentrations and deformations than the piston and shaft components. The basis for accepting these stress values is that they are below the yield strength of the current stainless steel material (207 MPa) which is also evident by acceptable values by many experimental based FE studies on pumps described in Table 4.3. The equivalent stress minimum factor of safety

based on yield limit criteria was found to be around 1.4 which is acceptable and is also quite closer to the literature studies (including experimental studies such as [49,51]). However, the analysis also concludes that the piston-shaft contact region is the critical area where highest stresses are found exceeding the material yield strength and also the allowable contact yield limit of 370 MPa estimated using Equation 4.9. The factor of safety for contact based on the contact yield limit is critically low i.e. 0.61.

Table 4.3: Comparison of acceptable maximum FE equivalent stress values in literature studies with the FE analysis of concept pump.

Study	Material	FE Maximum Equivalent Stress (MPa)	Material Yield Limit (MPa)	Factor of Safety	Maximum deformation (mm)
Golbabaei et al. [49]	AISI 304	305	450	1.47	
Guangjie et al. [48]	Cast steel ZG230-450	171	230	1.34	3
Mohammadian et al. [51]	Cast steel EN 1.4517	384.4	480	1.25	0.23
Rezvani et al. [52]	Carbon steel	103.87	159.3	1.53	
Bachche et al. [53]	Carbon steel	238	290	1.22	0.78
Sparrows case study [131]					0.85
Concept Pump (all components)					
Piston-shaft assembly (Excluding contact region)	Stainless steel (S.S) (ANSYS)	147.43	207	**1.4**	**0.32**
Piston-shaft assembly (Including contact region)		604.5	370 (contact yield limit)	**0.61**	
Main casing body		60.89	207	**3.4**	**1.54e-2**
Casing front cover		129.82		**1.62**	**6.9e-2**
Casing back cover		13.34		**15**	**6.9e-3**

Hence, this shows the limitations of contact design with the slider diameter of 10 mm. If the diameter of slider was assumed to be 19 mm similar to the bearing's diameter [94], safety factor was still below 1 i.e. 0.83. To overcome this, the FE analysis suggests mitigations which include, either to select a much higher strength material with higher contact yield strength than the occurring contact stresses or to increase the diameter of the shaft slider to reduced contact stress (see Equations 4.7 and 4.8) or both. Such as, Du and Carlson [55] optimised the geometry of the contact rollers in swashplate bearing to reduce contact stress in axial piston pump which were failing at 3000 hours well below the 12,000 hours targeted life.

Besides validation, FE results were also verified within the ANSYS program by conducting error estimation. Broadly, FE analysis is associated with three types of errors, (1) User error – Incorrectly setting up the model due to inexperience, (2) Modelling error – Incorrect representation of the real world scenario, and, (3) Discretisation error – Insufficient mesh density to properly capture the solution [132]. In this study, although much care has been taken for correctly modelling and setting up the pump components' models (as per their respective working operations), yet some simplifications are applied such as the removal of piston seal grooves in model as the effects on results are expected to be minimal and is not the region of interest, or the piston supports are taken frictionless over use of linear bearings (although some minute resistive friction force would be exerted by the bearings on the supports whose magnitude is considered as negligible to the applied piston force). From the above mentioned error types, the most commonly used error estimate is the discretisation error to check the FE results consistency [128]. The FE results of

this study's analysis were verified within ANSYS program with structural discretisation error defined in ANSYS as 'stress energy error' (SERR). This is the measure of discontinuity of the stress field from element to element or to check error between averaged and non-averaged results at adjacent element nodes [128,133]. The advantage of this technique is that it consumes less time and can cover the whole FE model compared to mesh sensitivity check which generates several mesh models and is conducted against limited values of stresses [134]. ANSYS normalises the energy error against the strain energy and reports this as the percentage error in the energy norm as described as, [120].

$$E_{error} = 100 \times \left(\frac{e}{e+U}\right)^{0.5} \tag{4.16}$$

where, 'E_{error}' is the percentage error in energy norm, 'U' is the strain energy of the entire model and 'e' is the energy error of the entire model.

The maximum stress energy error and normalised percentage stress energy error of piston-shaft assembly which occur at the slider contact region are shown in Figure 4.34. This region was earlier identified as the limitation in getting a very high-density mesh (see Section 4.3.1). This is the reason why a separate 2D analysis of contact region was conducted. The error estimates of 2D contact analysis are shown in Figure 4.35. The maximum stress energy error and normalised percentage energy error from 3D assembly model were found to be 2.3e-3 mJ (Figure 4.34(a)) and 415.7% (Figure 4.34(c)), respectively. Whereas, conducting a very fine meshed 2D analysis the energy error and normalised percentage energy error at contact were found to be around 10^{-12} mJ (Figure 4.35(b)) and 3.3e-4% (Figure 4.35(d)). The 2D results are

acceptable because they are below 5% which is mainly the maximum acceptable value for energy error estimates [133,135]. From the error estimation analysis, the FE results are thus verified within the software that the whole 3D assembly model is finely discretised for FE results except the contact region which is later mitigated with a separated 2D analysis.

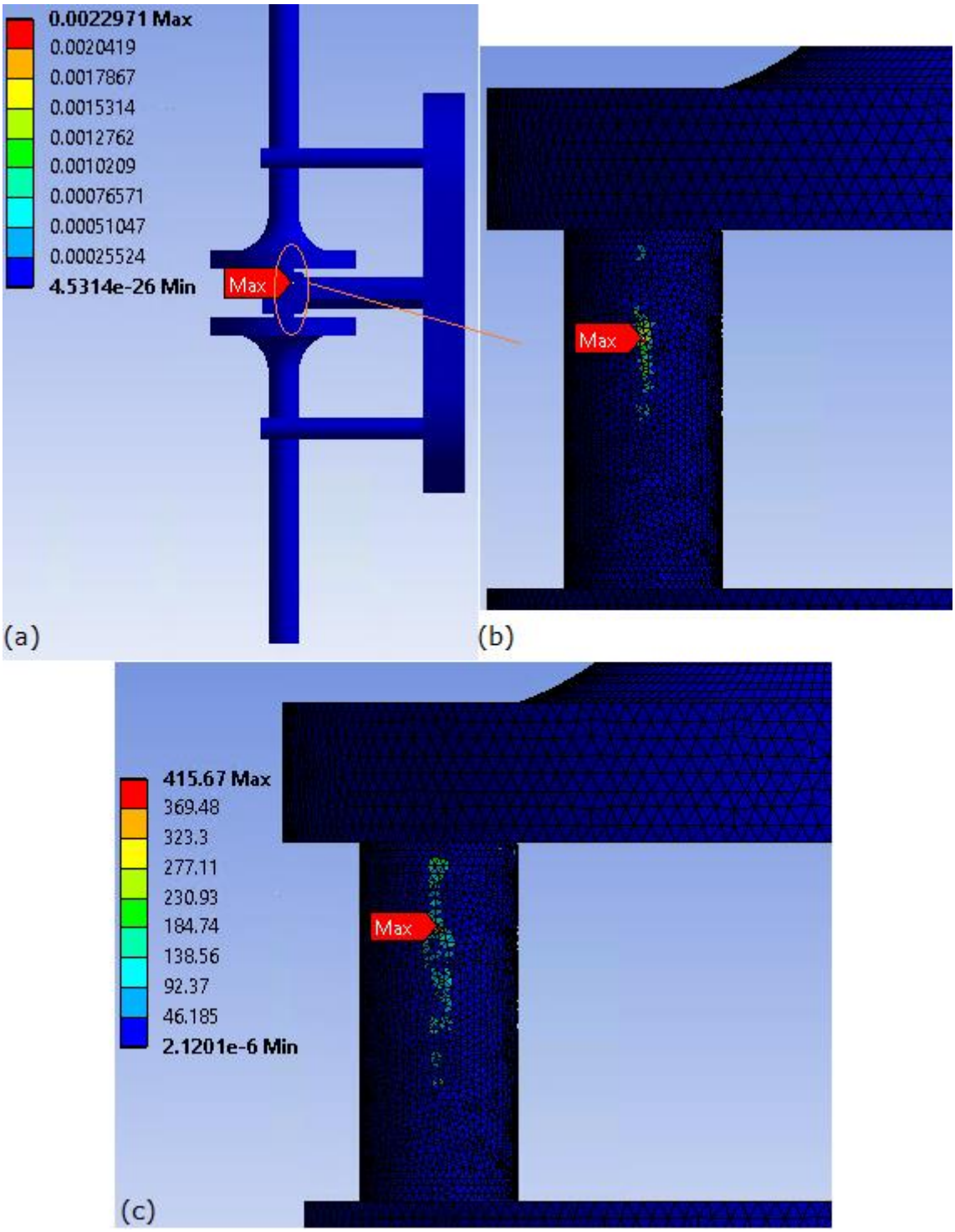

Figure 4.34: (a) Energy error of piston-shaft assembly (mJ), (b) Zoomed view of the slider contact with maximum error, and (c) Maximum normalised energy error (%) at slider contact.

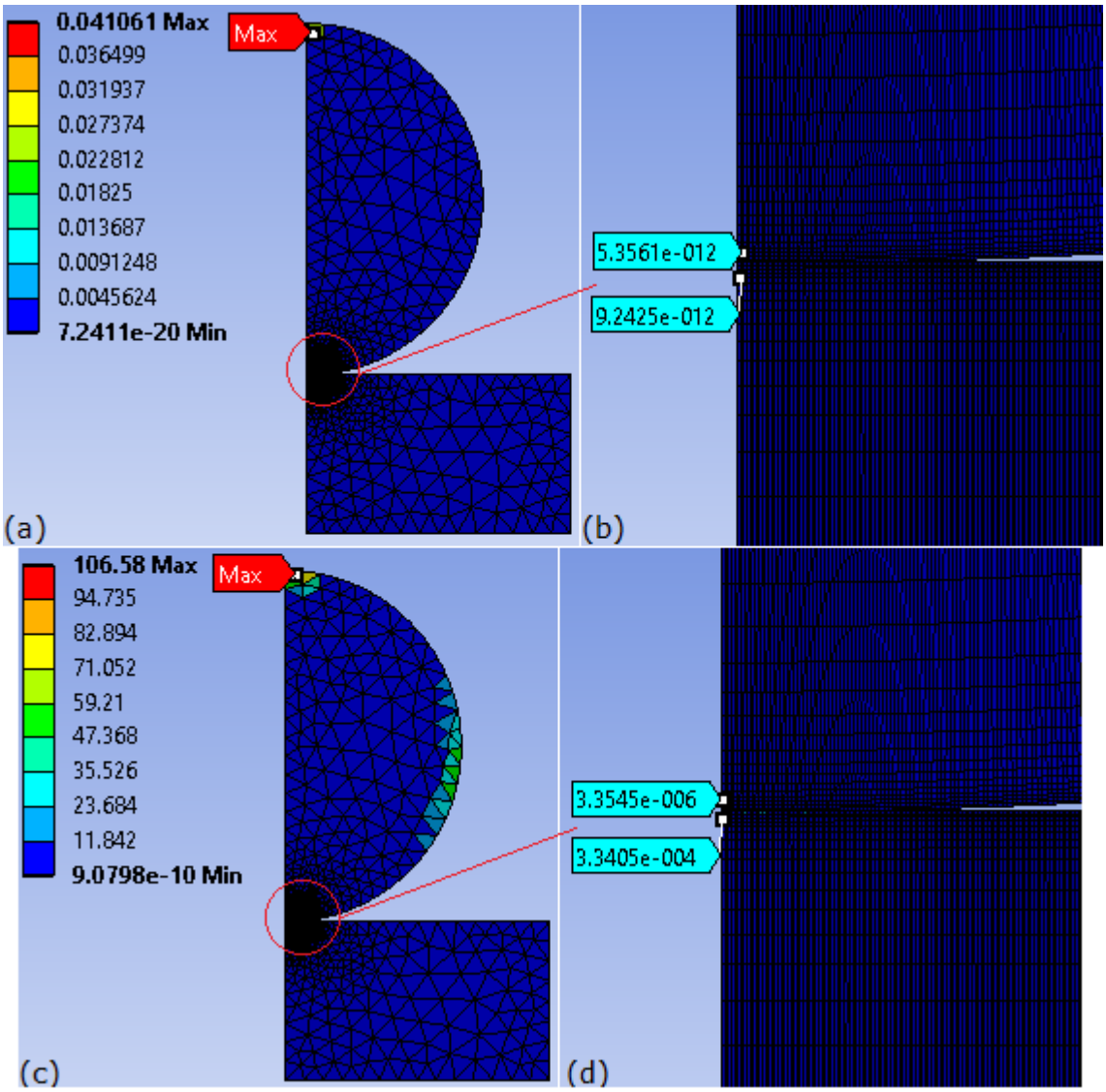

Figure 4.35: (a) Energy error of 2D slider-piston contact (mJ), (b) Zoomed view of energy error at contact, (c) Normalised energy error (%) at contact, and (d) Zoomed view of normalised energy error at contact.

Although the FE results are validated analytically, compared to literature studies and verified with discretisation error estimates and mesh sensitivity analysis which makes a justification for their acceptance, yet the simulation results can further be validated experimentally via fabrication of actual pump components. Due to the time and resources limitations fabrication option was not possible. The results validation processes can be extended to the other

components of the pump (though mesh convergence has been done). Much higher mesh refinements can further reduce the error between the theoretical and FE results.

4.5 Conclusion

A FEA was carried out on the new proposed conceptual design of a piston groundwater pump. The components of concept pump were subjected individually to steady state structural analysis under the 200 m head load which is constant at every cycle of pump operation. The piston-shaft assembly was modelled all together in a maximum moment state by the acting force and as the deformations were expected to be interlinked between the two parts. The piston-shaft components being the main driver of the pump design were analysed in detail with five variants with changes in the mid-web section for piston and shaft with and without lower section. It was found out that hybrid nature of both piston and shaft components exhibited lesser deformations and stresses than the variants (see Figures 4.23 – 4.27). The highest stress among all components excluding the contact region are found in the shaft at middle bearing support and is around 147.4 MPa with acceptable yield safety factor value of 1.4 among published literature (Table 4.3). Casing main body, front manifold and back cover were found with 3.6, 1.62 and 15 safety factors respectively. This means the components remain elastic in nature under load. However, the FE analysis critically predicted the contact area of piston-shaft assembly falling below the safety factor of value 1, i.e. 0.61 against the contact

yield limit. This could be improved with high strength material selection or change in slider diameter or both.

The FE results were validated analytically at various locations of piston and shaft components (Table 4.2) and compared with published research studies. Mesh sensitivity analysis and discretisation error estimation were also carried out which verified FE results. The maximum stress energy error was found to be 3.3e-4%.

Overall, the analysis suggested all components of the concept pump are under safe material elastic limits except the piston-shaft contact region which is a limitation and has room for improvement as addressed in upcoming material selection and optimisation chapters.

CHAPTER 5

MATERIAL SELECTION FOR PISTON, SHAFT AND CASING PARTS

The FE analysis carried out in Chapter 4 on the concept pump components suggested for a search for high strength materials. In this chapter, material selection and its validation is carried out for the pump components.

In this study, Ashby's approach has been adopted for the final material selection for the concept pump components using the popular CES Selector database (version 2018). For this study CES tool was selected due to:

- Easily accessible comprehensive material database that is up to date [136] and its integration to ANSYS software used in FE analysis part of the thesis. ANSYS itself has termed the CES materials reference data as gold standard, consistent, reliable with accurate information needed for any product development organisation [137].
- Friendly user interface to learn about wide spectrum of material families and sub-classes ranging from metals, polymers to composites and their typical applications, various grades and theoretical description of material properties, estimated costs and associated data for environmental effects (carbon footprint).
- It provides research and industry level materials shortlisting possibilities in form of clear and compelling material property selection charts and tables by restricting, putting-against one another or by comparing the properties, material categories, built-in or user input property 'optimisation factors' in terms of loading conditions or any other

constraints set manually. These features are useful in assessment and mitigation of risks in selection process with justifying conclusions.

5.1 Methodology

5.1.1 Problem Statement

The requirement of the devised concept design of a groundwater piston pump (introduced in Chapter 3) is to work under the loading condition of a total head of 200 m. Appropriate materials must be selected for the pump components to withstand such load with objectives of low cost and mass under the constraints of high strength and stiffness.

The aim of this material selection study is thus to identify suitable material(s) for the pump's components i.e. the piston, shaft and casing parts as per their designs drafted in Chapter 3 (see Section 3.2), this means that the design of components remains unchanged. Moving parts involving piston, shaft and main casing body with cylinder are searched for metals such as steel and aluminium alloys while non-moving parts i.e. front manifold and back cover are additionally searched for polymers or composites materials for weight reduction. The material should be able to withstand high stresses such as maximum shaft stress of around 148 MPa observed from FE analysis in Chapter 4.

The initiation of the material selection methodology unfolds with literature review of common pump materials, exploring detailed CES selector database, validation through TOPSIS MCDM method and FE analysis. The review of common materials used in groundwater commercial pumps would assist in the

determination of common class of materials normally used. Meanwhile, use of well-adopted CES database and its versatile chart selection method based on performance indices would be significant in determining wide range of materials in identified common material classes. Finally, validation and verification through a statistical decision making technique (TOPSIS) and FE simulations of pump components would be supporting outcomes for the material selection method.

5.1.2 Common Pump Materials from Literature

A general literature survey is conducted to determine the specific material type or family normally used for pump components such as piston, driving shaft and casing (includes cylinder, intake and discharge manifolds). The materials of these components were gathered from the literature in order to get rough idea about the material kind widely used particularly in groundwater pumps, this comprised of data from pump handbooks, research studies relating conceptual groundwater pumps and some pump manufacturers' specifications.

5.1.3 Material Selection using CES Selector

The CES Selector tool which is based on Ashby's approach in the selection process makes it easier to implement the performance or optimisation factors (or indices) for a respective component depending on its loading applications. Figure 5.1 shows the material selection process flowchart for this study using the CES tool.

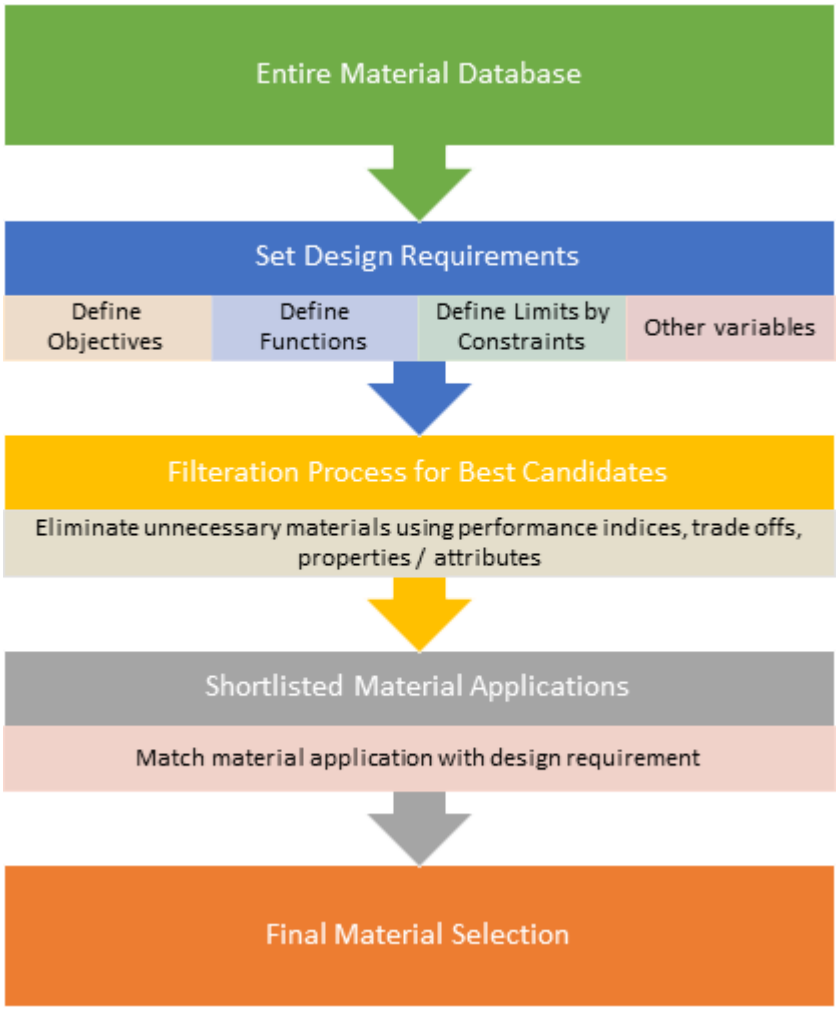

Figure 5.1: Material selection process flowchart.

The main criteria for material selection using CES Selector tool was to have a stronger and stiffed material which could withstand the loading forces during operation. In the proposed conceptual design of the pump, components experience various loading conditions. For instance, the piston head is in bending state as it must lift the weight of water in the pipe which acts like a bending beam. Therefore, the head during the discharge stroke must not deform or should be highly stiff. According to the stiffness equation,

$$S = {}^{F}/_{\delta} = \frac{CEI}{L^3} \tag{5.1}$$

where, 'S' is the stiffness, 'δ' is the deformation, 'E' is the Young's Modulus of the material, 'I' is the moment of area '$I = {bt^3}/{12}$' for rectangular cross-section (b is the width and t is the piston head thickness), 'L' is the length of the piston head and 'C' is the constant.

Additionally, the material should be less in weight (less density) and less in cost. By simple mass equation,

$$m = L \times b \times t \times \rho \tag{5.2}$$

where, 'm' is the mass and 'ρ' is the density of the material. In the proposed design of the piston, the thickness is the only flexible variable that is open to modification compared to the length and width of the piston due to the borehole size limitations and flow requirement. Substituting 't' in the Equation (5.1), we get for 'm'.

$$m = \left(\frac{12SL^5b^2}{C}\right)^{1/3}\left(\frac{\rho}{E^{1/3}}\right) \tag{5.3}$$

Hence the quantity, '$\left(\frac{\rho}{E^{1/3}}\right)$' reveals that minimum this ratio, greater would be the material stiffness. If the reciprocal quantity '$\left(\frac{E^{1/3}}{\rho}\right)$' is maximum, then it reveals lighter material. Furthermore, to add the cost optimisation factor 'C_m' in this ratio, multiply, the denominator with the 'cost per unit mass' i.e. '$\left(\frac{E^{1/3}}{C_m\rho}\right)$'.

It is expected that when the piston is in bending state, the associated stresses on the pump should be less than the yield strength of the material. Similarly, the same method is applied for the strength of the material with less

mass and cost. Hence, based on the bending stress, the optimisation factor is calculated as '$\left(\frac{\sigma^{1/2}}{C_m \rho}\right)$' where, '$\sigma$' is the yield strength of the material.

For pump shaft component, which is under mixed loading conditions i.e. it acts under both bending and torsional stresses, the same bending performance criteria based on low cost and density is applied. In order to have higher torsional stiffness, the material must have high shear modulus 'G'. For this purpose, the torsional stiffness optimisation factor '$\left(\frac{G^{1/2}}{\rho}\right)$' is derived from the torsional deflection of the shaft.

According to Ashby, no material selection technique is perfect to give an optimum material during selection due to common nature of materials properties, and a property trade-off is required after the final screening out of the best candidates [60,73,138].

A further criterion was adopted for the material selection based on the environmental factors such as ability to perform in salty water conditions and being corrosion resistant. A filtering feature based on these attributes was applied, i.e. a limitation criterion was setup in the CES tool in this regard which filter materials only with 'excellent and acceptable' salt water performance and 'pitting corrosion resistance number' (PREN) greater than 30. The 'PREN' is a measure of corrosion resistance of stainless steels and the PREN values of '32 or 33' is considered as the minimum requirement for sea water conditions [136], hence more applicable for groundwater conditions because the salinity of seawater is higher than groundwater which would result in longer life of the pump [139,140].

The casing in the proposed concept pump design comprises of the main casing body, front manifold and back cover. It is very much understandable that same material should be preferred for the casing parts or parts in contact with moving parts (see Table 5.2) as selected for the piston and shaft components to avoid operational hindrances such as irregular deformations due to thermal or mechanical loads, fluctuations, parts assembling issues or durability life. This in all increase complexities in manufacturing, assembling and operation of the device. Additionally, it was further worked to find some polymeric material for the casing parts to make it much lighter besides withstanding the stresses and deformations such as E-glass composites (glass fibre reinforced composites, GFRC) used for blowers [141].

Further, the casing body acts as a pressure vessel to withstand the pressure developed when the piston discharges water. The casing thickness being the flexible variable in the casing proposed design, the mass optimisation factor in terms of yield strength and stiffness was calculated to be '(σ/ρ)' and '(E/ρ)' respectively. Materials with higher this factor stand high stress and lesser values lead to the lighter mass.

Three polymer fibre reinforced composite groups which are widely used in pumps parts (casing, housing, impellers etc.) were analysed i.e. polyethylene [142–144], polypropylene [143,145–148] and polyamide [149]. Polymers with glass fibre were compared. Glass fibre strengthens the material load bearing capacity. Using the 'CES Selector' tool, following groups were compared.

- Polyamide group (Polyamide Glass Fibre Reinforced Composite PA/GFRC)
    - PA66 – 60% glass fibre (designated as PA66-60gf) (short fibre)

- PA66 – 60% long glass fibre (designated as PA66-60lgf)
- PA66 – 30 to 35% glass fibre (toughened)
- PA66 – 40% long carbon fibre (designated as PA66-40lcf)
- PA66 – 15% nickel-coated carbon fibre

- Polypropylene group (Polypropylene Glass Fibre Reinforced Composite PP/GFRC)
  - PP (30% long glass fibre) (designated as PP-30lgf)
  - PP (40% long glass fibre)
  - PP (50% long glass fibre)
  - PP (homopolymer, 40% glass and mineral)
  - PP (homopolymer, 40% glass fibre)
- Polyethylene group (Polyethylene Glass Fibre Reinforced Composite PE/GFRC)
  - PE-HD (also called HDPE) (20-30% long glass fibre)
  - PE-HD (30% glass fibre)

It is assumed that for the selection process, the pump parts which are moving and which are in contact with moving parts such as piston, shaft and main casing body (with piston cylinder) are constrained to metals selection only such as stainless steels or aluminium alloys, to avoid operational hindrances. However, the parts which are non-moving such as casing front manifold and

back cover are flexible to metals and composites (to reduce weight of the pump) materials.

5.1.4 Material Selection Process Validation

First, to verify the CES Selector database quality in terms of material properties data, an online survey was conducted for widely used stainless steel grades from 15 suppliers around the world [108,150,159–163,151–158]. The suppliers' materials datasheets were compared with CES properties data to see the extent of CES data deviation from actual market. The number of suppliers chosen was sufficient enough to generate an average estimation of comparison between the CES data and suppliers' data.

Secondly, the CES tool material selection process was validated using a multi-criteria decision-making (MCDM) method called TOPSIS. This method is eligible to be used for the real time material selection such as evident in mechanical design studies [69,75,76]. The TOPSIS method weighting criteria uses compromised weighing composed of AHP (analytic hierarchy process) and Shannon Entropy processes [75]. The AHP process uses an importance assigning scale (1 to 9) for the attributes being considered as shown in Table 5.1.

Table 5.1: The importance intensity scale for AHP process [75].

Importance Intensity Scale	Definition	Explanation
1	Equal importance	Two activities contribute equally to the objective
3	Moderate importance of one over another	Experience and judgment slightly favour one activity over another
5	Essential and strong importance	Experience and judgment strongly favour one activity over another
7	Very strong importance	An activity is strongly favoured and its dominance demonstrated in practice
9	Extreme importance	The evidence favouring one activity over another is of the highest possible order of affirmation
2,4,6,8	Intermediate values between the two adjacent judgments	When compromise is needed

The weights from the AHP process are calculated by devising a pairwise comparison matrix among the attributes/properties which weighs their relative importance. For an 'n' criteria, the pairwise matrix can be represented as;

$$M = \begin{bmatrix} a_{11} & a_{1j} & a_{1n} \\ a_{i1} & a_{ij} & a_{in} \\ a_{1n} & a_{nj} & a_{nn} \end{bmatrix}, a_{ii} = 1, a_{ij} = {}^{1}/_{a_{ji}}, a_{ji} \neq 0 \qquad (5.4)$$

where, the '$a_1, a_2, a_{3,\dots,} a_n$' are the pairwise indices of the attributes/properties being compared. The weights are derived by evaluating the eigenvector 'E' with respect to the largest eigenvalue 'λ_{max}' which is evaluated with condition '$(M - \lambda_{max})\alpha_j = 0$'. The accuracy of the comparative weights found from the pairwise matrix is found by calculating the consistency index '$C.I$', given as Equation 5.5. The value of '$C.I$' should be lower than 0.1 for a confident result. Another weights checking property called consistency ratio '$C.R$' (Equation 5.6)

is found using a random index number '$R.I$' evaluated at 'λ_{max}'. The value of '$C.R$' should also be less than 0.1 for a reliable result [164].

$$C.I = (\lambda_{max} - n)/(n-1) \tag{5.5}$$

$$C.R = {}^{C.I}/_{R.I} \tag{5.6}$$

The Entropy process uses the attributes values and mathematically generate the weights using Equation 5.7.

$$\beta_j = \frac{1 - E_j}{\sum_{j=1}^{n}(1 - E_j)} \tag{5.7}$$

Where,

'β_j' is weights from Entropy process. '$E_j = -({}^{1}/_{\ln(m)}) \sum_{i=1}^{m} p_{ij} \cdot \ln(p_{ij})$' is the entropy measure of project outcomes 'p_{ij}'. Project outcomes are the normalised data from the decision matrix (comprising performance indices 'x_{ij}') and are calculated as '$p_{ij} = {}^{x_{ij}}\Big/_{\sum_{i=1}^{m} x_{ij}}$'. The '$m$' is the number of alternatives.

The compromised weights for TOPSIS method are equated as;

$$w_j = \frac{\alpha_j \times \beta_j}{\sum_{j=1}^{n} \alpha_j \times \beta_j} \tag{5.8}$$

The TOPSIS method initiates with the normalisation of the decision matrix data as [75];

$$V_{ij} = w_j \times \frac{x_{ij}}{\sqrt{\sum_{i=1}^{m} {x_{ij}}^2}} \ , j = 1,2,\dots,n\,; i = 1,2,\dots,m \tag{5.9}$$

The ideal and nadir solutions are determined using the Equations 5.10 and 5.11, respectively.

$$\{V_1^+, V_2^+, \dots, V_n^+\} = \left\{\left(Max_i\, V_{ij} \middle| j \in K\right), \left(Min_i\, V_{ij} \middle| j \in K'\right)\right\}; i = 1,2, \dots, m \qquad (5.10)$$

$$\{V_1^-, V_2^-, \dots, V_n^-\} = \left\{\left(Min_i\, V_{ij} \middle| j \in K\right), \left(Max_i\, V_{ij} \middle| j \in K'\right)\right\}; i = 1,2, \dots, m \qquad (5.11)$$

Where, K and K' are the index sets of benefit criteria and non-benefit criteria, respectively. The TOPSIS method now evaluates the deviation from the ideal and nadir solutions by calculating the 'Euclidean distances for each alternative as given by Equations 5.12 and 5.13, respectively.

$$S_i^+ = \left\{\sum_{j=1}^{n} (V_{ij} - V_j^+)^2\right\}^{0.5} \qquad (5.12)$$

$$S_i^- = \left\{\sum_{j=1}^{n} (V_{ij} - V_j^-)^2\right\}^{0.5} \qquad (5.13)$$

Finally, the relative closeness to the ideal solution is calculated as shown by following Equation 5.14. The closeness can be converted in the ranking of the alternatives by taking from highest to the lowest values. The highest value represents the best possible alternative or solution.

$$C_i = \frac{S_i^-}{S_i^- + S_i^+} \;\; ; \;\; 0 \leq C_i \leq 1 \qquad (5.14)$$

5.1.5 FE Modelling with Selected Material

The suitable candidates from the material selection process for the concept pump design should further be evaluated with the FE analysis to concrete the selection process and beside predict the maximum life of the pump design with the selected materials.

All shortlisted materials from the selection process for the main pump components (piston, shaft and casing parts) were static structurally simulated based on the same FE setup (loading forces, constraints, assumptions, simplifications, mesh etc.) similar to Chapter 4 (see Section 4.2). This means that design shape of pump components remains unchanged without any optimisation, only selected materials are assigned in FE analysis. The properties data of selected materials was input to the ANSYS software.

Furthermore, the piston-shaft contact region with selected materials was simulated separately as 2D analysis due to the required high-density mesh and limited computer resources similar to the structural FE analysis carried out in Chapter 4 (see Section 4.2).

5.2 Results and discussions

5.2.1 Common Pump Components Materials from the Literature

The common materials for groundwater pump components from literature review are presented in Table 5.2. It was concluded from the literature review that the main material which is common for all the main pump components is the stainless steel (S.S), with mostly 300 and 400 series of stainless steel grades were found to be used in all pump components. It is also found that similar grades of materials are used among components for example, Mahendra [113] uses AISI 316 or AISI 431 for piston and drive shaft, HMS Cris [116] uses AISI 316 for pump shaft and casing, Lorentz [37] uses AISI 304/316 for both pump and motor ends etc. Hence, common material for groundwater pumps 'stainless steel' was selected as the initial material for all concept pump components.

However, this review did not provide in depth information for the materials such as physical, mechanical properties, material grades and costs needed for proper material selection. Such as was seen in study by Baram [165] no fatigue limit data was available for majority of shortlisted materials in literature. There are numerous grades of stainless steels with different characteristics. The selection of most suitable grade can be found using an extensive database such as the CES Selector and its selection process which is based on Ashby's [73] selection approach (see Figure 5.1). The in-depth selection process for pump components is discussed in next section.

Table 5.2: General list of water pump components' materials from literature review.

Source	Piston / Helical rotor	Pump Shaft	Casing
Apollo [19]	• High tempered brass • Delrin • Buna	• (piston drive rod) Fiberglass Steel	
Mahendra [113]	• AISI 316 coated with hard chromed. • AISI 431.	• AISI 316 (PD) • AISI 304 (CF) • AISI 431	• AISI 304
Lorentz [37]	• AISI 304/316 (also motor end)	• AISI 304/316	• AISI 304/316
Danfoss PAHT [117]			• AISI 304 • AISI 316 for high pressure pumps
Kyocera SD series [119]			• Bronze • AISI 304
Kyocera SC series [118]			• AISI 304
Grundfos [114]			• AISI 304
Fluxinos [166]			• AISI 304 • AISI 316
Mono Borehole Pumps [167]		• (drive rod) Steel or Carbon steel depends on the quality of water	

Table 5.2 (continued): General list of water pump components' materials from literature review.

Pump Handbook [18]	• Colmony No.6 on 1020, chrome plated on 1020, AISI 440c, AISI 316, ceramic on 1020 and solid ceramic.		• (cylinder materials down below) AISI 304, 316L, 1020, 4140, 17-4 PH 15-5 PH. Cast iron or Bronze (most economical) 400 series S.S (extended life)
	• Abrasive wear resistant (descending order) 400 S.S 300 S.S Cast steel Ni-Al bronze Manganese Bronze Bronze Cast iron • *Note:* If the liquid contains abrasive solids, then the material of construction should be selected primarily for abrasive wear resistance.		
Reciprocating Pump Book [115]	• Quenched and tempered 4150. • Quenched and tempered 4140. • AISI 304.		
HMS Cris [116]		• AISI 420, 304, 303, 316, 2205, 431	• AISI 316, 304, 316 • Gray cast iron EN GJL 250 , 200 • Bronze CC480K , CC333G
CONCEPTUAL GROUNDWATER PUMP STUDIES			
Andrada et al. [42]	• Brass	• Galvanised steel drive rod	• Cast Iron
Wade et al. [6]		• Steel	• Steel
Wade at al. [168]	• Brass	• Steel	• Steel
Burton and Short [35,45]	• N/A	• N/A	• N/A

5.2.2 Material Selection for Pump Components using CES Selector

5.2.2.1 Stainless Steels

Figure 5.2 displays the bubble material selection chart with optimised strength and stiffness factors with respect to low cost and density on vertical and horizontal axes, respectively. Higher values of these factors mean higher material strength and stiffness with low cost and density which are found in the top right quarter of the chart. The chart shows various families of materials highlighted as different colour. It is evident from the graph that 'cast iron EN GJN HV600' is the most possible material with highest strength and stiffness with respect to low cost and density in the 'metals and alloys' group.

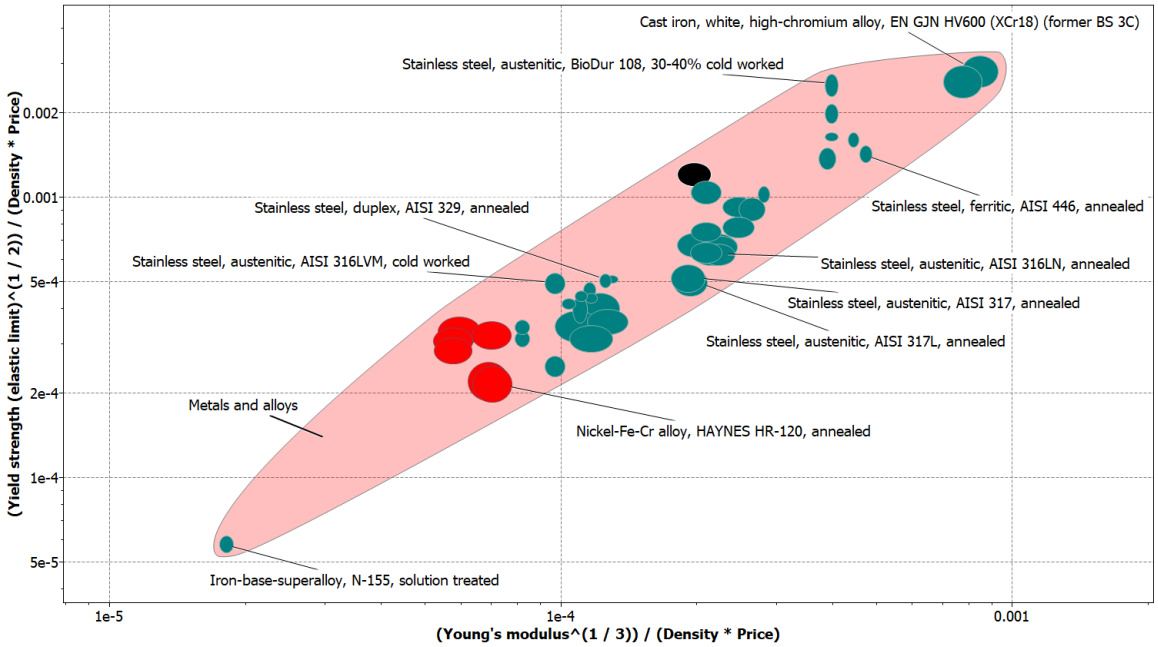

Figure 5.2: Stainless steel material selection bubble chart with bending strength and stiffness factors optimised for low cost and density.

The shaft component of the pump experiences mixed loading conditions i.e. it acts under both bending and torsional stresses. The bubble chart

illustrating the torsional and bending stiffness factors of materials with respect to low cost and density is shown in Figure 5.3. It is evident from the graph that AISI 446 is the most possible stiffed material in terms of both bending and torsional stiffness with minimum mass and cost, whereas cast iron EN GJN HV600 just falls behind in this regard.

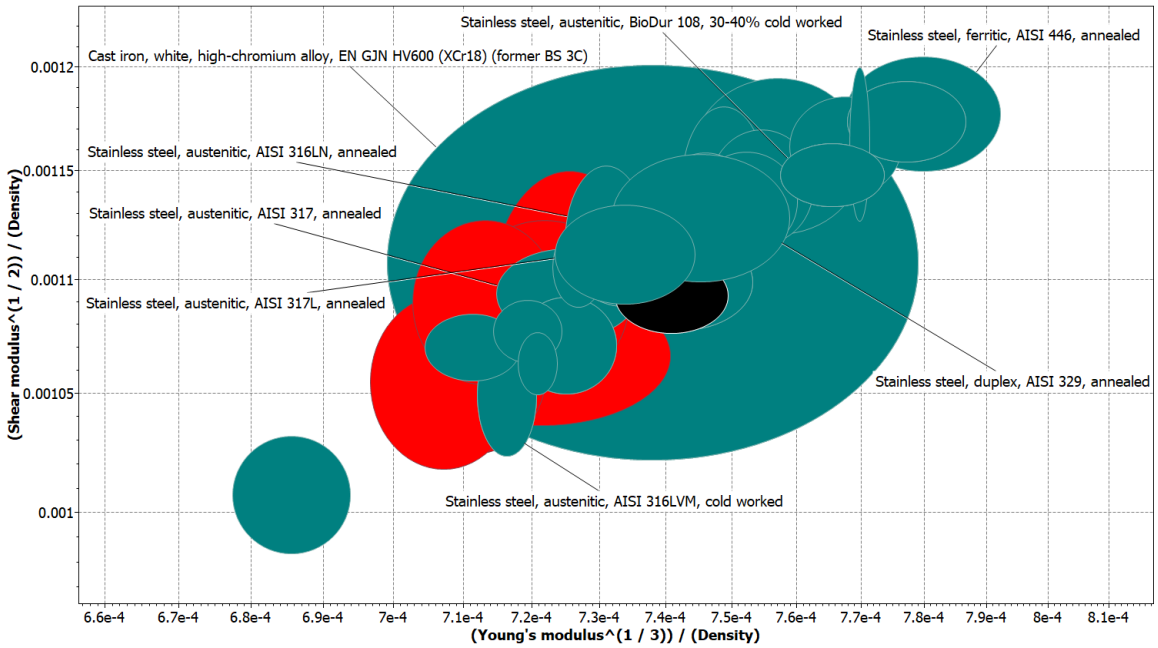

Figure 5.3: Stainless steel material selection bubble chart with torsional and bending stiffness factors optimised for low cost and density.

The selected materials are labelled in the chart, however, some materials are not which are omitted based on similarities in properties (closer to one another) and to diversify study results. The materials with highest values of optimisation strength and stiffness factors, and common pump materials from literature review (e.g. stainless steel AISI 300 and 400 series) were shortlisted from the chart and a final comparison was drawn among them for properties trade-off based on average values (from CES Selector database). The CES database displays bubble charts with properties as ranges only, based on

various data entries collected from various sources and averages are generated based on those entries by the program. Hence, average values are much more consolidated to accept rather than taking range values. The properties trade-off is carried out in Table 5.3, where it is evident that cast iron EN GJN HV600 despite being the cheapest and lightest material, has lower shear, Young's moduli and ductility index values compared to other stainless steel grades. It could not be selected as best candidate because the much lower ductility index makes this material as more brittle than stainless steels. The comparison table puts forward the stainless steel (S.S) 'BioDur108' as the strongest material in terms of strength, followed by AISI 316Lvm, AISI 329 and 446. However, AISI 446 was found to be the cheapest and lightest among all.

Table 5.3: Comparison of shortlisted materials properties for piston and shaft [136].

Property	S.S AISI BioDur 108	S.S AISI 317L	S.S AISI 316	S.S AISI 446	S.S AISI 316L	S.S AISI 316 Lvm	S.S AISI 317	S.S AISI 329	Cast iron EN GJN HV600
Price (USD/kg)	1.93	3.8	3.41	1.65	3.41	7.39	3.8	5.96	0.873
Density (kg/m^3)	7639.6	7969.4	7969.4	7499.3	7969.4	7990	7970	7800	7797.4
Mechanical Properties Data									
Young Modulus (GPa)	200	200	197	200	197	188	193	196	190.5
Yield Strength (MPa)	1370	226	252	310	230	848	241	548	367
Tensile Strength (MPa)	1600	560	565	543	546	1030	565	719	367
Strain Elongation (%)	15.1	37.1	38.7	16.1	38.7	16	35.4	26.5	1.41
Compressive Strength (MPa)	1370	256	252	310	230	848	252	548	671
Flexural Strength (MPa)	1370	256	252	310	230	799	252	548	814
Poisson Ratio	0.299	0.269	0.269	0.279	0.27	0.33	0.27	0.27	0.275
Shear Modulus (GPa)	76.9	78.5	77.9	77.9	77.9	70.3	76	77.4	74.6
Toughness (kJ/m^2)	22	19.8	21	44	19.3	45.7	25.9	39.8	1.27
Ductility index (μm)	0.0453	0.106	0.102	0.212	0.0995	0.132	0.127	0.261	0.00195

For distinction purpose, the strength, stiffness (as Young's modulus), density and cost properties of shortlisted stainless steel (S.S) variants are shown in Figure 5.4.

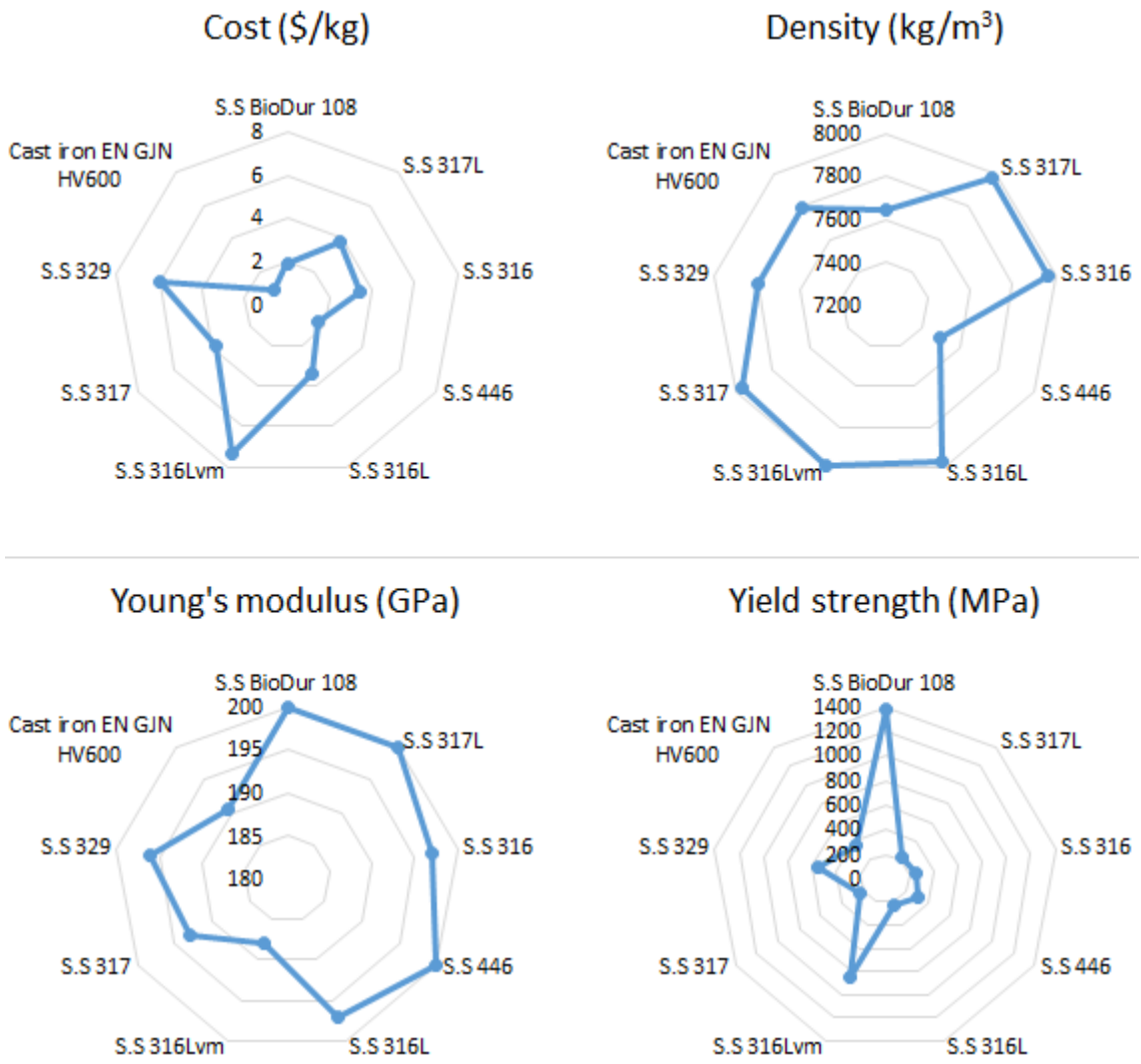

Figure 5.4: Properties of stainless steel variants with cost, density, young's modulus and yield strength.

Therefore, from the material selection comparison of stainless steel variants, AISI 446 was selected to be the best suitable material for the piston and shaft components. The judgment is based on the following reasons.

- It is cost and mass effective.
- It has high yield, compressive and flexural strengths (310 MPa) to bear maximum stresses such as shaft stress of 148 MPa (see Chapter 4, Section 4.3.1).

- It is much preferred to use with abrasive liquids [136] (see Table 5.2) (e.g. suitable in sandy water condition).
- It is tougher than other steel variants.
- The ductility index is also high, this indicates that the material will yield before it breaks compared to 'cast iron EN GJN HV600' (the least cost) and 'BioDur 108' (highest strength). The low values indicate that it will break (fracture) before it yields, with risk of brittle fracture and sudden catastrophic failure [136].
- The shear modulus is also high.

Furthermore, the CES material selection is found to be more advantageous in shortlisting the best stainless steel candidate when a comparison is drawn among the materials from the literature review (see Table 5.2). For instance, looking at the 300 and 400 series such as AISI 303, 304, 431, 420, 440c etc. All these materials were excluded by the set CES criteria mostly due to lower corrosion resistance (PREN values below 20).

5.2.2.2 Aluminium based Alloys

Apart from the stainless-steel (S.S) variants, lighter aluminium (Al) alloys (with excellent performance in salty water conditions) were also selected using the same selection criteria. Aluminium alloy variants would make the components lighter besides withstanding the water load e.g. as was evident in study by Findik and Turan [169] where aluminium alloys were searched using the CES database for lightness, acceptable stiffness, strength, corrosion

resistance and low cost in large-scaled wagon walls than steel walls. The top right corner in the bubble chart of Figure 5.5, shows materials with higher strength and stiffness. It can be observed that the top right corner has Aluminium 5182 as the best possible material candidate. It is also evident that the reference material from stainless steel variants AISI 446 (highlighted in grey) falls below due to its higher density.

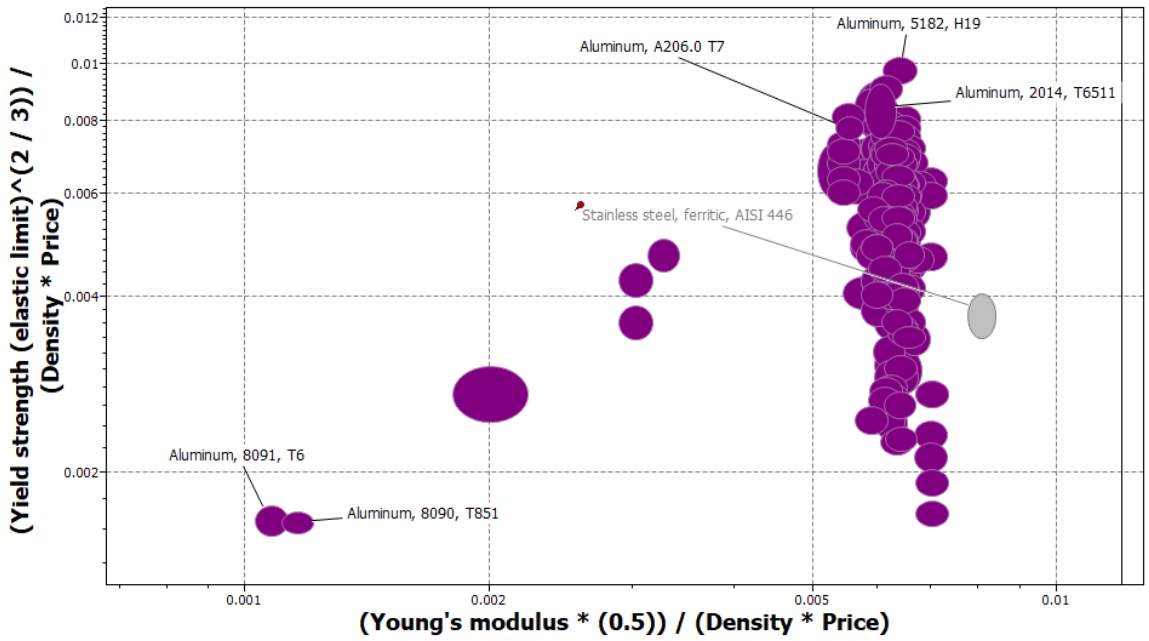

Figure 5.5: Aluminium alloy material selection bubble chart with bending strength and stiffness factors optimised for low cost and density.

The aluminium alloys material properties trade-off required to assist selection process further is carried out in Table 5.4. Aluminium alloy grades with mechanical properties closer to AL 5182 were arbitrary selected for comparison from the bubble chart top right corner (an area with highest optimised strength and stiffness factors). From Table 5.4, it can be observed that the lightest and cheapest material is the Aluminium 5182 (or AL 5182) but it is inferior on the toughness, elongation and ductility index compared to the A206 T7 grade.

Aluminium 2014 T6511 is second best and is much similar in properties to AL 5182 grade except in Young's Modulus which is slightly higher. AL 8091 despite being the lightest and stronger was omitted due to much higher cost than other variants. Therefore, aluminium A206 T7 is much suitable for piston and shaft components because the need is to have high abrasive resistance (reasonably high hardness) besides high stiffness with lower cost and high ductility index. Furthermore, aluminium A206 grade could reduce the weight of the components up to 63% compare to AISI 446 but with a higher cost of around 37%.

Table 5.4: Comparison of shortlisted aluminium variants properties for piston and shaft [136].

Property	Al 5182 H19	Al 2014 T6511	Al A206 T7	Al 8091 T6	AISI 446
Price (USD/kg)	2.07	2.24	2.26	14.2	1.65
Density (kg/m^3)	2650	2800	2800	2580	7499.3
Mechanical Properties Data					
Young Modulus (GPa)	70.3	75.9	70.2	79	200
Yield Strength (MPa)	392	375	345	471	310
Tensile Strength (MPa)	420	435	430	548	543
Strain Elongation (%)	3.99	2.65	10.2	7.25	16.1
Compressive Strength (MPa)	392	395	365	471	310
Flexural Strength (MPa)	392	375	345	471	310
Poisson Ratio	0.33	0.337	0.33	0.33	0.279
Shear Modulus (GPa)	26.7	28.7	26.7	29	77.9
Toughness (kJ/m^2)	15.4	17.5	26.2	15	44
Ductility index (μm)	0.118	0.127	0.205	0.103	0.212

For distinction purpose, the strength, stiffness (as Young's modulus), density and cost properties of shortlisted aluminium variants are shown in Figure 5.6.

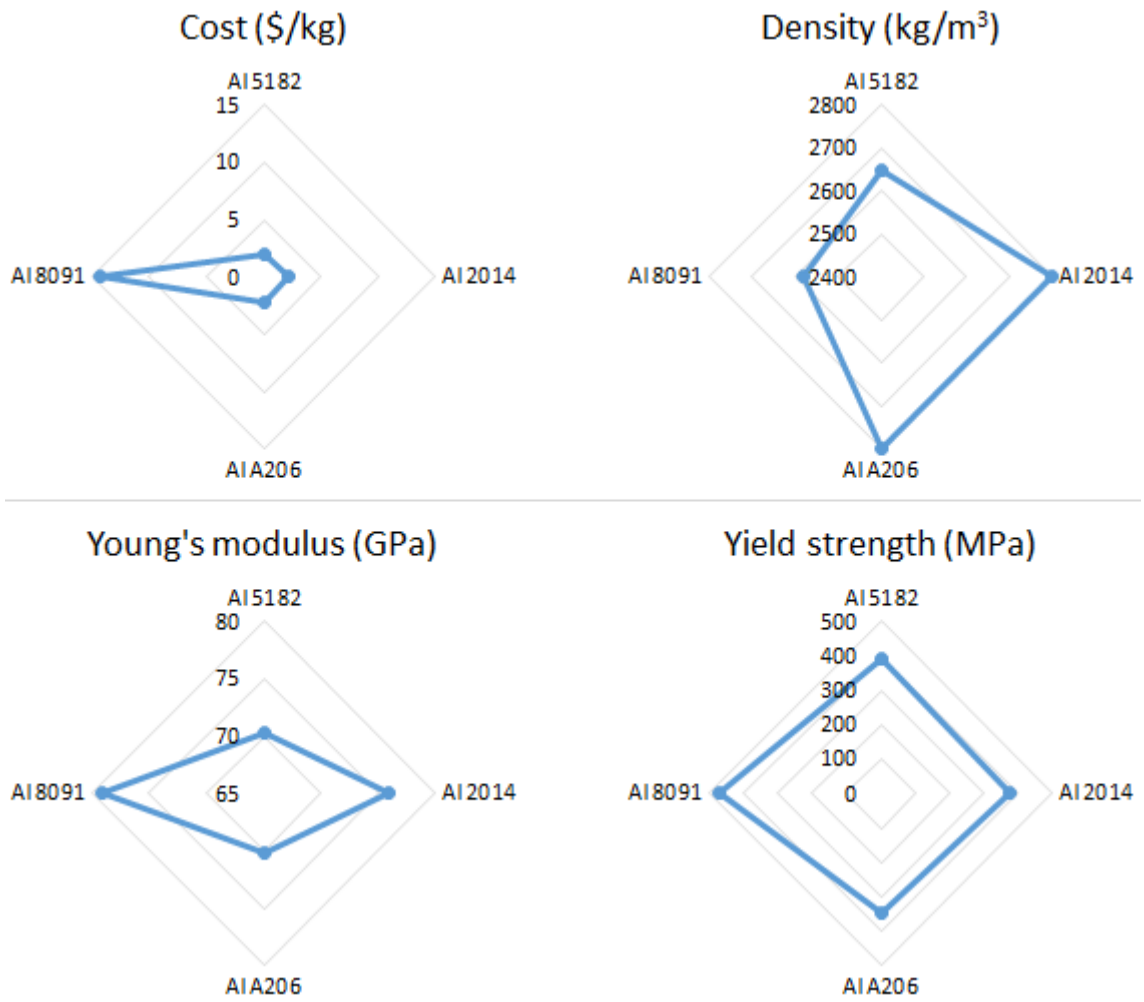

Figure 5.6: Properties of aluminium variants with cost, density, young's modulus and yield strength.

5.2.2.3 Composites Material Selection for Casing Covers

The composites material selection was also conducted for the casing front cover (manifold) and casing back cover. Figure 5.7 shows the results for the cost optimisations factors in terms of strength and stiffness for selected

composites. It is seen from the graph that, PA66-60% glass fibre is the cost effective with lighter mass material with higher strength and stiffness compared to others. However, in terms of mass optimisation factor only, the selection chart shows 'PA66 – 30% and 40% long carbon fibre-reinforced composites' lead as shown in Figure 5.8. However, the average material costs of these materials were quite high (discussed in trade-off comparison Table 5.5).

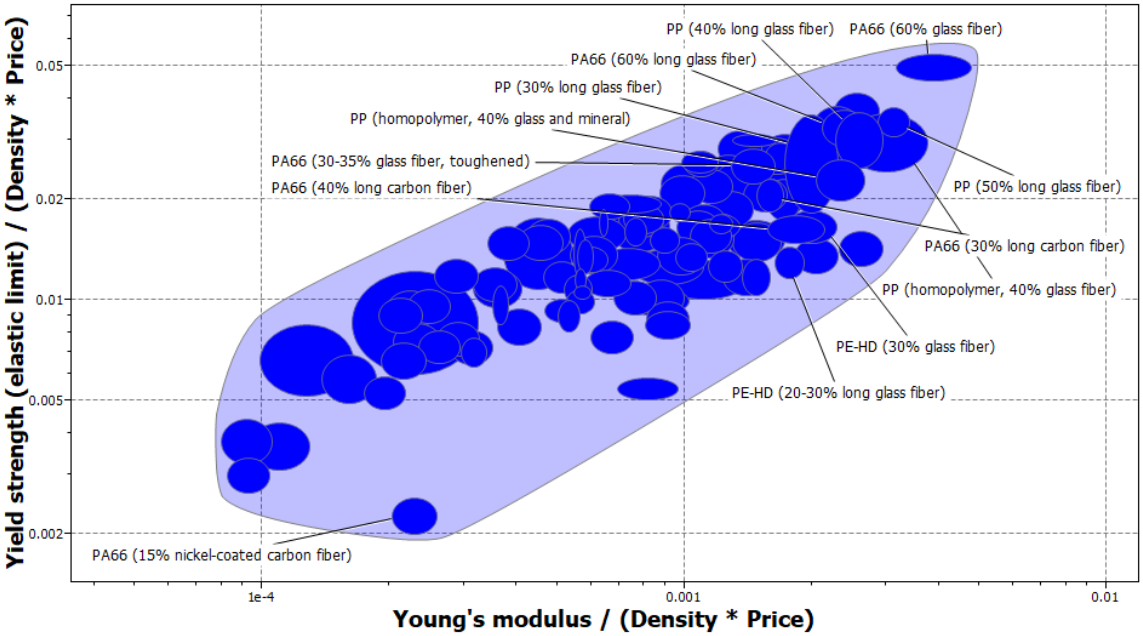

Figure 5.7: Composites material selection bubble chart for casing parts with strength and stiffness factors optimised for low cost and density.

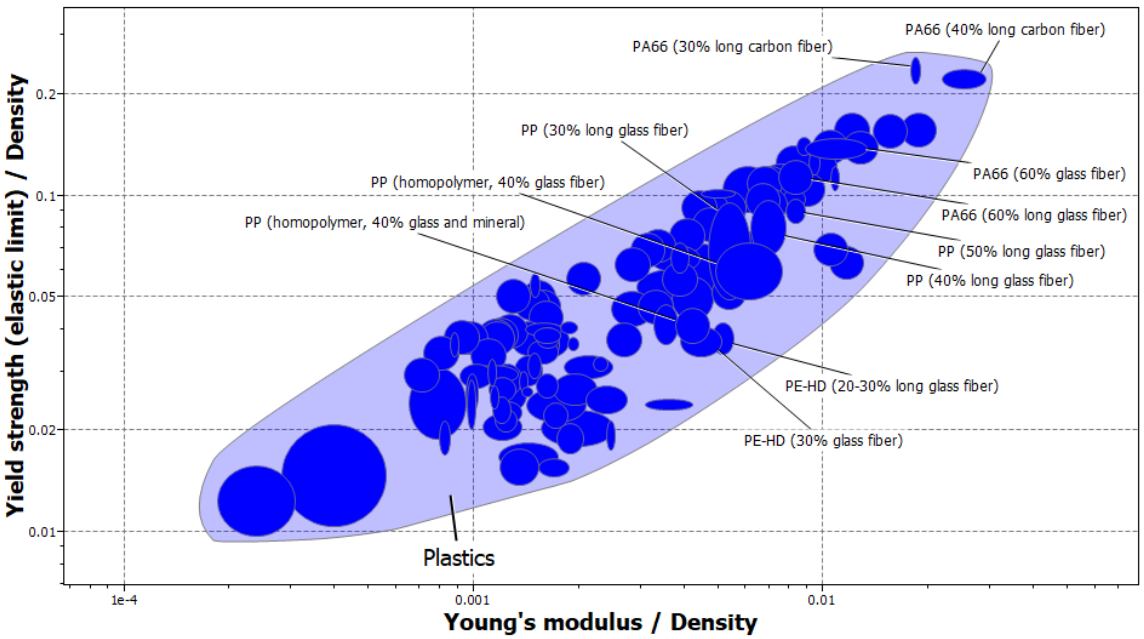

Figure 5.8: Composites material selection bubble chart for casing parts with strength and stiffness factors optimised for low mass.

The shortlisting of composites was done arbitrary for comparison among all composite material families in the selection charts (i.e. PP/GFRC, PA/GFRC and PE/GFRC) with more focus on the top right corner of the bubble charts (labelled in Figures 5.7 and 5.8) where values of optimisation factors are maximum. By comparing the shortlisted materials mechanical properties, it was concluded that higher the percentage of glass fibre, stronger is the material. Therefore, the filtration was further reduced to select at least one from each group and compare them. The filtered materials were PA66-60gf, PA66-60lgf, PA66-40lcf, PP-homo-40gf, PP-50lgf and PE-HD-30gf. The properties trade-off of shortlisted materials is presented in Table 5.5. From the tabular data, it can be concluded that PA66 – 40lcf is the best material in terms of strength and stiffness for the casing parts but with slightly higher density and much higher cost. A trade-off was made between this material and PA66-60gf due to the

better elongation and cost. The chosen composite material could be used as alternative to the steel variants for pump casing covers. However, the main casing body is not recommended to be used with composite materials as seen in literature review where same material family (stainless steel) are used for piston, shaft and casing (see Section 5.2.1). The moving components such as metal piston or shaft may create operational hindrances i.e. composites being less stiff than metals and may create possible higher deformations thus are prone to wear to the abrasive nature of groundwater.

Table 5.5: Comparison of shortlisted composite materials properties for casing parts [136].

Property	PA66 – 60gf	PA66 – 60lgf	PP – 50lgf	PP – Homo-40gf	PE-HD – 30gf	PA66 – 40lcf
Price (USD/kg)	2.8	3.49	2.66	2.03	2.24	13.7
Density (kg/m^3)	1700	1670	1330	1220	1230	1310
Mechanical Properties Data						
Young Modulus (GPa)	18.5	13.9	11.1	7.46	5.48	33.2
Yield Strength (MPa)	235	189	119	72.8	45.3	293
Tensile Strength (MPa)	235	189	121	88.5	56.7	308
Strain Elongation (%)	2.29	1.97	1.68	3.2	1.94	1.22
Compressive Strength (MPa)	207	228	101	73.6	44.7	370
Flexural Strength (MPa)	354	320	188	127	79.2	436
Poisson Ratio	0.324	0.325	0.348	0.36	0.374	0.321
Shear Modulus (GPa)	6.98	5.26	4.1	2.74	1.99	12.6
Toughness (kJ/m^2)	8.33	2.16	2.48	2.29	1.05	5.02
Ductility index (μm)	0.22	0.597	0.696	0.378	0.398	0.206

For distinction purpose, the strength, stiffness (as Young's modulus), density and cost properties of shortlisted composites are shown in Figure 5.9.

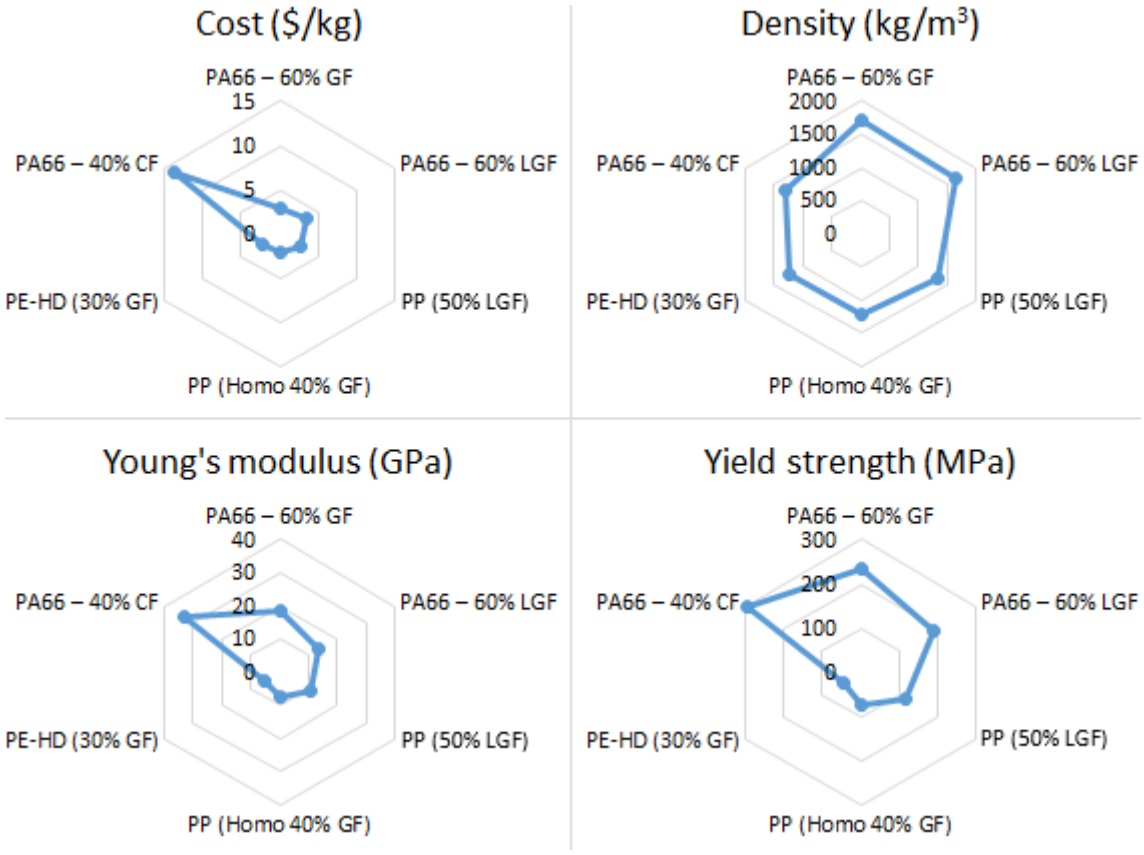

Figure 5.9: Properties of composites with cost, density, young's modulus and yield strength.

There are product design research studies which have selected composite materials for components and have given preference over metals based on lightness and material costs without compromising the strength and stiffness such as study by Thakker et al. [69] selected GFRP (glass fibre reinforced polymer) over titanium alloy for an impulse turbine blade with good corrosion resistance as well. Similarly, study by Findik and Turan [169] shortlisted PP, PE and PA based GFRP for lightness in a large-scale freight wagon walls. However, they were put as second option to aluminium alloy because of difficulty in joining methods. Aluminium was also given preference over low carbon steel due to lightness and reasonable strength, corrosion resistance and mild cost.

5.2.3 Validation of Material Selection Process and Results

A very good agreement was seen in the comparison of CES Selector data and commercial data presented in Table 5.6. The slight negative and positive percentage differences observed in the table show CES data deviation from the suppliers' data in higher and lower margins, respectively. Overall, the average comparison from the table data reveals CES data only deviates 3.44% from the commercial data making this a reliable database to select for material selection. Such data authenticity validation was not found in other conceptual pump design literature studies (see Table 5.2) where material selection process is either just based on past experiences, availability in local market or is just not specified. It is also justified that the averaged based material properties data was acceptable to use in the selection process (e.g. see Table 5.3).

Table 5.6: Comparison of material properties from CES program and commercial suppliers' data.

		Materials							
Property	**Data source**	**316**	**316L**	**316LN**	**317**	**317L**	**317LN**	**Biodur108 30-40% CW**	**Biodur108 annealed**
Density (kg/m^3)	Suppliers	7954	7970		7890	7935		7640	7645
	CES	7970	7970	8000	7970	7970	7970	7640	7640
	Difference (%)	-0.20	0.00		-1.01	-0.44		0.00	0.07
Yield Strength (MPa)	Suppliers	262	249.1	317.5	222.5	231.6	297.5	1444.25	838.6
	CES	252	230	290	241	226	226	1370	586
	Difference (%)	3.82	7.67	8.66	-8.31	2.42	24.03	5.14	30.12
Tensile strength (MPa)	Suppliers	572.5	573.1	607.5	515	525.8	575	1616.75	1200.4
	CES	565	546	673	565	560	560	1600	931
	Difference (%)	1.31	4.73	-10.78	-9.71	-6.50	2.61	1.04	22.44
Hardness	Suppliers	86.25	86.25		95	95			
	CES	86.6	78.9	94.9	89.9	87.2	87.2	116	103
	Difference (%)	-0.41	8.52		5.37	8.21			
Young's modulus (GPa)	Suppliers	197.2	195.4		200	196.5		200	202
	CES	197	197	200	193	200	200	200	200
	Difference (%)	0.10	-0.80		3.50	-1.78		0.00	0.99
Pitting corrosion number	Suppliers	25.1	24.44	29	29.7	29.35	32		
	CES	25.1	25.1	27.2	30.4	30.4	30.4	39.5	39.5
	Difference (%)	0.00	-2.70	6.21	-2.36	-3.58	5.00		
Poisson's ratio	Suppliers		0.287					0.3	0.3
	CES	0.27	0.27		0.27	0.27	0.27	0.3	0.3
	Difference (%)		5.92					0.00	0.00
Fatigue Limit (MPa)	Suppliers		415						382.7
	CES	240	280	306	268	285	285	658	382
	Difference (%)		32.53						0.18

The material selection was validated using TOPSIS method. All materials groups (stainless steel, aluminium and reinforced composites) were compared for their properties yield strength, Young's modulus, density, shear modulus and cost. The strength properties were given slight priority importance over the density and cost. These are the same attributes which were used previously for evaluating the performance factors using the CES tool. The weights from the MCDM processes i.e. AHP and Entropy, and the compromised weights for

TOPSIS method are shown in Table 5.7. The AHP process weights consistency index and ratio were found to be 0.08 and 0.074 respectively, lower than 0.1, thus making the weights importance as a reliable and confidently acceptable [164].

Table 5.7: Calculated criteria weights by AHP ($\boldsymbol{\alpha_j}$), Entropy ($\boldsymbol{\beta_j}$), and compromised weighting ($\boldsymbol{w_j}$) methods.

Weights	**Young Modulus**	**Yield Strength**	**Shear Modulus**	**Density**	**Cost**
α_j	0.3700	0.4162	0.0692	0.1112	0.0335
β_j	0.2342	0.2077	0.2390	0.1608	0.1584
w_j	0.4072	0.4062	0.0777	0.0840	0.0249

The TOPSIS ideal, nadir solution, closeness and ranking for the material selection process is shown in Table 5.8. It is clearly and broadly evident that the toped rank material in terms of strength is 'BioDur 108' which matches the CES selection chart (see Figure 5.2), followed by 'AISI 316lvm, 329 and 446' (see Table 5.3). For aluminium variants ranking, it is found the AL 5182 is a better candidate same as found in CES tool (see Figure 5.5). Comparing the polymeric materials, TOPSIS method found PA66-40lcf as the stronger material than others which matches the CES selection (see Figure 5.8), however, during the CES selection process, this material was dropped due to its comparatively higher cost. PA66-60gf was then selected which TOPSIS method also highlights as the second-best material.

Table 5.8: TOPSIS ideal and nadir solutions, closeness and ranking for material selection.

Materials	Ideal solution S_i^+	Nadir solution S_i^-	Closeness C_i	RANK
S.S BioDur108	0.0014	0.3105	0.9954	**1**
S.S AISI 446	0.2201	0.1541	0.4117	**4**
S.S AISI 316	0.2322	0.1481	0.3895	**5**
S.S AISI 316L	0.2369	0.1472	0.3833	**7**
S.S AISI 317	0.2345	0.1448	0.3817	**8**
S.S AISI 317L	0.2376	0.1488	0.3850	**6**
S.S AISI 329	0.1709	0.1755	0.5066	**3**
S.S AISI 316Lvm	0.1091	0.2142	0.6626	**2**
AL 5182	0.2247	0.0875	0.2803	**9**
AL 2014	0.2263	0.0868	0.2773	**10**
AL 206	0.2336	0.0795	0.2540	**11**
PP-50lgf	0.2948	0.0212	0.0671	**15**
PA66-60gf	0.2711	0.0429	0.1365	**13**
PA66-60lgf	0.2810	0.0331	0.1054	**14**
PE-HD-30gf	0.3103	0.0146	0.0449	**16**
PA66-40lcf	0.2561	0.0551	0.1771	**12**

Conclusively, TOPSIS method results significantly matches the results of the CES selection tool and thus validates its material selection process. However, TOPSIS method was found to be computationally and timely expensive than the CES tool and was limited to a few number of materials (alternatives). On the other hand, CES tool produced interactive selection charts and convenient user interface with a database of around 4000 materials. Furthermore, TOPSIS method is not a material database compared to CES tool.

5.2.4 FE Results of Pump Components Using Selected Materials

5.2.4.1 Piston and Shaft Assembly using Aluminium and Steel Alloy Grades

The FEA was conducted for piston shaft assembly using the shortlisted materials from variants of stainless steel (S.S) and aluminium (AL) alloy grades. It was assumed to use same material for each part similar to the FE setup done in initial static structural simulations carried out in Chapter 4 (see Section 4.2). The results comprising of stresses and deformations with selected materials are presented in Table 5.9. It can be observed from the tabular results that the stresses are almost same for the materials, the small difference is due to the Poisson's ratio i.e. lower the Poisson's ratio, lesser are the deformations and thus higher stresses. The results show that aluminium grades yielded higher deformations compared to steels due to lower shear and Young's moduli. These values are within the tolerances limit (1.5 mm, see Chapter 3) and are acceptable when compared with other pump related FE based product design and experimentally evaluated studies such as 0.233 mm [51] and 3 mm [48]. Within the steel groups, it is seen that AISI 317L has lower deformation compared to AISI 446 which is due to lesser Poisson's ratio. However, it has lower ductility index compared to AISI 446 (see Table 5.3). The same was judged for aluminium alloys AL 2014 T6511 and AL A206 T7 where the deformation in AL 2014 is lesser than AL 206, but, ductility index of AL 2014 is lesser than AL 206.

Table 5.9: FEA results of piston shaft assembly with selected materials.

Material / Property	E (GPa)	ϑ	σ_{yield} (MPa)	Piston Mass (kg)	Shaft Mass (kg)	Piston Deform. (mm)	Shaft Deform. (mm)	Shaft Equiv. Stress (MPa)
ANSYS default S.S	193	0.31	207	1.388	1.013	0.34084	0.46124	147.4
Stainless Steel Selected Materials								
S.S BioDur 108	200	0.299	1370	1.368	0.998	0.33614	0.45555	148.48
S.S AISI 446	200	0.279	310.24	1.343	0.98	0.33248	0.44984	149.02
S.S AISI 316	196.8	0.269	252.1	1.428	1.042	0.33545	0.45364	149.14
S.S AISI 316L	197.36	0.269	229.6	1.428	1.042	0.33457	0.45245	149.15
S.S AISI 317	192.96	0.269	241.2	1.428	1.042	0.34213	0.46268	149.1
S.S AISI 317L	200	0.269	226	1.428	1.042	0.33025	0.44662	149.18
S.S AISI 329	196.36	0.269	547.72	1.398	1.019	0.33626	0.45474	149.14
S.S AISI 316Lvm	187.5	0.33	848	1.432	1.045	0.36598	0.49626	148.15
Aluminium Selected Materials								
AL 5182	70.28	0.329	392.5	0.475	0.347	0.96694	1.312	145.78
AL 2014 T6511	75.87	0.336	375	0.5	0.365	0.90024	1.2218	145.87
AL A206 T7	70.22	0.329	345	0.501	0.366	0.96776	1.3132	145.78

The FE results of one of the selected materials 'AISI 446' are presented in Figure 5.10.

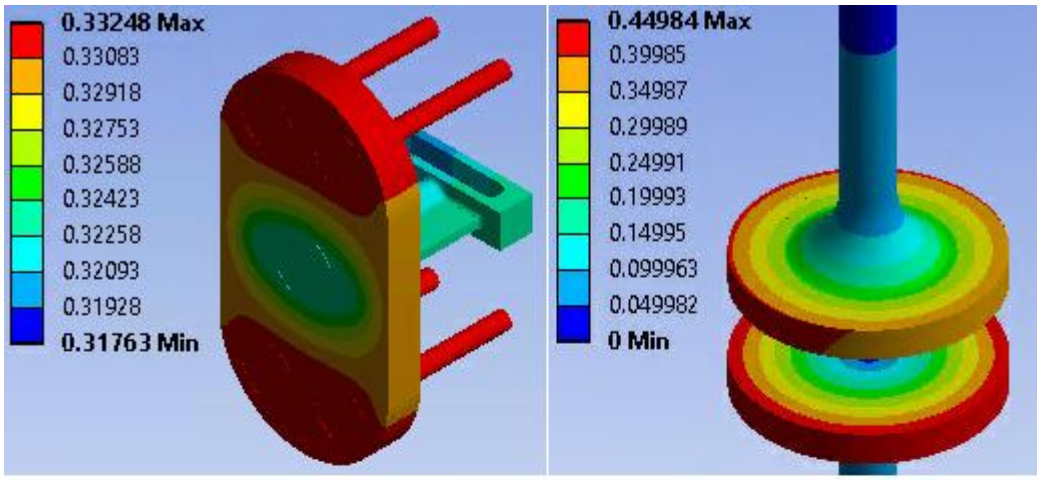

(a) Deformations in piston and shaft

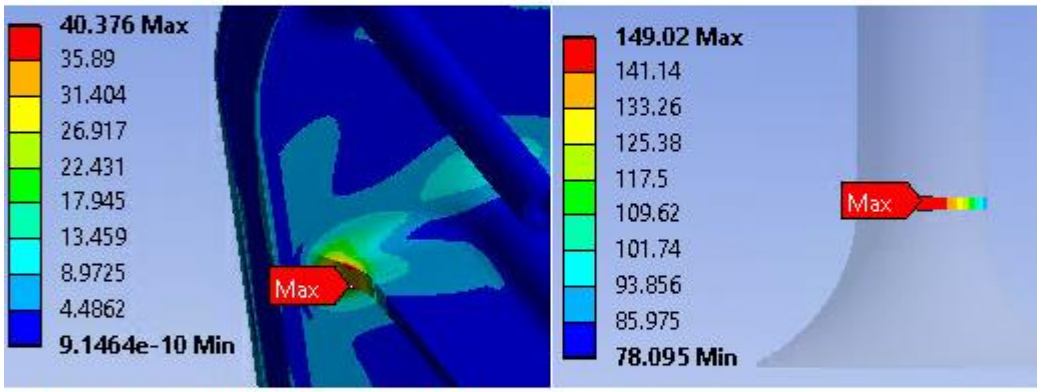

(b) Stresses in piston and shaft

(c) Fatigue safety factor for maximum stress in shaft

Figure 5.10: FE Results, (a) total deformation – mm, (b) equivalent stress – MPa, and (c) safety factor of piston-shaft assembly for AISI 446 stainless steel material.

A detailed chart highlighting the maximum equivalent stresses and deformations in the components with respect to Poisson's ratio of steel and

aluminium alloy variants is shown in Figure 5.11. It is evident from the graph that the maximum stresses for all materials are lower than the yield strengths (highlighted with red markers), (excluding the contact region which is discussed later in next section). Comparatively, significant deformations are seen in aluminium alloy grades which is due to lower modulus of elasticity (lower material stiffness) as evident in Figure 5.12. The shaft total deformations are basically the rotation of the shaft on its rotating axis due to slight backward motion of the piston when the load acts on it. The Figures 5.11 and 5.12 reveals that materials with high modulus and lower Poisson's ratios do not exhibit higher deformations as compared to aluminium alloys which have lower modulus and higher Poisson's ratios. These two properties are responsible for the stiffness in the materials. It is also evident that the stresses in aluminium alloys are slightly lower than steels due to being less stiff which adds more flexibility in the material.

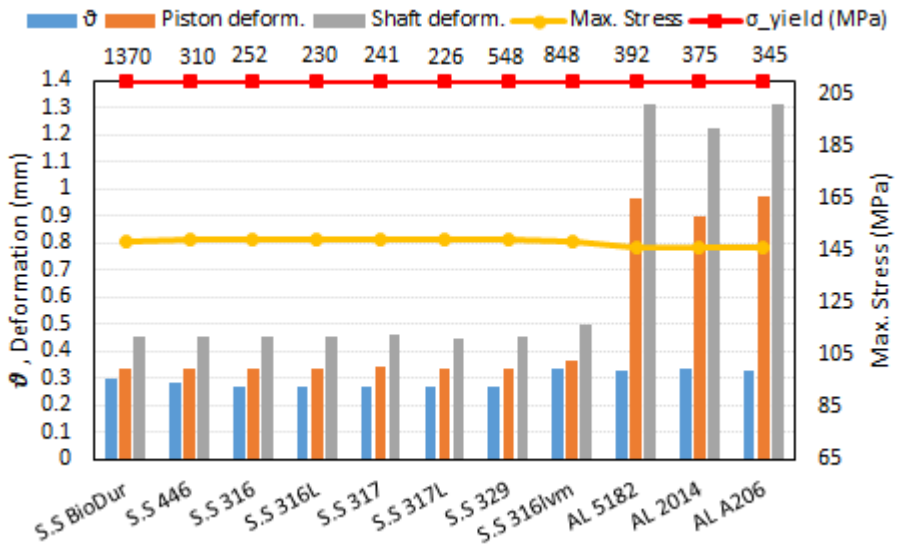

Figure 5.11: FE Results comparison of piston shaft assembly with selected materials with respect to yield strength.

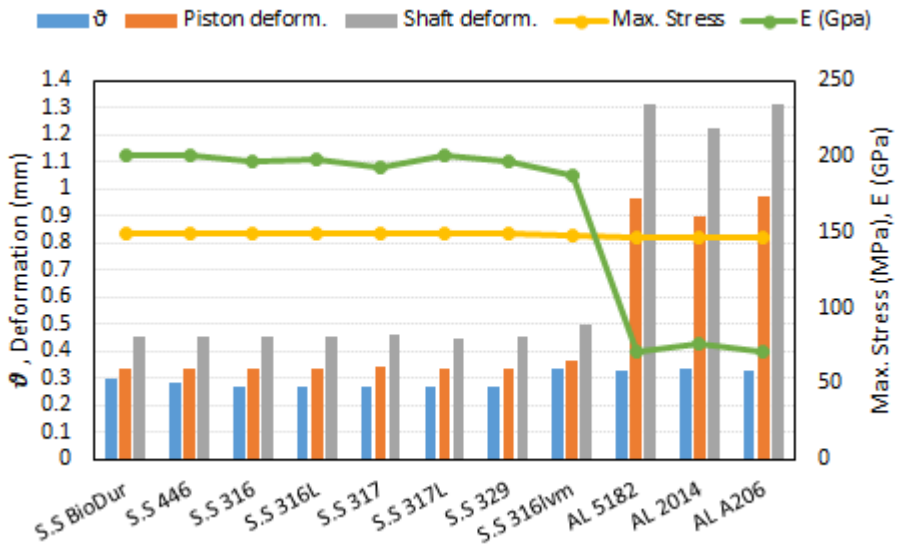

Figure 5.12: FE Results comparison of piston shaft assembly with selected materials with respect to Young's modulus.

The fatigue life safety factor was also evaluated to confirm maximum life (1e8 cycles from CES tool) operation for these components based on selected materials. The fatigue safety factor was evaluated against the yield and endurance limits of the materials (based on Soderberg criteria) [124]. The safety factor evaluation yielded that all selected materials were correctly shortlisted as the factor values are above 1, and are able to withstand the applied loading conditions as illustrated on Figure 5.13. It is also evident that among the performance in terms of safety factors of AISI BioDur 108, 316lvm, 329 and 446 are better than most currently used materials AISI 316, 316L (see Table 5.2).

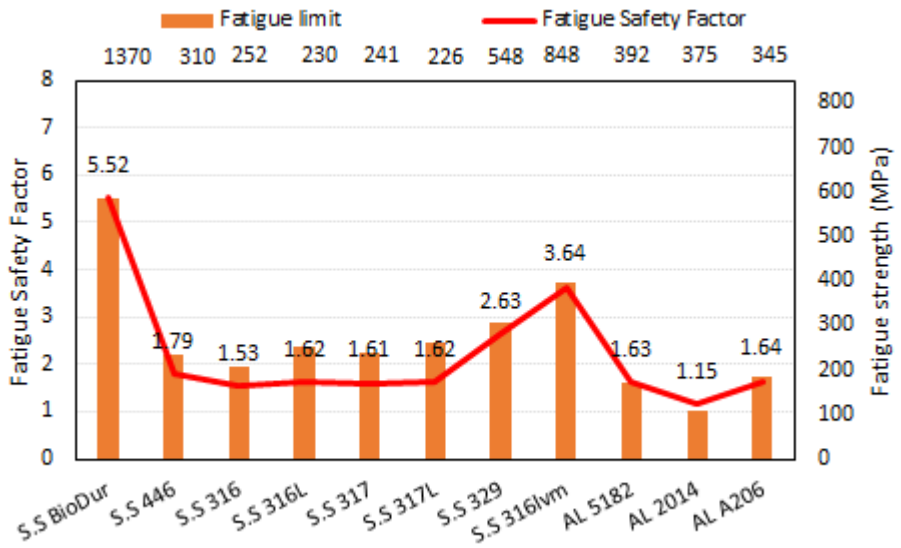

Figure 5.13: FE Results comparison of piston shaft assembly with selected materials with respect to minimum fatigue life safety factor.

5.2.4.1.1 Piston-Shaft Contact Analysis

The contact region in between the two parts was modelled using 2D model. An illustration of 'AISI 446' FE results is presented on Figure 5.14. The results show that the contact stress around 610 MPa is much higher than the yield strength of this material (310 MPa), however, since the loading is not reversed (depicting the pumping operation) then the mean alternating stresses are reduced to half for which the fatigue contact safety factor value is found to be 0.76 which is below 1 which means that the contact region cannot withstand the maximum life cycles (1e8 cycles) but could have attained the maximum life cycles or safety factor value of 1 only if the loading head was about 95 m. However, based on the actual contact yield criteria (see Section 4.1), the safety factor is found to be 0.91 as the contact yield strength is 555.5 MPa. The safety factor is still below 1, this is because of the shaft slider diameter which is

10 mm. The contact stresses and fatigue safety factor for other materials for 10 mm slider diameter are plotted in Figure 5.15. It is also observed that only AISI BioDur 108, 316lvm, 329 and AL206 pass the fatigue criteria. This implies that AISI 446 cannot achieve maximum life during the operation of the pump under the applied loading and with 10 mm of slider diameter. Thus, implementation of fatigue analysis proved an important factor in material selection process.

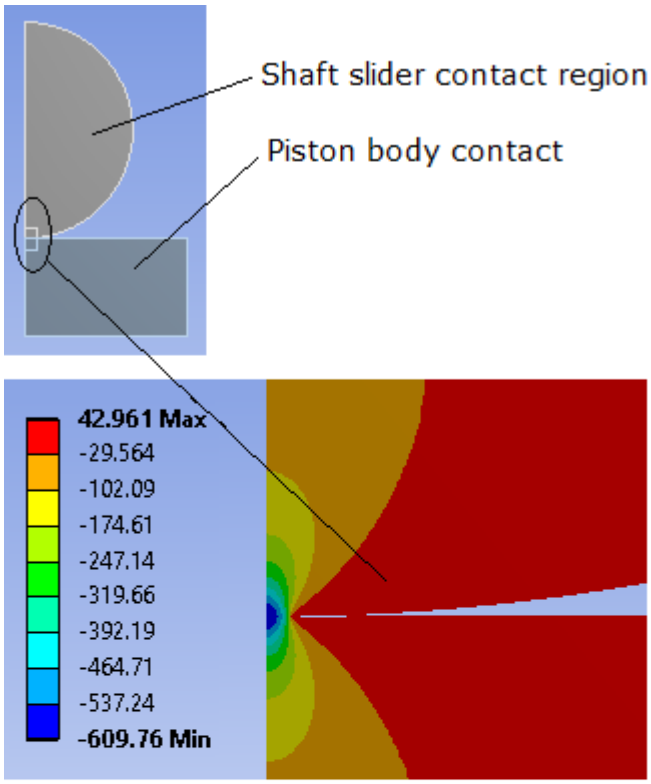

(a) Contact stress contours

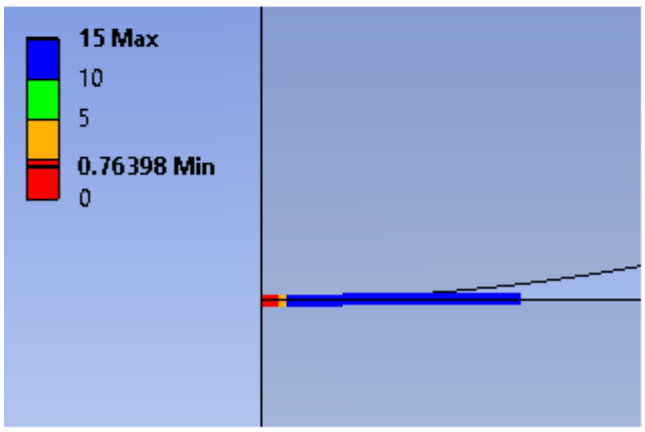

(b) Safety factor at contact

Figure 5.14: FE Results (a) contact stress – MPa, (b) fatigue safety factor of piston shaft assembly contact region for AISI 446 stainless steel material (slider diameter 10 mm).

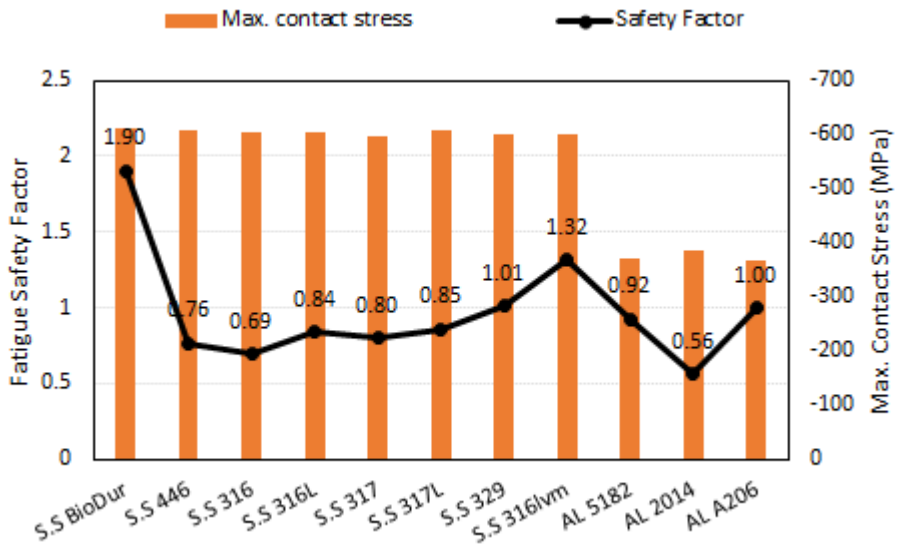

Figure 5.15: FE results; contact stress and fatigue safety factor of piston shaft assembly contact region with selected materials with 10 mm slider diameter.

However, optimising the slider diameter would certainly increase the fatigue safety factor value with AISI 446, such analysis has been conducted in Chapter 6. Optimising a diametric value of 19 mm (as per the ball bearings diameter [94]), the safety factor value reaches 1.05 with stresses reducing up to 444.8 MPa. While based on contact yield strength the safety factor reaches 1.25. This means with AISI 446 material and slider of 19 mm, maximum life cycles can be achieved with 200 m loading head. The contact stresses and safety factor for other materials with optimised slider diameter are plotted in graph shown in Figure 5.16. Furthermore, it is worth noting that the contact safety factor is much lower than the other regions of piston-shaft assembly, see Figure 5.17 reflecting on the importance of this region. Conclusively, the FE analysis of piston-shaft assembly was split into two separate analysis (1) with non-contact region and (2) contact region only. For the non-contact region analysis, no significant differences were observed in the stresses result outcome among the same materials group due to geometry being the same. The maximum stresses

were found to be lower than the yield strengths of all the materials, suggesting the safe design with the selected materials.

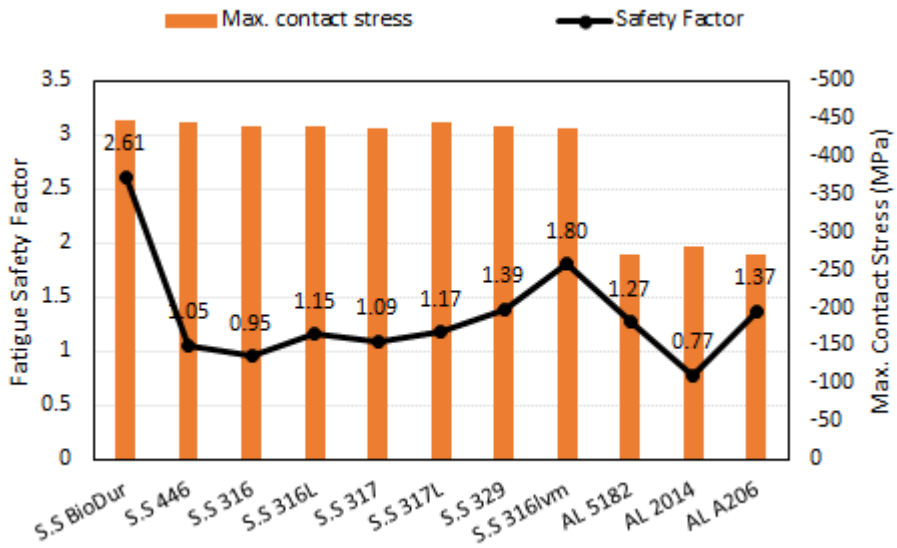

Figure 5.16: FE results; contact stress and fatigue safety factor of piston shaft assembly contact region with selected materials with optimised slider diameter.

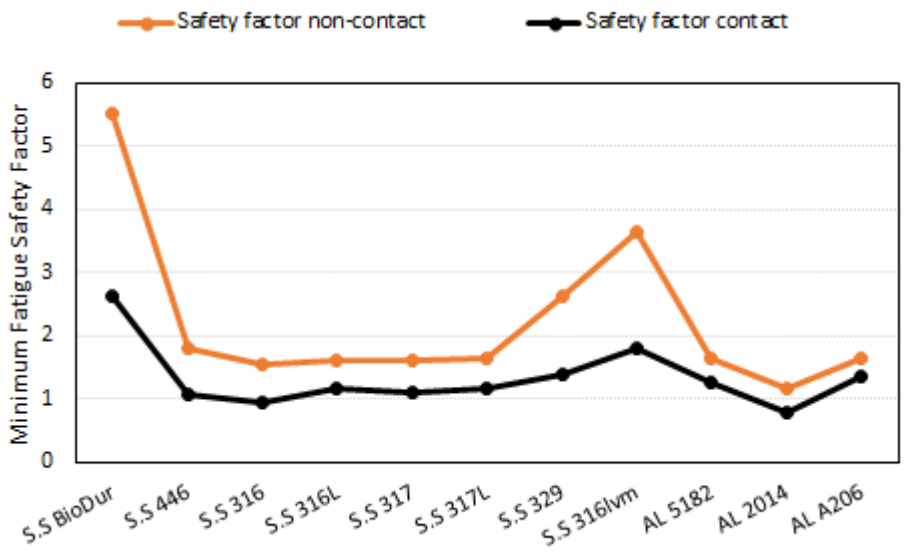

Figure 5.17: Minimum fatigue safety factors comparison of piston shaft assembly with and without contact region with optimised slider diameter with selected materials.

Higher safety factors were found for high strength stainless steel grades such as AISI BioDur108, 316Lvm, 329 and 446. This further validates CES material selection process with the same rankings for these materials which is also validated by TOPSIS method. The selection of AISI 446 based on lighter, cheaper and reasonably stronger material is thus also proved to be valid compared to BioDur108, 316Lvm and 329 based on the applied loading conditions. However, higher strength materials could be used if the loading is further increased, which gives a flexibility in this material selection process. Some aluminium grades also stood as reasonable candidates for the piston and shaft components. Thus, this analysis predicts that selected materials stainless steel AISI 446 and aluminium A206 T7 are safe for the piston shaft assembly with an optimised slider diameter.

5.2.4.2 Main Casing Body using Selected Materials

The FE deformations with respect to Poisson's ratio for all materials; stainless steel, aluminium and composite grades are presented in Figure 5.18. The chart also illustrates the mass of the casing with respect to the material. It was observed that deformations were insignificant under steel variants below 0.02 mm, slightly increased with aluminium grades still under 0.05 mm, but significant with polymers materials. The highest was seen with polyethylene PE-HD/30gf (30% glass fibre) around 0.53 mm. The best material among polymers was found to be polyamide PA66-40lcf (40% long carbon fibre) with maximum deformation of 0.09 mm. The mass comparison between S.S 446, AL 206 and PA66-60gf shows 63% less weight between aluminium and steel, 77% between

steel and composite, and 38.2% between aluminium and composite, respectively.

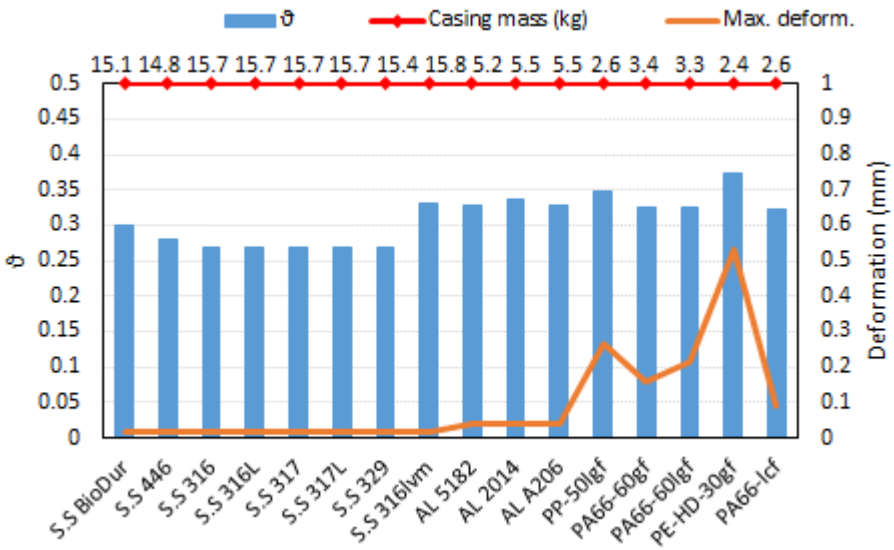

Figure 5.18: FE results comparison of main casing body with selected materials.

The maximum equivalent stress in the casing was found to be around 60 MPa for all the materials which occurs inside the cylinder with slight minimum changes observed due to the changes in the Poisson's ratios, as shown in Figure 5.19.

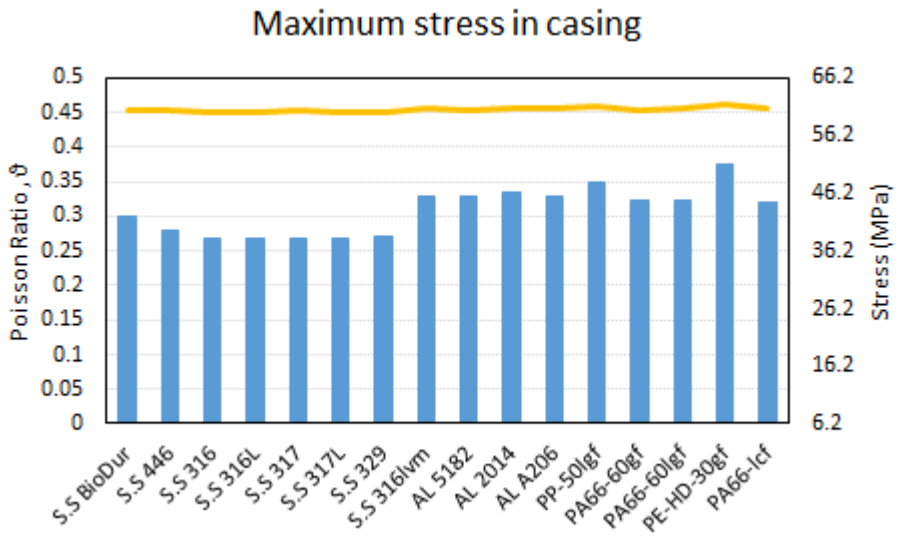

Figure 5.19: Equivalent stress comparison in main casing body with selected materials.

The obtained values of stresses were compared to the yield strengths of each material, however, fatigue life (maximum 1e8 cycles) safety factors found PP-50lgf and PE-HD-30gf polymeric materials failing to the criteria as shown in Figure 5.20. Rest of the materials passed the criteria suggesting safety of the proposed casing design. The performance by long and short fibre composites can also be seen between PA66-60gf and PA66-60lcf where long fibre composite showed relatively lower strength due to lower mechanical properties (see Table 5.5). However, composite materials would not be suitable for casing cylinder and would create operational hindrances in the pump e.g. the piston being metallic alloy sliding on the polymeric cylinder would cause wear. Also, most common pump materials for moving parts i.e. piston, shaft and casing are found to be same and are metals (see Table 5.2). The FE results of pump main casing with one of the selected materials 'AISI 446' are presented in Figure 5.21. The maximum stresses occurred at the very edge of the cylinder which is considered

as a singularity point in a FE analysis, hence the actual stresses are found just near to the maximum point to be 60.48 MPa.

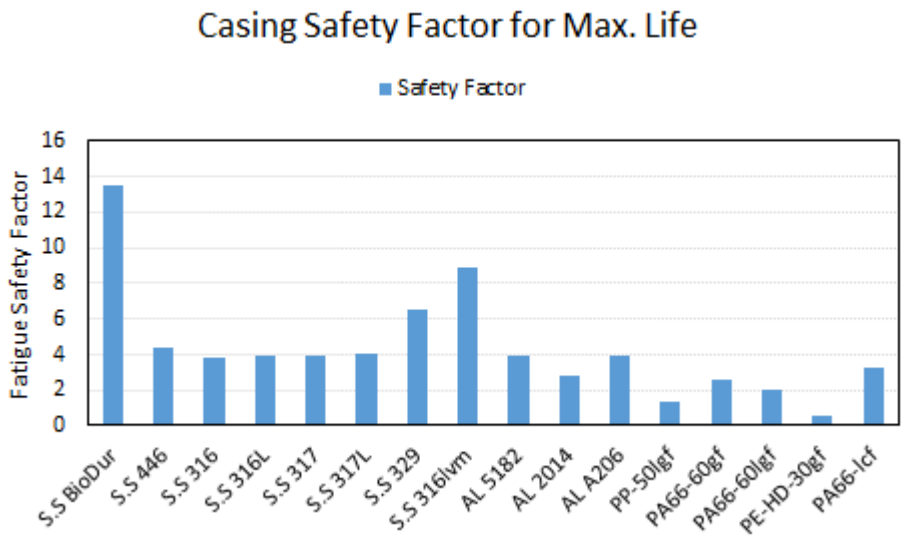

Figure 5.20: Fatigue safety factors for main casing with selected materials.

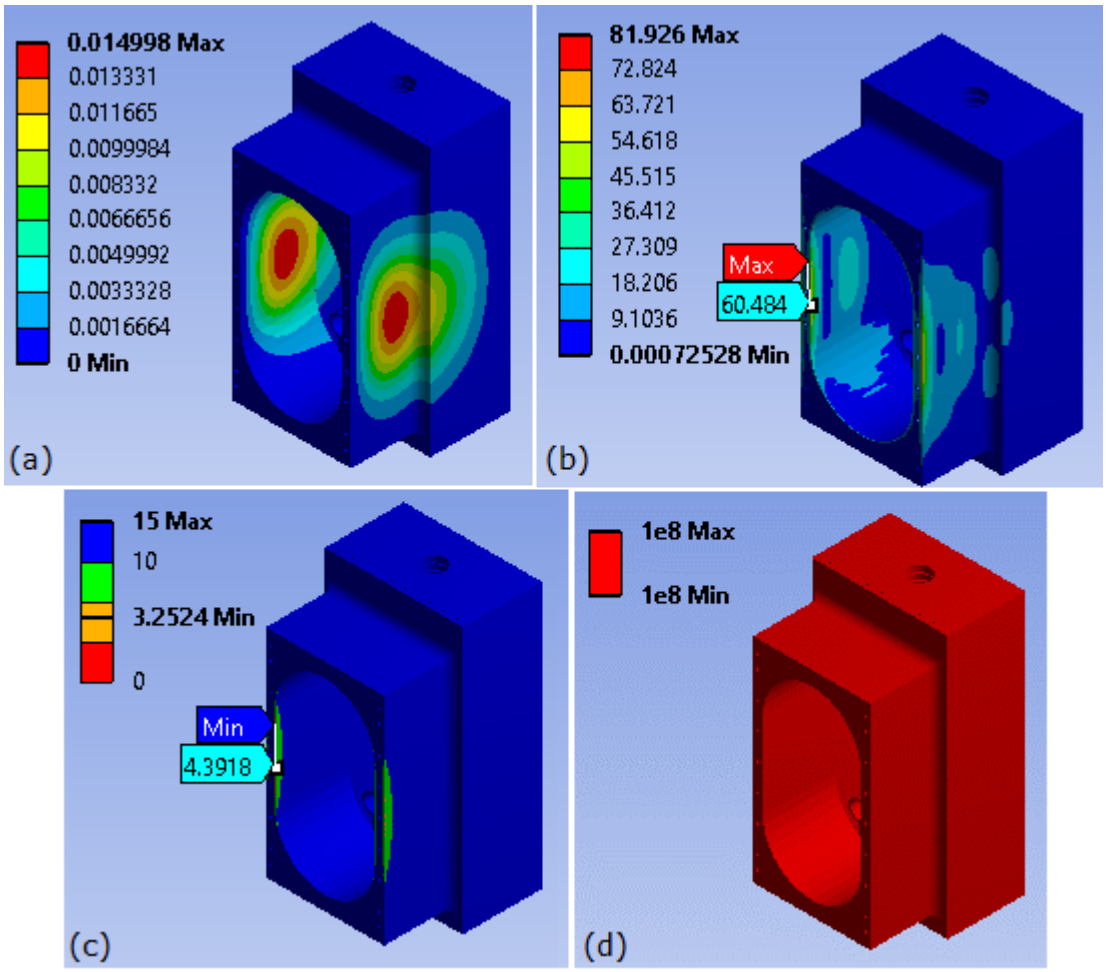

Figure 5.21: FE Results (a) total deformation – mm, (b) equivalent stress – MPa, (c) safety factor and (d) life – cycles, of main casing with AISI 446 stainless steel material.

5.2.4.3 Casing Covers with Selected Materials

The front cover (also the flow manifold) and back cover of the casing were simulated with selected materials under the same loading parameters and boundary conditions as were adopted for the other components i.e. the load of water weight for the applied head. Like the main casing body, the deformations and stresses in the components were seen following the same pattern. The deformations and stresses calculated by the FE simulation for front and back

covers are presented in Figure 5.22 and Figure 5.23 respectively. The masses of the covers are much lower with composite materials e.g. with PA66-60gf weight of front cover reduces up to 77.78% (compared to S.S 446) and 40% (compared to AL 206), and for back cover 76.67% and 36.36%, respectively.

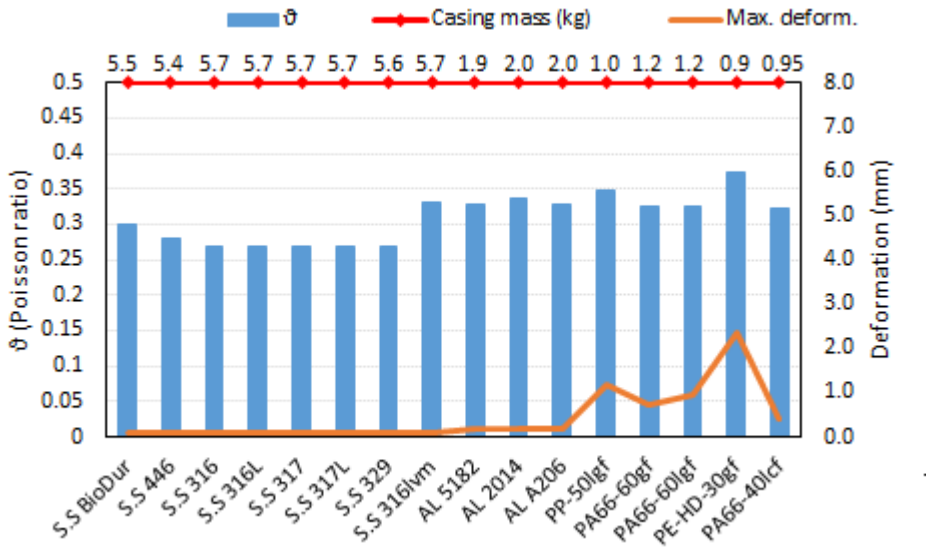

Figure 5.22: FE results comparison of front casing cover with selected materials.

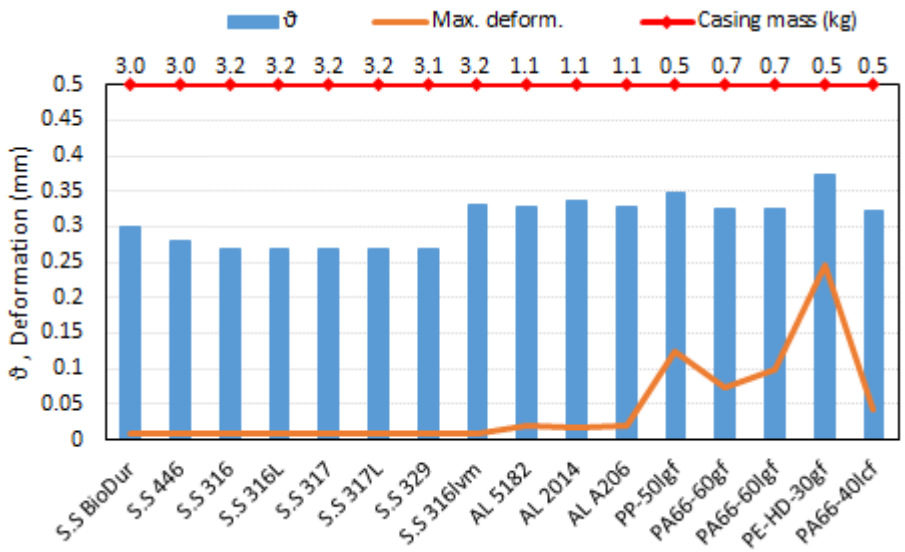

Figure 5.23: FE results comparison of back casing cover with selected materials.

By comparing the two graphs, it is observed that the front and back casing covers have insignificant deformations with stainless steel and aluminium variants within 0.1 mm, whereas contrary to that, significant deformations were seen with the polymers specifically PP50-lgf and PE-HD-30gf, and may not be suitable due to deformations greater than 0.1 mm specifically in the back cover where deformations will cause the pump shaft to be fluctuating which is certainly not desirable.

The equivalent stresses produced in front and back covers are found to be almost same among individual material groups, although small variations are due to the Poisson's ratios of materials, as illustrated in Figure 5.24 and Figure 5.25, respectively.

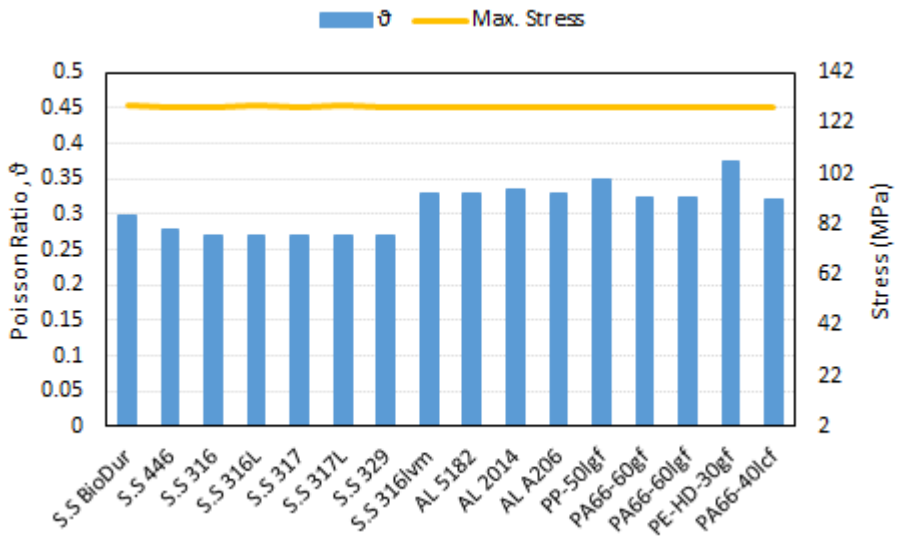

Figure 5.24: Equivalent stress comparison in casing front cover with selected materials.

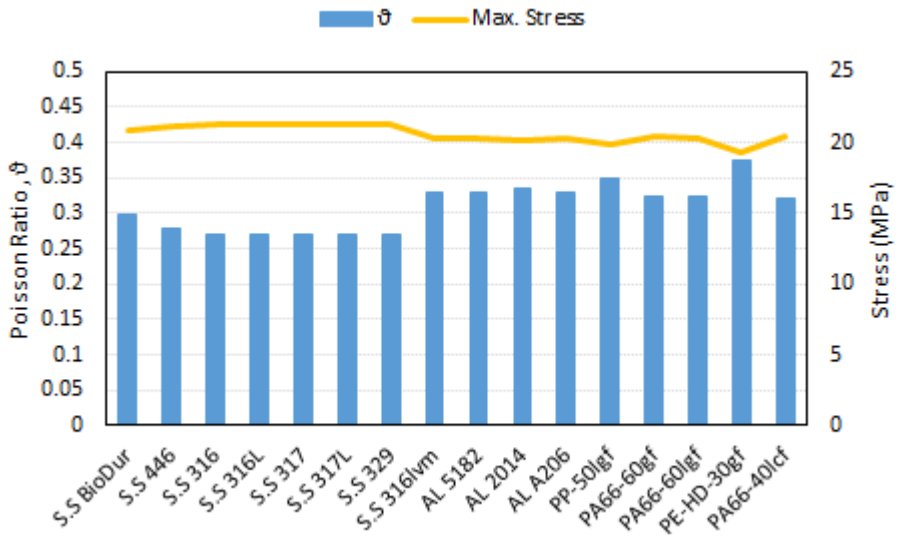

Figure 5.25: Equivalent stress comparison in casing back cover with selected materials.

The fatigue life safety factors were also evaluated for the selected materials to ensure the maximum operational life for the components. Figure 5.26 and 5.27 shows the minimum safety factor for front and back covers respectively. Composite materials PP-50lgf and PE-HD-30gf were observed to be not meeting the maximum fatigue life particularly with the front cover where front manifold thickness of 4 mm was used compared to back cover thickness of around 10 mm. Similar trend is seen for long and short fibre composites as observed in the main casing results. PA66-60gf performs better than PA66-60lgf. The composite materials with fatigue life above unity are safe for the front manifold but are not recommended to be used with back cover to avoid minute fluctuations in the shaft motion.

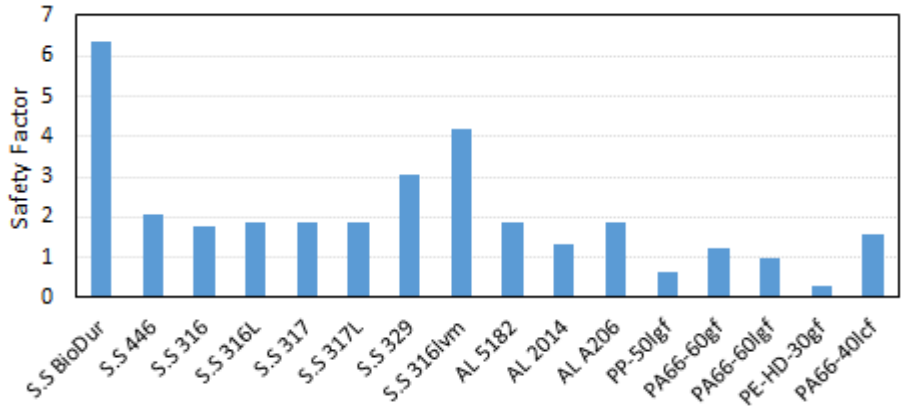

Figure 5.26: Minimum safety factors comparison of casing front cover with selected materials.

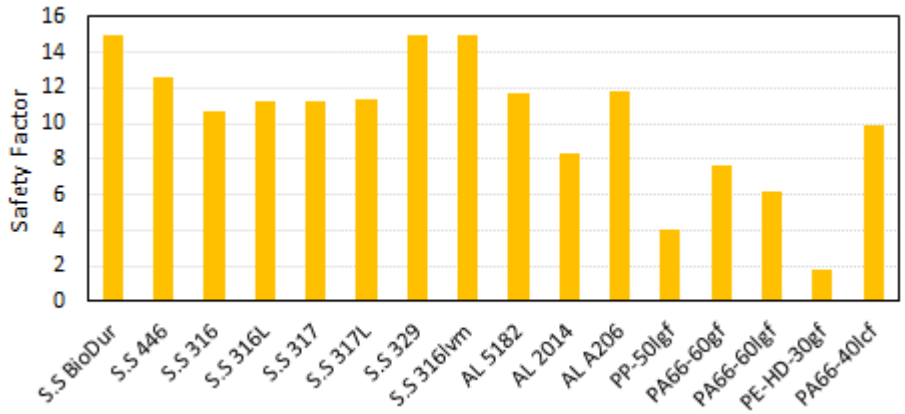

Figure 5.27: Minimum safety factors comparison of casing back cover with selected materials.

An illustration of the FE results for the front and back casing covers with stainless steel material AISI 446 is presented in Figure 5.28 and Figure 5.29 respectively. The maximum deformation occurs at the front manifold area which is expected while the maximum stresses are found at the inner surface of manifold. Additionally, as expected the minimum fatigue life safety factor was found to be at the maximum stress areas. The back-cover results reveal much lower stresses and deformations due to higher thickness value of 10 mm.

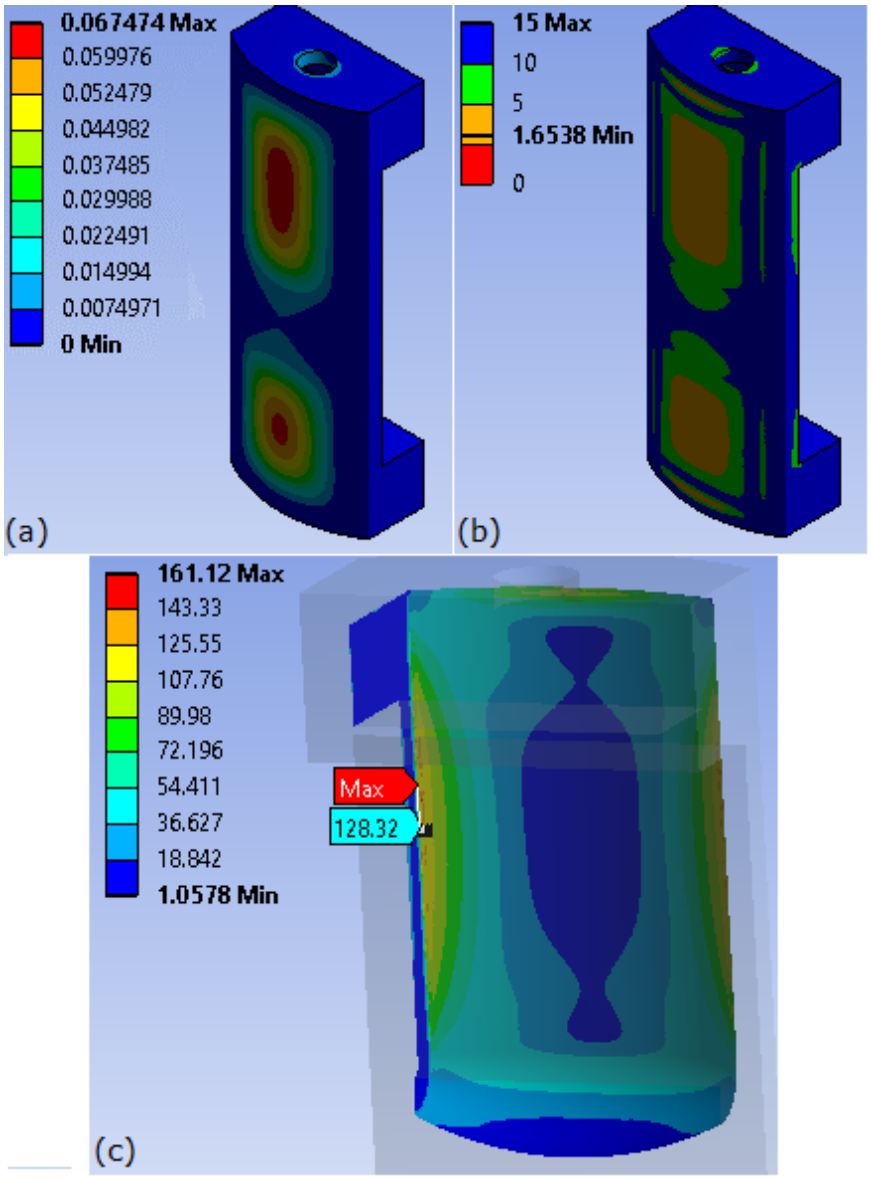

Figure 5.28: FE results of casing front cover (a) deformation – mm, (b) fatigue safety factor and (c) maximum stress – MPa with AISI 446 material.

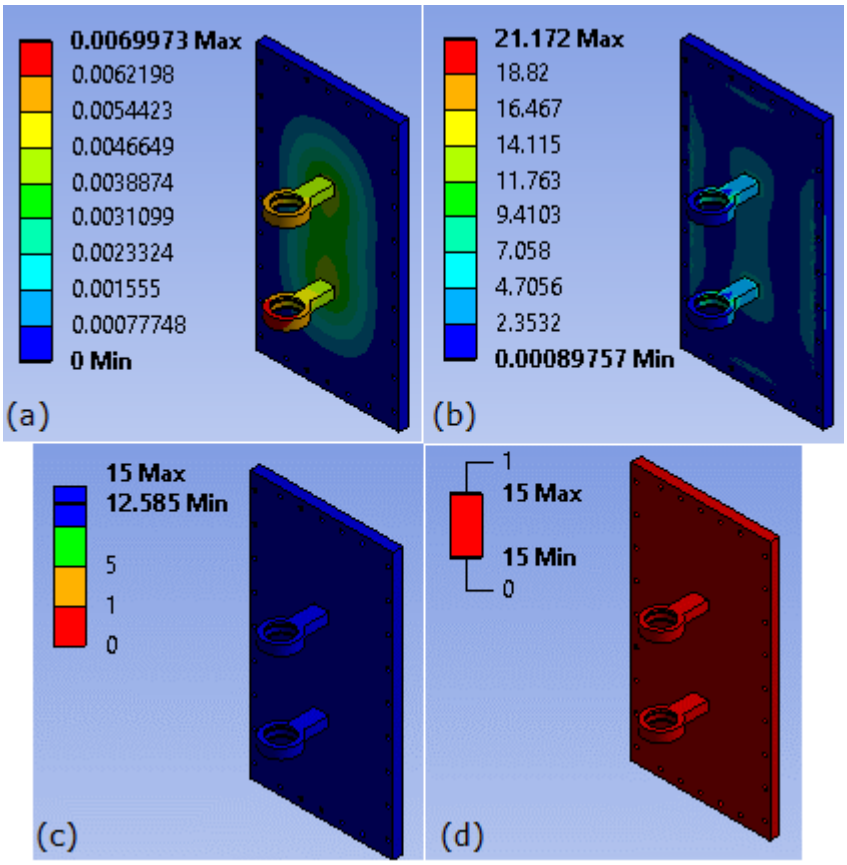

Figure 5.29: FE results of casing back cover (a) deformation – mm, (b) maximum stress – MPa (c) fatigue safety factor and (d) fatigue life with AISI 446 material.

Conclusively, the material selection process adopted in this study for concept pump components initiates by screening common materials through literature (handbooks and commercial data) and details through using CES Selector database only based on various optimisation factors and properties trade-offs until opting out best candidates without using any other methods [65] (saving computational time). The CES data validity with the commercial data proved to strengthen confidence in the database usage. Finally, the material selection was validated with TOPSIS (weighting based on individual material properties not performance indices) and FE analysis (fatigue based) for all

selected materials. This method is different from studies found in the literature as it incorporates fatigue analysis. For instance, study by Thakker et al. [69] first, splitting the material selection into stages with CES database used for broad screening only (density and strength). A ranking list is then prepared with additional MCDM methods using further performance criteria (corrosion, weight), and finally FEA is carried out only for the selected material without fatigue analysis [69]. Similarly, study by Ermolaeva et al. [70] used CES database for material families screening based on mass optimisation indices coupled with weighting factors for ranking (also observed in study by Yazdani and Payam [76]). This creates biasness towards the validity of CES shortlisting and ranking list based on the weights. To avoid biasness, weights should be based on individual properties rather than indices. The FE analysis excluding fatigue analysis was carried out only with the selected material not among all shortlisted materials. Some studies does not even implement FE analysis with the material selection such as [61,65,66]. Hence, this is important because fatigue analysis with selected materials helps in justifying prolong component life than just a yield strength- based analysis where failure may possibly occur at the very next cyclic loading despite being considered safe, and additionally, it strengthens the validation for the material selection process e.g. safety factor evaluation for each component revealed top three candidates as 'AISI BioDur 108, 316 lvm and 329'.

5.2.5 Weight Analysis for Studied Pump Components

The mass of the pump components was compared among the selected materials. Since, piston-shaft assembly is assumed to consist of same material but restricted to stainless steel and aluminium variants only, hence the mass evaluation was also restricted to metals. The casing parts main, body, front and back covers were compared with all materials. The detailed mass comparison of pump components is presented in Table 5.10.

Table 5.10: Comparison of pump mass with selected materials.

	Mass (kg)				
Material	**Piston Shaft**	**Main casing**	**Front cover**	**Back cover**	**TOTAL**
Stainless steel					
S.S BioDur 108	2.366	15.097	5.487	3.023	25.973
S.S AISI 446	2.323	14.819	5.386	2.968	25.496
S.S AISI 316	2.47	15.748	5.723	3.154	27.095
S.S AISI 316L	2.47	15.748	5.723	3.154	27.095
S.S AISI 317	2.47	15.748	5.723	3.154	27.095
S.S AISI 317L	2.47	15.748	5.723	3.154	27.095
S.S AISI 329	2.42	15.412	5.602	3.087	26.521
S.S AISI 316lvm	2.48	15.789	5.739	3.162	27.17
Aluminium Alloys					
AL 5182	0.822	5.246	1.906	1.0507	9.0247
AL 2014 T6511	0.865	5.524	2.007	1.1064	9.5024
AL A206 T7	0.867	5.532	2.011	1.108	9.518
Composites					
PP-50lgf	---	2.622	0.9529	0.5251	4.1
PA66-60gf	---	3.359	1.2209	0.6727	5.2526
PA66-60lgf	---	3.299	1.199	0.6608	5.1588
PE-HD-30gf	---	2.428	0.8827	0.486	3.7967
PA66-40lcf	---	2.598	0.944	0.520	4.026

It is observable from the table data that heaviest mass of pump comes from steels followed by aluminium grades. Steel materials provide higher strength as discussed in previous sections compared to the other groups. The FE simulations results have revealed that the front and back covers for the concept pump could be replaced with the polymeric material for overall lighter weight of the pump as long as they were found to be safe and had a maximum fatigue life.

5.3 Limitation of the study

The material selection process in this study is carried out for the concept pump components. The limitations in this study based on the assumptions taken are;

- Material selection was carried out using CES Selector data which is based on various sources as ranges and averages. Although, CES data being in good agreement with the commercial suppliers' data, yet for actual manufacturing of the pump and its components, real commercial material data sheets should be surveyed for selection and should be used in the simulations. For instance, material cost data is updated every year in CES database [170], which is not the case with often volatile market values, hence, a real-time data from suppliers will positively contribute more to the selection process.
- Further attributes can also be incorporated in the selection such as temperature, environmental factors, etc.

5.4 Conclusion

The CES tool usage was validated in three stages; first with CES data authenticity comparison with commercial data, second with TOPSIS method and finally with FE simulations to come up with best materials for the conceptual pump components. The validation of material selection process three times helps to suggest that the process can be made concrete as it tries to suppress the uncertainty about the best materials outcomes. 'AISI 446', 'AL A206 T7' and 'PA66-60% glass fibre' were selected from the stainless steel, aluminium and composite groups, respectively.

The FE analysis of the concept pump found that a single stainless steel grade is recommended for all the components with lower deformations than aluminium alloys. The analysis suggest that selected materials are able to withstand the 200 m head load with the current pump components design. However, the slider diameter of 10 mm needs to be optimised with materials for maximum durability such as AISI 446 not meeting the fatigue criteria. Thus, implementation of fatigue analysis proved an important criterion in material selection process. Among the metal materials, higher strength is achieved from the steels compromising with mass, much lighter weight is possible with aluminium grades with slight increase in cost. However, the pump casing cover and manifold can be used with composite materials rather than stainless steel to reduce costs and weight of the entire pump (see Table 5.10). The composites experienced high deformations in the casing and casing covers than other class of materials. The casing front (manifold) and back covers are found to be weaker with the composites specifically the PE-HD-30gf and PP-50lgf compared

to metals. The selection process has flexibility to include the materials with much higher strengths depending on the load increment.

The concept pump design is still not optimised for power consumption as the design needs to be optimised for mass. Hence, future recommendations include the geometrical optimisations of the components design with selected materials to optimise the mass, material cost and performance as discussed in Chapter 6.

CHAPTER 6

MASS OPTIMISATION OF PUMP AND ITS COMPONENTS GEOMETRY FOR FATIGUE PERFORMANCE

In this chapter, FE based geometric parametric approach has been used for weight reduction of important conceptual pump components affecting the power consumption i.e. the piston and the shaft, with a constraint of maximum fatigue life, along with material variation incorporated in the analysis to option out suitable materials with respect to geometrical changes. The main objective of this analysis is to optimise the mass of components for low power consumption based on maximum fatigue life by varying parameters i.e. dimensions and materials. The analysis significantly improves associated material cost benefit and energy consumption efficiency by the pump components.

6.1 Optimisation Model Setup

6.1.1 Parametric Optimisation Process Setup for Mass Reduction

In order to optimise the initial design geometries for reducing mass to lessen the power consumption by concept pump moving parts i.e. piston and the shaft, there were two possibilities, one to reduce the initially drafted dimensions, and second to optimise the material of choosing as well i.e. a lighter and high strength material with best possible optimised geometry. To accomplish this goal, an optimisation model was developed which results in the

best combinations of geometrical parametric values among the set of different materials. The shortlisted materials (shortlisted in Chapter 5, see Section 5.2.2) were used in the optimisation model which could further filter out the best material candidates on the account of performance of the pump components i.e. to reduce power consumption. The fatigue life factor was incorporated for materials set and was the main constraint in the geometrical optimisation model for mass reduction. The initially developed FE model of piston-shaft assembly (Chapter 4, see Section 4.2) was incorporated with material and geometrical parameters variation. An overview of the optimisation process is illustrated on Figure 6.1.

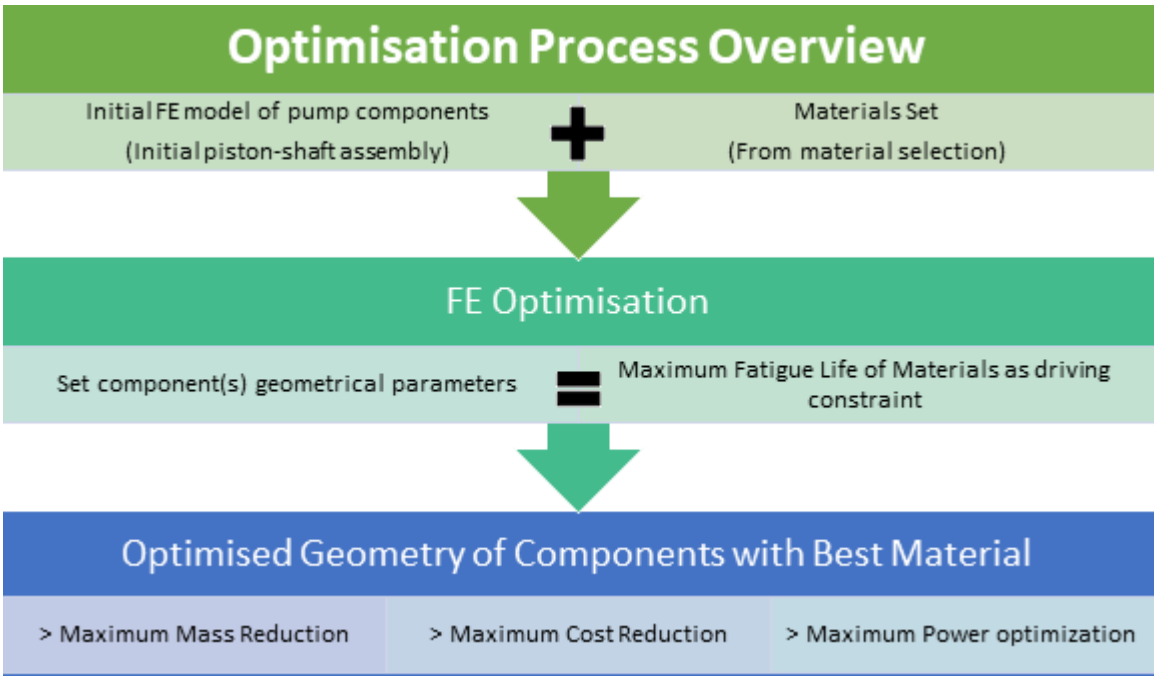

Figure 6.1: Overview of the optimisation process.

The most critical locations with a possibility of significant reduction in material in the piston and shaft components were identified from the initial design simulations and were parameterised to the point of failure i.e. the least

parametric value result should withhold the fatigue endurance limit criteria. These critical locations are:

1. For piston part, the piston head thickness as it is the first to face the load.
2. The shaft main diameter which also bears the maximum stresses. The locations are shown in Figure 6.2.
3. Another critical location in the shaft was found to be the slider which drives the piston. The contact stresses in this component was noted to be significantly high in the FE design results. However, this component was omitted from the mass optimisation due to its very small mass of just 14 g for 10 mm diameter (stainless steel) which would result in insignificant improvement in power consumption. Slider component was however studied for optimum diameter optimisation for sustaining high stresses discussed later in Section 6.2.3.

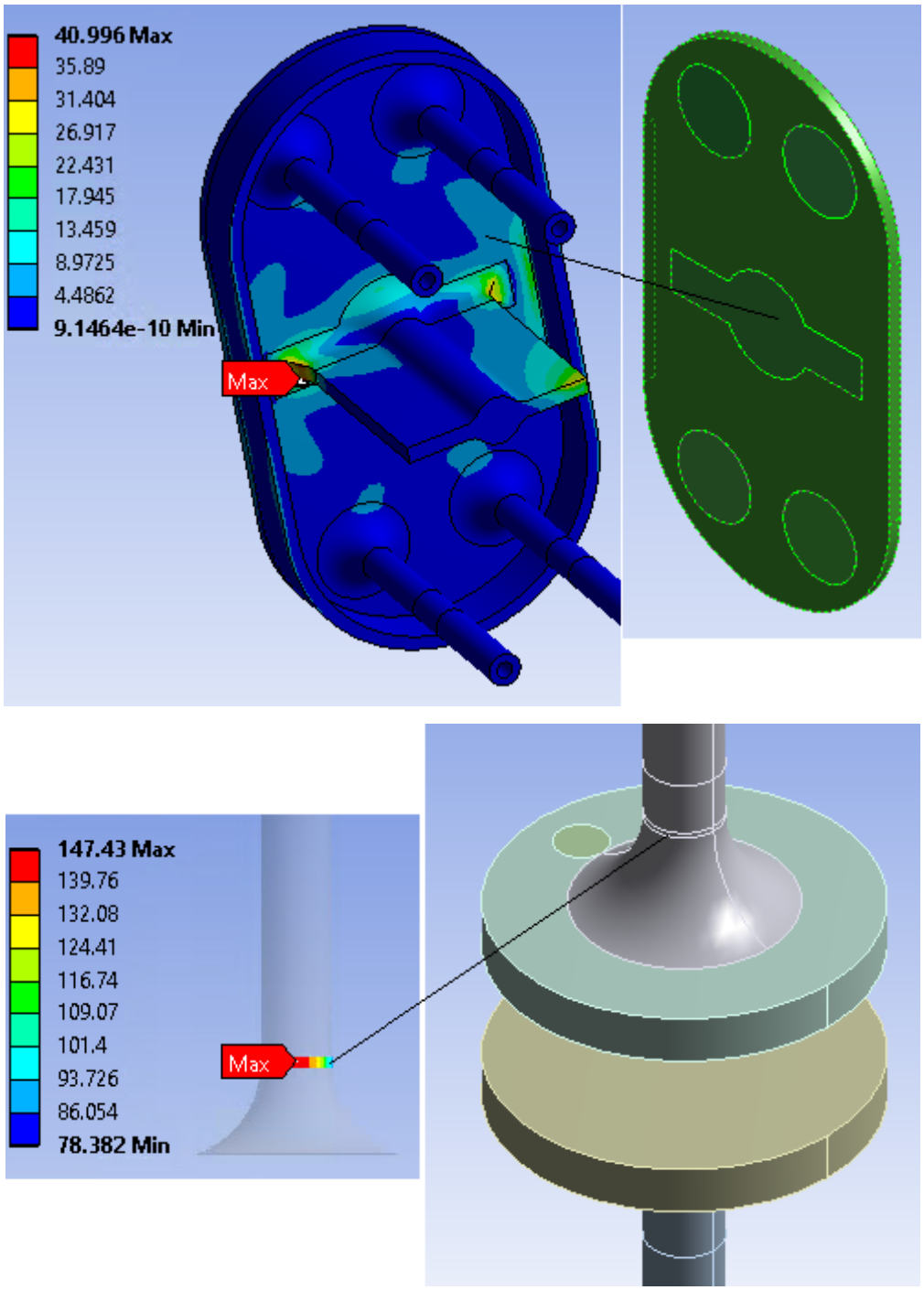

Figure 6.2: Critical location of piston and shaft components for optimisation.

Table 6.1: Initial data of piston and shaft critical locations.

Parameter	Initial Value / Material	Maximum Stress	Fatigue Life
Piston Head thickness	4 mm / Steel (ANSYS)	24.81 MPa (On head only)	1e6 cycles (Maximum life)
Shaft Main Diameter	14.5 mm / Steel (ANSYS)	147.43 MPa	3.5845e5 cycles
Shaft Slider Diameter (cylindrical contact with piston body)	10 mm / Steel (ANSYS)	604.45 MPa	6.145e3 cycles

The initial design values of these critical locations and FE results are presented in Table 6.1. Steel was used as the first reference material normally used in pumps for initial FE model.

The optimisation process only involves the geometrical and materials parameterisation. The geometrical parametric values of piston and shaft components are illustrated in Figure 6.3. The individual geometries of piston and shaft components with these parameters were altered in the SolidWorks CAD program and simulated individually. The initial FE model setup of piston-shaft assembly was copied on all geometric alterations.

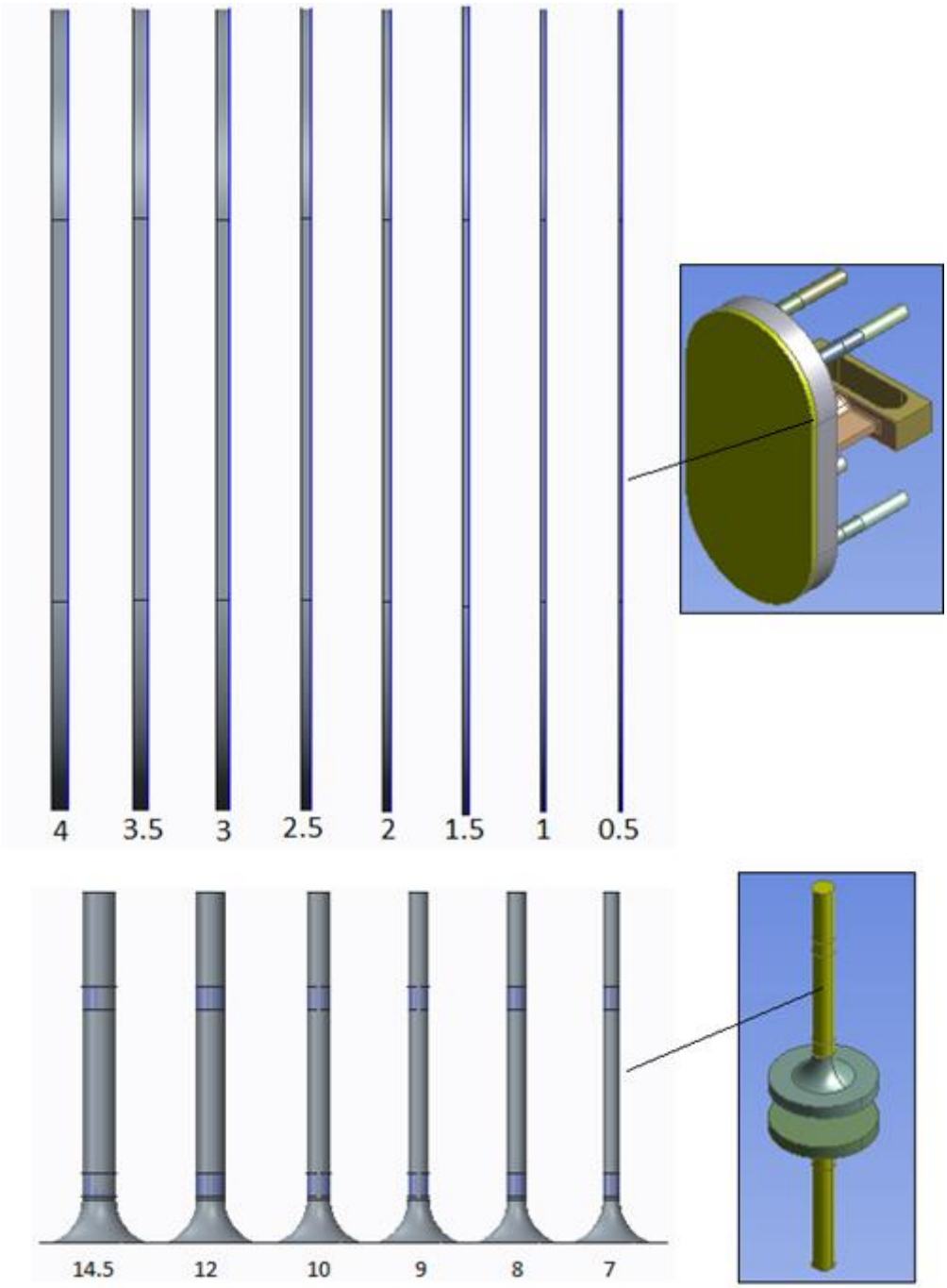

GEOMETRICAL PARAMETERS	
Piston Head thickness	4, 3.5, 3, 2.5, 2, 1.5, 1, 0.5 (mm) A reduction of 0.5 mm in value from initial 4 mm
Shaft Main Diameter	14.5, 12, 10, 9, 8, 7 (mm) Reduction as per available shaft bearing diameters from initial 14.5 mm, and 200 m pump head load [94]

Figure 6.3: Parametric dimension values (in mm) of piston head and shaft main diameter.

The materials properties were input into the optimisation model. The materials fatigue life alternating stress and number of cycles curves (S/N curve) for repetitive loadings were extracted from the CES program and imported to ANSYS FE model database. The simulations were run for each geometric parameter value with selected materials. The materials set fatigue limit data (also called endurance limit) is presented in Table 6.2.

Table 6.2: Materials set data with fatigue limit.

MATERIALS SET (STAINLESS STEEL GRADES)					
Property	**Density (kg/m^3)**	**Young's Modulus (GPa)**	**Poisson Ratio**	**Yield limit (MPa)**	**Endurance limit (MPa) at 1e8 cycles**
SS BIODUR 108	7639.62	199	0.299	1370	585
SS 329	7799.36	196.36	0.269	547.72	305
SS 446	7499.33	199	0.279	310.24	233.5
SS 317L	7969.37	199	0.269	226.03	260.5
SS 317	7969.37	192.96	0.269	241.18	237.5
SS 316	7969.37	196.84	0.269	252.09	208.5
SS 316L	7969.37	197.36	0.269	229.56	253.5
SS 316LVM	7990	187.5	0.33	848	395
MATERTIALS SET (ALUMINIUM ALLOY GRADES)					
AL 5182	2654.88	70.28	0.329	392.49	170.5
AL 2014	2795.64	75.87	0.337	374.98	108.05
AL 206	2799.86	70.22	0.329	344.96	183.6

In order to have a maximum life of the component area being optimised, it was necessary to establish a fatigue life criterion through which all the parametric values must pass. Soderberg criteria was adopted as it calculates the fatigue life based on the yield strength of material, while Goodman on the ultimate strength [120,124]. The reason is because the stresses developed in the component should remain in the elastic region, any stresses above the yield

point would ultimately yield to the deformation (plasticity) and which is not feasible for an optimised design. The Soderberg evaluation of fatigue safety factor is described by equation 6.1.

$$\frac{1}{n} = \frac{\sigma_a}{S_e} + \frac{\sigma_m}{\sigma_y} \tag{6.1}$$

Where,

'n' is the fatigue life safety factor.

'σ_a' is the stress amplitude.

'σ_m' is the mean stress.

'σ_y' is the yield strength of the material.

'S_e' is the fatigue endurance limit of the material.

Zero-based cyclic loading was applied as the stress amplitude which matches the operation of a piston pump where load is exerted only once i.e. in discharge the stroke. In the FE model, the maximum fatigue life of 1e8 cycles was set as the constraint which corresponds to the infinite number of cycles and which is the maximum limit available in the S/N curves for materials in the CES program. The maximum equivalent (von Mises) stresses, fatigue life safety factor and fatigue life cycles were evaluated for the piston head thickness and shaft main diameter locations for each parameter against each material. Any values of the fatigue life below 1e8 cycles were omitted in the shortlisting process as discussed in following section.

6.1.2 Optimisation Procedure for Analysis of Parametric FE Results

The FE parametric simulations (14 geometric parametric values and 11 materials) results of the components obtained were subjected to a filtering process individually, where the parameters not passing the Soderberg fatigue criteria with maximum life of 1e8 cycles were omitted. On the contrary, the parameters passing the criteria were further shortlisted in the process which finds;

(A) Minimum or best parametric value for individual material.

(B) One best parametric value and material among all materials.

(C) One best value more common in the material set per vote count.

The information from point (A) for each component is gathered to further filter out the best combination of parameters and material. This gives one decision of best combined parametric values and one best suitable material. The model further filters out best parameter and material candidates based on minimum mass, cost and higher performance improvement. It finally compares the optimised outcome with initial design.

The main objective of the optimisation process was to reduce the mass of the components. The mass optimisation is linked to the optimisation of material cost and energy (power) involved in the operation of the components. The one best combination of parametric values and material from the filtering process now allow the optimisation model to evaluate the mass, cost and power optimisation by comparing the very first initial design parameters and the optimised ones. The cost calculation is linked to the material cost per unit (kg). The optimised power calculation is linked to the mechanical operation of

components such as piston reciprocates linearly while the shaft rotates. The detailed optimisation process is illustrated as flowchart in Figure 6.4.

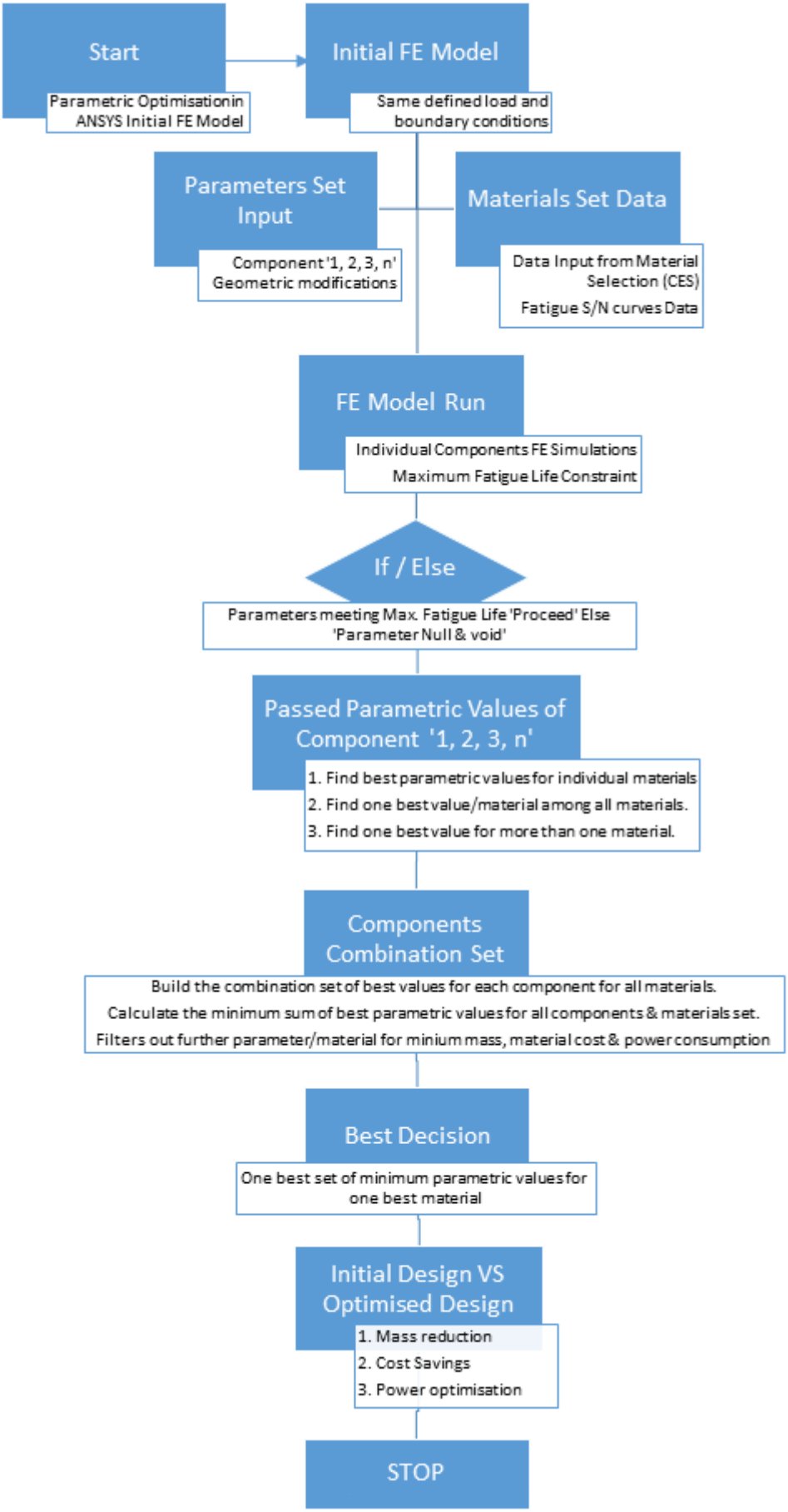

Figure 6.4. Flowchart of geometrical optimisation of piston and shaft components

6.2 Results and Discussions

6.2.1 Piston Head Thickness Parametric FE and Optimisation Results

The FE simulations results for piston head thickness (from 4 to 1 mm) were evaluated for maximum equivalent stress and total deformation presented as Figure 6.5. A linear trend can be seen with stresses and deformation in the initial values of the head thickness compared to the last values among materials. This is because of the effects of FE singularity locations near the piston head and seal web adjacent sharp edges (see Figure 6.2). Due to limited computational resources, higher density of mesh was not possible to obtain in such region. The effects can easily be distinguished between initial 4 mm and 0.5 mm head thickness values, see Figure 6.6.

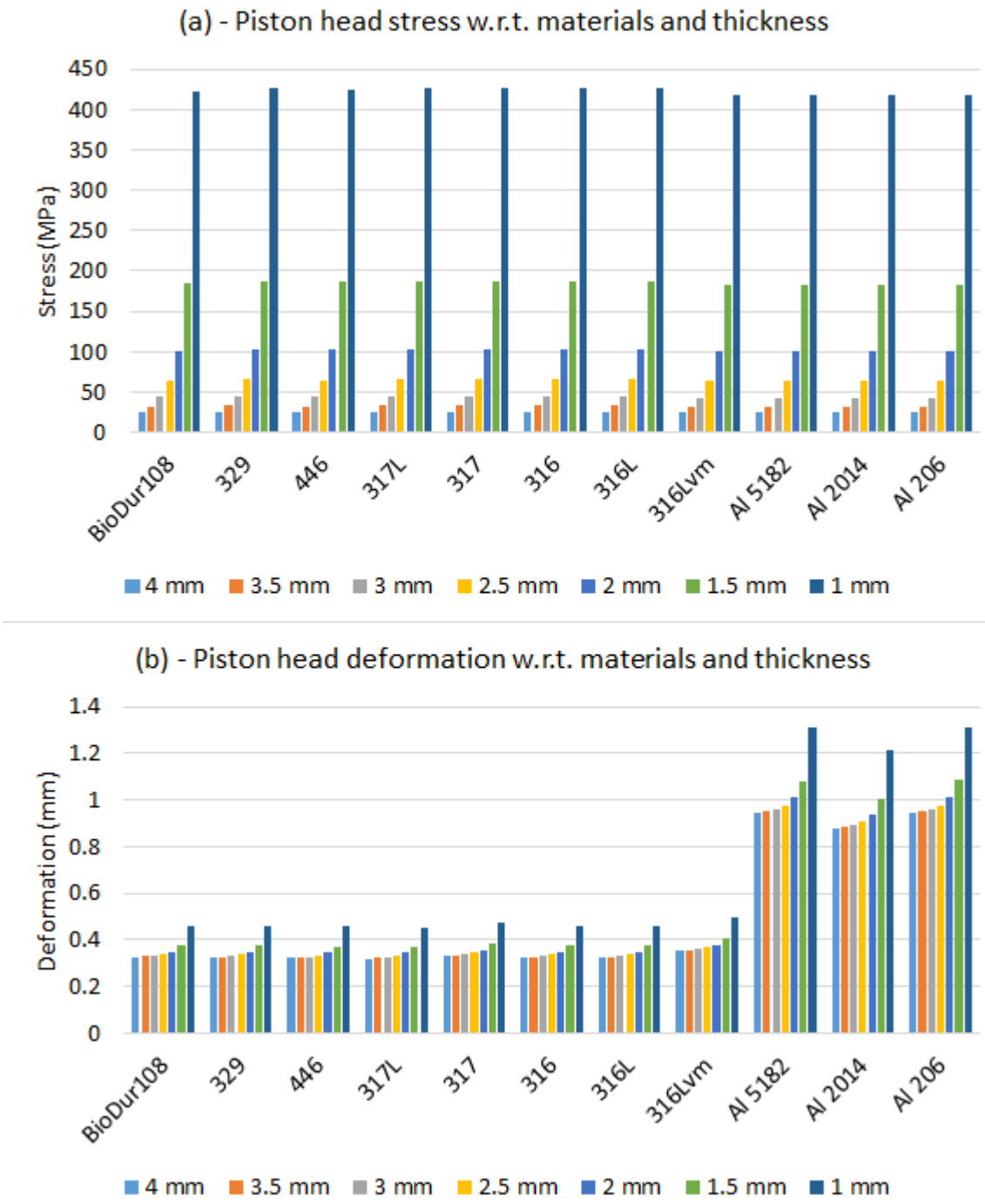

Figure 6.5: Piston head FEA results (a) stresses and (b) deformation w.r.t thickness (4 to 1 mm) and materials.

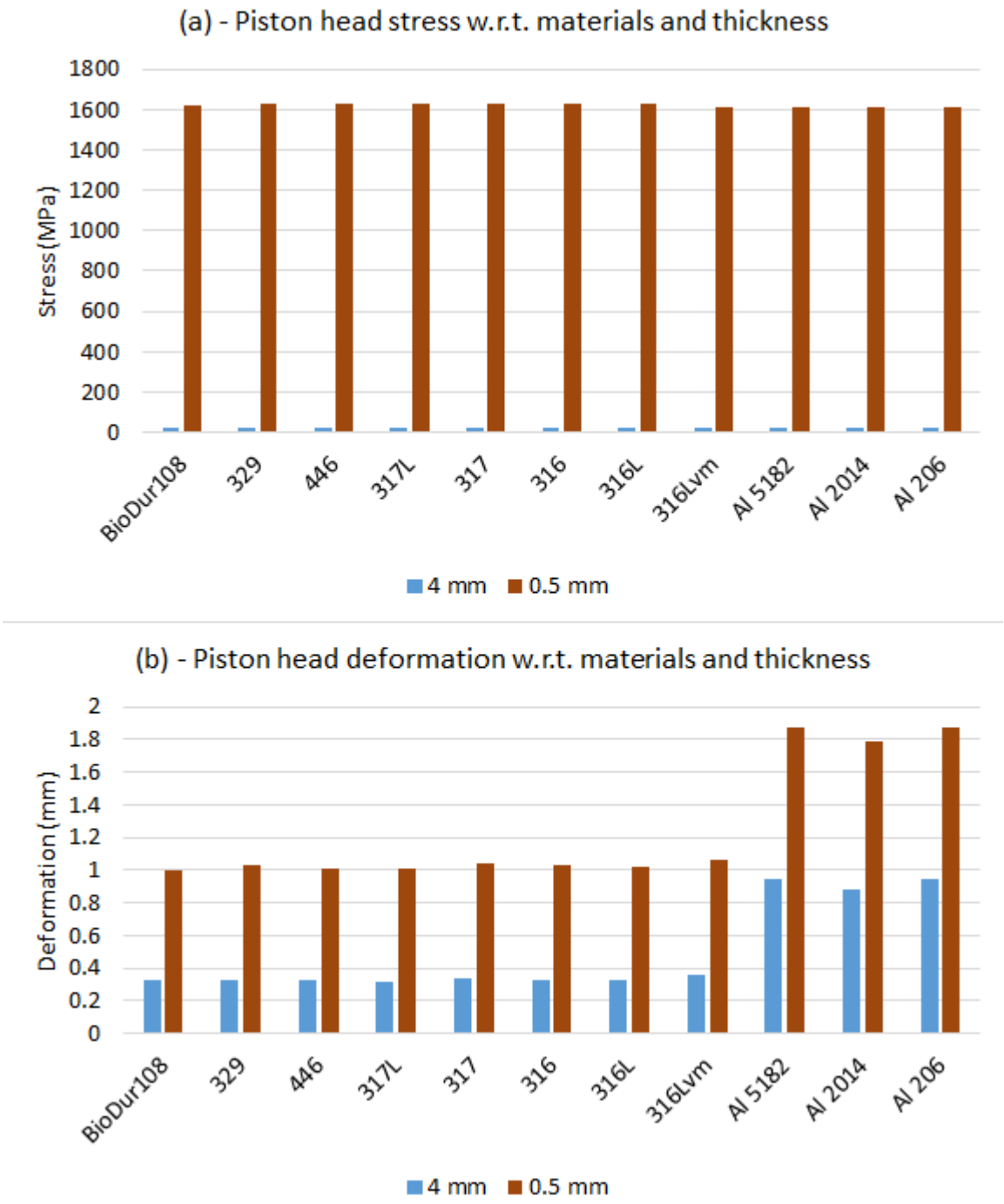

Figure 6.6: Piston head FEA results (a) stresses and (b) deformation w.r.t thickness (4 and 1 mm) and materials.

The FE results for piston head fatigue life and minimum fatigue life safety factor are plotted in Figure 6.7. The fatigue data of piston head FE parametric

results show that whichever material passes the fatigue safety factor value of '1', it passes maximum life cycles (1e8 cycles). The fatigue calculations are driven by the Soderberg fatigue criteria (see Section 6.1.1). The majority of materials fail for thicknesses of '1 and 0.5 mm'. '0.5 mm' is totally unacceptable for the head where safety factor is very low which gives zero life cycles. Only two materials 'BioDur 108' and '316lvm' were found to withstand the loading at up to '1 mm' of thickness.

However, even 0.5 mm thickness value could work if load is reduced than currently applied (200 m head), for instance, even with the strongest material 'BioDur 108' the maximum life for 0.5 mm thickness is achieved around at 103 m head. The analysis shows that endurance limit and yield strength of the materials play important role in the life of the component. For instance, for comparison purpose, if reference material 'steel' (yield limit of 250 MPa and fatigue limit of 86.2 MPa) from a pump mass optimisation study by Lee et al. [79] is used in this study's analysis for 2 mm piston head thickness, then the life of component based on yield safety factor criteria (study's criteria) and fatigue safety factor criteria (this study's) would be 2.5 and 1.28 respectively. This shows that for 2 mm head thickness value, although the maximum fatigue life is achieved yet the yield criteria is exaggerated (up to 48.8%) than the fatigue criteria to predict the maximum life. Hence, the weight reduction optimisation carried out in Lee et al. study had left a room for up to 48.8% further reduction in mass if had been used the fatigue criteria for failure rather than yield. Similarly, many other mass optimisation studies have used yield or tensile strength only criteria which does not optimally reduce the weights [81–85].

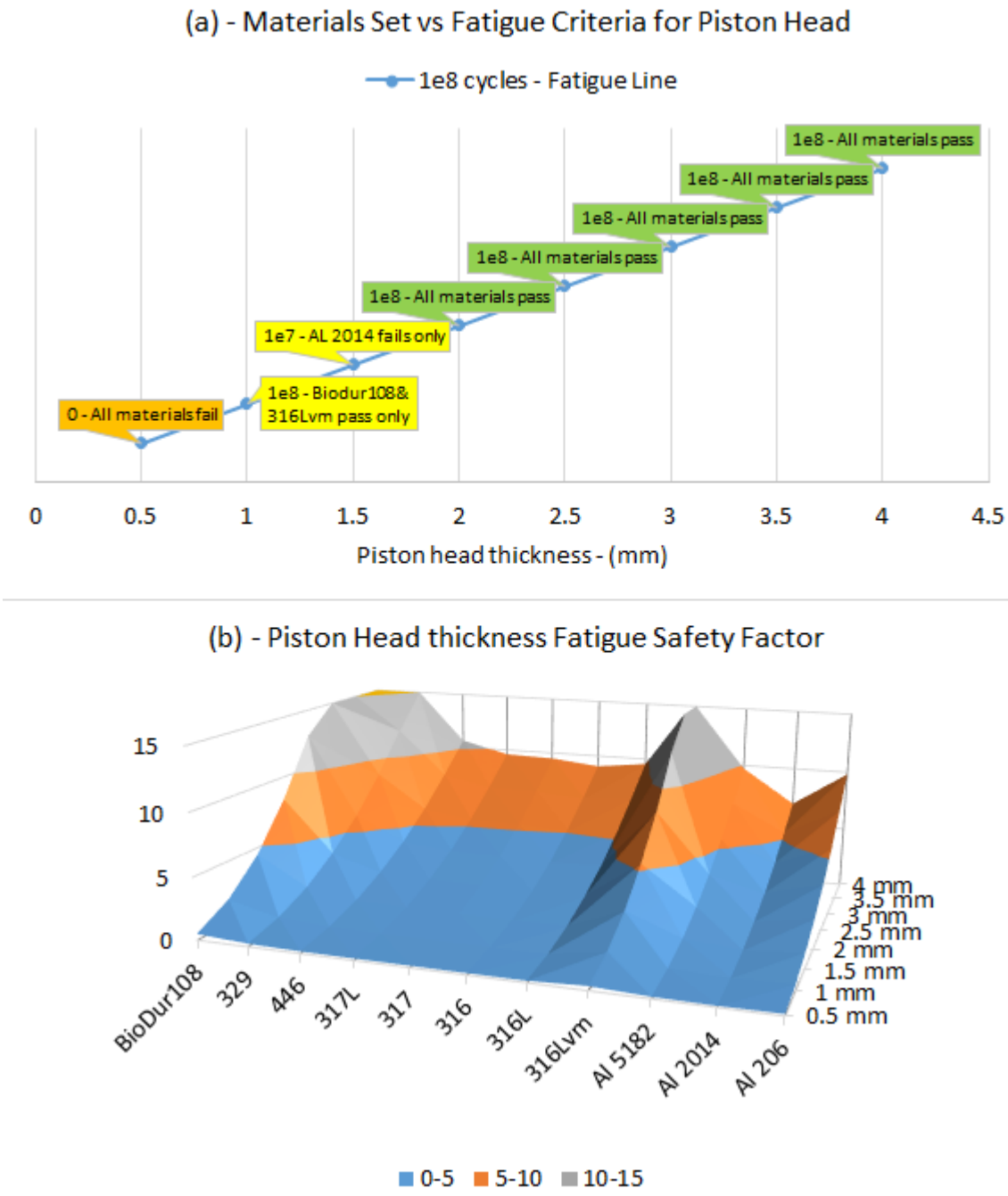

Figure 6.7: Piston head FEA results (a) fatigue life (b) fatigue safety factor w.r.t thickness and materials.

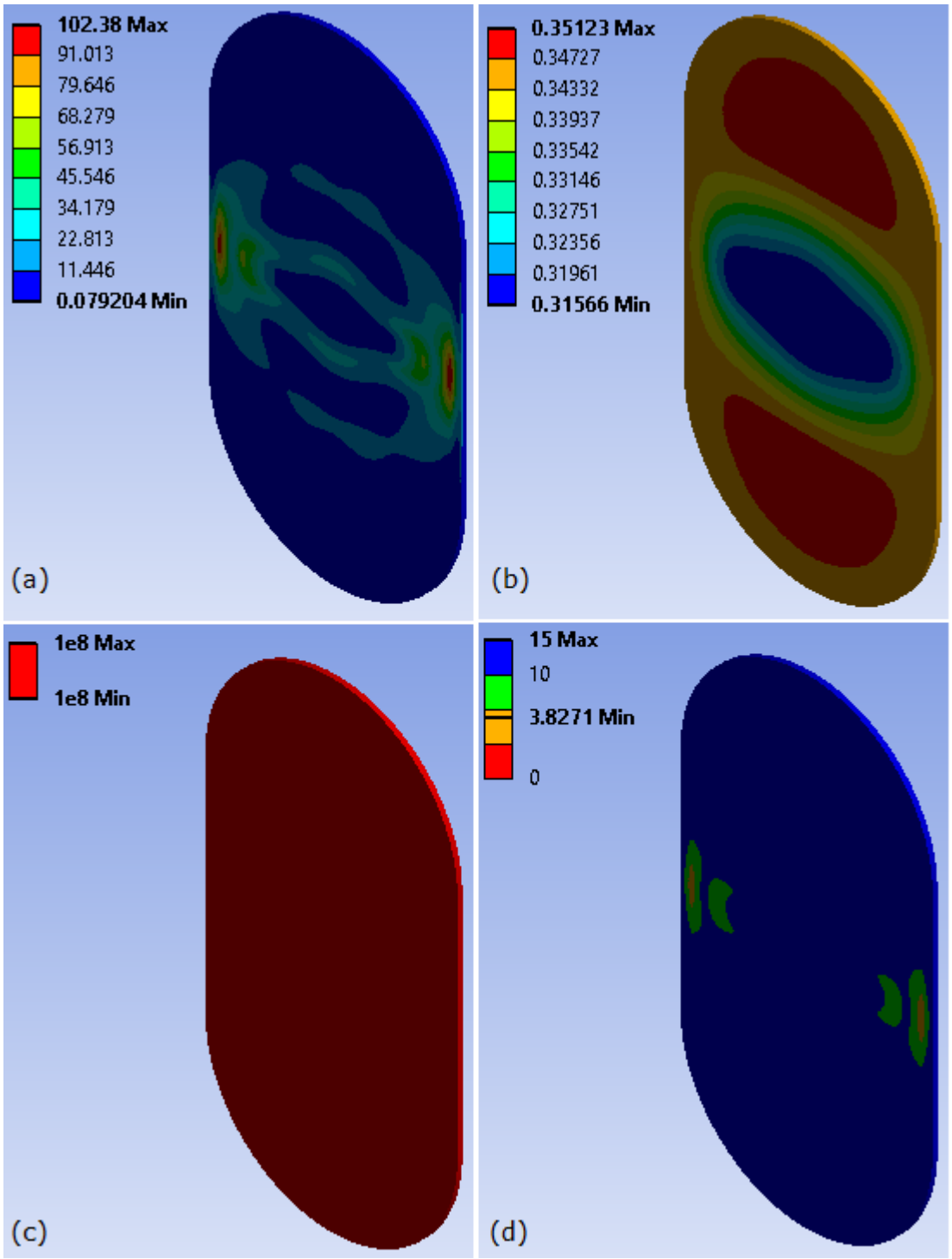

Figure 6.8: FE results of piston head (a) equivalent stress, (b) deformation and (c) fatigue life and (d) safety factor for 2 mm thickness and 329 material.

The FE results of one optimisation case of 2 mm piston head thickness and 329 stainless steel material is shown in Figure 6.8 which illustrates

maximum equivalent stress, total deformation, minimum fatigue life and fatigue safety factor for piston head.

The fatigue FE results of the piston head thicknesses at a constant load of 200 m head were exported to the optimisation model for parameters filtering process, presented in Table 6.3.

The parametric values with respect to materials which passed the failure criteria i.e. maximum fatigue life cycles are shown as green boxes as shown by 'TABLE 6.3(A)'. The second 'TABLE 6.3(B)' shows values passing the failure criteria for individual materials. The data in this table gives the minimum passed value for each material designated as 'RESULT (A)'. The 'RESULT (B)' shows one minimum passed or best value among all materials set. This value is identified as '1 mm' of piston head thickness for materials 'BioDur 108' and '316lvm' of stainless steel grades. 'RESULT (C)' in the table filters out parametric value of '1.5 mm' as the most abundant value among the materials set which passes the failure criteria, which is evaluated as per vote counts for the geometric parametric values. 'RESULT (B)' is a tighter filtering process while 'RESULT (C)' offers selection convenience if the material from 'RESULT (B)' might be unavailable in any circumstances such as in market.

Table 6.3: Results of piston head thickness geometric optimisation.

TABLE (A)

	Head 200 m , Fatigue Life Data for materials set											
Thickness	ssAnsys	ssBioDur	ss329	ss446	ss317L	ss317	ss316	ss316L	ss316lvm	Al5182	Al2014	Al206
4	1.00E+06	1.00E+08	1.00E+08	1.00E+08	1.00E+08	1.00E+08	1.00E+08	1.00E+08	1.00E+08	1.00E+08	1.00E+08	1.00E+08
3.5	1.00E+06	1.00E+08	1.00E+08	1.00E+08	1.00E+08	1E+08	1.00E+08	1.00E+08	1.00E+08	1.00E+08	1.00E+08	1.00E+08
3	1.00E+06	1.00E+08	1.00E+08	1.00E+08	1.00E+08	1E+08	1.00E+08	1.00E+08	1.00E+08	1.00E+08	1.00E+08	1.00E+08
2.5	1.00E+06	1.00E+08	1.00E+08	1.00E+08	1.00E+08	1.00E+08	1.00E+08	1.00E+08	1.00E+08	1.00E+08	1.00E+08	1.00E+08
2	1.00E+06	1.00E+08	1.00E+08	1.00E+08	1.00E+08	1E+08	1.00E+08	1.00E+08	1.00E+08	1.00E+08	1.00E+08	1.00E+08
1.5	5.43E+04	1.00E+08	1.00E+08	1.00E+08	1.00E+08	1E+08	1.00E+08	1.00E+08	1.00E+08	1.00E+08	7.08E+06	1.00E+08
1	5.05E+01	1.00E+08	3.07E+06	0.00E+00	0.00E+00	0.00E+00	0.00E+00	0.00E+00	1.00E+08	0.00E+00	0.00E+00	0.00E+00
0.5	0.00E+00	0.00E+00	0.00E+00	0.00E+00	0.00E+00	0.00E+00	0.00E+00	0.00E+00	0.00E+00	0.00E+00	0.00E+00	0.00E+00

TABLE (B)

Parametric values passing the fatigue criteria

4	4	4	4	4	4	4	4	4	4	4	4
3.5	3.5	3.5	3.5	3.5	3.5	3.5	3.5	3.5	3.5	3.5	3.5
3	3	3	3	3	3	3	3	3	3	3	3
2.5	2.5	2.5	2.5	2.5	2.5	2.5	2.5	2.5	2.5	2.5	2.5
2	2	2	2	2	2	2	2	2	2	2	2
	1.5	1.5	1.5	1.5	1.5	1.5	1.5	1.5	1.5		1.5
	1							1			

RESULT (A)

Best paramteric value from individual materials

Best value	2	1	1.5	1.5	1.5	1.5	1.5	1.5	1	1.5	2	1.5

RESULT (B)

Best parametric value from all materials

Best value	1											
Material		ssBioDur							ss316lvm			

RESULT (C)

Best parametric value from all materials as per votes count

Thickness	4	3.5	3	2.5	2	1.5	1	0.5				
Votes	0	0	0	0	2	8	2	0				
Best value						1.5						
Materials			ss329	ss446	ss317L	ss317	ss316	ss316L		Al5182		Al206

6.2.2 Shaft Main Diameter Parametric FE and Optimisation Results

Similarly, the geometrical parametric FE simulations results for shaft main diameter were evaluated for maximum equivalent stresses and total deformation, and, fatigue life and minimum fatigue life safety factor, presented by Figures 6.9 and 6.10, respectively. The equivalent stresses and total deformations in the shaft are same for parametric values among all materials which is due to the slight difference in Poisson's ratio values. The higher total

deformation values include the rotation of the shaft due to the piston force restricted by the shaft bearings to lean backward.

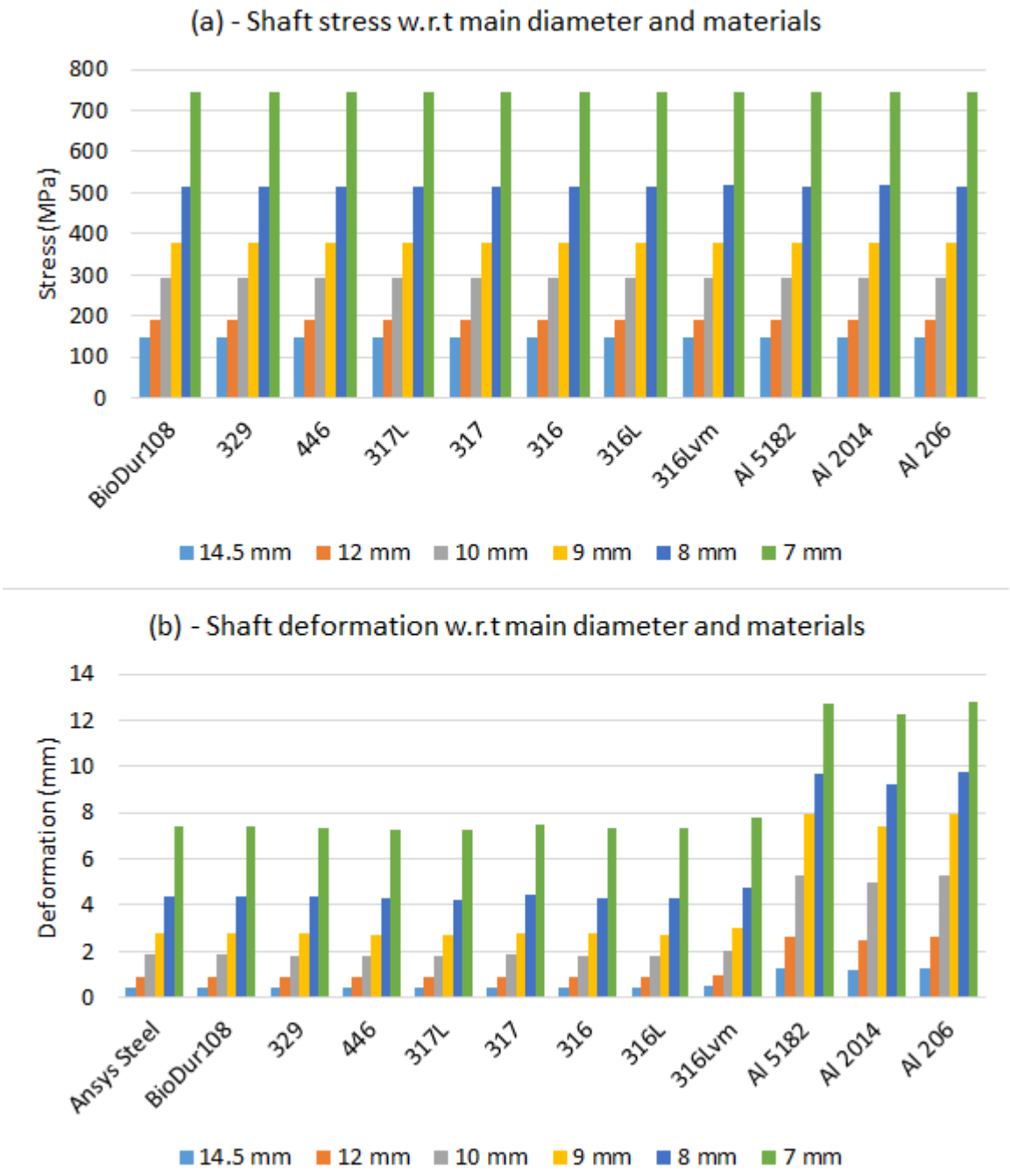

Figure 6.9: Shaft FE results (a) stress and (b) deformation w.r.t main diameter and materials.

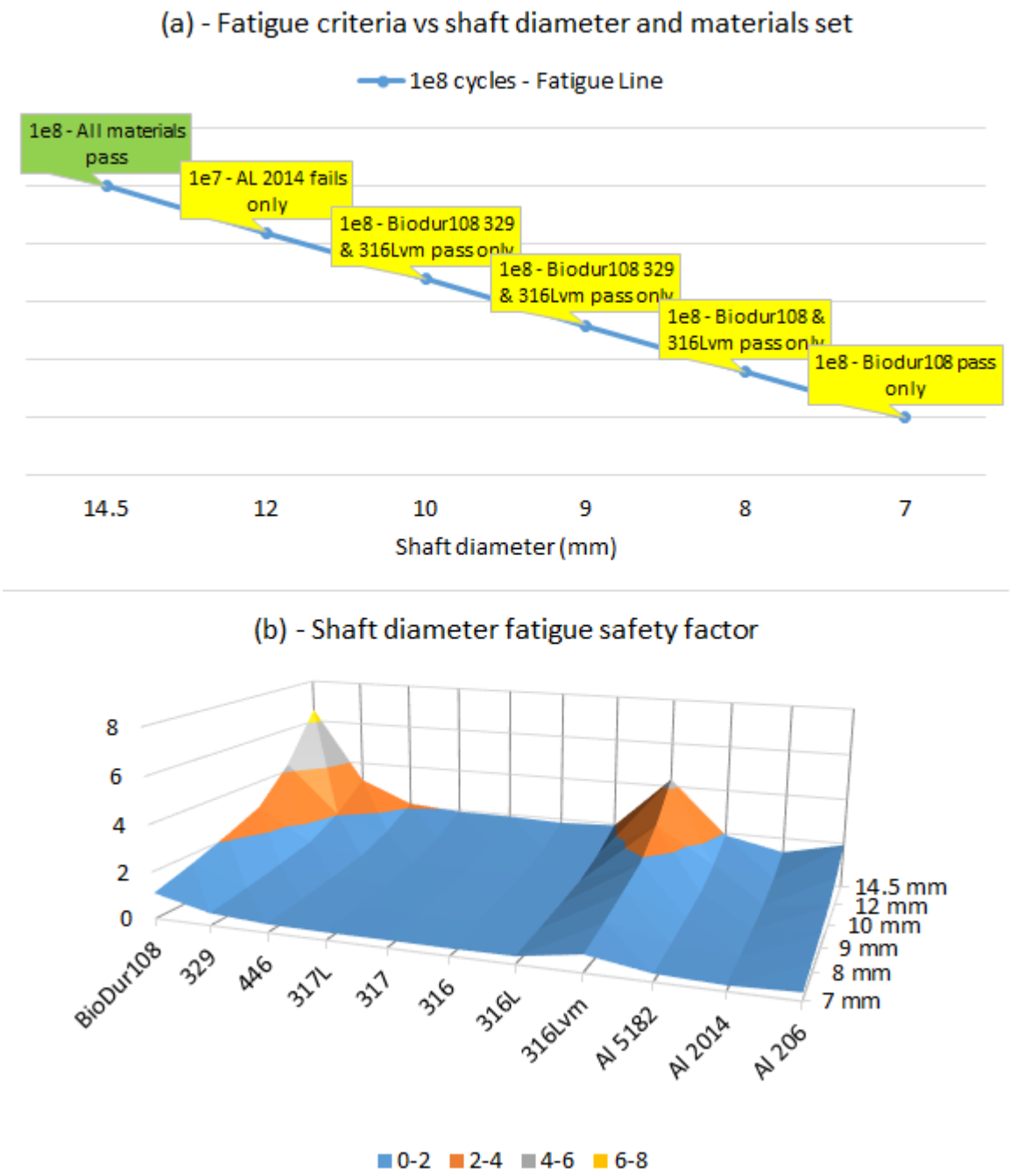

Figure 6.10: Shaft FEA results (a) fatigue life (b) fatigue life safety factor w.r.t main diameter and materials.

The fatigue life results from the shaft parametric analysis show similar outcome as that for piston head thicknesses. Less materials are seen to pass the fatigue criteria as seen in the Figure 6.10. Only one material 'BioDur 108'

can support minimum diameter of '7 mm' for the specified loading conditions. This is due to very high strength and endurance limit of this material.

The FE results of one optimisation case of 8 mm shaft diameter and 329 stainless steel material is shown in Figure 6.11 which illustrates maximum equivalent stress just below the shaft bearing location, total deformation, minimum fatigue life and fatigue safety factor for the shaft.

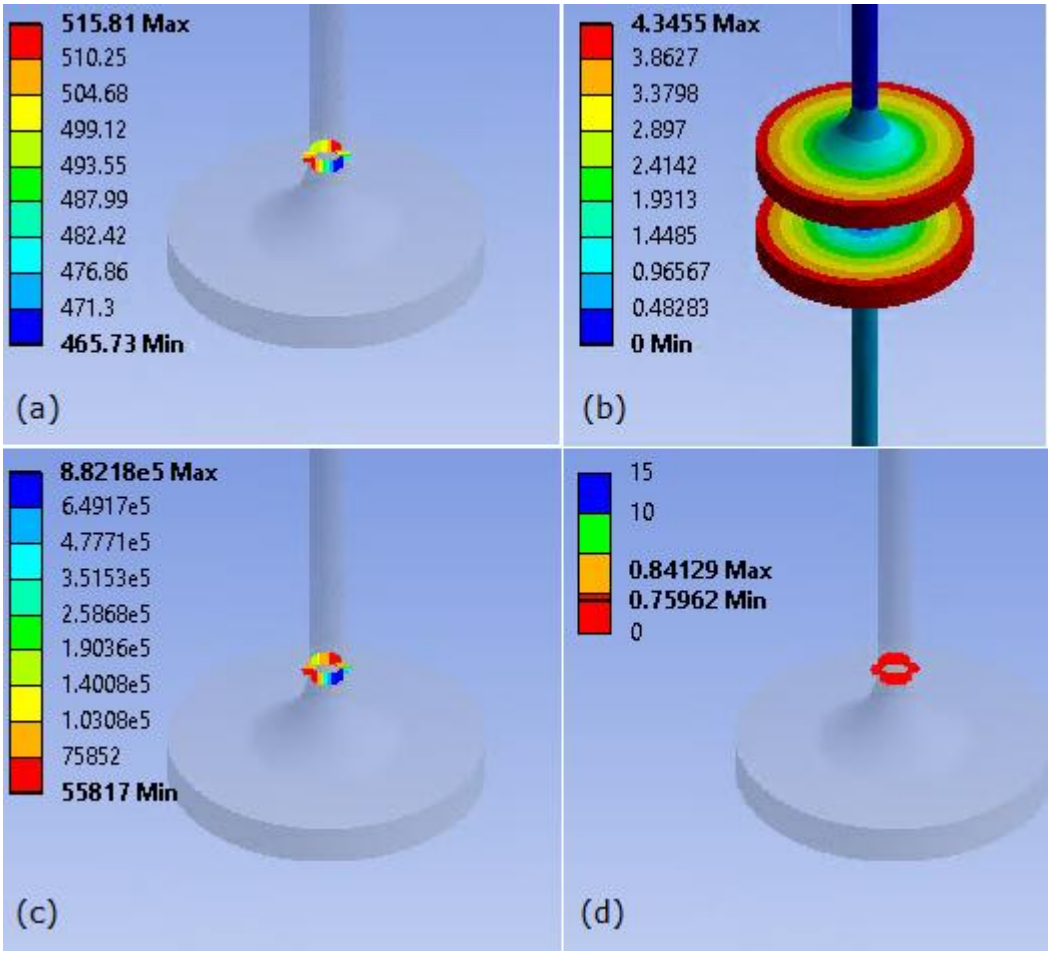

Figure 6.11: FE results of shaft (a) equivalent stress, (b) deformation and (c) fatigue life and (d) safety factor for 8 mm diameter and 329 stainless steel material.

Similarly, the same filtering procedure was followed for the optimisation of shaft main diameter along with suitable materials. The fatigue FE results of parametric analysis are presented in 'TABLE 6.4(A)'. It is noticeable a large number of parametric values do not meet the fatigue life criteria because of high stresses in the shaft. For the initial parameter value of '14.5 mm', all material passes the criteria. The parameters passing the criteria are shown in the 'TABLE 6.4(B)'. 'RESULT (A)' in the table shows individual best values for individual materials, whereas 'RESULT (B)' shortlists '7 mm' diameter as the best minimum value which is only possible with stainless steel 'BioDur 108' material. However, as per votes count 'RESULT (C)' finds '12 mm' as the most abundant parametric value among the materials set.

Table 6.4: Results of shaft main diameter optimisation.

TABLE (A)

	Head 200 m , Fatigue Life Data for materials set											
Diameter	ssAnsys	ssBioDur	ss329	ss446	ss317L	ss317	ss316	ss316L	ss316lvm	Al5182	Al2014	Al206
14.5	1.00E+06	1.00E+08	1.00E+08	1.00E+08	1.00E+08	1.00E+08	1.00E+08	1.00E+08	1.00E+08	1.00E+08	1.00E+08	1.00E+08
12	6.63E+04	1.00E+08	1.00E+08	1.00E+08	1.00E+08	1.00E+08	1.00E+08	1.00E+08	1.00E+08	1.00E+08	1.16E+07	1.00E+08
10	4.00E+03	1.00E+08	1.00E+08	4.47E+06	6.18E+04	9.04E+04	8.52E+04	6.34E+04	1.00E+08	3.89E+05	5.43E+03	3.55E+05
9	4.48E+02	1.00E+08	1.00E+08	2.72E+02	1.77E-09	1.06E-10	5.19E-10	3.37E-10	1.00E+08	8.88E-11	5.51E-11	1.13E-10
8	1.40E-11	1.00E+08	5.58E+04	0.00E+00	0.00E+00	0.00E+00	0.00E+00	0.00E+00	1.00E+08			
7	0.00E+00	1.00E+08	0.00E+00			0.00E+00			7.76E+07			

TABLE (B)

Parametric values passing the fatigue criteria

	14.5	14.5	14.5	14.5	14.5	14.5	14.5	14.5	14.5	14.5	14.5	14.5
		12	12	12	12	12	12	12	12	12		12
		10	10						10			
		9	9						9			
		8							8			
		7										

RESULT (A)

Best parametric values from individual materials

Best value	14.5	7	9	12	12	12	12	12	8	12	14.5	12

RESULT (B)

Best parametric values from all materials

Best value	7	
Material	ssBioDur	

RESULT (C)

Best paramteric values from all materials as per votes count

Diamter	14.5	12	10	9	8	7						
Votes	2	7	0	1	1	1						
Best value		12										
Materials			ss446	ss317L	ss317	ss316	ss316L		Al5182		Al206	

6.2.3 Shaft Slider Parametric FE and Optimisation Results

The third component to optimise was identified as shaft slider which engages with the piston. The initial diameter of the slider (10 mm) was a failure with lower strength steel as the initial material (ANSYS database) due to high contact stresses of 604.45 MPa and almost non-important fatigue life of just 6.145e3 cycles, found in the initial model of the FE simulations (see Table 6.1). This component was subjected to opposite geometrical optimisation using the same procedure i.e. to have an optimum diameter and material with a constraint of maximum fatigue life. The diameter of the slider was increased from the base value of 10 mm to a limit of 20 mm only. This was adopted due to borehole size limitation because increasing the slider diameter would cause other dimensions of components to increase same fold and also due to limited bearing diameters [94]. The parametric values of slider diameter are presented in Table 6.5 and the FE parametric results of slider diameter with contact stresses are shown in Figure 6.12. All grades exhibit nearly same stresses. The negative values of contact stresses show their compressive nature.

Table 6.5: Components optimisation parameters and material set data.

GEOMETRICAL PARAMETERS	
Shaft Slider Diameter	10, 12, 15, 17, 20 (mm) Increment as per available bearing diameters [94]

.

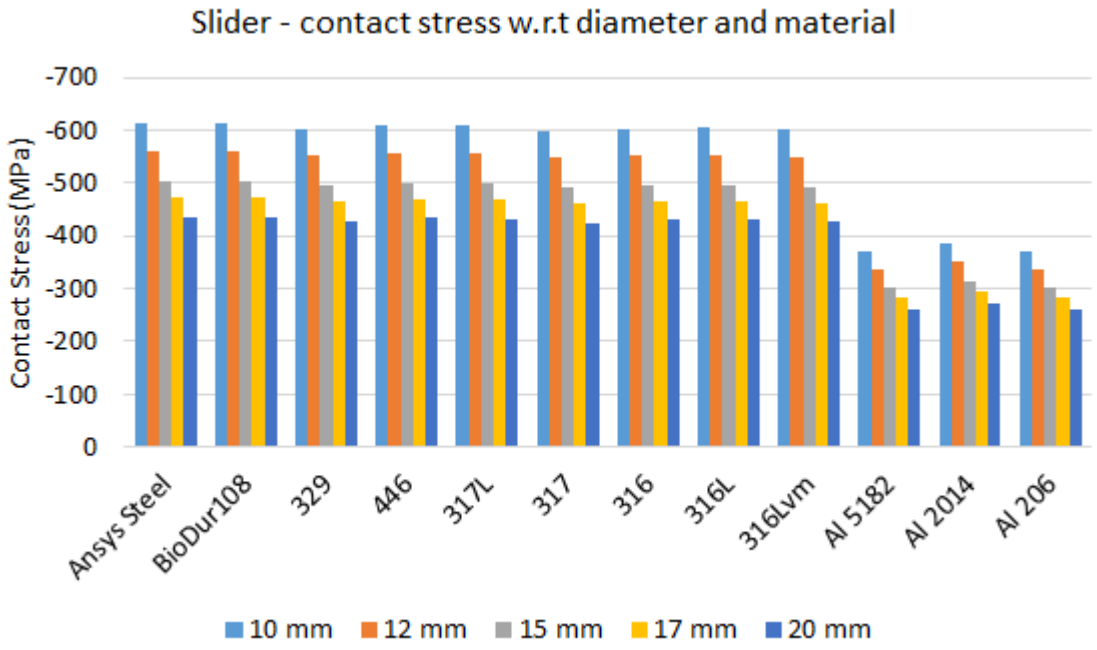

Figure 6.12: Shaft slider contact stresses with the piston w.r.t its diameter and materials.

The fatigue life and fatigue safety factor are presented in Figure 6.13. The fatigue results were evaluated based on the maximum contact stresses between the piston and the slider. The results show that for majority of materials fail for ’10 mm’ diameter except couple of candidates passing the fatigue criteria i.e. ‘BioDur 108, 329 and 316lvm’. This is because of their high endurance limit values against the contact stresses.

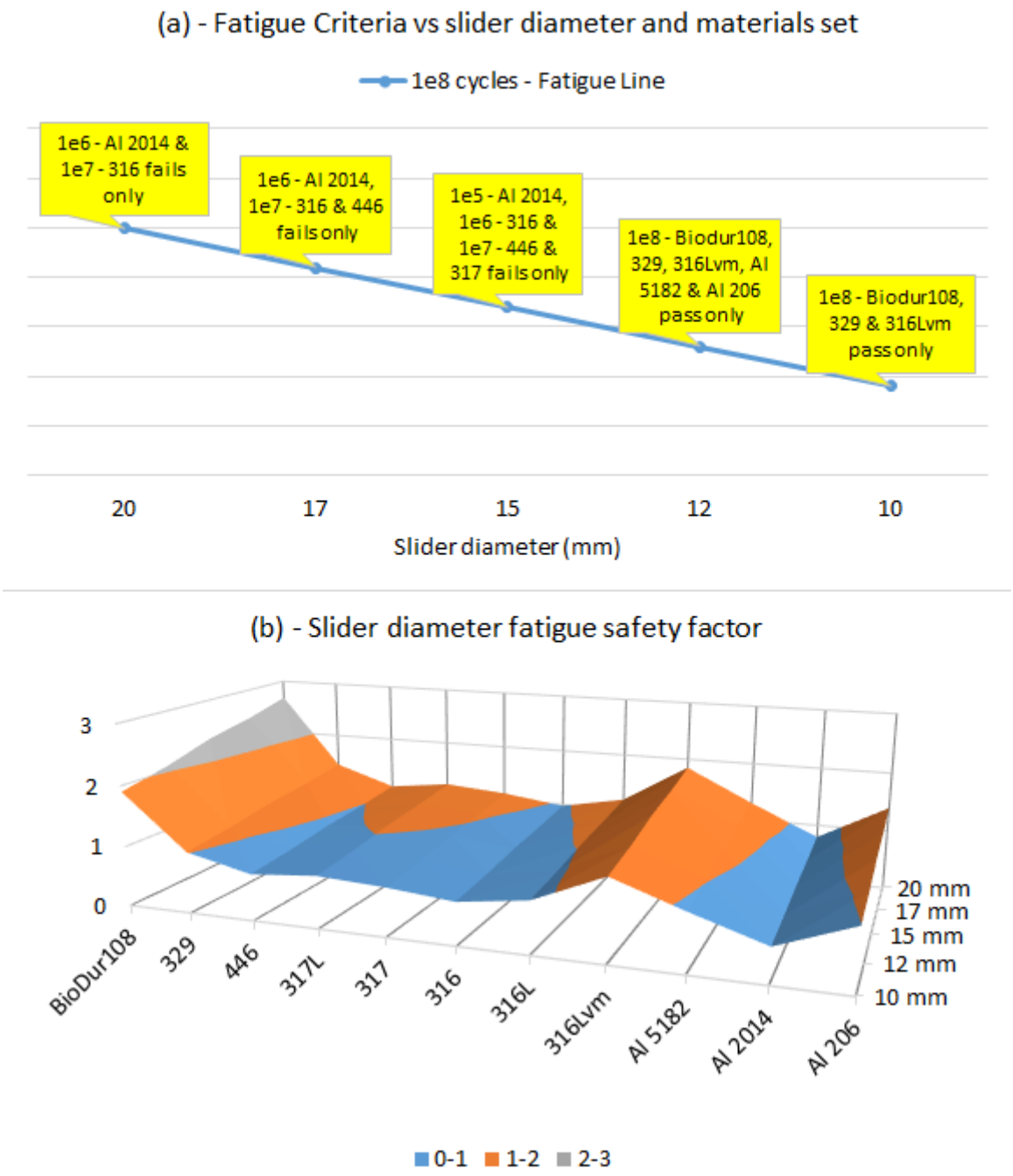

Figure 6.13: Shaft slider (a) fatigue life and (b) fatigue safety factor w.r.t its diameter and materials.

The FE results from 2D analysis of one optimisation case of 10 mm shaft slider diameter and 329 stainless steel material in contact with the piston body is shown in Figure 6.14 which illustrates maximum contact stress, shear stress,

minimum fatigue life, fatigue safety factor and total deformation. The fatigue safety factor was evaluated based on the maximum contact stress which was found to be the highest stress between the parts. The value of factor just above one allows the model to pass the fatigue life criteria to reach maximum life.

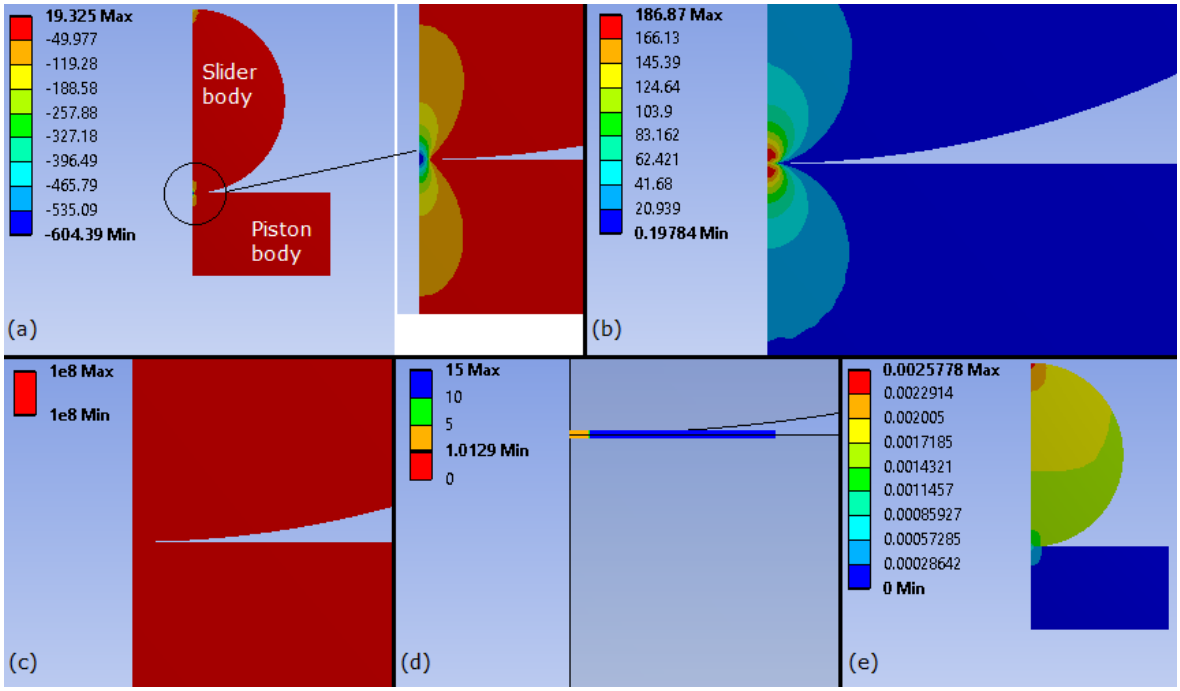

Figure 6.14: FE results of slider-piston contact with (a) contact stress, (b) shear stress, (c) fatigue life, (d) safety factor and (e) total deformation for 10 mm diameter and 329 stainless steel material.

The FE fatigue results were then put into the optimisation filtering process which is presented in 'TABLE 6.6(A)'. 'TABLE 6.6(B)' show parametric values which passed the fatigue life criteria. 'RESULT (A)' in the table reveals individual best or minimum parametric values with respect to materials. 'RESULT (B)' focuses on the minimum value among all materials and finds '10 mm' as the acceptable dimension for 'BioDur 108', '329' and '316lvm' stainless steel grades. 'RESULT (C)' also filters out '10 mm' as the most abundant value among the

whole materials set with same materials as in 'RESULT (B)'. It is worth noting that '10 mm' parametric value could further be optimised with these optimised materials to evaluate if any further reduction in diameter is achievable beyond the current study limitations bound to the borehole size limitation and availability of bearings (see Table 6.5) under 200 m head load.

Table 6.6: Results of shaft slider diameter optimisation.

TABLE (A)

	Head 200 m , Fatigue Life Data for materials set											
Diameter	ssAnsys	ssBioDur	ss329	ss446	ss317L	ss317	ss316	ss316L	ss316lvm	Al5182	Al2014	Al206
20	1.87E+04	1.00E+08	1.00E+08	1.00E+08	1.00E+08	1.00E+08	6.74E+07	1.00E+08	1.00E+08	1.00E+08	4.65E+06	1.00E+08
17	1.42E+04	1.00E+08	1.00E+08	8.63E+07	1.00E+08	1.00E+08	2.09E+07	1.00E+08	1.00E+08	1.00E+08	2.01E+06	1.00E+08
15	1.15E+04	1.00E+08	1.00E+08	2.74E+07	1.00E+08	6.17E+07	8.94E+06	1.00E+08	1.00E+08	1.00E+08	8.51E+05	1.00E+08
12	8.07E+03	1.00E+08	1.00E+08	4.10E+06	3.26E+07	1.09E+07	2.45E+06	2.38E+07	1.00E+08	1.00E+08	2.93E+05	1.00E+08
10	6.15E+03	1.00E+08	1.00E+08	8.24E+05	7.02E+06	3.34E+06	7.47E+05	5.25E+06	1.00E+08	2.06E+07	7.36E+04	9.29E+07

TABLE (B)

Parametric values passing the fatigue life criteria

20	20	20	20	20		20	20	20	20
17	17		17	17		17	17	17	17
15	15		15			15	15	15	15
12	12						12	12	12
10	10						10		

RESULT (A)

Best parametric values from individual materials

Best value	0	10	10	20	15	17	0	15	10	12	0	12

RESULT (B)

Best parametric values from all materials

Best P.val	10											
Material		ssBioDur	ss329						ss316lvm			

RESULT (C)

Best parametric values from all materials as per votes count

Diameter	20	17	15	12	10							
Votes	1	1	2	2	3							
Best value					10							
Materials		ssBioDur	ss329						ss316lvm			

6.2.4 Decision on Combination of Components Optimisations

The optimisation model now decides one combination of best parametric values and material from each component by taking values from 'RESULT (A)' (from Tables 6.3, 6.4 and 6.6) of the optimised results (see previous sections), here consolidated in Table 6.7. The parametric combined values are sum

together for each material and the minimum sum shows the best combination of parameters and the associated material. It is evident that 'BioDur 108' has the least sum of 18 among the parametric values set, followed by '316Lvm' with sum of 19. The model however selects the 'BioDur 108' as the optimum material with the optimum parametric values. Any component with failed parameter value not passing the fatigue criteria results in the omission of the whole set as found in case of 'Ansys steel', '316' and 'aluminium AL 2014'.

Table 6.7: Optimised geometric values for components with respect to materials set.

Parametric values of components which passed fatigue life criteria for individual materials

	Head 200 m , Maximum Fatigue Life (1e8 cycles)											
Part	ssAnsys	ssBioDur	ss329	ss446	ss317L	ss317	ss316	ss316L	ss316lvm	Al5182	Al2014	Al206
Shaft diameter	14.5	7	9	12	12	12	12	12	8	12	14.5	12
Piston head thickness	2	1	1.5	1.5	1.5	1.5	1.5	1.5	1	1.5	2	1.5
Slider diameter	0	10	10	20	15	17	0	15	10	12	0	12
Design Possibe?	No	Yes	Yes	Yes	Yes	Yes	No	Yes	Yes	Yes	No	Yes
Sum passed values		18	20.5	33.5	28.5	30.5		28.5	19	25.5		25.5

Finally, as the combination outcome, see Figure 6.15, the model found best geometrical parametric values as '7 mm' for shaft diameter, '1 mm' for piston head thickness and '10 mm' for slider diameter with 'BioDur108' as one optimum material. If any two or more materials results in the same combination sum, then either all combination would be acceptable or they could be further filtered out based on the characteristics such as cost and performance etc. The model up to this point only recommends the optimised combination based on geometrical aspects of components. The model further filters out geometric

values and materials by the evaluation of mass reduction, material cost effectiveness and power optimisation of components as discussed in following sections.

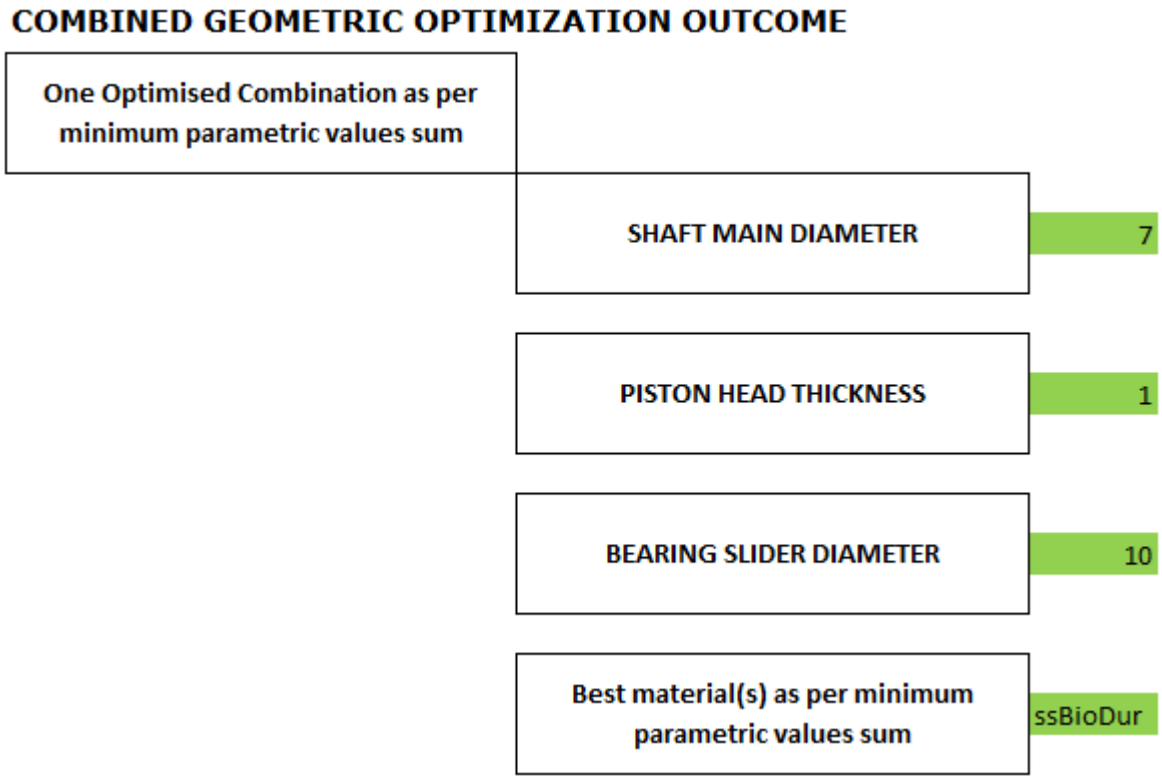

Figure 6.15: Parametric combination of components geometrical optimisations and material.

6.2.5 Evaluation of Mass, Cost and Power Optimisations of Components

After geometric optimisation of components, the next step was to calculate the mass reduction, material cost saving and performance improvement (in this study power consumption) of the components among all materials. Power and cost are related to the mass of the material. The evaluation procedure for mass optimisation is presented in Table 6.8. The model only evaluates the masses with passed (optimised) geometrical parametric values

(based on Table 6.7) of each component as shown in 'TABLE 6.8(A)'. The slider component of the shaft was omitted from the mass optimisation analysis due to its very small mass of just 14 g with 10 mm diameter with steel as material which would result in insignificant optimisation.

Another reason was the nature of its optimisation as the diameter was not reduced further than the initial value. Results from 'TABLE 6.8(A)' show suitable material candidate with optimum value of total components' mass. 'Al 5182' was found out to be the least weighted assembly of piston and shaft components among all materials set, while, 'BioDur 108' from the stainless steel group. 'TABLE 6.8(C)' shows the percentage mass reduction by comparing the total masses of components in their initial designs (calculated in 'TABLE 6.8(B)') with the optimised masses. It was found that significant maximum reduction of 29.39% was seen for 'BioDur 108' followed by 28.24% of '316lvm'. It is worth mentioning that 'Al 5182' despite being the least weighted material for piston-shaft assembly has mass improvement of 22.29% less than 'BioDur 108' due to the larger geometric parametric values which allocates more mass. 'BioDur 108' comes out to be the best candidate for mass optimisation. The 'TABLE 6.8(C)' also shows individual components mass reduction by comparing values between 'TABLE 6.8(A)' and 'TABLE 6.8(B)'.

Table 6.8: Parametric components' mass optimisation with respect to materials.

TABLE (A)

	Head 200 m , Optimised Mass (kg) of components per 'TABLE A' parametric values											
Part	ssAnsys	ssBioDur	ss329	ss446	ss317L	ss317	ss316	ss316L	ss316lvm	Al5182	Al2014	Al206
Shaft		0.67523	0.746242	0.82233	0.873872	0.873872		0.873872	0.733726	0.291118		0.307015
Piston		0.941589	1.029403	0.989804	1.051842	1.051842		1.051842	0.984773	0.327216		0.369541
Total mass	0	1.616819	1.775645	1.812134	1.925714	1.925714	0	1.925714	1.718499	0.618334	0	0.676557
Minimum	0.618334											
All set										Al5182		
Min. Mass	1.616819											
Steel set		ssBioDur										
Min. Mass	0.618334											
AL set										Al5182		

TABLE (B)

			Initial Mass (kg) of components as per their initial design values											
Part	Parameter	Value	ssAnsys	ssBioDur	ss329	ss446	ss317L	ss317	ss316	ss316L	ss316lvm	Al5182	Al2014	Al206
Shaft	diameter	14.5	0.973997	0.947894	0.967714	0.930487	0.988808	0.988808	0.988808	0.988808	0.991367	0.329407	0.346872	0.347396
Piston	thickness	4	1.378931	1.341975	1.370035	1.317332	1.399899	1.399899	1.399899	1.399899	1.403523	0.466356	0.491082	0.491823
	Total Mass		2.352928	2.289869	2.337749	2.247819	2.388707	2.388707	2.388707	2.388707	2.394891	0.795763	0.837954	0.839219

TABLE (C)

		Mass reduction (%) - Optimised mass values vs initial mass values of components											
Part	Parameter	ssAnsys	ssBioDur	ss329	ss446	ss317L	ss317	ss316	ss316L	ss316lvm	Al5182	Al2014	Al206
Shaft	main diameter		28.76517	22.88607	11.62366	11.62366	11.62366		11.62366	25.98854	11.62366		11.62366
Piston	head thickness		29.83563	24.86302	24.86302	24.86302	24.86302		24.86302	29.83563	29.83563		24.86302
Total Improvement (%)			29.39251	24.04466	19.38257	19.38257	19.38257		19.38257	28.24312	22.29676		19.38257

Similarly, with the significant mass reduction for components, material cost savings were also evaluated in the same fashion as discussed previously i.e. the cost filtering procedure is based on the same optimised geometric values found during the geometric optimisation (see Table 6.7). The material with highest savings was shortlisted by the optimisation model. The individual components materials costs in USD/kg for optimised geometries are shown in 'TABLE 6.9(A)'. The unit cost data was input from the CES program into the model. Summing the total cost of piston-shaft components in 'TABLE 6.9(A)' gives 'Al 5182' as the cheapest material among all materials and 'AISI 446' as cheapest from stainless steel group. However, as expected, after comparing optimised and initial cost values between 'TABLE 6.9(A)' and 'TABLE 6.9(B)' of components, the material cost savings were found to be same as the mass

reduction i.e. with 'BioDur 108' as the best candidate with highest savings of 29.39%. This is because the material removal is linked to the unit cost i.e. USD/kg, therefore, the material removed in optimising the components geometry, same proportional cost savings would result. It is also worth mentioning that individual outcome showed '446' as the best cost saver than 'BioDur 108' the best candidate from mass optimisation, this is because cost is not material dependent, while cost is mass dependent.

Table 6.9: Parametric components' cost optimisation with respect to materials.

TABLE (A)

	Head 200 m , Optimised Cost (USD/kg) of components 'TABLE A' parametric values											
Part	ssAnsys	ssBioDur	ss329	ss446	ss317L	ss317	ss316	ss316L	ss316lvm	Al5182	Al2014	Al206
shaft		1.303195	4.447602	1.356845	3.320714	3.320714		2.979904	5.422232	0.602614		0.693855
Piston		1.817266	6.135243	1.633176	3.997	3.997		3.586781	7.277474	0.677337		0.835163
Total cost	0	3.120461	10.58285	2.990021	7.317714	7.317714	0	6.566685	12.69971	1.279951	0	1.529018
Minimum	1.279951											
All set										Al5182		
Min. cost	2.990021											
Steel set				ss446								
Min. cost	1.279951											
AL set										Al5182		

TABLE (B)

			Initial Cost (USD/kg) of components as per their initial design values											
Part	Parameter	Value	ssAnsys	ssBioDur	ss329	ss446	ss317L	ss317	ss316	ss316L	ss316lvm	Al5182	Al2014	Al206
Shaft	diameter	14.5	n/a	1.829435	5.767573	1.535304	3.75747	3.75747	3.371835	3.371835	7.326206	0.681872	0.776993	0.785114
Piston	head	4	n/a	2.590013	8.165411	2.173598	5.319617	5.319617	4.773657	4.773657	10.37204	0.965357	1.100024	1.111521
Total cost			0	4.419447	13.93298	3.708902	9.077087	9.077087	8.145491	8.145491	17.69824	1.64723	1.877017	1.896635

TABLE (C)

		Cost reduction (%) - Optimised material cost vs Initial material cost of each components											
Part	Parameter	ssAnsys	ssBioDur	ss329	ss446	ss317L	ss317	ss316	ss316L	ss316lvm	Al5182	Al2014	Al206
Shaft	diameter		28.76517	22.88607	11.62366	11.62366	11.62366		11.62366	25.98854	11.62366		11.62366
Piston	head thickness		29.83563	24.86302	24.86302	24.86302	24.86302		24.86302	29.83563	29.83563		24.86302
Total improvement (%)			29.39251	24.04466	19.38257	19.38257	19.38257		19.38257	28.24312	22.29676		19.38257

Finally, with the significant mass reductions in the components during the optimisation which makes them lighter than their initial designs, performance improvement are duly expected. Power is consumed during the operation of components i.e. piston reciprocates while the shaft rotates. The evaluation process of power consumption improvement which is also based on optimised

geometric parametric values (presented in TABLE 6.7) is shown in Table 6.10. The data in 'TABLE 6.10(A)' shows power in watts consumed by individual components' respective to the nature of their motions, and later summed for total power consumption by piston-shaft assembly.

Individual results from 'TABLE 6.10(A)' shows 'Al 5182' as the most power efficient material candidate among the group due to being lightest, and 'BioDur 108' as best from stainless steel group. The comparison of power consumption by optimised components to the very initial design is done in 'TABLE 6.10(C)' where total power values of piston-shaft assembly before and after optimisation are compared (i.e. between 'TABLE 6.10(A)' and 'TABLE 6.10(B)'). The model found 'BioDur 108' as the most efficient for power consumption with as significant improvement of 29.25%. This will significantly affect positively the operation of the whole pump compared to the initial design.

However, 'Al 5182' with nearly same improvement in power consumption cannot be selected as the optimised candidate due higher deformations values which are a matter of tight tolerances in the pump operation, an example of shaft deformation with respect to diameter change is shown in Table 6.11.

Table 6.10: Parametric components' power optimisation with respect to materials.

TABLE (A)

	Head 200 m , Optimised power consumption (W) of components per 'TABLE A' parametric values											
Part	ssAnsys	ssBioDur	ss329	ss446	ss317L	ss317	ss316	ss316L	ss316lvm	Al5182	Al2014	Al206
shaft		0.005385	0.00553	0.005395	0.005733	0.005733		0.005733	0.005647	0.00191		0.002014
Piston		0.170609	0.18652	0.179345	0.190586	0.190586		0.190586	0.178434	0.059289		0.066958
Total Power	0	0.175994	0.19205	0.18474	0.196319	0.196319	0	0.196319	0.184081	0.061199	0	0.068972
Minimum	0.061199											
All set										Al5182		
Minimum power	0.175994											
Steel set		ssBioDur										
Minimum power	0.061199											
Aluminium set										Al5182		

TABLE (B)

			Initial Power (W) of components as per their initial design values											
Part	Parameter	Value	ssAnsys	ssBioDur	ss329	ss446	ss317L	ss317	ss316	ss316L	ss316lvm	Al5182	Al2014	Al206
Shaft	diameter	14.5	0.00576	0.005606	0.005723	0.005503	0.005848	0.005848	0.005848	0.005848	0.005863	0.001948	0.002051	0.002054
Piston	head	4	0.249852	0.243156	0.248241	0.238691	0.253652	0.253652	0.253652	0.253652	0.254308	0.0845	0.088981	0.089115
Total Power			0.255612	0.248762	0.253963	0.244194	0.259499	0.259499	0.259499	0.259499	0.260171	0.086448	0.091032	0.091169

TABLE (C)

		Power consumption reduction (%) - Optimised design values vs Initial design values for each component											
Part	Parameter	ssAnsys	ssBioDur	ss329	ss446	ss317L	ss317	ss316	ss316L	ss316lvm	Al5182	Al2014	Al206
Shaft	diameter		3.933591	3.374933	1.959812	1.959808	1.959808		1.959808	3.684304	1.959813		1.959812
Piston	head thickness		29.83563	24.86302	24.86302	24.86302	24.86302		24.86302	29.83563	29.83563		24.86302
Total Improvement (%)			29.25195	24.37881	24.34692	24.34692	24.34692		24.34692	29.24633	29.20747		24.34692

Table 6.11: Parametric FE analysis of AL 5182 shaft with respect to diameter.

	Shaft diameters					
Result Property	**14.5**	**12**	**10**	**9**	**8**	**7**
Total deformation (mm)	1.281374	2.63357	5.31082	7.957782		
Equivalent Stress (MPa)	142.3598	189.9751	290.8946	376.8484		
Equivalent Stress Safety Factor	2.757028	2.066013	1.349255	1.041509	Simulation Failure	
Fatigue Life Safety Factor	1.674148	1.251371	0.817235	0.630835		
Fatigue Life (cycles)	1.00E+08	1.00E+08	3.89E+05	8.88E-11		
Decision (Life = 1e8 cycles)	pass	pass	fail	fail	fail	fail

Overall, 'BioDur 108' stainless steel was found to be the best material with optimised geometry, highest mass and material cost reduction and lowest power consumption in this parametric study. The optimisation summary of piston and shaft components based on parameters and materials which passed the fatigue criteria are shown by Figure 6.16. The figure comprehensively

compares the initial and optimised design of improved factors of these components. It is observable from the figure that the initial and optimised masses of these components are dependent on density of materials. The cost savings since associated with the material removal follow the same trend as of mass optimisation. The power optimisation trend is slightly different in case because of the optimised mass of shaft which does not follow the same trend as the initial design as shown in Figure 6.17. This is due to more reduced values of the main diameter than the initial design e.g. 'BioDur 108 has reduced to 7 mm from 14.5 mm'. The power calculations of the rotating shaft were evaluated based on the mass moment of inertia ($I=mr^2$). The optimised masses of shaft among materials does not significantly affect the rotating inertia about shaft axis. Hence, the power calculations do not follow the same trend as the mass as evident in the figure.

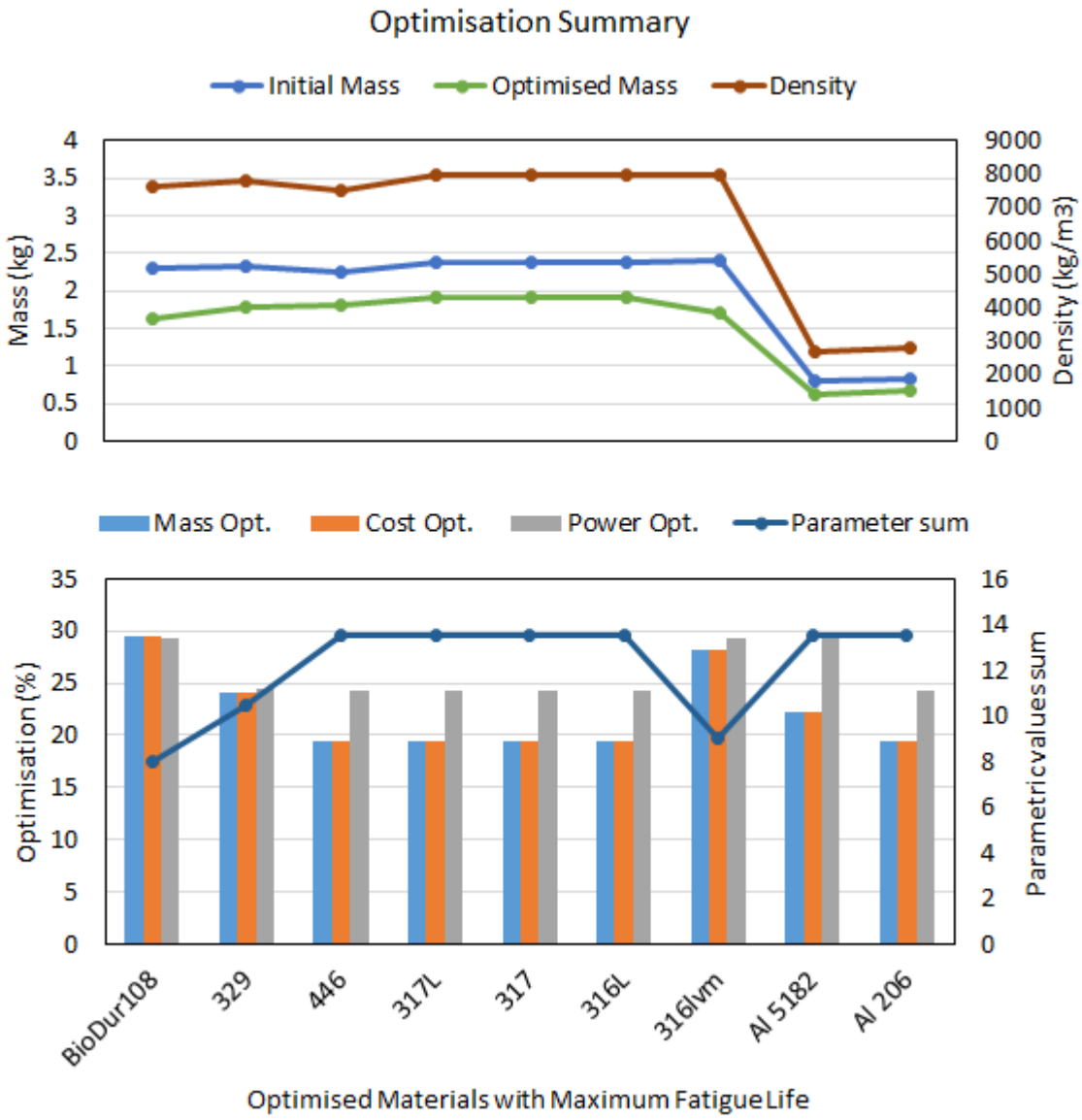

Figure 6.16: Optimisation summary of piston-shaft assembly w.r.t. optimum materials.

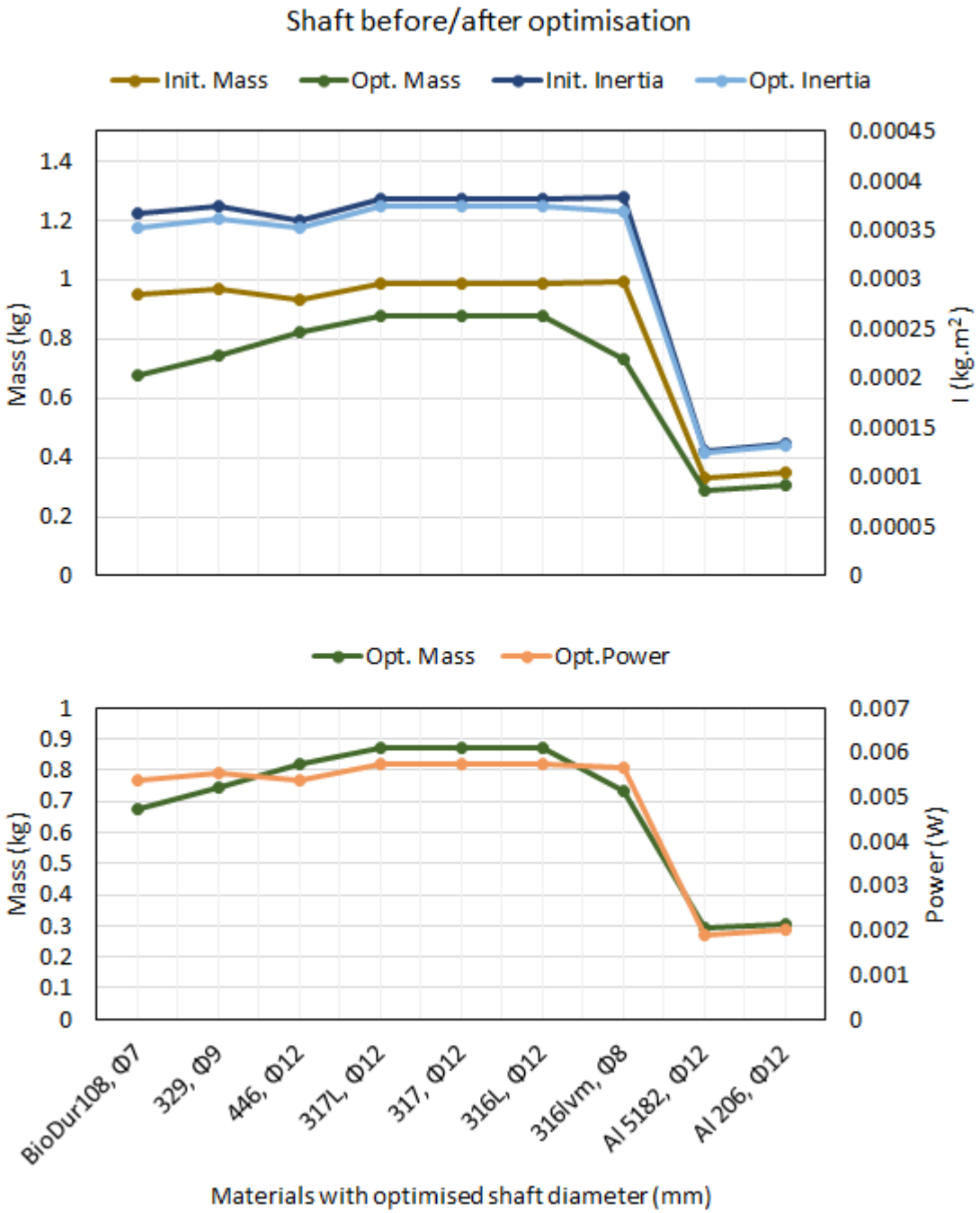

Figure 6.17: Optimisation summary of shaft w.r.t. optimised materials; mass and inertia (top), optimised mass and power (bottom).

The mass optimisation process described in this study is based on maximum life constraint i.e. the fatigue strength of materials which optimally reduces the mass of components contrary to only yield strength criteria.

Additionally, the method incorporates the geometrical parametric mass optimisation with components performance factors i.e. material cost, mass and energy consumption coupled with material variation and selection. The optimisation process developed in this study is slightly an improved version of weight optimisation techniques found in literature studies such as [79,81–85], where FE technique is solely based on optimising the geometries within the safe yield or tensile limits of material failure either by reducing dimensions or by randomly removing unwanted material allocation by producing different time consuming design concepts. However, Saoudi et al. [80] optimised mass based on fatigue failure constraint but lacked material optimisation. This current study's mass optimisation method could assist designers or engineers to have best suitable material along with a flexibility of providing other possible candidates.

6.2.6 Comparison of Parametric Optimised Results with Material Selection Process

The results from parametric analysis were compared with the material selection process to check their validity. The material selection criteria for stainless steels from CES program is shown as bubble chart in Chapter 5, see Figure 5.2. The chart x-axis increment shows stiff, lighter and cheaper while y-axis increment shows stronger and cheaper materials. In material selection process, trade-off was made for '446' stainless steel than 'BioDur 108' due its less weight and cost and reasonable strength. However, parametric analysis shows the best material with best optimum dimensions for overall less mass,

less cost and less power requirement is ‘BioDur 108’ which being slightly expensive and weighs a little more than ‘446’, provided more variation in parametric values by passing the optimisation failure criteria for its infinite life due to its high strength mechanical properties. This is why it is found to be the ‘first contender’ in the parametric analysis which also validates the material selection process. Although ‘446’ passed almost all parametric analyses with high parametric values than ‘BioDur 108’, it is slightly heavier, more expensive and more power consuming candidate. If both ‘BioDur 108’ and ‘446’ had same optimised parametric values then, ‘446’ would have been the winner as per the material selection process adopted. Similarly, both aluminium grades, ‘AL 206’ and ‘AL 5182’ passed the optimisation process with the later coming as the dominant contender over the other. However, ‘AL 206’ was selected on trade-off during the material selection process because of slightly higher strength. This is better understood by comparing the pass fatigue safety factors for all components between AL 5182 and AL 206 i.e. 1.30 and 1.31 for piston head, 1.25 and 1.26 for shaft diameter and 1.01 and 1.08 for slider diameter respectively. These values are so close meaning that the ‘AL 206’ was a satisfactory decision in material selection. However, in mass optimisation ‘AL 5182’ being slightly lighter dominates along with performance factors. Hence, this shows the importance of this method where optimisation evolves with material selection based on fatigue performance.

6.3 Further Extension of the Optimisation Process and Limitations

In previous sections, the optimisation model had the focus on just critical locations of piston-shaft assembly due to limitation of available time and resources. The components were optimised for reducing weight so that less power is consumed in their operation. The optimisation model can further be extended with the whole same process to cover up all geometrical aspects of the components. The optimisation process can also be applied to other pump components such as covers and main casing body for optimising the weight or overall pump cost. For instance, the total mass of the pump components with 'BioDur 108' per initial design is 25.9 kg (see Table 5.10), however, this could be reduced with mass optimisation further. Also, if the front manifold and casing back cover were used with composite 'PA66-60gf', then initial design mass reduces to 19.4 kg. Comparatively, this is less than the conventional high head (up to 200 m or higher) pumps e.g. 94.2 kg of 'Grundfos SP8A-37' [38], 78 kg of 'Lorentz PS9kc-CJ8-44' [39], or can be competitive after optimisation with 13 kg of 'Lorentz PS2-1800HR-05HL' [37]. The associated material cost would also reduce further.

In the optimisation process, loading was kept constant, however, variation in loading can also be implemented to have variation in optimised geometries. This gives flexibility of the optimisation process.

However, there are some limitations for the optimisation process which is driven by constraints. For instance, shaft main diameter parameterisation was only restricted to values which are acceptable for manufacturing process i.e. fitting of commercial bearings on the shaft diameter. Similarly, some dimensions

may not be parametrized more than the size constraints of boreholes where placing whole pump is a challenge. This means that without such constraints a parametric value in optimisation could be any theoretically but due to the limitations (such as bearings diameter or borehole size), the value is only restricted to them.

6.4 Conclusion

Geometrical optimisation is important for an initial design of any conceptual model in development as it is linked to mass reduction which in turn is connected to the material cost and performance factors such as energy, power, efficiency etc. In this chapter, an advancement in mass optimisation methodology is introduced with a multi-objective process which includes maximum fatigue life and minimum mass, material cost and power consumption by concept pump components with respect to different materials. This allows the mass optimisation process to conclude with optimum geometrical parameters with best suitable materials with fatigue life as an important constraint. The advantage is to have components designs with optimised mass for maximum life where geometric optimisation evolves with material selection.

Optimising the piston and shaft components initial designs, certainly optimised power consumption as well. The optimisation model found stainless steel 'BioDur 108' as the overall best material with least values of optimised dimensions in the whole process whether within geometrical parametric analysis or mass and material cost savings or the power consumption. The study noticed that up to 29.39% mass, 29.39% material cost reductions along with 29.25%

improvement in power consumption for the components. This could be further increased considering full geometrical optimisation.

Furthermore, the optimisation model is flexible in terms of loading, geometrical parameters and materials set size but commercial constraints may limit the extent of parametrization such as manufacturing, operational constraints etc. which must also be incorporated with the process to remain as realistic as possible to avoid uncertainty during these phases.

CHAPTER 7

CONCLUSIONS AND RECOMMENDATIONS

7.1 Conclusions

In rural remote regions, SPWPS is a cost-effective option to fetch groundwater located hundreds of metres beneath the ground surface. High head requirements for such regions prevails (such as 200 m) with limited borehole size of 10-inch. Two types of groundwater pumps used are centrifugal and positive displacement (PD) pumps. Centrifugal pumps perform optimally for a specific head and flowrate, whereas, positive displacement piston pumps are independent of head and offers versatility whenever the head changes.

The PD pumps compared to centrifugal pumps offer high efficiency and low power consumption for high head application. A few attempts have been made to alter piston pump designs for design simplicity or to improve SPWPS output which include induced flow and linear actuators pumps' concepts. Induced flow pump is unsuitable for high heads and linear actuator pumps are less efficient with built-in complex electronics which are prone to leakage. The unsubmerged linear actuator concept with conventional long piston drive rod is costly, difficult to install or disassemble during maintenance and acts as a load bearing component significantly affecting pump power and ultimately the PV source. Therefore, new groundwater piston pump design is much needed in groundwater sector.

In this study, a new design of a groundwater piston pump design is developed which is optimised for low power consumption for high head SPWPS

in rural remote areas. The structural adequacy of the proposed concept design is also checked by FE analysis, material selection and design optimisation. The proposed pump does not include any of the above noted limitations and offers significantly simplified option to optimise the power consumption for higher head SPWPS i.e. no complex electronics and less power consuming parts such as long piston drive rod or internal components (crossheads, crossways, connecting rod, meshing gears etc.).

First, widely used CAD technique was used to develop the initial concept pump 3D model within a limited 10-inch borehole size constraint for rural remote regions. The model was developed with a horizontal oval piston directly engaged with the vertical motor drive shaft using scotch yoke mechanism which eliminated the use of long piston drive rod and internal components. A mathematical model was also developed to calculate the power sizing of the conceptual pump with respect to 200 m head and 34.72 lpm flow demands. The model is applicable to piston rod or non-piston groundwater pumps. The model was twice validated with two referenced long piston rod pumps.

Eliminating the long piston rod saves power depending on the rod material. For instance, for 200 m head and 10.2 lpm, concept pump has 7% and 22.4% less power consumption compared to GFRC and steel rods, respectively. The hydraulic efficiency of concept pump for the same head is estimated to be 76.7% compared to 71.4% using GFRC rod and 59.5% steel rod. Additionally, significant energy savings are also observed without using long piston rods, for instance compared to lighter GFRC rod at 122 m head, up to 243.2 W daily savings can be achieved, a value near to that of a 250 W solar panel costing from £227 - £300. No use of piston rod also saves its associated cost as well

e.g. savings of $1600 (£1227.1) GFRC rod with 400 pieces for 122 m head. This would further save installation and maintenance costs and time. The mathematical model results also predicted lower power consumption and higher hydraulic efficiency by the concept pump compared to commercially available solar operated groundwater pumps including piston rod, positive displacement and centrifugal pumps with same head and flow (see Table 3.5). For 200 m head and 34.72 lpm, an estimated power of 1.67 kW is evaluated for the concept pump as per actual design specifications or requirements for rural remote regions. With seen significant savings from the concept pump against the piston rod pumps, the 3D CAD model was then set to be analysed structurally to check its load bearing capacity for high heads (such as 200 m).

Secondly, widely used FEA method was used to analyse the initial design of concept pump model under the maximum load of 200 m. Steady state structural analyses was performed on pump components as the maximum load is constant at every cycle of pump operation. The piston and shaft being the main driver of the concept design were analysed with five variants with changes in the mid-web section for piston and shaft with and without lower section. It was observed that hybrid nature of both piston and shaft components exhibited lesser deformations and stresses than the variants (see Figures 4.23 – 4.27). The contact region between the piston and shaft showed highest stress followed by the shaft top middle section i.e. 604.5 MPa and 147.4 MPa respectively.

Apart from the contact region, all components were found to be under acceptable yield safety factor values (common among literature studies) i.e. 1.4, 3.6, 1.62 and 15 for shaft, casing main body, front cover with manifold and back cover, respectively. The contact yield safety factor for the contact region

was 0.61. The FE results were also validated with analytical approach and compared with published research studies. The verification was carried out with mesh sensitivity analysis and discretisation error estimation. The maximum stress energy error was found to be 3.3e-4%. Overall, the FE analysis of initial pump design suggested all components are under the materials elastic limit except the piston-shaft contact region which acted as a limitation. This was further improved with material selection process or change in slider diameter or both.

In order to have suitable material candidates for the concept pump components, material selection process was carried out for high strength and stiffness properties with respect to low cost and weight using 'CES selector' a well maintained, accurate database and with graphical chart selection method. The selection process incorporated performance factors of the components such as shape and loading conditions (bending, torsional) along with other attributes such as corrosion resistance, ductility index, toughness, shear modulus etc. The moving pump parts involving piston, shaft and main casing body with cylinder were searched for metals such as steel and aluminium alloys while non-moving parts i.e. front manifold and back cover are additionally searched for polymers or composites materials for weight reduction. 'AISI 446', 'AL A206 T7' and 'PA66-60% glass fibre' were selected from the stainless steel, aluminium and composite groups, respectively.

The material selection process was validated in three stages; first with CES data authenticity, second with TOPSIS method and finally with FE simulations implemented with fatigue analysis. As per the FE results, a single stainless-steel grade is recommended for all components with lower

deformations than a lighter aluminium grade. However, the pump casing front manifold can be used with composite materials rather than stainless steel to reduce costs and weight of the entire pump. Overall, 'AISI 446' was found to be suitable for all the components (for 200 m head loading) with maximum fatigue life, however, slider diameter of 10 mm (at piston-shaft contact region) still was not sufficient to meet fatigue criteria. Thus, implementation of FE analysis based on fatigue analysis proved to be an important criterion in material selection process. Furthermore, the selection process has flexibility to include higher strength materials as per load increment or vice versa.

The material selection process opted out the suitable candidates, however, the selection process along with FE analysis was carried out on the initial design of the pump components. The design still needed to be optimised for mass optimisation which in turn is linked to material cost and power consumption, or optimisation of areas with above yield limit stresses such as found in piston-shaft contact region. The mass optimisation method was incorporated with a multi-objective process which included maximum fatigue life, minimum mass, cost and power consumption with selected materials from the material selection process. The advantage of such process was to have components' designs with optimised mass for maximum life where geometric optimisation evolves with material selection.

The optimisation model developed optimally reduces the mass with optimum safety factors contrary to yield strength criteria. Piston and shaft which are the power consuming components were optimised for mass. The optimisation process resulted in optimum geometrical parameters with best suitable material under important constraint of maximum fatigue life. Stainless

steel ‘BioDur 108’ was noted to be the overall best material candidate with least dimensions than ‘AISI 446’ saving 29.39% of mass and cost, along with 29.25% reduction in power consumption. ‘BioDur 108’ is also found to be a better candidate compared to traditionally used ‘AISI 316 and 316L’ with up to 43.4% less expensive and 4.13% lighter. However, the optimisation analysis was only limited to critical locations of the piston-shaft components, and it could be extended to the whole design of these components. Furthermore, similar to the material selection process, the optimisation process is flexible in terms of load, geometrical parameters and materials set size, however, commercial constraints limit the extent of optimisation such as manufacturing, operational constraints etc. to remain as realistic as possible to avoid uncertainty during these phases.

Based on the identified objectives for this research study (see Section 1.3), following conclusions are drawn.

- A low power concept groundwater piston pump is developed using scotch-yoke mechanism eliminating long piston drive rods and internal components.
- The low power consumption claim for the concept pump is verified by the mathematical model. The model calculated up to 22.4% and 7% reduction in power consumption for the same head and flowrate by the concept pump when compared with a traditionally used long-piston steel and GFRC rods pump, respectively. Increase in hydraulic efficiency is also observed compared to steel and GFRC rod pump.

- The FE structural analysis of the developed concept pump components revealed performance safety factors within the safe limits under the high head load such as 200 m i.e. 1.4, 3.6, 1.62 and 15 for shaft, casing main body, front cover with manifold and back cover, respectively. However, the contact yield safety factor for the contact region was found to be 0.61 which was identified as the region of interest for optimisation either by using high strength material or geometrical modification or both.

- The search for low mass and high strength material revealed 'AISI 446', 'AL A206 T7' and 'PA66-60% glass fibre' as suitable candidates from the stainless steel, aluminium and composite groups, respectively. Stainless steel was recommended for moving components such as piston, shaft and main casing body, while composite for casing parts to shed overall pump mass.

- The mass optimisation of the initially developed concept pump model with respect to maximum fatigue life under high head load revealed 'AISI BioDur108' as the best candidate - saving 29.39% of mass and cost, along with 29.25% reduction in power consumption. 'BioDur 108' was also found to be a better candidate compared to traditionally used 'AISI 316 and 316L' with up to 43.4% less expensive and 4.13% lighter.

In summary, the outcome of the study is a new concept of groundwater piston pump design with estimated low power consumption for high head (such as 200 m) SPWPS applications under limited borehole size constraint (10 inches), normal conditions found in rural remote regions (such as Nairobi, Kenya). The developed model was subjected to FE structural analysis for such

load with detailed material selection and optimised for maximum mass reduction in order to optimise for cost and power consumption. An advancement in mass optimisation methodology relevant to SPWPS was introduced with a multi-objective process which includes maximum fatigue life and minimum mass, material cost and power consumption by concept pump components with respected to different materials. This new routine allows the mass optimisation process to conclude with optimum geometrical parameters with best suitable material with fatigue life as an important constraint. A 3D printed model was also tested experimentally for mechanism and submerged operational testing of the full scaled pump. The concept groundwater pump is structurally suitable for rural areas with high head application. The pump can also be used for other locations as well depending on its ability to withstand head loads with suitable materials and design changes if needed.

7.2 Recommendations

The recommendations for further study and room for improvements include;

- The 3D model of the pump can be subjected to some fine refinements such as tolerances or minute dimensional changes which may be needed during the manufacturing phase in future which may include CAM processes such as computer aided machining or metal 3D printing process.
- Material selection process was carried out using CES Selector which is based on ranges and average values from various sources. Although, CES

data being in good agreement with the commercial supplier's data, yet for actual manufacturing of the pump and its components, real commercial material data sheets should be surveyed for selection and should be used in the simulations. Further attributes can also be incorporated in the selection such as temperature, environmental factors, etc.

- The FE analyses can be verified experimentally with manufactured components with selected materials and under the same loading conditions.
- Mass optimisations can be extended to the whole pump i.e. on all components which would contribute to the light-weighted design and material cost savings.
- Future FE dynamic analyses with fluid and structural interaction can be carried out on the whole pump model with all components built as an assembly in order to have more realistic results of the design. However, such analyses would require a high specifications performance computer.
- The failure modes and effects analysis can be carried out on the pump design to discover potential failures.
- Further analyses can include seal abrasion analysis which would assist to determine the optimum speed of the concept pump in relation with the optimum seal life.

- With no borehole size limitation, diversity in product design and development for groundwater pumps and other types of applications e.g. oil and gas sector can also be considered.

REFERENCES

1. United Nations Development Programme; Clean water and sanitation Available online: https://www.undp.org/content/undp/en/home/sustainable-development-goals/goal-6-clean-water-and-sanitation.html (accessed on Mar 9, 2020).

2. United Nations Development Programme; Industry, innovation and infrastructure Available online: https://www.undp.org/content/undp/en/home/sustainable-development-goals/goal-9-industry-innovation-and-infrastructure.html (accessed on Mar 9, 2020).

3. United Nations Development Programme; Affordable and clean energy Available online: https://www.undp.org/content/undp/en/home/sustainable-development-goals/goal-7-affordable-and-clean-energy.html (accessed on Mar 9, 2020).

4. Daima Energy Ltd. Industrially accepted practices for African regions 2017.

5. Al-Smairan, M. Application of photovoltaic array for pumping water as an alternative to diesel engines in Jordan Badia, Tall Hassan station: Case study. *Renew. Sustain. Energy Rev.* **2012**, *16*, 4500–4507.

6. Wade, N.S.; Short, T.D. The performance of a new positive displacement

pump targeted to improve rural water supplies. *Proc. Inst. Mech. Eng. Part A J. Power Energy* **2007**, *221*, 1163–1171.

7. Short, T.D.; Thompson, P. Breaking the mould: solar water pumping - the challenges and the reality. *Sol. Energy* **2003**, *75*, 1–9.

8. Purcell, J.E.; Silvaggio, J. a. A comparison of positive displacement and centrifugal pump applications. *Proc. 14th Int. pump users Symp.* **1997**, 99–104.

9. Yoshizawa, T.; Nango, J.; Koguchi, T. Experimental analysis of a water-pump driving mechanism using an orthogonal double-slider joint. *Mech. Eng. J.* **2016**, *3*, 15–551.

10. Protogeropoulos, C.; Pearce, S. Laboratory evaluation and system sizing charts for a "second generation" direct pv-powered, low cost submersible solar pump. *Sol. Energy* **2000**, *68*, 453–474.

11. Chandel, S.S.; Naik, M.N.; Chandel, R. Review of performance studies of direct coupled photovoltaic water pumping systems and case study. *Renew. Sustain. Energy Rev.* **2017**, *76*, 163–175.

12. Ould-Amrouche, S.; Rekioua, D.; Hamidat, A. Modelling photovoltaic water pumping systems and evaluation of their CO2 emissions mitigation potential. *Appl. Energy* **2010**, *87*, 3451–3459.

13. Gopal, C.; Mohanraj, M.; Chandramohan, P.; Chandrasekar, P. Renewable energy source water pumping systems—A literature review. *Renew. Sustain. Energy Rev.* **2013**, *25*, 351–370.

14. Dhiaa Halboot, M.; Tamer, K.; Farrukh, N. A review of photovoltaic water

pumping system designing methods, control strategies and field performance. *Renew. Sustain. Energy Rev.* **2017**, *68*, 70–86.

15. Sontake, V.C.; Kalamkar, V.R. Solar photovoltaic water pumping system - A comprehensive review. *Renew. Sustain. Energy Rev.* **2016**, *59*, 1038–1067.

16. Chandel, S.S.; Nagaraju Naik, M.; Chandel, R. Review of solar photovoltaic water pumping system technology for irrigation and community drinking water supplies. *Renew. Sustain. Energy Rev.* **2015**, *49*, 1084–1099.

17. Grundfos The Centrifugal Pump Available online: http://machining.grundfos.com/media/16620/the_centrifugal_pump.pdf (accessed on Mar 11, 2020).

18. Karassik, I.J. Pump Handbook. In; 2011; pp. 3.30-3.32.

19. BlackhawkCo. Blackhawk Apollo Piston Pumps Available online: www.blackhawkco.com (accessed on Jun 6, 2017).

20. Ramos, J.S.; Helena M., R. Solar powered pumps to supply water for rural or isolated zones: A case study. *Energy Sustain. Dev.* **2009**, *13*, 151–158.

21. GSES Australia; *Solar water pumping guide*; First Edit.; 2015;

22. Bucher, W. Aspects of solar water pumping in remote regions. *Energy Sustain. Dev.* **1996**, *3*, 8–27.

23. Ranjan, P.; Pokharel Govind, R.; Ostergaard Poul, A. A comparison of diesel, bio diesel and solar PV - based water pumping systems in the

context of rural Nepal. *Int. J. Sustain. Energy* **2014**, *33*, 536–53.

24. Bannister, M. Solar power for community water supply. In Proceedings of the 26th WEDC Conference—Water, Sanitation and Hygiene: Challenges of the Millennium, Dhaka, Bangladesh; 2000; pp. 311–314.

25. Daud, A.-K.; Marwan M., M. Solar powered induction motor-driven water pump operating on a desert well, simulation and field tests. *Renew. Energy* **2005**, *30*, 701–714.

26. Hamidat, A.; Benyoucef, B.; Hartani, T. Small-scale irrigation with photovoltaic water pumping system in Sahara regions. *Renew. Energy* **2003**, *28*, 1081–1096.

27. Aliyu, M.; Hassan, G.; Said, S.A.; Siddiqui, M.U.; Alawami, A.T.; Elamin, I.M. A review of solar-powered water pumping systems. *Renew. Sustain. Energy Rev.* **2018**, 61–76.

28. Setiawan, A.A.; Purwanto, D.H.; Pamuji, D.S.; Huda, N. Development of a Solar Water Pumping System in Karsts Rural Area Tepus, Gunungkidul through Student Community Services. *Energy Procedia* **2014**, *47*, 7–14.

29. Benghanem, M.; Daffallah, K.O.; Alamri, S.N.; Joraid, A.A. Effect of pumping head on solar water pumping system. *Energy Convers. Manag.* **2014**, *77*, 334–339.

30. Benghanem, M.; Daffallah, K.O.; Joraid, A.A.; Alamri, S.N.; Jaber, A. Performances of solar water pumping system using helical pump for a deep well: A case study for Madinah, Saudi Arabia. *Energy Convers. Manag.* **2013**, *65*, 50–56.

31. Posorski, R. Photovoltaic Water Pumps, An Attractive Tool For Rural Drinking Water Supply. *Sol. Energy* **1996**, *58*, 155–163.

32. Lorentz; *Solar-powered Drinking Water Pumps for Communities, Case Study 6*; Garissa County, Kenya, 2013;

33. Protogeropoulos, C.; Tselikis, N. Technical evaluation of a low cost, low power photovoltaic water pumping system and comparison assessment with a typical marketed PV pump. *Proc. 14th EC Photovolt. Sol. energy Conf.* **1997**, 2542–2545.

34. Vick, B.; Clark, R. Determining the optimum solar water pumping system for domestic use, livestock watering or irrigation. *Proc. from 38th ASES Annu. Conf.* **2009**, *4*, 2212–2239.

35. Burton, J.D.; Short, T.D. Induced flow reciprocating pumps Part 1. *Proc. Inst. Mech. Eng. Part A, IMechE* **1999**, *213*, 363–373.

36. Grundfos SQF 2.5-2 Available online: https://product-selection.grundfos.com (accessed on Sep 5, 2019).

37. Lorentz PS2-1800 HR-05HL Available online: https://lorentzpumps.co.za/product/ps2-1800-hr-05hl/ (accessed on Sep 5, 2019).

38. Grundfos SP8A-37 Available online: https://product-selection.grundfos.com (accessed on Sep 5, 2019).

39. Lorentz PSK2-9C-Sj8-44 Available online: https://lorentzpumps.co.za/product/psk2-9-c-sj8-44/ (accessed on Sep 5, 2019).

40. Wade, N.S.; Short, T.D. Optimization of a linear actuator for use in a solar powered water pump. *Sol. Energy* **2012**, *86*, 867–876.

41. Xin, Q.; Xin, Q. Friction and lubrication in diesel engine system design. *Diesel Engine Syst. Des.* **2013**, 651–758.

42. Andrada, P.; Castro, J. Solar photovoltaic water pumping system using a new linear actuator. *Renew. Energy Power Qual.* **2007**, *5*, 321–326.

43. Wade, N.S.; Short, T.D. Behaviour of a linear actuator for use in a low technology solar water pump. *Proc. 3rd IET Int. Conf. power Electron. Mach. drives* **2006**, 182–186.

44. Short, T.; Oldach, R. Solar powered water pumps: the past, the present and the future. *J. Sol. Energy Eng.* **2003**, *125*, 76–82.

45. Short, T.D.; Burton, J.D. The benefits of induced flow solar powered water pumps. *Sol. Energy* **2003**, *74*, 77–84.

46. Fiaschi, D.; Graniglia, R.; Manfrida, G. Improving the effectiveness of solar pumping systems by using modular centrifugal pumps with variable rotational speed. *Sol. Energy* **2005**, *79*, 234–244.

47. Chen, X.; Liu, Y. *Finite Element Modeling and Simulation with ANSYS Workbench*; CRC Press, 2015;

48. Guangjie, P.; Zhengwei, W.; Zongguo, Y.; Ruixiang, L. Strength analysis of a large centrifugal dredge pump case. *Eng. Fail. Anal.* **2009**, *16*, 321–328.

49. Golbabaei Asl, M.; Torabi, R.; Nourbakhsh, S.A. Experimental and FEM failure analysis and optimization of a centrifugal-pump volute casing.

Eng. Fail. Anal. **2009**, *16*, 1996–2003.

50. Lienau, W.; Welschinger, T. Finite element testing – a solution to deformation in HPDM pumps. *World Pumps* **2007**, *2007*, 30–31.

51. Mohammadian, Z.; Ayremlouzadeh, H.; Doniavi, A. Numerical investigation on the effect of mold design on shrinkage of sand casted multistage BB3-6×6 pump casing. *Int. J. Eng.* **2016**, *29*.

52. Rezvani, M.; Strehlow, J.; Baliga, R. Structural analysis and evolution of a mixer pump in a double-shell tank at the hanford site. In Proceedings of the 4th Department of energy natural phenomena hazards mitigation conference; 1993.

53. Bachche, P.J.; Tayade, R.M. Finite element analysis of shaft of centrifugal pump. *IOSR J. Mech. Civ. Eng.* **2013**, *7*, 37–42.

54. Cho, I.S. A study on the optimum design for the valve plate of a swash plate-type oil hydraulic piston pump. *J. Mech. Sci. Technol.* **2015**, *29*, 2409–2413.

55. Du, H.; Carlson, D.J. Fatigue life improvement of the roller swashplate bearing of an axial swashplate type piston pump 2014.

56. Zloto, T.; Stryjewski, P. Modeling the load of the kinematic pair piston-cylinder in an axial piston pump by means of FEA. In Proceedings of the Procedia Engineering; 2017.

57. Rosu, C.; Vasiliu, N. Researches on the main components of a positive displacement pump by FEM. In Proceedings of the The 2nd FPNI – PhD symposium; 2002.

58. Shannon, R. *Space shuttle main engine structural analysis and data reduction evaluation. High pressure oxidizer turbo-pump preburner pump housing stress analysis report*; 2005;

59. Sapuan, S.M.; Wright, I.M.; C.S., M. State of the art review of engineering materials selection methods. *Multidiscip. Model. Mater. Struct.* **2009**, *5*, 263–268.

60. Brifcani, N.; Day, R.; Walker, D.; Hughes, S.; Ball, K.; Price, D. A review of cutting-edge techniques for material selection. In Proceedings of the 2nd International Conference on Advanced Composite Materials and Technologies for Aerospace Applications; 2012; pp. 58–64.

61. Qian, J.; Zhao, Y.-P. Materials selection in mechanical design for microsensors and microactuators. *Mater. Des.* **2002**, *23*, 619–625.

62. Guisbiers, G.; Van Overschelde, O.; Wautelet, M. Materials selection for thin films for radio frequency microelectromechanical systems. *Mater. Des.* **2007**, *28*, 1994–1997.

63. Guisbiers, G.; Wautelet, M. Materials selection for micro-electromechanical systems. *Mater. Des.* **2007**, *28*, 246–248.

64. Parate, O.; Gupta, N. Material selection for electrostatic microactuators using Ashby approach. *Mater. Des.* **2011**, *32*, 1577–1581.

65. Rashedi, A.; Sridhar, I.; Tseng, K.J. Multi-objective material selection for wind turbine blade and tower: Ashby's approach. *Mater. Des.* **2012**, *37*, 521–532.

66. Weaver, P.M.; Ashby, M.F.; Burgess, S.; Shibaike, N. Selection of

materials to reduce environmental impact: a case study on refrigerator insulation. *Mater. Des.* **1996**, *17*, 11–17.

67. Colmek, S.; Cope, B.; Chabrillat, A.-L. How Tecumseh use systematic materials selection to reduce costs while enhancing quality and reliability.

68. Fredriksson, C.; Galos, J. *Truck trailer lightweighting*; 2017;

69. Thakker, A.; Jarvis, J.; Buggy, M.; Sahed, A. A novel approach to materials selection strategy case study: Wave energy extraction impulse turbine blade. *Mater. Des.* **2008**, *29*, 1973–1980.

70. Ermolaeva, N.S.; Kaveline, K.G.; Spoormaker, J.L. Materials selection combined with optimal structural design: concept and some results. *Mater. Des.* **2002**, *23*, 459–470.

71. van Kesteren, I.E.H. Product designers' information needs in materials selection. *Mater. Des.* **2008**, *29*, 133–145.

72. Ramalhete, P.S.; Senos, A.M.R.; Aguiar, C. Digital tools for material selection in product design. *Mater. Des.* **2010**.

73. Ashby, M.F.; Bréchet, Y.; Cebon, D. Selection strategies for materials and processes. *Adv. Eng. Mater.* **2002**, *4*, 327–334.

74. Jahan, A.; Ismail, M.Y.; Sapuan, S.M.; Mustapha, F. Material screening and choosing methods – A review. *Mater. Des.* **2010**, *31*, 696–705.

75. Çalişkan, H.; Kurşuncu, B.; Kurbanoĝlu, C.; Güven, şevki Y. Material selection for the tool holder working under hard milling conditions using different multi criteria decision making methods. *Mater. Des.* **2013**.

76. Yazdani, M.; Payam, A.F. A comparative study on material selection of microelectromechanical systems electrostatic actuators using Ashby, VIKOR and TOPSIS. *Mater. Des.* **2015**, *65*, 328–334.

77. Barea, R.; Novoa, S.; Herrera, F.; Achiaga, B.; Candela, N. A geometrical robust design using the Taguchi method: application to a fatigue analysis of a right angle bracket. *DYNA* **2018**, *85*, 37–46.

78. Roylance, D. Fatigue. In; 2001; pp. 1–9.

79. Lee, D.G.; Or, S.W.; Carman, G.P. Design of a piezoelectric-hydraulic pump with active valves. *J. Intell. Mater. Syst. Struct.* **2004**, *15*, 107–115.

80. Saoudi, A.; Bouazara, M.; Marceau, D. Study of the fatigue life and weight optimization of an automobile aluminium alloy part under random road excitation. *Shock Vib.* **2010**, *17*, 107–121.

81. Ruiqiang, Q. Weight optimization of stiffened cylinders under axial compression. *Comput. Struct.* **1985**, *21*, 945–952.

82. Thejasree, P.; Dileep Kumar, G.; Leela Prasanna Lakshmi, S. Modelling and analysis of crankshaft for passenger car using ANSYS. *Mater. Today Proc. vol. 4* **2017**, 11292–11299.

83. Gopinath, D.; Sushma, C. V. Design and optimization of four wheeler connecting rod using finite element analysis. *Mater. Today Proc. vol. 2* **2015**, 2291–2299.

84. Neelakandan, V.; Ganesan, T.; Rao, P.C. Weight optimization of housing bracket for electrical starter motor using FEA. *Procedia Struct. Integr.*

2019, *14*, 345–353.

85. Kirthana, S.; Nizamuddin, M.K. Finite element analysis and topology optimization of engine mounting bracket. *Mater. Today Proc.* **2018**, *5*, 19277–19283.

86. Elhewy, A.M.H.; Hassan, A.M.A.; Ibrahim, M.A. Weight optimization of offshore supply vessel based on structural analysis using finite element method. *Alexandria Eng. J.* **2016**, *55*, 1005–1015.

87. COMSOL Inc. Material Fatigue Available online: https://uk.comsol.com/multiphysics/material-fatigue (accessed on Dec 27, 2019).

88. Sumitomo Drive Technologies; Comparison of gears efficiencies Available online: http://www.smcyclo.com/modules.php?name=Documents&op=viewlive&sp_id=57 (accessed on Sep 13, 2019).

89. KHK Stock Gears; Gear types and characteristics Available online: https://khkgears.net/new/gear_knowledge/abcs_of_gears-b/gear_types_and_characteristics.html (accessed on Sep 13, 2019).

90. Ahmed Ali, M.; Xianjun, H.; Turkson, R.; Ezzat, M. An analytical study of tribological parameters between piston ring and cylinder liner in internal combustion engines. *Proc. Inst. Mech. Eng. Part K J. Multi-body Dyn.* **2015**, *230*.

91. MIT University; Engine friction and lubrication Available online: http://web.mit.edu/2.61/www/Lecture notes/Lec. 19 Friction and

tribology.pdf (accessed on Mar 9, 2020).

92. Honda Motor Co. The Oval Piston Engine Available online: https://global.honda/heritage/episodes/1979pistonengine.html (accessed on Jan 23, 2020).

93. Ward, W. Oval pistons Available online: https://www.highpowermedia.com/Archive/oval-pistons (accessed on Jan 23, 2020).

94. Schaeffler UK; Available online: www.schaeffler.co.uk (accessed on Aug 9, 2019).

95. American Roller Bearing Company (AMROL); Friction and frequency factors Available online: https://www.amroll.com/friction-frequency-factors.html (accessed on Sep 16, 2019).

96. SKF Bearings; Steel on steel sliding Friction Available online: https://www.skf.com/uk/products/bearings-units-housings/plain-bearings/general/selection-and-application/friction/index.html (accessed on Sep 16, 2019).

97. British Stainless Steel Association (BSSA); Frictional properties of stainless steel Available online: https://www.bssa.org.uk/topics.php?article=99 (accessed on Jan 22, 2020).

98. Arakelian, V.; Baron, J.-P. Le; Mkrtchyan, M. Design of scotch yoke mechanisms with improved driving dynamics. *Proc. Inst. Mech. Eng. Part K J. Multi-body Dyn.* **2016**, *230*, 379–386.

99. Ward, W. The scotch yoke Available online: https://www.highpowermedia.com/Archive/category/con-rods/the-scotch-yoke (accessed on Jan 24, 2020).

100. Edgar, J. The SyTech scotch yoke engine Available online: http://www.autospeed.com/cms/article.html?&title=The-SyTech-Scotch-Yoke-Engine&A=0948 (accessed on Jan 24, 2020).

101. Kirk, J.D. Design of a two-stroke cycle spark ignition engine employing a scotch-yoke crankshaft mechanism. *SAE Trans.* **1985**, *94*, 654–670.

102. Wang, X.; A., S.; Watson, H. Two-dimensional lubrication analysis and designoptimization of a Scotch Yoke engine linear bearing. In Proceedings of the Proceedings. Part C: Journal of Mechanical Engineering Science; Institution of Mechanical Engineers, 2006; pp. 1575–1587.

103. *Personal Conversation with Daima Energy Ltd.*; 2017;

104. Pipe flow (fluid thinking software solutions); Pipe Roughness Available online: https://www.pipeflow.com/pipe-pressure-drop-calculations/pipe-roughness.

105. Pumps&Systems; Reciprocating pumps vs centrifugal pumps (efficiency) Available online: https://www.pumpsandsystems.com/topics/pumps/reciprocating-pumps/reciprocating-pumps-vs-multi-stage-centrifugal-pumps?page=2 (accessed on Sep 5, 2019).

106. Graco Inc. *Two-check and priming piston pumps*; First.; 1996;

107. Dotmar Plastic Solutions; Dotmar engineering thermopastics coefficient of friction (polystone ultra) Available online: http://www.dotmar.com.au/products.php?p=378 (accessed on Sep 5, 2019).

108. RS Components UK. Available online: uk.rs-online.com (accessed on Aug 5, 2019).

109. Zhang, Z.; Zhang, W.; Zhai, Z.J.; Chen, Q.Y. Evaluation of various turbulence models in predicting airflow and turbulence in enclosed environments by CFD: Part 2—comparison with experimental data from literature. *HVAC&R Res.* **2007**, *13*, 871–886.

110. Photonic Universe Ltd. 250W 12V solar panel Available online: https://www.photonicuniverse.com/en/catalog/full/366-250W-12V-solar-panel-with-5m-cable-German-solar-cells.html (accessed on Jan 21, 2020).

111. CCL Components Ltd. Panasonic 250W solar module Available online: https://www.cclcomponents.com/panasonic-hit-n250-250w-hybrid-solar-module-black-frame-white-backsheet (accessed on Feb 21, 2020).

112. Anders, N. *Deep well, low flow photovoltaic water pumping system design*; 2008;

113. Mahendra; Solar submersible pumps S.A.S series Available online: www.mahendrapumps.in (accessed on Mar 11, 2020).

114. Grundfos solar submersible pumps Available online: www.grundfos.com.

115. Miller, J.E. *The reciprocating pump*; 2nd ed.; 1995;

116. HMS Group. HMS Ciris borehole submersible pumps Available online: www.hms.biz.

117. Danfoss PAHT pumps Available online: www.danfoss.com.

118. Kyocera SC series pumps Available online: www.kyocerasolar.com.

119. Kyocera SD series solar pumps Available online: www.kyocerasolar.com.

120. Ansys Version 17 Available online: www.ansys.com.

121. Khurmi, R.S.; Gupta, J.K. *A textbook of machine design*; 14th ed.; 2005;

122. Kurowski, P.M. Failure Assessment Available online: http://debis.deu.edu.tr/userweb/zeki.kiral/MEE5049_2014/Failure_Assesment.pdf (accessed on Jun 6, 2018).

123. SimScale; What is von mises stress Available online: https://www.simscale.com/docs/content/simwiki/fea/what-is-von-mises-stress.html (accessed on Jun 6, 2018).

124. G. Budynas, R.; Nisbett, K.J. *Shigley's mechanical engineering design*; Tenth.; McGraw Hill, 2015;

125. P. Boresi, A.; Schmidt, J.R. *Advanced mechanics of materials*; Sixth.; John Wiley & Sons, 2003;

126. Wang, Q.J.; Zhu, D. Contact Yield. In *Encyclopedia of Tribology*; Wang, Q.J., Chung, Y.-W., Eds.; Springer US: Boston, MA, 2013; pp. 559–566 ISBN 978-0-387-92897-5.

127. Moaveni, S. *Finite Element Analysis: Theory and Application with ANSYS*; 2nd ed.; 1999;

128. Mac Donald, B.J. *Practical stress analysis with finite elements*; 2nd Editio.; 2011;

129. Fraenkel, P.L. *Water lifting devices*; FAO United Nations, 1986;

130. Bhushan, B. *Modern tribology handbook (Chapter 3)*; First.; CRC Press, 2000;

131. Sparrows Group; Gear box design analysis Available online: https://www.sparrowsgroup.com/products-and-services/engineering-support/equipment-design.html (accessed on Feb 10, 2020).

132. Shah, C. Mesh discretization error and criteria for accuracy of finite element solutions. In Proceedings of the ANSYS Users Conference; 2002.

133. Thompson, M.K.; Thompson, J.M.; Thompson, M.K.; Thompson, J.M. Meshing. *ANSYS Mech. APDL Finite Elem. Anal.* **2017**, 181–199.

134. Hale, S. How do I know if my mesh is good enough Available online: https://caeai.com/blog/how-do-i-know-if-my-mesh-good-enough (accessed on Jan 17, 2020).

135. Stevens, N. ANSYS percentage stress error Available online: https://nickjstevens.netlify.com/post/2019/ansys-percentage-stress-error/ (accessed on Jan 16, 2020).

136. GrantaDesign; CES Selector Available online: www.grantadesign.com (accessed on Mar 11, 2020).

137. ANSYS Inc. ANSYS 2020 R1 Release Highlights - Materials Available online: https://www.ansys.com/products/release-highlights (accessed on Feb 7, 2020).

138. Ashby, M. *Material selection in mechanical design*; Fourth.; Elsevier, 2010;

139. APEC Water Systems; Water quality - How salty is sea water in comparison to fresh water Available online: https://www.freedrinkingwater.com/water_quality/quality2/j-10-08-salty-seawater-comparison-with-fresh-water.htm (accessed on Feb 18, 2020).

140. Govt. of Western Australia - Department of Water and Environmental Regulation; Understanding salinity Available online: http://www.water.wa.gov.au/water-topics/water-quality/managing-water-quality/understanding-salinity (accessed on Feb 18, 2020).

141. Sampathkumar, M.; Varaprasad, D.; Kumar, V. Static Analysis of Centrifugal Blower Using Composite Material. *Int. J. Eng. Sci.* **2014**, *3*, 25–31.

142. Koshin-Ltd. ARGO MATE Thermoplastic pumps Available online: http://www.koshin-ltd.jp/english/usefultool/catalog_leaflet/pdf_ca/vol4/AGRO_MATE_21.pdf (accessed on Jun 7, 2018).

143. PSG Dover; Pneumatic diaphragm pump materials Available online: https://www.psgdover.com/en/almatec/technology/materials (accessed on Jun 7, 2018).

144. Durapump Pump Stations Available online: http://www.durapump.co.uk/dura-pump/pump-stations-overview/pump-

stations/ (accessed on Jun 7, 2018).

145. Jee Pumps; Polypropylene Pumps Available online: http://www.jeepumps.com/Polypropylene Pumps.htm (accessed on Jun 7, 2018).

146. Mackwell Pumps; Corrosion resistant polypropylene centrifugal pumps Available online: http://www.mackwellpumps.com/resistant-pp-centrifugal-pumps.html (accessed on Jun 7, 2018).

147. Plasticopumps; Polypropylene pumps Available online: http://www.plasticopumps.com/ (accessed on Jun 7, 2018).

148. Rotomech Industries; Polypropylene Pumps Available online: http://www.rotomechpump.com/polypropylene-pump.htm (accessed on Jun 7, 2018).

149. Ming, W. Water pump with shell and impeller made of polyamide 2012.

150. AK Steel Available online: www.aksteel.com (accessed on Aug 5, 2019).

151. Outokumpu Stainless Steel Grades Available online: www.outokumpu.com (accessed on Aug 5, 2019).

152. Aperam Available online: www.aperam.com (accessed on Aug 5, 2019).

153. Acerinox Stainless Steel Available online: www.acerinox.com (accessed on Aug 5, 2019).

154. Midland Bright Steels UK Available online: midlandbrightsteels.co.uk (accessed on Aug 5, 2019).

155. Sandmeyer Steel Available online: www.sandmeyersteel.com (accessed

on Aug 5, 2019).

156. Smiths Advanced Metals Available online: www.smithsadvanced.com (accessed on Aug 5, 2019).

157. West Yorkshire Steel UK Available online: www.westyorksteel.com (accessed on Aug 5, 2019).

158. Nippon Steel Available online: www.nipponsteel.com (accessed on Aug 5, 2019).

159. Interlloy Available online: www.interlloy.com.au (accessed on Aug 5, 2019).

160. MetalTek International Available online: www.metaltek.com (accessed on Aug 5, 2019).

161. Industeel France Available online: industeel.arcelormittal.com (accessed on Aug 5, 2019).

162. Carpenter Technology Available online: www.carpentertechnology.com (accessed on Aug 5, 2019).

163. Kleinmetals Available online: www.kleinmetals.ch (accessed on Aug 5, 2019).

164. Tzeng, G.-H.; Huang, J.-J. *Multiple attribute decision making: methods and applications*; First.; CRC Press, 2011;

165. Baram, J. Material selection for A 2000 HP pump shaft. *Theor. Appl. Fract. Mech.* **1985**, *3*, 1–11.

166. Fluxinos solar pumps Available online: www.fluxinos.com.

167. Mono-pumps; Mono lineshaft pumps Available online: www.mono-pumps.com.

168. Wade, N.S.; Short, T.D. Optimization of a linear actuator for use in a solar powered water pump. *Sol. Energy* **2012**, *86*, 867–876.

169. Findik, F.; Turan, K. Materials selection for lighter wagon design with a weighted property index method. *Mater. Des.* **2012**, *37*, 470–477.

170. GrantaDesign Workshop - CES Selector 2018.

171. Redwood, B.; Schoffer, F.; Garret, B. *The 3D printing handbook: technologies, design and applications (3D Hubs)*; 2017;

172. Imakr Intamsys 3d printer materials Available online: https://www.imakr.com/uk/intamsys- (accessed on Sep 25, 2019).

173. Intamsys 3d printing material properties compare Available online: https://www.intamsys.com/products-compare/ (accessed on Sep 25, 2019).

APPENDIX A

CONCEPTUAL IDEAS FOR GROUNDWATER LIFTING WITH NO BOREHOLE SIZE LIMITATION

As a part of this study's start journey, some following ideas were generated roughly with no borehole size limitation. However, these ideas were dropped as soon as borehole size constraint of 10 inch in rural remote regions from the client was received for up to 200 m head and 25k litres per day.

A.1. Modified Rope Pump

Rope pumps are one of the oldest means of lifting groundwater to the surface. A rope driven by a wheel carries either pistons or small buckets to carry water to the surface as shown in Figure A.1. Current design of rope pumps uses one wheel and the whole rope runs in a cycle. The motor bears the weight of the rope, attached pistons or buckets and the water being lifted up. This cannot be feasible if used for greater depths.

The proposed modified design uses a counter-weight under to a 'to and fro' motion coupled to the motor. It is like a pulley mechanism in an elevator. The motor bears the less load of lifting the weight of rope components and water for a particular lift because the counter-weight will be helping the motor due to its own weight acting downward. This concept can be doubled, tripled or may be configured as a quad or more. Every wheel will be driven by an independent

motor. The configuration is shown in Figure A.2. The possible advantages and disadvantages are discussed in Table A.1.

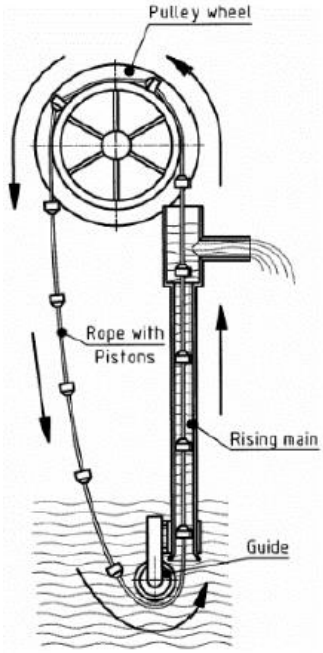

Figure A.1: Typical rope pump.

Table A.1: Possible advantages and disadvantages of modified rope pump concept.

Advantages	Disadvantages / Solution to limitations
1. Cheap due to less complexity. May not require piping. Less motor power input due to the assist of the counter-weight. 2. All maintenance can be done on the top. 3. Less PV input. 4. If there is loss of power, this system can be operated manually.	1. Rope, pistons / buckets weight for greater depth. This point can fail if the rope cannot bear the weight of its components and along with the water weight to be lifted for greater head such as 200 m. 2. For 25k L/day which is equivalent to 0.5 L/s if operated for 12 hours, the speed of the system could be very high. It depends upon the size of the buckets or pistons to lift certain amount of water. The speed of the pump can be an issue for its working components motor fatigue, rope fatigue etc.

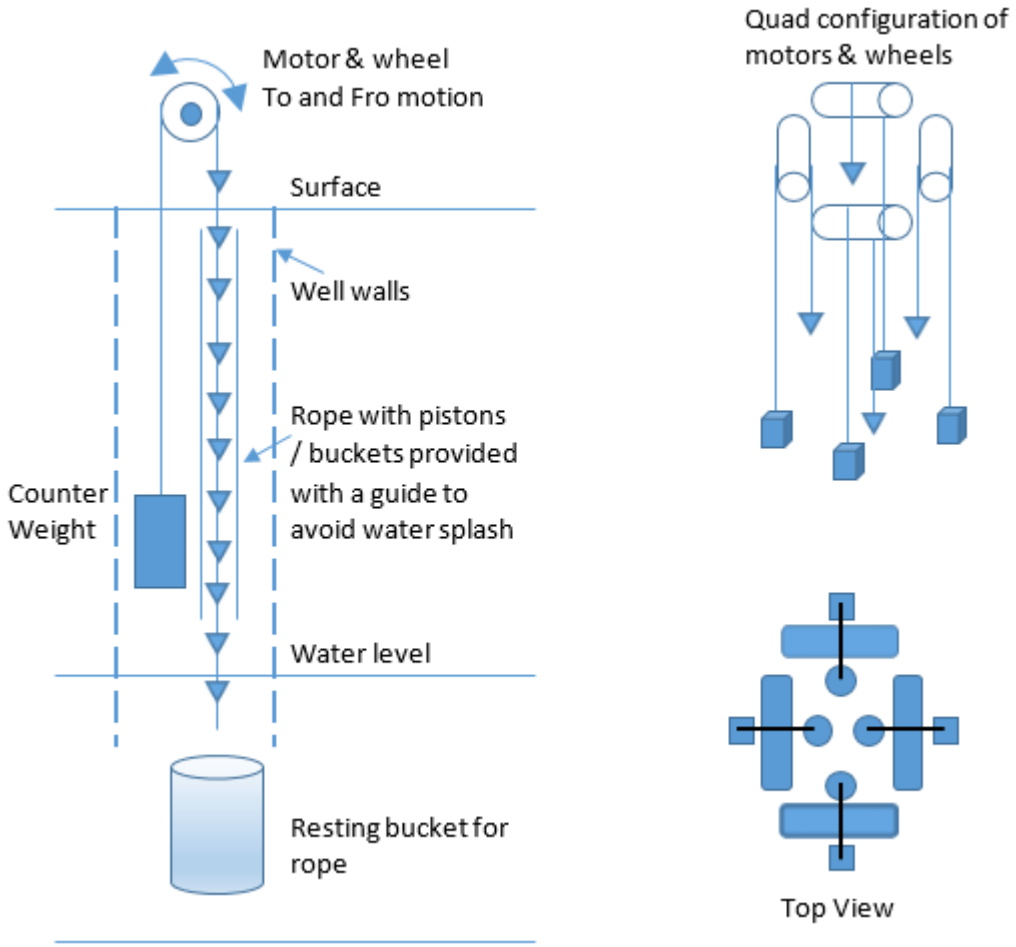

Figure A.2: Modified rope pump concept.

A.2. Motor Coupled Cam Operated Diaphragm Pump

The proposed design consists of a motor coupled to a cam. The cam operates individual diaphragms pumps in their respective cylinders. The system can be mounted on the ground surface for suction effect for the groundwater AND/OR it can also be installed as a submerged pump into the well as shown in the Figure A.3. The submerged part can be used for the lifting effect. Most available surface diaphragm pumps in the market can lift the water for maximum 70 m which fails this study design head of 200 m. Therefore, in order to make it to work, a tertiary pump can also be installed somewhere in the

middle of the head so that the third pump will assist of the lift as well. The advantages and disadvantages are discussed in Table A.2.

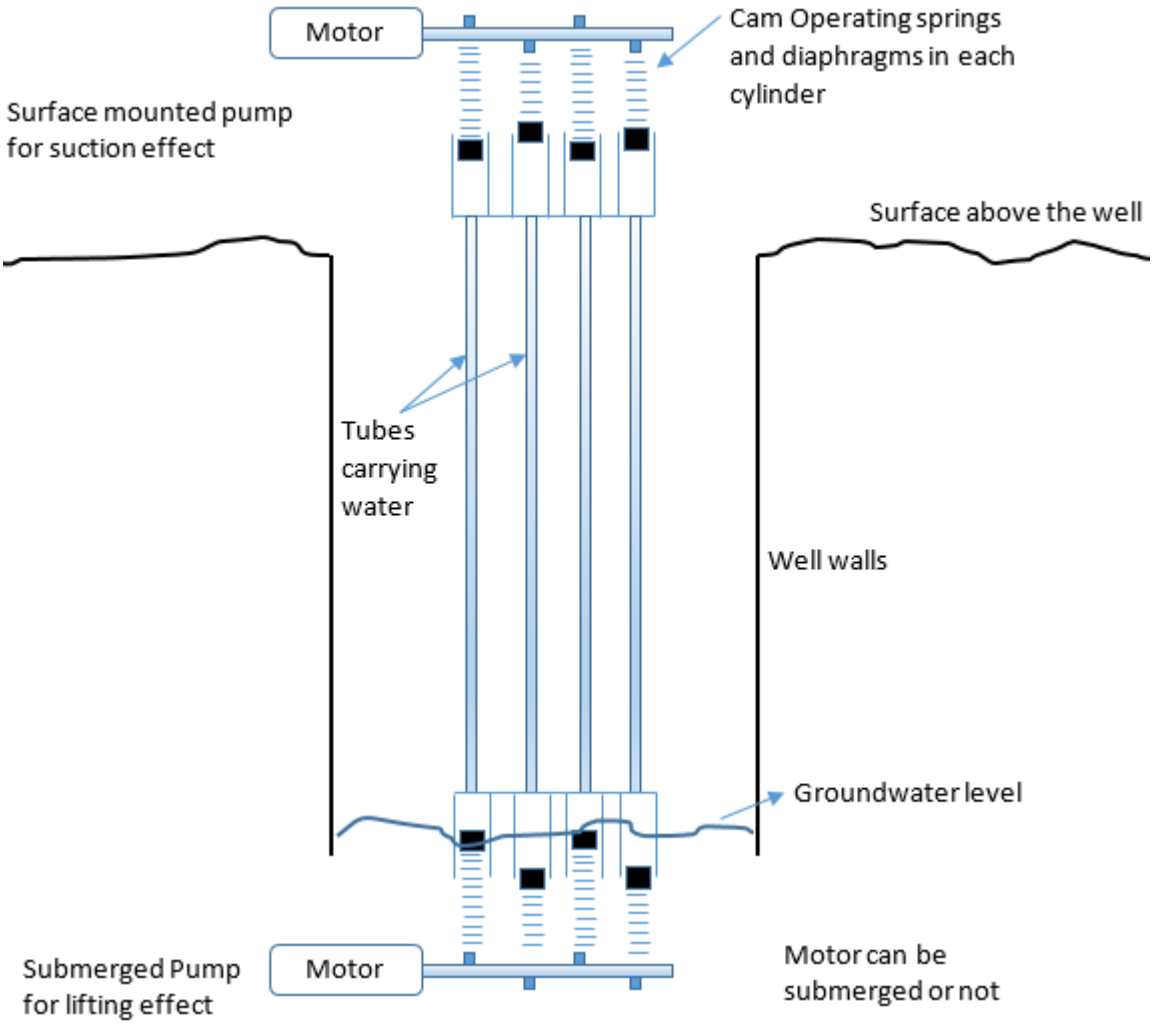

Figure A.3: Motor coupled cam operated diaphragm pump.

Table A.2: Possible advantages and disadvantages of cam operated diaphragm pump concept.

Advantages	Disadvantages / Solution to limitations
1. Cheap, less cost due to usage of tubes instead of long cast iron or PVC piping. 2. Less PV input due to less heavy components like impellers and shafts. Also, diaphragm is much lighter compared to a centrifugal pump impeller. 3. Tubing replaces the traditional piping.	1. Suction limitation, as the head is high 200 m. As said earlier most diaphragm pumps available in the market operate maximum for 70m head. So more than two pumps can cover this drawback. 2. Complexity of the system due to more components. 3. Maintenance issues because it would be difficult for the local people to disassemble. Also for the submerged pump. 4. Size of the bottom section. 5. If loss of power, cannot operate.

A.3. Motor Powered Capsule/Container Lift

The proposed design uses the capsule or container to lift the water up along with the motor, only if the weight of the motor(s) is less than the traditional components e.g. rope and buckets. The amount of water being lifted up depends upon the size of the capsule and the speed of the motor. When the motor reaches top at the surface, the water inside the capsule is taken out, the motor gears get disengage from the gear line and fall freely to the bottom of the well to refill the capsule. The motor(s) are stopped at the bottom by soft braking system where the gears again engages with the gear line. After the capsule at the bottom refills, the motor(s) again move towards the surface for another cycle. The proposal is shown in the Figure A.4. The advantages and disadvantages of this system are discussed in Table A.3.

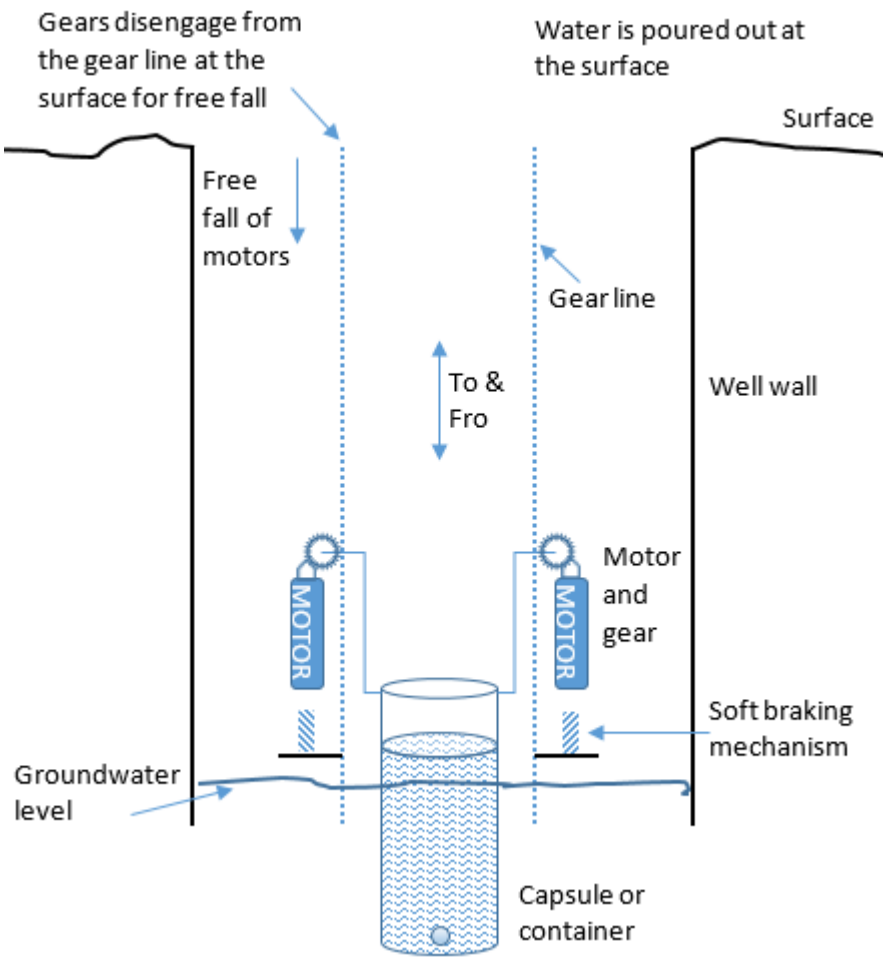

Figure A.4: Motor powered capsule lift.

Table A.3: Possible advantages and disadvantages of motor-powered capsule lift concept.

Advantages	Disadvantages / Solution to limitations
1. Simple except the engaging and disengaging mechanism. 2. Cheap, but not actually for gear line in well for high depths. 3. Can lift bulk quantity of water in one cycle. 4. Less weight capsule/container can be used e.g. plastic bags, glass etc. 5. Can be lowered easily if groundwater level goes down by lowering the gear line. 6. No other loads for the motor(s) to bear such as shafts, impellers, gears etc. 7. If loss of power, can be operated manually	1. Complex design in terms of engaging and disengaging of the gears with the gear line and free fall soft braking mechanism. 2. Free falling of the motor can damage the components after certain time. So proper braking system is needed. 3. Frequent of ups and downs by the motor(s) may result in frequent maintenance and components wear. 4. Oil lubrication can drip down into the groundwater and further reduce water quality despite sand content.

A.4. Motor Powered Piston Pump

This proposed design consists of a hollow piston in a cylinder which acts as the positive displacement of fixed amount of water inside the pump. The piston is operated through a crankshaft and connect rod kind of mechanism just like in conventional mechanical engines. Both upper and lower surface of the piston are open to valves which closes and opens on their respective stroke. In the downward stroke, the lower valves open, drawing in fixed amount of water, whereas at this stage the upper valve is closed. In the upward stroke, the lower valve closes and the upper valve opens to push the fixed enclosed amount of water inside the piston to push up. Again, in the downward stroke the lower valve opens again, and the cycle is repeated. The piston is equipped with seals to avoid the leakage of water. The motor(s) of the system can be used in both submerged and non-submerged applications. The higher the speed of the piston/motor(s) the higher is the flowrate on the surface. This system can be coupled with more cylinders to increase the flowrate. The schematic is shown in the Figure A.5. The advantages and disadvantages of this kind of proposed pump are discussed in Table A.4.

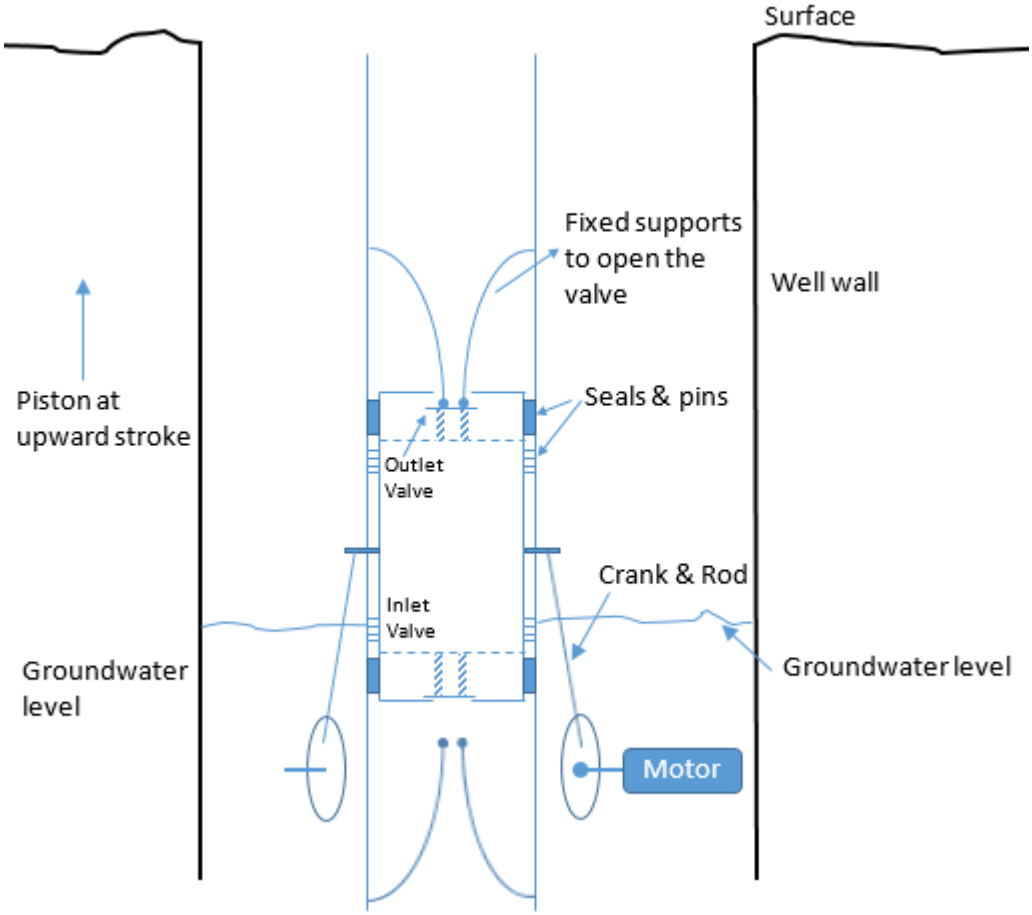

Figure A.5: Motor powered piston pump (upward stroke).

Table A.4: Possible advantages and disadvantages of motor-powered piston pump concept.

Advantages	Disadvantages / Solution to limitations
1. Can deliver high head flowrate. 2. More configurations can be connected to increase the flowrate through one single channel. 3. Easy to maintain each component. 4. If off power, can operate manually.	1. Size in the bottom section of the well. Need larger well compared to traditional pumping systems. 2. If water level goes down, it cannot be lowered. For this more piping must be connected from the surface. 3. Complexity is the crank and rod mechanism and their maintenance. For this a lubrication pipe can be lowered from the surface for maintenance. 4. Weight of the components e.g. crankshaft and connected rod, increases the load for the motor(s). 5. Motor disassembling an issue for the maintenance from top.

APPENDIX B

3D PRINTING OF CONCEPT PUMP MODEL FOR MECHANISM AND OPERATIONAL TESTING

The developed conceptual model of groundwater piston pump was tested for mechanism and submerged pumping operation using 3D printing technique using polymeric material to save cost rather than metal machining or printing. The whole pump was fabricated at full scale. A manufacturing path comparison between 3D printing technique and commercial machining is shown in Figure B.1.

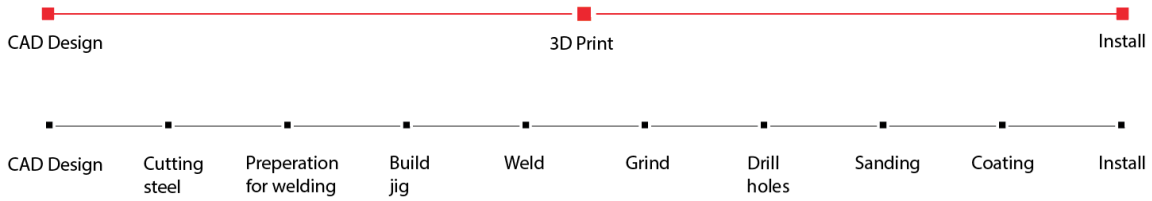

Figure B.1: Comparison of manufacturing paths between 3D printing and conventional machining processes [171].

B.1 Objectives of 3D Printing of Conceptual Pump

The following objectives were set for the 3D printing of the conceptual pump model.

1. Test the working mechanism of the pump.
2. Test water pumping ability of the pump for the mechanism.
3. Identify possible changes in the model needed.

B.2 3D Printing Setup

B.2.1 Printing Process Selection

The 3D printing process selected was FDM (Fused Deposition Modeling) because it is cheaper and supports cheaper printing materials. Most home desktop printers use FDM technology. The material cost of a FDM process is around $25/kg coil of filament compared to other 3D printing processes such as SLA costing $150/kg or SLS (Selective laser sintering) with Nylon around $70/kg. Additionally, FDM process is also feasible for non-critical load prototyping and consume less printing time [171].

Although FDM is not directly recommended for functional prototyping with moving parts due to low quality of surface finish which is due to printed layers accumulated on each other. Even with smallest layer height, the surface finish is not smooth as a machined process or other 3D printing processes such as SLS/SLA etc. Post processing is required on the prints in order to improve the quality such as sanding, acetone dipping or spraying, material removing machining etc.

An industrial grade 3D printer 'INTAMSYS FUNMAT PRO HT' with larger printable volume W450 x L450 x H600 mm^3 was used in the printing of the conceptual model with volume of around W143.6 x L228.01 x H425.75 mm^3.

B.2.2 Printing Material for FDM Process

The criteria for the selecting the printing material was same as the printing process i.e. a cheaper material with the ability to withstand non-critical

loads for functional prototyping. A comparison of a few printing materials supported by FDM process is shown in Table B.1. Following the selection criteria, three candidates - PLA, ABS and PC - were shortlisted and decision was made between ABS and PC as PLA prints are too brittle to work as functional prototypes. ABS was finally selected as the printing material with much cheaper cost and support for functional prototyping than PC.

Table B.1: Comparison of 3D printing materials for FDM process [172], [173].

Material / Attribute	**PLA**	**ABS**	**PC**	**Nylon**	**PEEK**
Cost (£/kg)	35	35	55	75	630
Tensile strength (MPa)	103	480	65	65	3700
Elongation (%)	180	20	130	231	9.1
Ability for functional prototyping	No (visual aids only)	Yes	Yes	Yes	Yes

PLA	Polylactic acid / Polylactide
ABS	Acrylonitrile butadiene styrene
PC	Poly Carbonate
PEEK	Polyether ether ketone

B.2.3 CAD Model to Prints G-code Generation and Parts Assembling

The concept pump CAD model (see Figure 3.11) was split into individual components such as piston, shaft, casing and front flow manifold. A 3D printer works similar to a CNC machine which requires a g-code to print. A g-code is a set of instructions for a computer numeric control unit (equipped inside the printer) to activate various elements such as extruder motion, heating, cooling,

printing speed etc. These instructions are defined in a program called 'slicing' which finally generates the ready to use g-codes for prints.

Each component from the concept model was transformed into a meshing format 'stereolithography (stl)' which the 3D printer slicing software reads. This format is required to generate g-codes. An illustration of sliced pump parts is shown in Figure B.2 which are now generated as g-codes. The blue surfaces are the supports for the prints and red/yellow surfaces represent the body. The printer initiates the printing from the bottom layer and ascending to the top. An illustration of printed parts is shown in Figure B.3. The prints were initiated with some hollowness (up to 80%) to avoid over use of the materials.

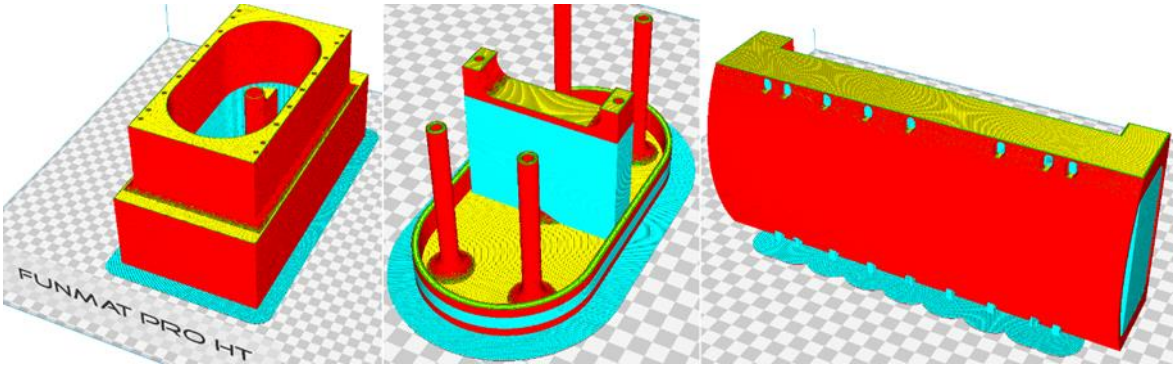

Figure B.2: An illustration of sliced pump parts; casing, piston and manifold.

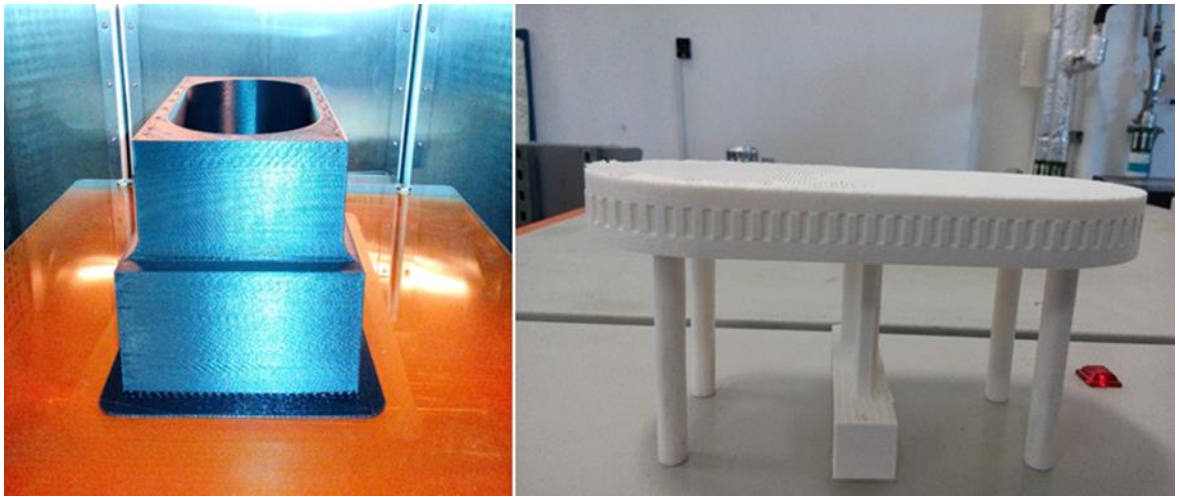

Figure B.3: An illustration of printed pump parts; casing and piston.

The individual printed parts from the printer were post processed to improve the surface quality i.e. improve smoothness by sanding the locations wherever components were in motion such as the casing cylinder, piston reciprocating surfaces and tight tolerances etc. Post processing also involved removal of extra printed features such as print supports. Later on, all parts were assembled together as shown in Figure B.4.

Figure B.4: An illustration of printed pump parts assembly.

B.3 Mechanism and Pumping Tests Outcomes

The 3D printed model of the concept pump was put to a submersible test. The setup included a small high torque 30 rpm DC motor, a 12 V battery, a water filled container and motor speed controller. The assembly was submerged in water to the point just below the battery to avoid damage. The testing showed

successful running of the mechanism and water pumping operation, an illustration of which is shown in Figure B.5.

Figure B.5: Mechanism and water pumping test of 3D printed concept pump model.

The outcomes from the test results drawn are as follows;

- The scotch-yoke mechanism worked successfully for the reciprocating groundwater submersible piston pump concept which directly engages the piston with shaft without using any meshing gears, connecting rods, and pins normally found in a reciprocating piston pump. Also, the no use of long piston rod made of steel or polymeric material is also justified.
- The 3D printed pump model successfully pumped water while in submerged stage running at 30 rpm. However, it was recorded that in two strokes, 700 ml of water was pumped out which is less than the 887.5 ml per stroke. The reason is because of leakages through the piston seal

and the swing valves (outlet and inlet) made from plastic films. The pumping would surely improve with proper sealing and valves in place.

- The motor placement also proved to be feasible which was directly coupled to the pump shaft just above the casing. However, a sealed motor casing could be devised for real pump model for submersible operation or could be installed directly from the market.
- The high torque geared motors are recommended for this conceptual piston pump real model which use less power and support high loads.
- Analysing the 3D printed model, a feature was identified to be less effective during the mechanism test. The shaft supports were not holding the shaft firmly in position and were remodeled in the CAD program as shown in Figure B.6. Originally modeled supports (2D) were only drafted to support the backward motion of the shaft during the discharge stroke when the piston faces maximum load. Slight lateral movements in shaft were observed normal to the backward motion which were restricted using the modified version of the supports. This also proved to be an advantage of considering 3D printing prototyping option over the conventional manufacturing which could have costed much higher.

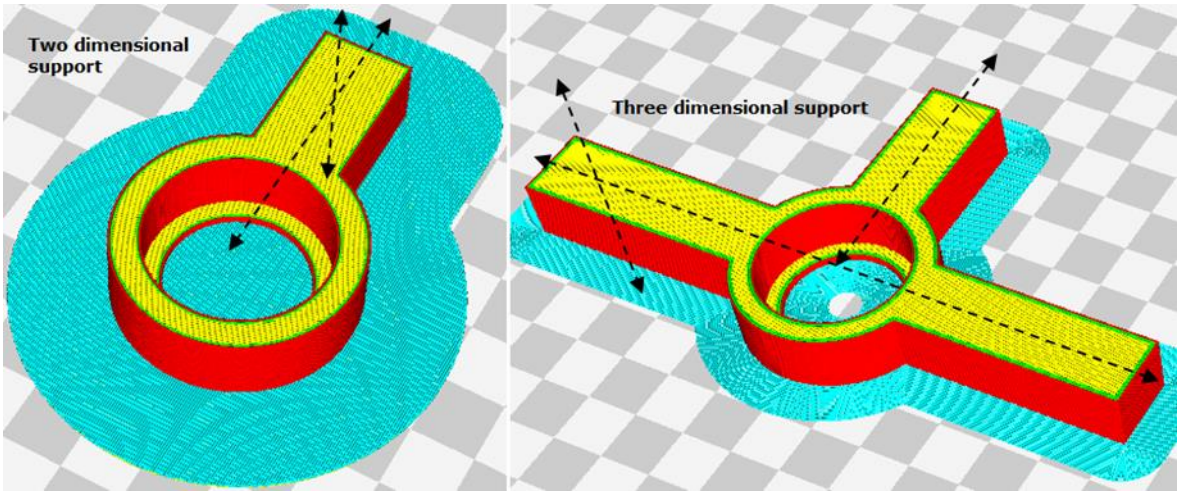

Figure B.6: Shaft motion supports; original drafted (left) and modified (right).

- The lighter 3D printed material 'ABS' proved to be a cost effective functional prototyping material than polycarbonate. No damage was observed before and after the tests.

B.4 Conclusion

The overall purpose of building a 3D printed prototype of concept piston pump was to test simpler scotch-yoke mechanism, pumping operation and to identify any useful changes for futuristic real manufacturing. The submerged experimental analysis of the printed pump successfully demonstrated and justified the goals of this study. It is justifiable that the real produce of this concept pump would almost work as designed. The study also identified a few regions of improvement such as the shaft motion supports in the casing to firmly restrict slight unnecessary fluctuations.

Conclusively, the study supports the future manufacturing of the real concept model using metal (stainless steel alloy) based on the successful outcomes of this study.

APPENDIX C

FE MESH INDEPENDENCY CHECK FOR CONCEPT PUMP COMPONENTS

The following charts show mesh sensitivity or independency analysis carried out on each concept pump component against respective stresses.

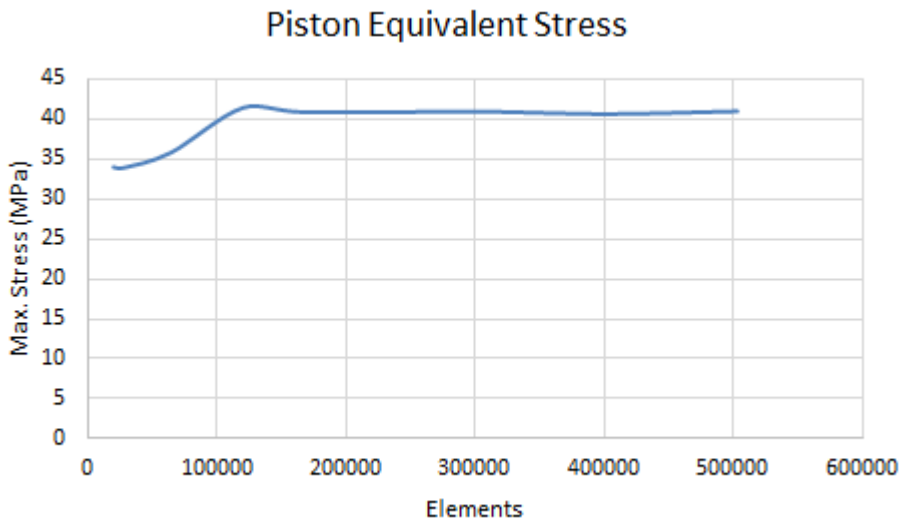

Figure C.1: Mesh sensitivity graph for maximum piston stress.

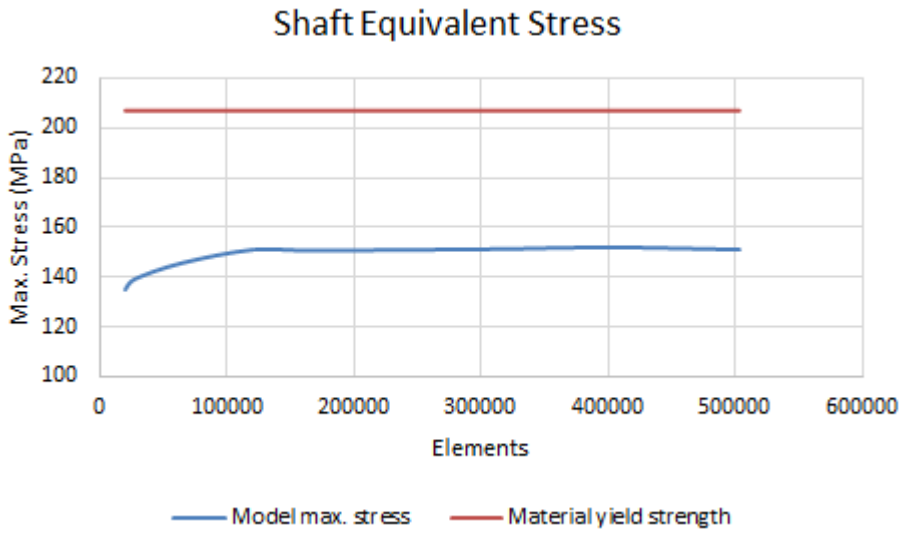

Figure C.2: Mesh sensitivity graph for maximum shaft stress.

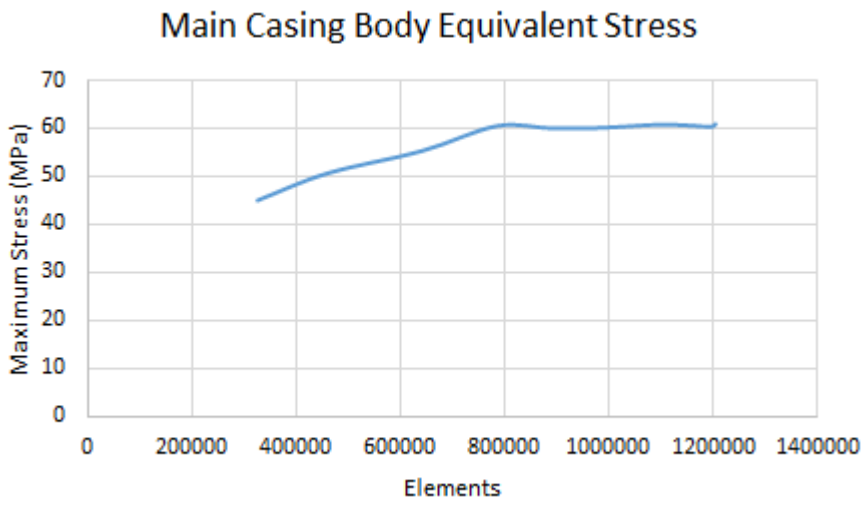

Figure C.3: Mesh sensitivity graph for maximum stress in main casing body.

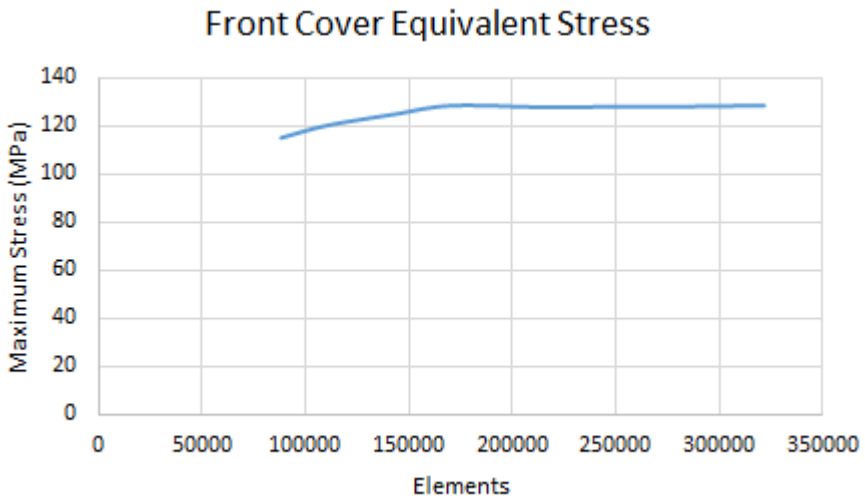

Figure C.4: Mesh sensitivity graph for maximum stress in casing front cover.

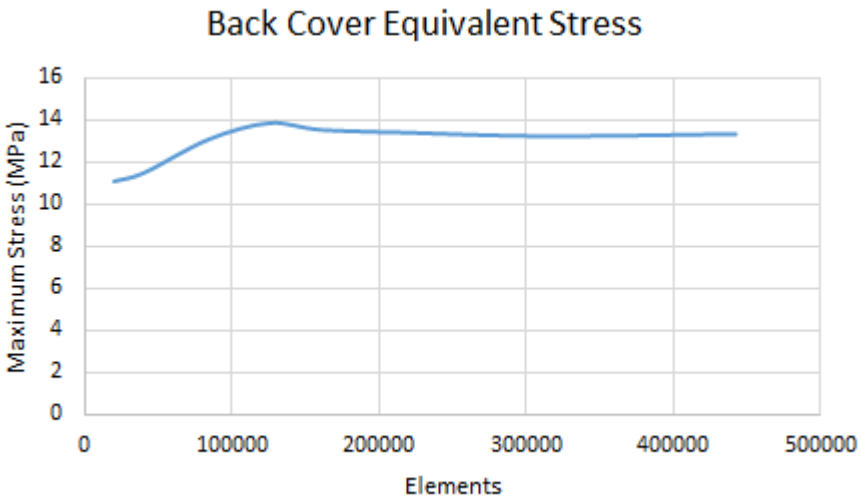

Figure C.5: Mesh sensitivity graph for maximum stress in casing back cover.

APPENDIX D

ANALYTICAL VALIDATION OF FE ANALYSIS RESULTS

The FE analysis results for the concept pump piston and shaft components were validated analytically at different locations under different loading conditions. The FE results presented in Table 4.2 are shown with theoretical calculations in this appendix.

D.1 Shaft Top Section above Centre Top Bearing under Torsion

The concept pump shaft was analysed using FE analysis with a fixed support boundary condition at the top face which means the shaft is coupled to the motor which restricts its rotation motion. This condition has torsional effects of the top section of the shaft as the bottom section is free to rotate. The top shaft section above the middle bearing is under torsional stress due to the moment created by the piston force through shaft slider as shown in Figure D.1.

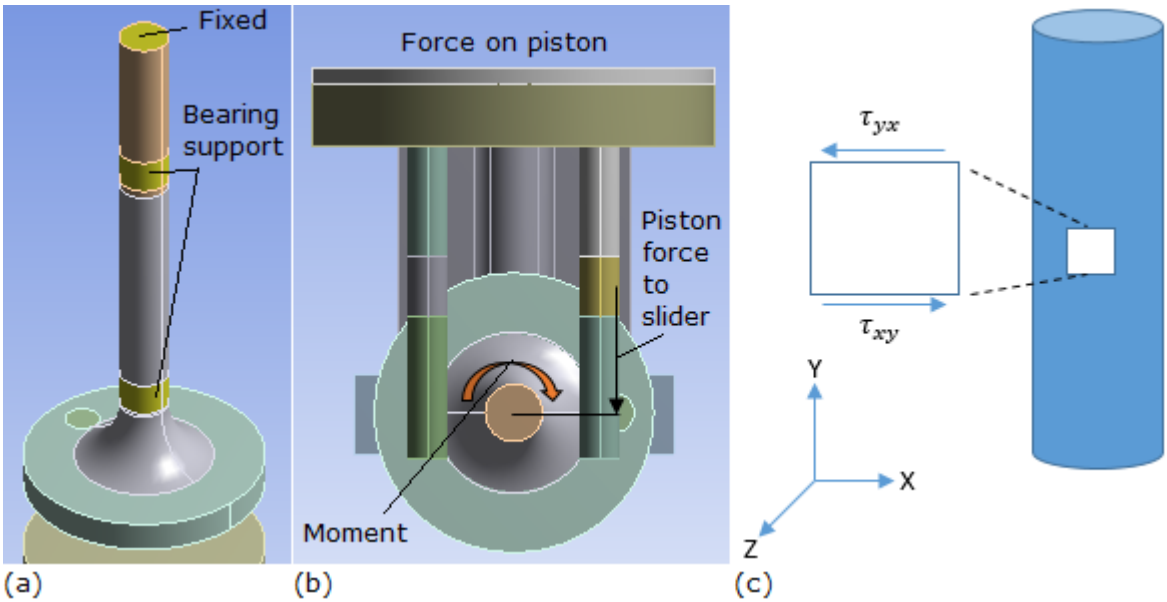

Figure D.1: (a) Fixed and free boundary condition at top shaft section, (b) Moment on shaft due to piston force, (c) shear stress element diagram on the outer diameter of top shaft section.

The shear stress acting on the top shaft section can be evaluated by equation 4.1, where polar moment of inertia is '$J = \frac{\pi d^2}{32}$'. This gives shear stress of 46.68 MPa compared to FE result of 47.2 MPa. The equivalent stress can also be evaluated using Equation 4.4 where normal stresses terms become zero and only shear stress term 'τ_{xy}' is present. The maximum equivalent stress is calculated to be 80.86 MPa compared to FE value of 78.34 MPa.

D.2 Shaft Section below Centre Top Bearing under Combined Bending and Torsion

The shaft section just below the middle shaft bearing faces combined loading condition i.e. twisting and bending. The twisting occurs due to the free moment supported by the bearings with top face as fixed, and, bending occurs

due to the piston force transmitted to the shaft slider. The combined loading condition is shown in Figure D.2. The point 'A' experiences maximum stresses under the combined loading.

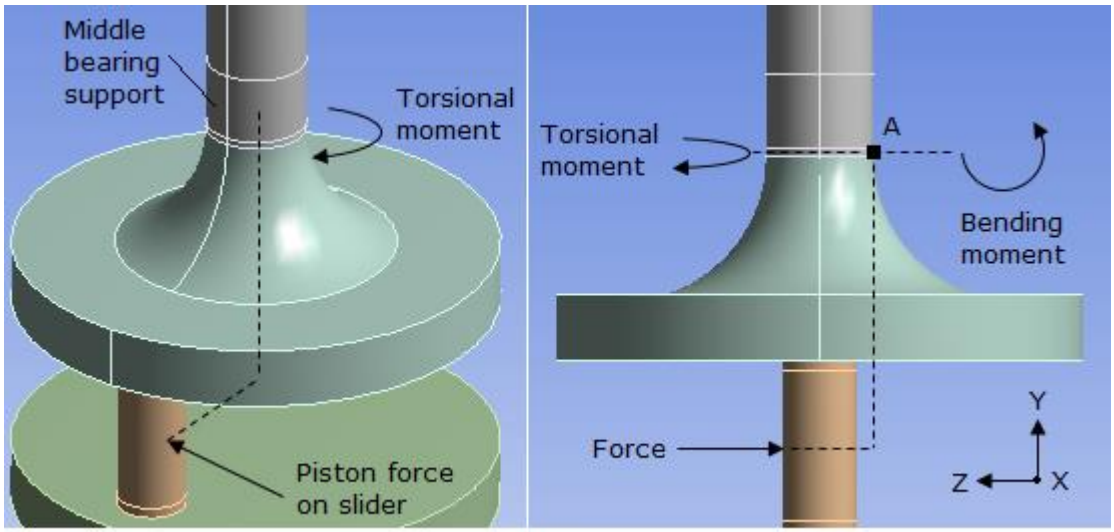

Figure D.2: (a) Torsional moment due to piston force on slider, (b) side view showing both torsional and bending moments as combined loading at point 'A'.

The point 'A' if taken as an element, also experiences combined moments which cause torsional and bending stresses as shown in Figure D.3. The combined moment can be calculated using Equation 4.3, and based on which, the torsional and bending stresses can be evaluated using equations 4.1 and 4.2, respectively. The equivalent stress from Equation 4.4 gives 142.32 MPa under bending 'σ_y' and shear 'τ_{xy}' stress terms compared to FE value of 147.43 MPa.

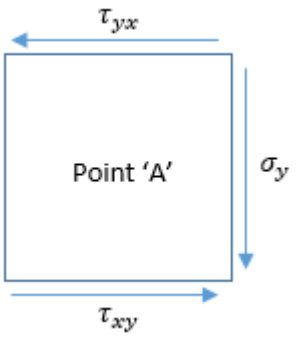

Figure D.3: Elemental diagram of point 'A' under torsional and bending stresses.

D.3 Piston Supports at Linear Bearing Edge under Bending

The free body diagram of forces acting on the piston supports is shown in Figure D.4. The four piston supports restricted by the linear bearings in the casing are under the bending load along their lengths due to the position of the shaft slider at extreme moment-arm of the piston at the contact region. The piston faces a force 'F' of 1100 N and so as the slider as a reactive force 'Fs' slightly position outward to the piston support. The reactive force 'R' acting on the piston support is responsible for supporting the bending which can be calculated by the summation of moments at point 'A' as shown by equation D.1.

$$F(21.8) + Fs(3.6) + R(48.9) = 0 \qquad \text{(D.1)}$$

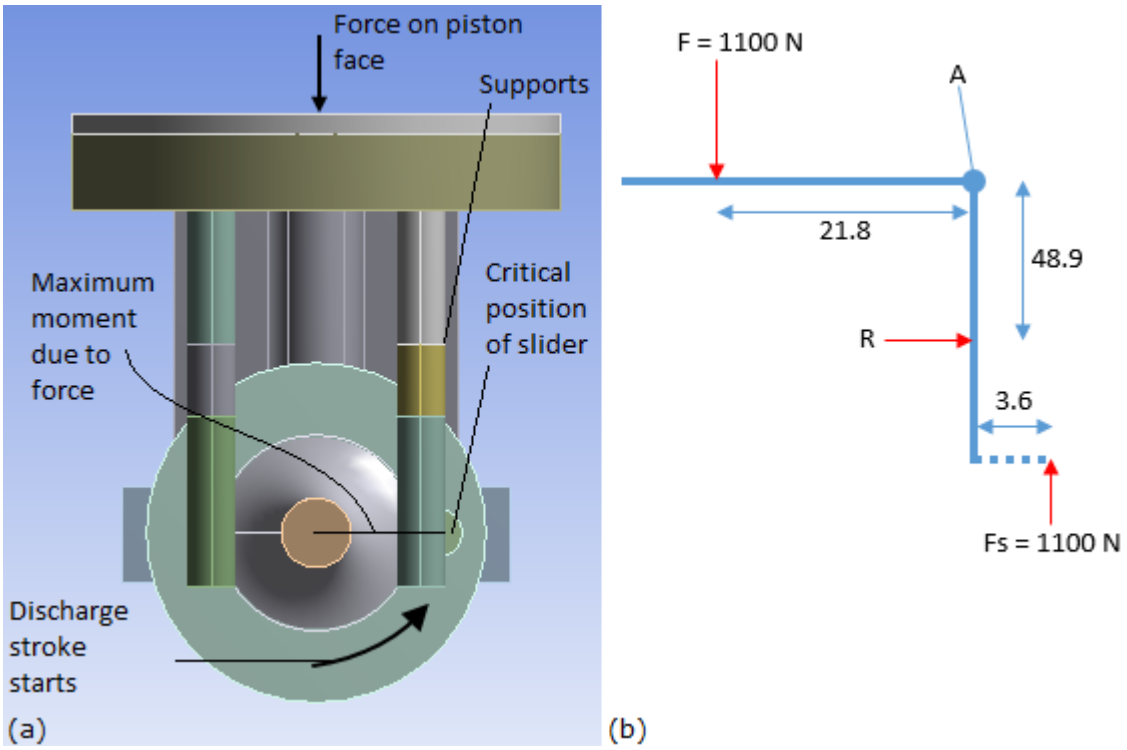

Figure D.4: (a) Schematic of piston-shaft assembly under load, (b) Free body diagram of forces and distances responsible for bending in piston supports.

There are four piston supports and the slider reactive force acting in the middle is responsible for the two sections of the piston (top and bottom). Hence, the force 'R' acting on once piston support is found to be 71.42 N. Hence, the maximum bending stress in single piston support along its length till point of action of force 'R' is calculated by equation 4.2, where, $I = \frac{\pi}{64}(D_o^4 - D_i^4)$, $y = \frac{D_o}{2}$. The bending stress at outer diameter of piston support is found to be 26.29 MPa closer to FE value of 27.17 MPa. The probed FE result of piston bending stress is shown in Figure D.5 where the maximum stress occurs at the singularity location.

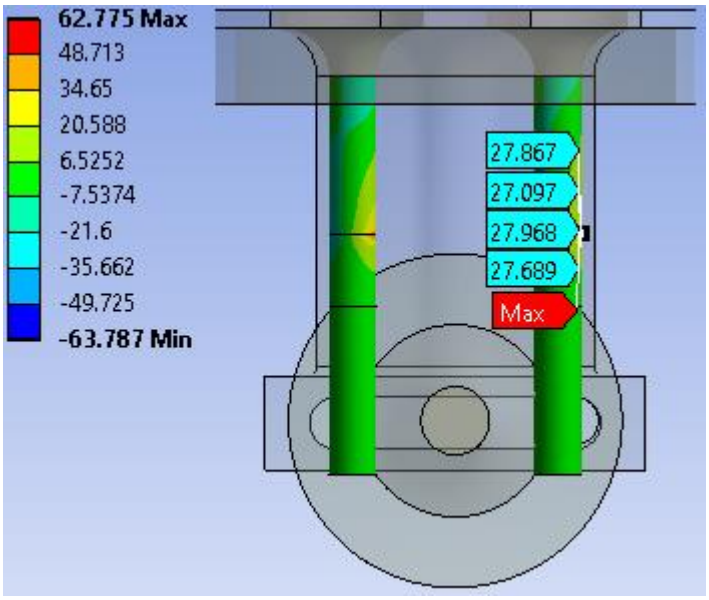

Figure D.5: FE result of bending stress in piston supports.

D.4 Piston Middle Web Section under Buckling Load

The piston middle web section is subjected to the buckling when the force acts on piston head. The middle web buckling condition depicts the one end fixed (at contact region) and one end free (where force acts). In order to check the buckling occurrence, the critical buckling load was calculated analytically using equation 4.6. The rectangular cross section of the web was considered as shown in Figure D.6. The second moment of area along the length of the web is calculated as,

$$I = \frac{wt^3}{12} \tag{D.2}$$

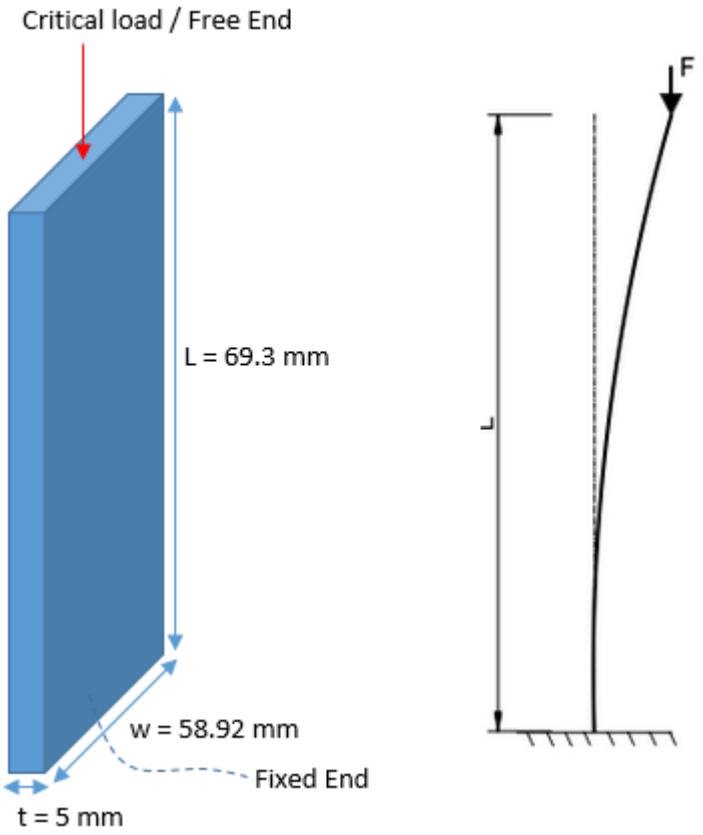

Figure D.6: Piston middle web section with free and fixed condition; length 'L', width 'w' and thickness 't' (left), line body view of the buckling (right).

The critical buckling load using equation 4.6 was found to be 60843.4 N while FE results showed critical load of 60657 N. The critical buckling load is far greater than the piston force due to weight of the water i.e. 1100 N which means the designed piston web does not go into buckling. It is notified here that ANSYS FE program does not show the critical load as contours but rather as a maximum load where deformation due to buckling starts as shown in Figure D.7.

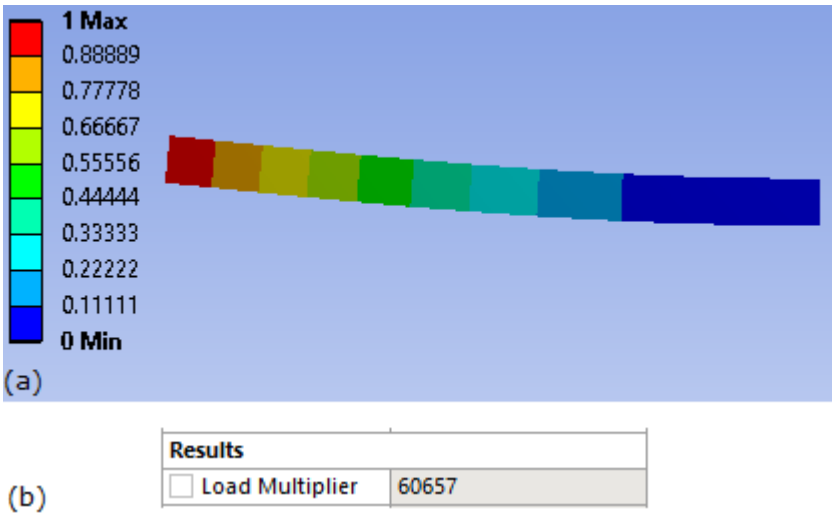

Figure D.7: (a) Piston middle web section deformation (mm) due to critical buckling load, (b) screenshot of the critical load causing buckling.

D.5 Piston and Shaft Contact under Contact Stress

The FE results of piston shaft contact region were validated using Hertz contact Equations 4.7 and 4.8. The maximum contact stress, shear stress and contact width were calculated analytically. The shaft slider and piston rectangular contact area depicts cylinder over plane condition of Hertzian contact as shown in Figure D.8. The piston force can be equated as the reactive force of the slider and thus, piston contact area can be made as fixed while the force acts on the slider (see Figure 4.10). A 2D schematic of contact width is shown in Figure D.9.

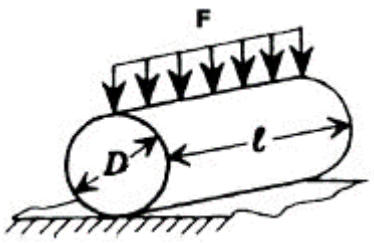

Figure D.8: A Hertzian contact of cylinder over plane configuration, 'F' force on the cylinder, 'D' diameter and 'l' cylindrical contact length.

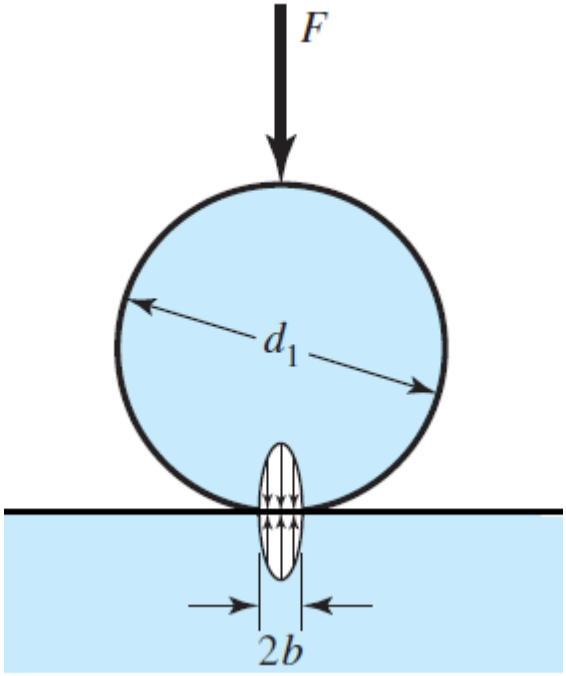

Figure D.9: A schematic of cylinder over plane showing elliptical contact width formation under the application of force.

The material properties in Equations 4.7 and 4.8 were taken from Table 4.1. The slider diameter here is 10 mm and length is 20 mm and the acting force is 1100 N. For cylinder over plane scenario, the value of 'd_2' in Equation 4.7 is infinite, thus eliminating the term '$\frac{1}{d_2}$'. The half contact width 'b' is calculated to be 0.0573 mm, whereas FE evaluated 0.0591 mm. The maximum shear stress was found to be 183.42 MPa using Equation 4.8, whereas FE analysis gave 184.73 MPa. The maximum contact stress of 611.4 MPa was found analytically '$\sigma = \frac{2F}{\pi bl}$', whereas, FE resulted 604.45 MPa.

APPENDIX E

BLACKHAWK PISTON ROD PUMP QUOTATION

Blackhawk Technology Company
21 W 211 Hill Ave
Glen Ellyn, Illinois 60137
Tel: 630-469-4916
Fax: 630-469-4896

QUOTE

Date	Quote #
04/01/19	BLKQ5692

Sold To:
Azeem Uddin

Phone:
Fax:

Ship To:
Azeem Uddin

Phone:
Fax:

Here is the quote you requested.

Terms	Rep	Ship Via
NET 30	Ben Bertane	UPS

Qty	Part #	Description	Disc	Unit Price	Ext. Price
		Pump Actuator			
1.00	200-ED422	Apollo Driver- 42RPM - DC		$3,420.00	$3,420.00
1.00	810-SCHRB	Delrin Cartridge Assembly, with 1in Hat Ring Buna Seals		$226.80	$226.80
1.00	700-LU100	Apollo Lubricator Assembly		$321.21	$321.21
1.00	WS-10-2011	10x2x(1.25x1.5)x1 Steel Flanged Well Seal		$496.00	$496.00
1.00	1000-BK03	10",12" Flange Bolt Kit-Steel (12 Bolts)		$140.00	$140.00
		Down Hole Assembly			
400.00	RO-70-0250	3/8in Fiberglass Drive Rod-Per Foot		$4.00	$1,600.00
1.00	100-DH152	Pump Barrel, 101 SS, Includes internal Foot Valve Assembly, 101 SS Strainer, 1-1/4" SS Tee		$788.00	$788.00
1.00	400-PA120	Piston, 101 Delrin U-Cup, No Seals		$271.36	$271.36
1.00	800-P01DSB	Seal Kit, Piston, 101, Buna		$9.28	$9.28
		Solar Panel			
1.00	300-SP155	DC Apollo Solar Panel Package-300W/24 Volt Solar Panel, side of pole mount (Fits a 3"-4.5" pole), 10Amp Solar Controller D, 30 ft Cable		$1,817.00	$1,817.00

SubTotal	$9,089.65
Shipping charges will be determined at time of shipping.	
Total	**$9,089.65**

04/01/19 09:34:14 Page 1